Jointly Organised by:

THE HONG KONG INSTITUTION OF ENGINEERS 香港工程師學會
Geotechnical Division 岩土分部

HKGES 香港岩土工程學會 Since 2003

THE HKIE GEOTECHNICAL DIVISION 35TH ANNUAL SEMINAR, 2015

SOIL-STRUCTURE INTERACTION: FROM MODELLING TO OBSERVATIONS

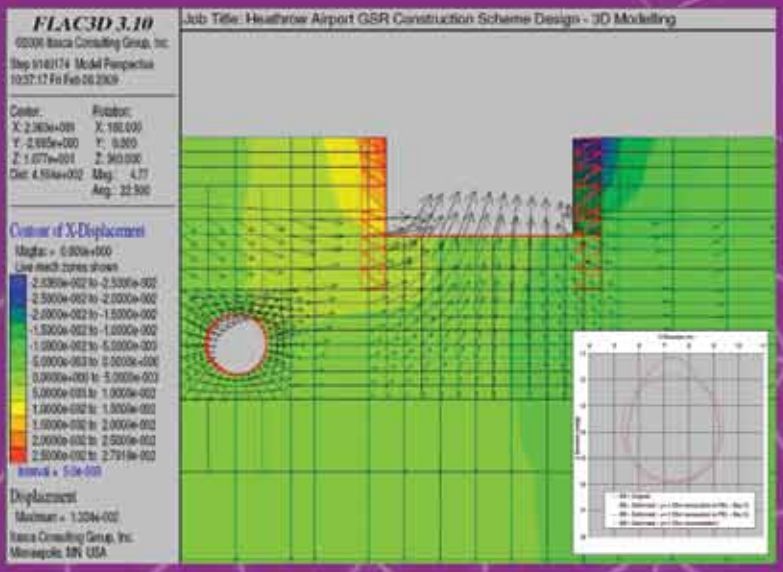

Supporting Organisations:

THE HONG KONG INSTITUTION OF ENGINEERS 香港工程師學會
Civil Division 土木分部

THE HONG KONG INSTITUTION OF ENGINEERS 香港工程師學會
Structural Division 結構分部

With The Compliments
to
The Hong Kong Institution of Engineers
Geotechnical Division 35th Annual Seminar

我們的主要業務包括：
Our Business includes:

- 基礎工程
  Foundation Works
- 斜坡及擋土牆長遠防治山泥傾瀉工程
  Construction of Landslip Preventive and Mitigation Works to Slopes and Retaining Walls
- 道路及渠務工程
  Roads and Drainage
- 水務工程
  Waterworks
- 地盤平整工程
  Site Formation

CIC 中国地质工程集团公司
CHINA GEO-ENGINEERING CORPORATION

香港灣仔港灣道 30 號新鴻基中心 24 樓 2421-25 室
Rm. 2421-25, 24/F., Sun Hung Kai Centre, 30 Harbour Road, Wanchai, Hong Kong
Tel: (852) 2511 9001 Fax: (852) 2580 0697

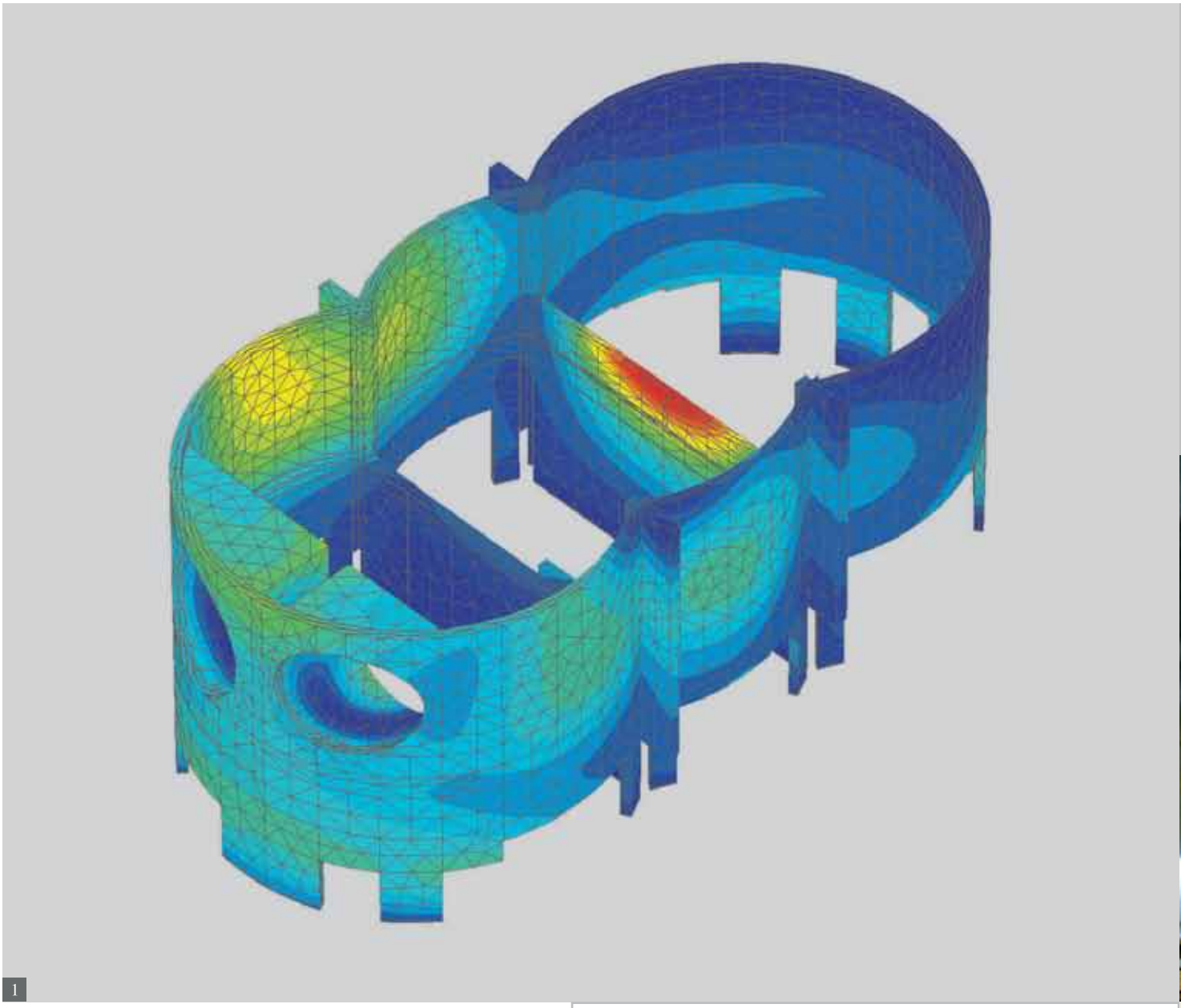

1

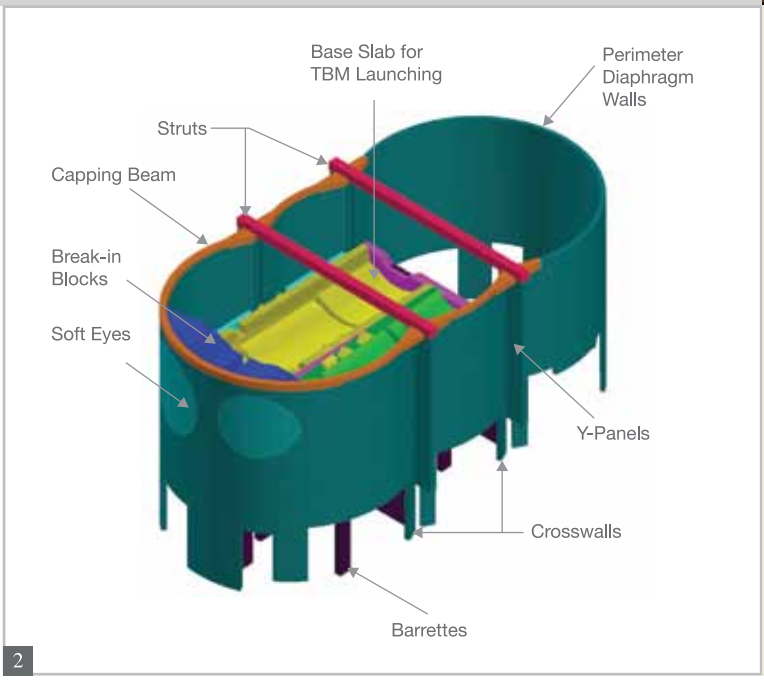

2

Image

1&2. 3-D FE analysis for cost effective caterpillar shape TBM launching shaft for Tuen Mun-Chek Lap Kok Link

3&4. 3-D analysis for integrated cavern and tunnel design for MTR SIL Contract 901

5. 3-D Plaxis analysis for piled raft foundation design for Lotte World Tower

ARUP

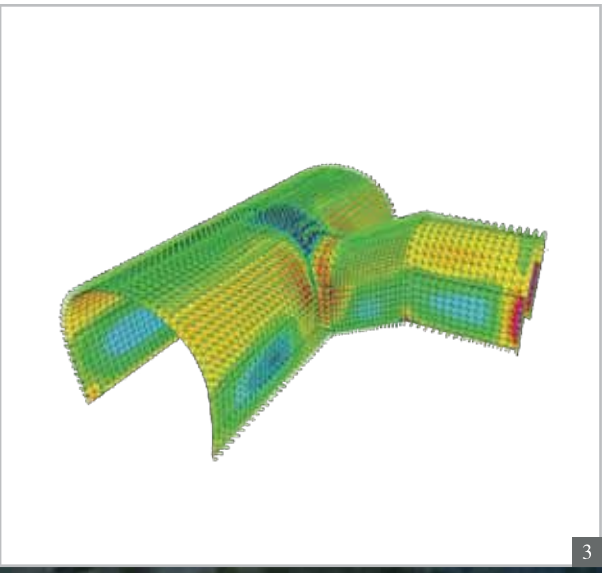

3

4

Innovating to meet complex challenges

As an acknowledged leader in geotechnics, Arup pushes the skills and science of designing and building structures in all ground conditions, providing robust and advanced solutions.

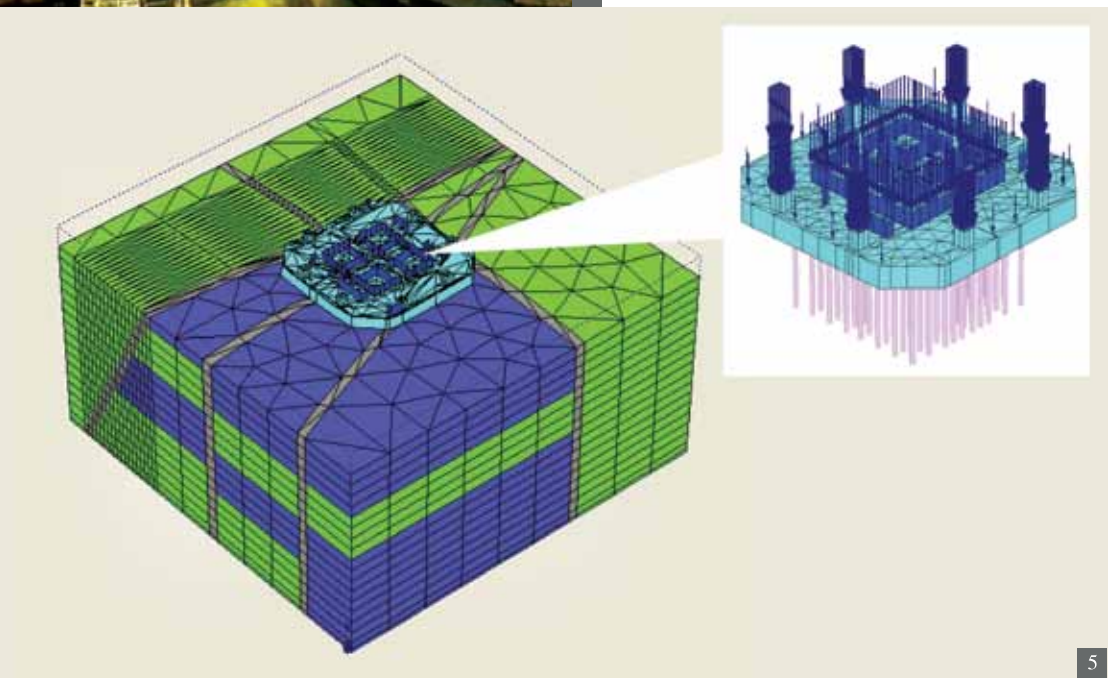

5

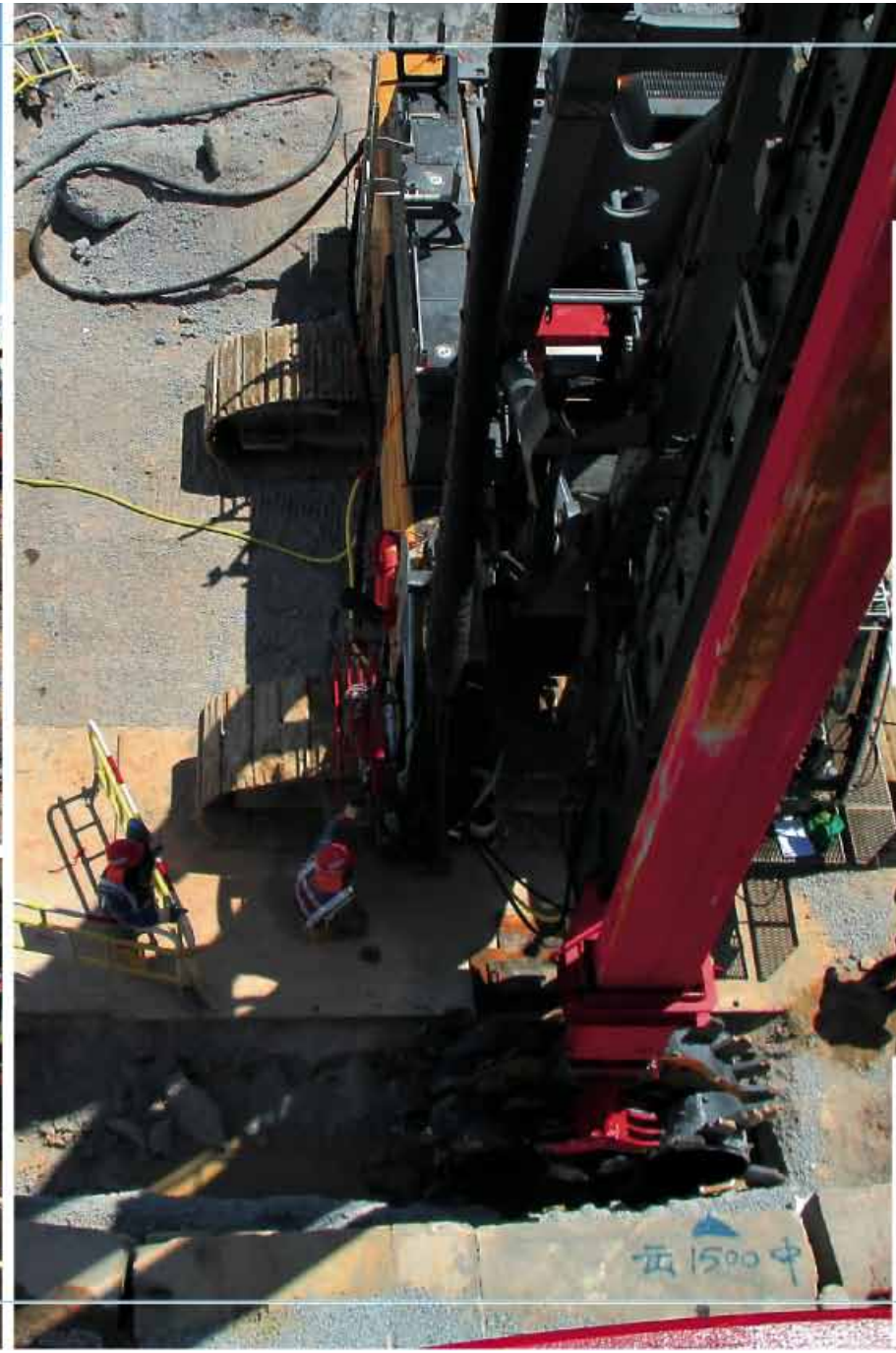

Contract HY/2012/08

Tuen Mun - Chek Lap Kok Link

A dual two-lane sub-sea tunnel between Tuen Mun Area 40 and the Hong Kong - Zhuhai - Macao Bridge at the Hong Kong Boundary Crossing Facilities.

The works comprise a Cement Soil Mixing (CSM) and Jet Grouting plug for the 2 tunnels (14.5m and 17.6m diameter).

BACHY SOLETANCHE
法國地基建築公司

泰錦建築工程有限公司
Tai Kam Construction Engineering Company Limited

Slope Stabilization & Site Formation
Specialist Contractor

Director : K S LAU
BSc(Hon) Msc DIC LLB(Hon)
MHKIE FHKIHT RPE(Civil) RSO RSA ASA

Address : Room 1114, 11/Floor, Wealth Commercial Centre,
42 - 56 Kwong Wa Street, Mong Kok, Kowloon, HK.

Tel.: 2473 4428 Fax : 2473 4418

e-mail : taikamsafety@hotmail.com

Mott MacDonald

MODELLING UNDERGROUND WORKS FOR A MORE EFFECTIVE DESIGN

West Island Line C704, HK

We create underground structures that are innovative, safe, easy to build and cost-effective through the extensive use of some of the latest soil-structure interaction modelling and visualisation tools including: BIM, FLAC, FLAC 3D, SAP 2000 and UDEC

Victoria Station, UK

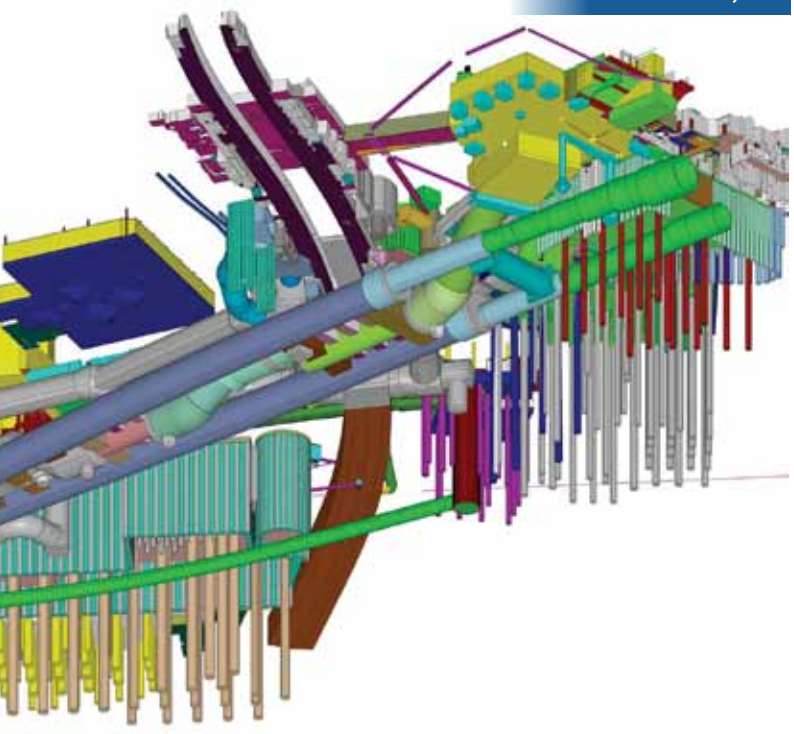

West Island Line HKU Station, HK

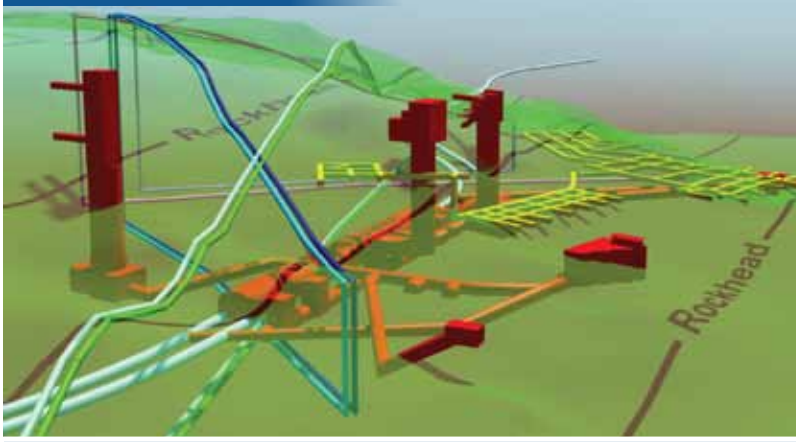

For general enquiries:

Mott MacDonald

T +852 2828 5757

E marketing.hk@mottmac.com.hk

W www.mottmac.hk

Hyder
An ARCADIS Company

LESS RISK, SAFER HOMES, BETTER CITY

Hyder Consulting, an ARCADIS Company, is a multinational design and engineering consultancy with a global workforce of over 4,600 employees. As part of ARCADIS we can also call upon the skills and expertise of over 28,000 colleagues. With 230 years of history and heritage, Hyder is the world's longest established engineering consultancy still in operation today. For over 35 years, we have been actively engaged in geo-hazard investigation and prevention, contributing to ensuring a safer living environment in Hong Kong.

For more information please contact:
T: (852) 2911 2233
E: hyder.hk@hyderconsulting.com

www.hyderconsulting.com

Mahanakorn Tower
Bangkok - Thailand

International Commerce Center
Hong Kong - China

Burj Khalifa
Dubai - United Arab Emirates

Dextra Group
Solutions for the Construction Industry

30+
years of experience

Dextra Group is the world leader in mechanical splicing systems for reinforcing steel bars and a pioneer in FRP bar solutions for the building and civil engineering industries.
The company was established in 1983 and its solutions are used every day in high-rise buildings and concrete structures.
Dextra is also accredited by major independent regulatory bodies on all continents.

Dextra Pacific
www.dextragroup.com
dpbuilding@dextragroup.com

Dextra

LAMBETH

Distinctly Different




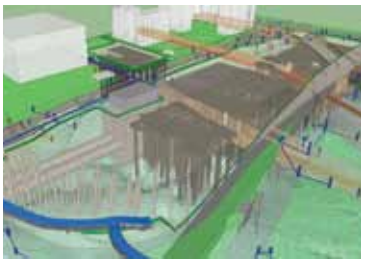


Lambeth brings together the diverse experience of operations, planning, commercial and design professionals – from within Gammon and Balfour Beatty – ensures it remains at the forefront of new techniques and new thinking. We set the standard for both innovation and technological advancement in building, civil, environmental, foundations, geotechnical and safety disciplines.

A member of the Gammon *Group*

28/F Devon House, Taikoo Place, 979 King's Road, Hong Kong Tel: 2516 8823 Fax: 2516 6352

CMA

C M WONG & ASSOCIATES LTD
黃志明建築工程師有限公司

11/F Universal Trade Centre
3-5A Arbuthnot Road, Hong Kong
Tel: (852)2522-1068
Fax: (852)2526-3111
www.cmwal.com
cmwal@cmwal.com


C M Wong & Associates Ltd is a Hong Kong based consulting engineer in providing a full range of professional services including feasibility studies, planning, design and supervision in relation to building and infrastructure projects. Our clients include various Hong Kong Government departments, institutions and major developers.

We adopt a flexible approach to suit clients' needs. We are also renowned for providing innovative engineering solutions for challenging projects especially for those with difficult ground conditions.

ISO 9001 : 2008
Certificate No.: CC 801

ISO 14001 : 2004
Certificate No.: CC 5408

OHSAS 18001 : 2007
Certificate No.: CC 5409

Proceedings of the 35th Annual Seminar
Geotechnical Division, The Hong Kong Institution of Engineers

Soil-structure Interaction: From Modelling to Observations

22 May 2015
Hong Kong

Jointly organised by:
Geotechnical Division, The Hong Kong Institution of Engineers
The Hong Kong Geotechnical Society

Supported by:
Civil & Structural Divisions, The Hong Kong Institution of Engineers

Captions of Figures on the Front Cover
Left Top to Bottom:
1) Ground Movement Vectors below Proposed Grade Separated Road and the Predicted Transverse Lining Deformation of a Nearby Tunnel in UK
(By courtesy of Jacobs China Ltd and Jacobs UK Ltd)
2) Aerial View of Debris Flow Event above Yu Tung Road on Lantau Island
(By courtesy of GEO of HKSAR)
Right Top to Bottom:
3) Excavation and Lateral Support Works for Underground Stormwater Storage Scheme in Happy Valley
(By courtesy of DSD of HKSAR, ONLY Geotechnics Ltd and Black & Veatch Hong Kong Ltd)
4) Flexible Debris-resisting Barrier and the Simulated Debris-Barrier Interaction
(By courtesy of GEO of HKSAR, Department of Civil and Environmental Engineering of HKUST and Ove Arup & Partners Hong Kong Ltd)

Soft copy of the proceedings can be downloaded from the HKIE Geotechnical Division's website http://hkieged.org/geodiv/annualseminar.aspx

ORGANISING COMMITTEE

Chairman
Ir Patrick Chao

Members
Ir Dr Johnny Cheuk
Ir Dr Julian Kwan
Ir David Lai
Ir Chris Lee
Ir Rupert Leung
Ir David Mak
Ir Clifford Phung
Ir Vincent Tam
Dr Ryan Yan
Ir Patrick Yong
Ir Irene Yu

Technical Sub-committee
Ir Dr Johnny Cheuk
Ir Dr Julian Kwan
Ir David Lai
Ir Chris Lee
Ir Dr S W Lee
Dr Andy Leung
Ir Clifford Phung
Ir Dr H W Sun
Dr Ryan Yan
Ir Patrick Yong

Published by:
Geotechnical Division
The Hong Kong Institution of Engineers
9/F., Island Beverley, 1 Great George Street, Causeway Bay, Hong Kong
Tel: 2895 4446 Fax: 2577 7791

Printed in Hong Kong

FOREWORD

"Soil-structure Interaction: From Modelling to Observations" is set as the theme of the 35th Annual Seminar of the Geotechnical Division of the Hong Kong Institution of Engineers. The last time soil-structure interaction was chosen as the theme of HKIE Geotechnical Division's Annual Seminar was in 1988. At that time, the industry was just starting to embrace the use of personal computers in their day-to-day work. Progress in technology since then has allowed much more powerful tools at our finger tips. Yet key to advancement in the understanding of soil-structure interaction behaviours are the development of theories and constitutive models, design methodologies, and their verification through testing and observations, which required the concerted effort of engineers both in the academia and in professional practice.

This volume of proceedings contains a paper by Prof. H.G. Poulos, who is invited to deliver the keynote lecture, and twenty papers contributed by both academics and practicing engineers. The topics of the papers span across a wide spectrum, covering material behaviour, design methodologies and case studies. While the classical soil-structure interaction problems of deep excavation, foundation and tunneling are well represented, we have also seen the expansion of the study of soil-structure interaction into a new area - the behaviour of landslide debris-resisting barriers.

Soil-structure interaction is a cross-discipline engineering problem, which requires engineers to have a good understanding of behaviours of both structural systems and earth materials. Its role in the design of civil engineering works cannot be overstated as essentially all civil engineering works are in touch with the ground. I am delighted of contribution of papers from engineers of the civil and structural disciplines. And I trust this Seminar will serve as an occasion for exchange of ideas among fellow civil, structural and geotechnical engineers.

On behalf of the Geotechnical Division, I would like to thank the Hong Kong Geotechnical Society for jointly organising this seminar, and HKIE Civil Division and Structural Division for their support. I am grateful to our Guest-of Honour, Mr HUI Siu-wai JP, Director of Buildings of the Government of the Hong Kong Special Administrative Region, and our Keynote Speaker, Prof. H.G. Poulos. I would also like to express my gratitude to the authors and speakers contributing to this seminar and the Organising Committee, under the leadership of Ir Patrick Chao, for their hard work in making this seminar possible.

Ir Rupert Leung
Chairman, Geotechnical Division
Hong Kong Institution of Engineers (2014/2015 Session)
May 2015

ACKNOWLEDGEMENTS

The Organising Committee would like to acknowledge the support of Civil and Structural Divisions of HKIE and the following sponsors for their generous support of the Seminar:-

AECOM Asia Co Ltd.
Arup
China Geo-Engineering Corporation
Earth Products China Ltd.
Bachy Soletanche Group Limited
Dextra Pacific Ltd.
Hyder Consulting Ltd.
Mott MacDonald Hong Kong Ltd.
Tai Kam Construction Engineering Co Ltd.
C M Wong & Associates Ltd.
Lambeth Associates Limited

TABLE OF CONTENTS

Soil-structure Interaction in Tall Building Foundation Design

H.G. Poulos
Coffey Geotechnics, Australia & University of Sydney, Australia

ABSTRACT

This paper reviews some of the challenges that face designers of foundations for very tall buildings, primarily from a geotechnical and a soil-structure interaction viewpoint. Some characteristic features of such buildings are reviewed and then a three-stage process of foundation design and verification is described. Design procedures for ultimate and serviceability limit state design are outlined, and the importance of proper ground characterization and assessment of geotechnical parameters is emphasized. Consideration is given to a number of soil-structure interaction issues, including pile-soil-pile interaction, superstructure stiffness effects and the effects of incorporating raft stiffness into the design analyses. The application of these effects is illustrated via three high-rise projects.

1 INTRODUCTION

The last two decades have seen a remarkable increase in the rate of construction of "super-tall" buildings in excess of 300m in height. Figure 1 shows the significant growth in the number of such buildings either constructed (to 2010) or projected (2015 and beyond). A large number of these buildings are in the Middle East or in China. Dubai has now the tallest building in the world, the Burj Khalifa, which is 828m in height, while in Jeddah Saudi Arabia, the Kingdom Tower is currently under construction and will eventually exceed 1000m in height.

Super-tall buildings are presenting new challenges to engineers, particularly in relation to structural and geotechnical design. Many of the traditional design methods cannot be applied with any confidence since they require extrapolation well beyond the realms of prior experience, and accordingly, structural and geotechnical designers are being forced to utilize more sophisticated methods of analysis and design. In particular, geotechnical engineers involved in the design of foundations for super-tall buildings are leaving behind empirical methods and are increasingly employing state-of-the art methods.

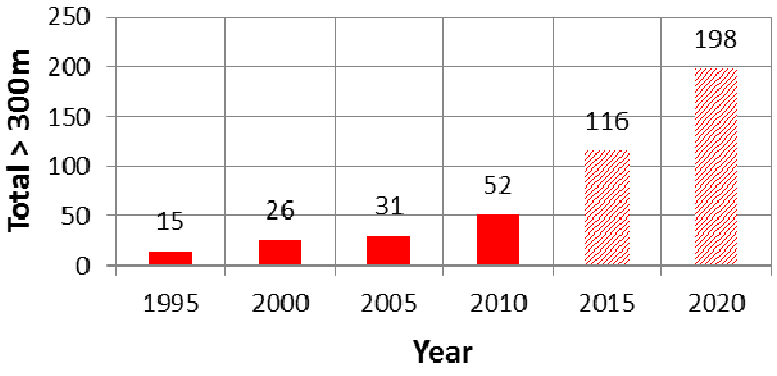

Figure 1: Total number of buildings in excess of 300m tall (after CTBUH, 2011)

This paper will summarize, relatively briefly, some of the challenges that face designers of foundations for very tall buildings, primarily from a geotechnical viewpoint. Some characteristic features of such buildings will be reviewed and then the options for foundation systems will be discussed. Some important aspects of

soil-structure interaction will be described, and then some case histories will be presented to illustrate the importance of considering soil-structure interaction in foundation design.

2 CHARACTERISTICS OF TALL BUILDINGS

There are a number of characteristics of tall buildings that can have a significant influence on foundation design, including the following:

- The building weight, and thus the vertical load to be supported by the foundation, can be substantial. Moreover, the building weight increases non-linearly with height, and so both ultimate bearing capacity and settlement need to be considered carefully.
- High-rise buildings are often surrounded by low-rise podium structures which are subjected to much smaller loadings. Thus, differential settlements between the high- and low-rise portions need to be controlled.
- The lateral forces imposed by wind loading, and the consequent moments on the foundation system, can be very high. These moments can impose increased vertical loads on the foundation, especially on the outer piles within the foundation system. The structural design of the piles needs to take account of these increased loads that act in conjunction with the lateral forces and moments.
- The wind-induced lateral loads and moments are cyclic in nature. Thus, consideration needs to be given to the influence of cyclic vertical and lateral loading on the foundation system, as cyclic loading has the potential to degrade foundation capacity and cause increased settlements.
- Seismic action will induce additional lateral forces in the structure and also induce lateral motions in the ground supporting the structure. Thus, additional lateral forces and moments can be induced in the foundation system via two mechanisms:
    - Inertial forces and moments developed by the lateral excitation of the structure;
    - Kinematic forces and moments induced in the foundation piles by the action of ground movements acting against the piles.
- The wind-induced and seismically-induced loads are dynamic in nature, and as such, their potential to give rise to resonance within the structure needs to be assessed. The risk of dynamic resonance depends on a number of factors, including the predominant period of the dynamic loading, the natural period of the structure, and the stiffness and damping of the foundation system.

3 FOUNDATION OPTIONS

The common foundation options include the following:

1. Raft or mat foundations;
2. Compensated raft foundations;
3. Piled foundations;
4. Piled raft foundations;
5. Compensated piled raft foundations.

The majority of recent high rise buildings are founded on the latter three foundation types. In particular, piled raft foundations have been used increasingly. Within a piled raft foundation, it may be possible for the number of piles to be reduced significantly (as compared with a fully piled system) by considering the contribution of the raft to the overall foundation capacity. In such cases, the piles provide the majority of the foundation stiffness while the raft provides a reserve of load capacity. In situations where a raft foundation alone might be used, but does not satisfy the design requirements (in particular the total and differential settlement requirements), it may be possible to enhance the performance of the raft by the addition of piles. In such cases, the use of a limited number of piles, strategically located, may improve both the ultimate load capacity and the settlement and differential settlement performance of the raft and may allow the design requirements to be met. It has also been found that the performance of a piled raft foundation can be optimized by selecting suitable locations for the piles below the raft. In general, the piles should be

concentrated in the most heavily loaded areas, while the number of piles can be reduced, or even eliminated, in less heavily loaded areas (Horikoshi and Randolph, 1998).

4 THE DESIGN PROCESS

There are commonly three broad stages employed in foundation design:

1. A preliminary design stage, which provides an initial basis for the development of foundation concepts and costing;
2. A detailed design stage, in which the selected foundation concept is analysed and progressive refinements are made to the layout and details of the foundation system. This stage is desirably undertaken collaboratively with the structural designer, as the structure and the foundation act as an interactive system;
3. A final design phase, in which both the analysis and the parameters employed in the analysis are finalized.

It should be noted that the geotechnical parameters used for each stage may change as more knowledge of the ground conditions, and the results of in-situ and laboratory testing, become available. The parameters for the final design stage should also incorporate the results of foundation load tests.

5 DESIGN ISSUES

The following issues will generally need to be addressed in the design of foundations for high-rise buildings:

1. Ultimate capacity of the foundation under vertical, lateral and moment loading combinations;
2. The influence of the cyclic nature of wind, earthquakes and wave loadings (if appropriate) on foundation capacity and movements;
3. Overall settlements;
4. Differential settlements, both within the high-rise footprint, and between high-rise and low-rise areas;
5. Possible effects of externally-imposed ground movements on the foundation system, for example, movements arising from excavations for pile caps or adjacent facilities;
6. Dynamic response of the structure-foundation system to wind-induced (and, if appropriate, wave) forces;
7. Earthquake effects, including the response of the structure-foundation system to earthquake excitation, and the possibility of liquefaction in the soil surrounding and/or supporting the foundation;
8. Structural design of the foundation system, including the load-sharing among the various components of the system (for example, the piles and the supporting raft), and the distribution of loads within the piles. For this, and most other components of design, it is essential that there be close cooperation and interaction between the geotechnical designers and the structural designers.

The analyses required to examine the above design issues require consideration of soil-structure interaction effects. Such analyses range from hand calculation methods for preliminary design to detailed three dimensional finite element analyses for final design. However, the latter analyses should always be checked for reasonableness by comparison with simpler methods and with available prior experience.

6 DESIGN ANALYSES

6.1 Ultimate limit state

There is an increasing trend for limit state design principles to be adopted in foundation design, for example, in the Eurocode 7 requirements and those of the Australian Piling Code AS2159-2009. In terms of limit state design using a load and resistance factor design approach (LRFD), the design criteria for the ultimate limit state can be stated as follows:

$$R_s^* \geq S^* \quad (1)$$

$$R_g^* \geq S^* \quad (2)$$

where R_s^* = design structural strength = $\phi_s . R_{us}$,
R_g^* = design geotechnical strength = $\phi_g . R_{ug}$,
R_{us} = ultimate structural strength,
R_{ug}= ultimate strength (geotechnical capacity),
ϕ_s = structural reduction factor,
ϕ_g = reduction factor for geotechnical strength, and
S^* = design action effect (factored load combinations).

The above criteria are applied to the entire foundation system, while the structural strength criterion (equation 1) is also applied to each individual pile. It is not considered to be good practice to apply the geotechnical criterion (equation 2) to each individual pile within the group, as this can lead to considerable over-design. R_s^* and R_g^* can be obtained from the estimated ultimate structural and geotechnical capacities, multiplied by appropriate reduction factors.

The structural and geotechnical reduction factors are often specified in national codes or standards. The selection of suitable values of ϕ_g requires engineering judgment and should take into account a number of factors that may influence the foundation performance. As an example, the Australian Piling Code AS2159-2009 specifies an approach involving a subjective risk assessment, with lower values of ϕ_g being associated with greater levels of uncertainty and higher values being relevant when ground conditions are reasonably well-known and a significant amount of load testing is to be carried out (see Section 6.6).

If any of the design requirements are not satisfied, then the design will need to be modified accordingly to increase the strength of the overall system or of those components of the system that do not satisfy the criteria.

6.2 Cyclic loading

In addition to the normal design criteria, as expressed by equations 1 and 2, it is suggested that an additional criterion be imposed for the whole foundation of a tall building to cope with the effects of repetitive loading from wind and/or wave action, as follows:

$$\eta R_{gs}^* \geq S_c^* \quad (3)$$

where R_{gs}^* = design geotechnical shaft capacity,
S_c^* = maximum amplitude of wind loading,
η = a reduction factor.

This criterion attempts to avoid the full mobilization of shaft friction along the piles, thus reducing the risk that cyclic loading will lead to a degradation of shaft capacity. In most cases, it is suggested that η can be taken as 0.5, while S_c^* can be obtained from computer analyses which give the cyclic component of load on each pile, for various wind loading cases.

6.3 Serviceability

The design criteria for the serviceability limit state are as follows:

$$\rho_{max} \leq \rho_{all} \quad (4)$$

$$\theta_{max} \leq \theta_{all} \quad (5)$$

where ρ_{max} = maximum computed settlement of foundation,
ρ_{all} = allowable foundation settlement,
θ_{max} = maximum computed local angular rotation,

θ_{all} = allowable angular rotation.

For the serviceability analysis, the best-estimate (unfactored) values of foundation resistances and stiffnesses are employed and the serviceability limit state (SLS) loads are applied. The design will be satisfactory if the computed deflections and rotations are within the specified allowable limits (equations 4 and 5).

Values of ρ_{all} and θ_{all} depend on the nature of the structure and the supporting soil. Table 1 sets out some suggested criteria from work reported by Zhang and Ng (2006). This table also includes values of intolerable settlements and angular distortions. The figures quoted in Table 1 are for deep foundations, but Zhang and Ng also consider allowable settlements and angular distortions for shallow foundations, different types of structure, different soil types, and different building usage. Criteria specifically for very tall buildings do not appear to have been set, but it should be noted that it may be unrealistic to impose very stringent criteria on very tall buildings on clay deposits, as they may not be achievable. In addition, experience with tall buildings in Frankfurt suggests that total settlements well in excess of 100mm can be tolerated without any apparent impairment of function. It should also be noted that the allowable angular rotation, and the overall allowable building tilt, reduce with increasing building height, both from a functional and a visual viewpoint.

Table 1: Suggested Serviceability Criteria for Structures (Zhang and Ng, 2006)

Quantity	*Value*	*Comments*
Limiting Tolerable Settlement mm	106	Based on 52 cases of deep foundations.
Observed Intolerable Settlement mm	349	Based on 52 cases of deep foundations.
Limiting Tolerable Angular Distortion rad	1/500	Based on 57 cases of deep foundations.
Limiting Tolerable Angular Distortion rad	1/250 (H<24m) to 1/1000 (H>100m)	From 2002 Chinese Code H = building height
Observed Intolerable Angular Distortion rad	1/125	Based on 57 cases of deep foundations.

6.4 Dynamic loading

Issues related to dynamic wind loading are generally dealt with by the structural engineer, with geotechnical input being limited to an assessment of the stiffness and damping characteristics of the foundation system. However, the following general principles of design can be applied to dynamic loadings:

- The natural frequency of the foundation system should be greater than that of the structure it supports, to avoid potential resonance phenomena. The natural frequency depends primarily on the stiffness of the foundation system and its mass, although damping characteristics may also have some influence.
- The amplitude of dynamic motions of the structure-foundation system should be within tolerable limits. The amplitude will depend on the stiffness and damping characteristics of both the foundation and the structure.

The dynamic stiffness and damping of the foundation system can be estimated via solutions and analyses such as those provided by Gazetas (1983, 1991). For high-rise structures, the first natural period is relatively large, and so dynamic effects on stiffness may be relatively small, while the radiation damping may also be small, especially for rotational modes of excitation. Thus, damping may arise primarily from internal damping of the soil. Higher modes of vibration may then become more significant.

6.5 Earthquake loading

Soil deposits at a site subjected to an earthquake may experience the following effects:

- Increases in pore pressure;
- Time-dependent vertical ground movements during and after the earthquake;
- Time-dependent lateral ground movements during and after the earthquake.

In foundation design, consideration must therefore be given to possible reductions in soil strength arising from the build-up of excess pore pressures during and after the earthquake. In extreme cases, the generation of pore pressures may lead to liquefaction in relatively loose sandy and silty soils.

As a consequence of the earthquake-induced ground movements, piles and other deep foundations will be subjected to two sources of additional lateral loading:

a. Inertial loadings – these are forces that are induced in the piles because of the accelerations generated within the structure by the earthquake. Consideration is generally confined to lateral inertial forces and moments, which are assumed to be applied at the pile heads;
b. Kinematic loadings – these are forces and bending moments that are induced in the piles because of the ground movements that result from the earthquake. Such movements will interact with the piles and, because of the difference in stiffness of the piles and the moving soil, lateral stresses will be developed between the pile and the soil, resulting in the development of shear forces and bending moments in the piles. These actions will be time-dependent and need to be considered in the structural design of the piles.

Thus, in addition to the usual design considerations for static loading, the above factors of strength reduction, inertial loadings, and kinematic loadings, need to be incorporated into the design process.

When considering both the strength and stiffness of soils, consideration should also be given to the effects of the rapid rate of loading that occurs during a seismic event. In addition to generating an undrained response in finer grained soils, loading rate effects tend to increase both the strength and stiffness of such soils.

Appropriate assessment of the geotechnical parameters for earthquake response is a critical component of geotechnical design for seismic actions, as it is for other types of imposed loadings. Reference can be made to sources such as Kramer (1996) who discusses such issues as the effects of strain, cyclic loading and loading rate effects on soil stiffness and damping.

6.6 Summary of design analysis process

A summary of the analyses that are recommended to be carried out for building foundation design are summarized in Table 2. These analyses involve various combinations of factored/unfactored geotechnical strengths and Ultimate Limit State (ULS) or Serviceability Limit State (SLS) loadings.

The assessment of the geotechnical reduction factor ϕ_g is an important part of the design process. Procedures are described in various codes and standards, for example Eurocode 7, and Standards Australia Piling Code (AS2159-2009). Various attempts have also been made to rationalise the selection of ϕ_g based on probabilistic methods and the achievement of a target reliability index.

In practice, a series of factors need to be considered in making an assessment of $_{g,}$ including the following in AS2159-2009:

- The geological complexity of the site;
- The extent of ground investigation;
- The amount and quality of geotechnical data;
- Experience with similar foundations in similar geological conditions;
- The method of assessment of geotechnical parameters for design;
- The design method adopted;
- The method of utilizing the results of in-situ test data and pile installation data;
- The level of construction control;
- The level of performance monitoring of the supported structure during and after construction.

ϕ_g can typically range between 0.4 for conservative designs involving little or no pile testing and uncertain ground conditions prevail to 0.8 for cases in which a significant amount of testing is carried out and the ground conditions and design parameters have been carefully assessed.

Table 2: Summary of Design Analyses

Case	*Purpose*	*Factor applied to Geotechnical Strength Parameters*	*Load Case*	*Comment*
i	Geotechnical Design Capacity	φ_g	ULS	Geotechnical reduction factor, φ_g, applied to strength parameters to assess overall stability of the pile group
ii	Structural Design Capacity	1.0	ULS	Unfactored geotechnical strength parameters are adopted to assess maximum pile axial load and pile bending moment using short term pile modulus.
iii	Serviceability	1.0	SLS	Unfactored geotechnical strength parameters are adopted to assess pile head deflections and rotations

7 DESIGN ISSUES RELATED TO SOIL-STRUCTURE INTERACTION

7.1 Pile-Soil-Pile interaction

There is ample evidence of the fact that the behaviour of a pile within a group is influenced by the surrounding piles, via transmission of stresses and strain through the supporting soil. The main effects of such interaction are:

1. The settlement of a pile in a group is influenced by the settlement of other piles within the group;
2. Consequently, there is generally an increase in settlement due to interaction among the piles, and therefore a reduction in stiffness of each pile within the pile group as compared with a single isolated pile carrying the same average load.
3. The interaction among piles within the group may lead to a re-distribution of load within the piles, and a change in the ratio of the load carried by shaft friction and by end bearing. In general, there will be a tendency for the end bearing component to increase while the shaft load component decreases.

Various methods of analysis can be employed to incorporate such interaction effects. Some of the earlier methods employed the concept of superposition of two-pile interaction factors, while more modern numerical methods such as the finite element method automatically include such effects, depending on the soil model adopted.

The consequences of including pile-soil-pile interaction into a design analysis will be discussed later in this paper in relation to the Emirates Twin Towers project.

7.2 Stiffening effect of superstructure

It is common in geotechnical design to analyse a raft or piled raft without considering the stiffening effect of any structure that is supported by the raft. Methods of incorporating the stiffness of a structure into a raft analysis have been examined by several authors including Lee and Brown (1972), Poulos (1975) and Brown and Yu (1986). Zhang and Small (1994) analysed 3-dimensional framed buildings on raft foundations, and demonstrated that the larger the relative stiffness of the building frame, the smaller the differential deflections in the raft. Such approaches can be extended to piled raft foundations.

Gusmao Filho and Guimaraes (1997) have looked at construction sequence and have noted that the loads in columns reach a maximum (or minimum) value as more stories are added to the building, leading to the idea of the building reaching a "limit stiffness".

It may be concluded that the stiffness of a structure will influence the calculated settlements and differential settlements of a raft or piled raft foundation, but this depends on the stiffness of the structure relative to the raft. For buildings with rigid shear walls, the stiffening effect on the raft will be significant. However, for flexible light framed structures, the effect of the structure on a thick raft, will be small.

When undertaking a piled raft analysis, it may be convenient to represent the stiffness of the structure by using thicker raft elements at locations where are walls and larger columns. While not providing any information on the structural behaviour, such an approach can provide a more realistic assessment of differential settlements within the footprint of a structure (Russo et al, 2013).

A convenient approach to foundation-structure interaction is for the piles to be represented by springs, the stiffness of which are computed by the geotechnical engineer and which include the important effects of interaction among the piles and the raft. Such interaction can significantly reduce the axial and lateral stiffness of piles within a group, as compared with the values for an isolated single pile. In this way, a more reliable analysis can be undertaken to compute not only the structural forces, but also the pile loads, the raft moments and the distribution of settlement within the foundation system.

An example of the effects of incorporating superstructure stiffness into a geotechnical settlement analysis is given later in this paper via the Burj Khalifa project.

7.3 The effects of raft flexibility, and the estimation of pile load distribution

In checking the structural loads within the piles in a piled raft system, it is essential to give proper consideration to the flexibility of the raft. Making the common assumption that the raft is rigid can lead to very misleading outcomes, as it tends to over-estimate the loads in the outer piles within the system. In addition, consideration of the superstructure stiffness in a piled raft analysis can also have a significant influence on the computed distribution of axial pile loads. As a consequence, the computed values of pile head stiffness may also be affected. The case of the Incheon Tower in South Korea is an example of the importance of incorporating the flexibility of the raft, and this is presented later in this paper.

7.4 Factoring of resistances

When considering soil-structure interaction to obtain foundation actions for structural design (for example, the bending moments in the raft of a piled raft foundation system), the most critical response may not occur when the pile and raft capacities are factored downwards. For example, at a pile location where there is not a column, load acting, the negative moment may be larger if the pile capacity is factored up, rather than down.

For this reason, in the structural design of the raft and the piles, the results of the ULS overall stability analysis are <u>not</u> considered to be relevant, because the loads that can be sustained by the piles would then be artificially reduced by the geotechnical reduction factor. Consequently, it is suggested that the most rational approach is one in which a separate ULS analysis is carried out using the various ULS load combinations but in which the <u>unfactored</u> resistances of the foundation components are employed. The consequent computed foundation actions (i.e. pile forces and, if appropriate, raft moments and shears) are then multiplied by a structural action factor (for example 1.5) to obtain the values for structural design.

8 ASSESSMENT OF GEOTECHNICAL DESIGN PARAMETERS

8.1 Key parameters

For contemporary foundation systems that incorporate both piles and a raft, the following parameters require assessment:

- The ultimate skin friction for piles in the various strata along the pile;
- The ultimate end bearing resistance for the founding stratum;
- The ultimate lateral pile-soil pressure for the various strata along the piles;
- The ultimate bearing capacity of the raft;

- The stiffness of the soil strata supporting the piles, in the vertical direction;
- The stiffness of the soil strata supporting the piles, in the horizontal direction;
- The stiffness of the soil strata supporting the raft.

It should be noted that the soil stiffness values are not unique values but will vary, depending on whether long-term drained values are required (for long-term settlement estimates) or short-term undrained values are required (for dynamic response to wind and seismic forces). For dynamic response of the structure-foundation system, an estimate of the internal damping of the soil is also required, as it may provide the main source of damping. Moreover, the soil stiffness values will generally vary with applied stress or strain level, and will tend to decrease as either the stress or strain level increases.

8.2 Methods of parameter assessment

The following techniques are used for geotechnical parameter assessment:

1. Empirical correlations – these are useful for preliminary design, and as a check on parameters assessed from other methods.
2. Laboratory testing, including triaxial and stress path testing, resonant column testing, and constant normal stiffness testing.
3. In-situ testing, including various forms of penetration testing, pressuremeter testing, dilatometer testing, and geophysical testing.
4. Load testing, generally of pile foundations at or near prototype scale. For large diameter piles or for barrettes, it is increasingly common to employ bi-directional testing to avoid the need for substantial reaction systems.

8.3 Geophysical testing

Geophysical testing is becoming more widely used in geotechnical investigations. At least three major advantages accrue by use of such methods:

1. Ground conditions between boreholes can be inferred.
2. Depths to bedrock or a firm bearing stratum can be estimated.
3. Shear wave velocities in the various layers within the ground profile can be measured, and tomographic images developed to portray both vertical and lateral inhomogeneity.
4. From the measured shear wave velocity, v_s, the small-strain shear modulus, G_{max}, can be obtained as follows:

$$G_{max} = \rho \, v_s^{\,2} \qquad (6)$$

where ρ = mass density of soil.

For application to routine design, allowance must be made for the reduction in the shear modulus because of the relatively large strain levels that are relevant to foundations under normal serviceability conditions. As an example, Poulos et al (2001) have suggested the reduction factors shown in Figure 3 for the case where $G_{max} / s_u = 500$ (s_u = undrained shear strength). This figure indicates that:

- The secant modulus for axial loading may be about 20-40% of the small-strain value for a practical range of factors of safety;
- The secant modulus for lateral loading is smaller than that for axial loading, typically by about 30% for comparable factors of safety.

An important outcome of the strain-dependence of soil stiffness is that the operative soil modulus below the foundation system will tend to increase with depth, even within a homogeneous soil mass. When modelling a foundation system using a soil model that does not incorporate the stress- or strain–dependency of soil stiffness, it is still possible to make approximate allowance for the increase in stiffness with increasing depth below the foundation by using a modulus that increases with depth. From approximate calculations using the Boussinesq theory to compute the distribution of vertical stress with depth below a loaded foundation, it is

possible to derive a relationship between the ratio of the modulus to the small strain value, as a function of relative depth and relative stress level. Such a relationship is shown in Figure 4 for a circular foundation, and may be used as an approximate means of developing a more realistic ground model for foundation design purposes. When applied to pile groups, the diameter can be taken as the equivalent diameter of the pile group, and the depth is taken from the level of the pile tips.

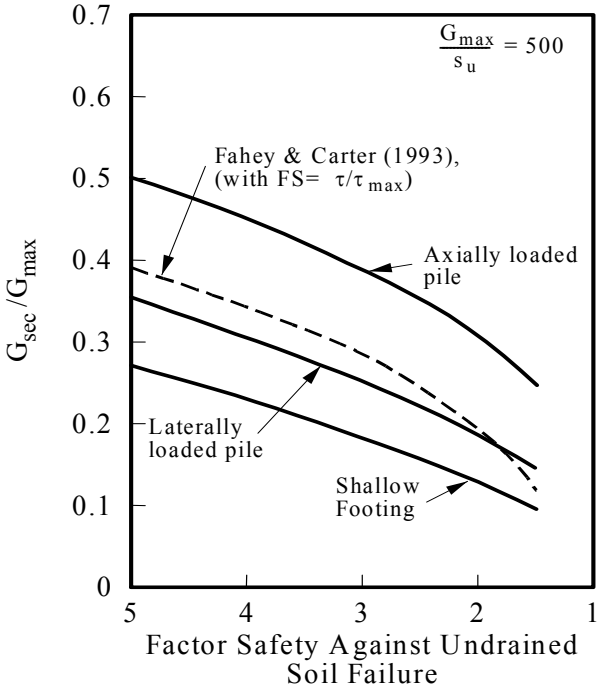

Figure 3: Example of ratio of secant shear modulus to small-strain value (Poulos et al, 2001)

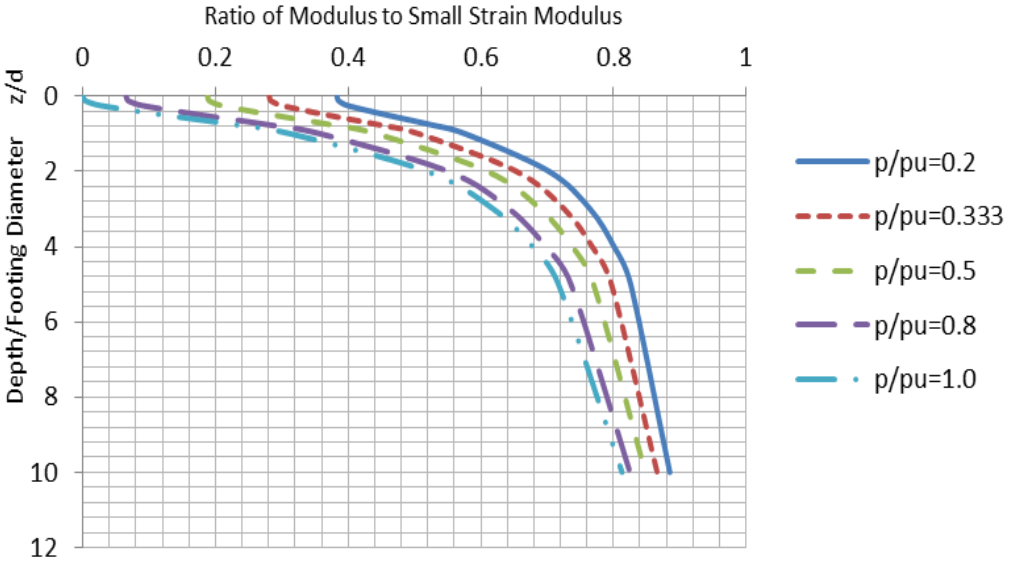

Figure 4: Ratio of operative modulus to small-strain modulus versus relative depth
Note: p/pu = ratio of applied pressure to ultimate pressure.

Haberfield (2013) has demonstrated that, when allowance is made for strain level effects, modulus values derived from geophysical tests can correlate well with those from pressuremeter tests. Figure 5 reproduces such an example in which a reduction factor of 0.2 has been applied to the small-strain modulus values

derived from cross-hole seismic test results. The modulus values so derived were found to be consistent with values obtained from subsequent pile load tests.

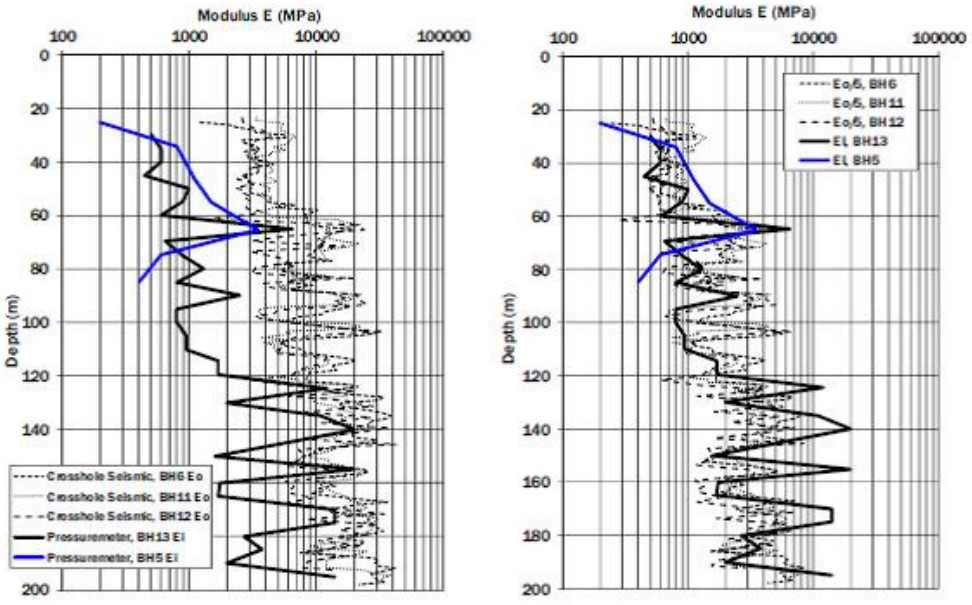

Figure 5: Comparison of modulus values from pressuremeter and cross-hole seismic tests (Haberfield, 2013)

9 TYPICAL HIGH-RISE FOUNDATION SETTLEMENTS

It can be useful to review the settlement performance of some high-rise buildings in order to gain some appreciation of the settlements that might be expected from two foundation types founded on various deposits. Table 3 summarizes details of the foundation settlements of some tall structures founded on raft or piled raft foundations, based on documented case histories in Hemsley (2000), Katzenbach et al (1998), and from the author's own experiences. The average foundation width in these cases ranges from about 40m to 100m. The results are presented in terms of the settlement per unit applied pressure, and it can be seen that this value decreases as the stiffness of the founding material increases. Typically, these foundations have settled between 25 and 300mm/MPa. Some of the buildings supported by piled rafts in stiff Frankfurt clay have settled more than 100mm, and despite this apparently excessive settlement, the performance of the structures appears to be quite satisfactory. It may therefore be concluded that the tolerable settlement for tall structures can be well in excess of the conventional design values of 50-65mm. A more critical issue for such structures may be overall tilt, and differential settlement between the high-rise and low-rise portions of a project.

Table 3: Examples of Settlement of Tall Structure Foundations

Foundation Type	*Founding Condition*	*Location*	*No. of Cases*	*Settlement per Unit Pressure mm/MPa*
Raft	Stiff clay	Houston; Amman; Riyadh	2	227-308
	Limestone		2	25-44
Piled Raft	Stiff clay	Frankfurt	5	218-258
	Dense sand	Berlin; Niigata	2	83-130
	Weak Rock	Dubai	5	32-66
	Limestone	Frankfurt	1	38

10 THE EMIRATES TWIN TOWERS, DUBAI

10.1 The project

The Emirates Project is a twin tower development in Dubai, one of the United Arab Emirates. The towers are triangular in plan, with a face dimension of approximately 50 m to 54 m. The taller Office Tower has 52 floors and rises 355 m above ground level, while the shorter Hotel Tower is 305 m tall. These towers are more than double the height of the nearby World Trade Centre, which was once the tallest building in Dubai. The twin towers are located on a site of approximately 200000 m^2, which also incorporates low level retail and parking podium areas. Poulos and Davids (2005) have presented details of the towers, the geotechnical investigations, and the foundation design.

The main geotechnical investigation involved the drilling of 23 boreholes, to a maximum depth of about 80m. It was found that the stratigraphy was relatively uniform across the whole site, so that it was considered adequate to characterize the site with a single geotechnical model. The groundwater level was relatively close to the surface.

Because of the relatively good ground conditions near the surface, it was assessed that a piled raft system would be appropriate for the foundation of each of the towers. The design of such a foundation system required information on both the strength and stiffness of the ground, and as a consequence, a comprehensive series of in-situ tests was carried out, together with both conventional and advanced laboratory testing.

The geotechnical model developed for foundation design under static loading conditions was based on the relevant available in-situ and laboratory test data, and is shown in Fig. 6.

10.2 Load testing

As part of the foundation design process, a program of pile load testing was undertaken, the main purpose being to assess the validity of the design assumptions and parameters. The test program involved the installation of three test piles at or near the location of each of the two towers. All piles were drilled under bentonite slurry support, with steel casing being provided in the upper 3-4m of each shaft. Because of the very large design loads on the piles, it was not considered feasible to test full-size piles in compression, and as a consequence, the maximum pile diameter for the pile load tests was 0.9m.

Figure 7 shows the test setup for the compression tests on 0.9 m diameter test piles. For the compression tests, the loading was supplied by a series of jacks, while the reaction was provided by 22 anchors drilled into the underlying calcisiltite. The anchors were connected to the test pile via two crowns (a larger one above a smaller unit) located above the jacks and load cells. For the tension tests, the reaction was supplied by a pair of reaction piles 12 m long, with a cross-beam connecting the heads of the test and reaction piles. In the lateral load tests, the test pile was jacked against the adjacent 0.9m diameter compression test pile.

In order to provide some guidance on the expected behaviour of the piles during the test pile program, “Class A” predictions of the load-deflection response of the test piles were carried out and communicated to the main consultant prior to the commencement of testing. The geotechnical model was similar to that used for design (Fig. 6), with some minor modifications to allow for the specific stratigraphic conditions at the test pile locations, as revealed during installation of the test piles.

Comparisons between predicted and measured test pile behaviour were made after the results of the tests were made available. Figure 8 compares the measured and predicted load-settlement curves for Test P3(H), and reveals a fair measure of agreement in the early stages. The predicted settlements exceed the measured values, and the maximum load of 30 MN reached exceeded the estimated ultimate load capacity of about 23 MN. The corresponding comparison for the Office Tower test pile P3(O), revealed excellent agreement, with the predicted ultimate load capacity of 23 MN again being exceeded.

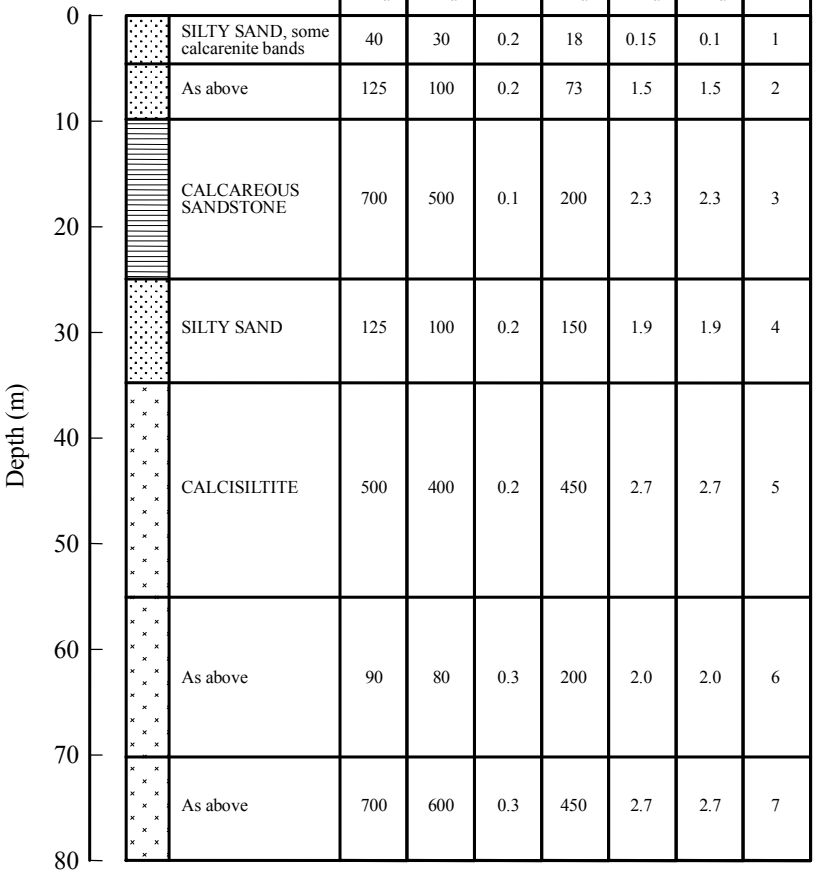

		E_u MPa	E' MPa	ν'	f_s kPa	f_b MPa	p_u MPa	Unit
	SILTY SAND, some calcarenite bands	40	30	0.2	18	0.15	0.1	1
	As above	125	100	0.2	73	1.5	1.5	2
	CALCAREOUS SANDSTONE	700	500	0.1	200	2.3	2.3	3
	SILTY SAND	125	100	0.2	150	1.9	1.9	4
	CALCISILTITE	500	400	0.2	450	2.7	2.7	5
	As above	90	80	0.3	200	2.0	2.0	6
	As above	700	600	0.3	450	2.7	2.7	7

Figure 6: Geotechnical model adopted for design.

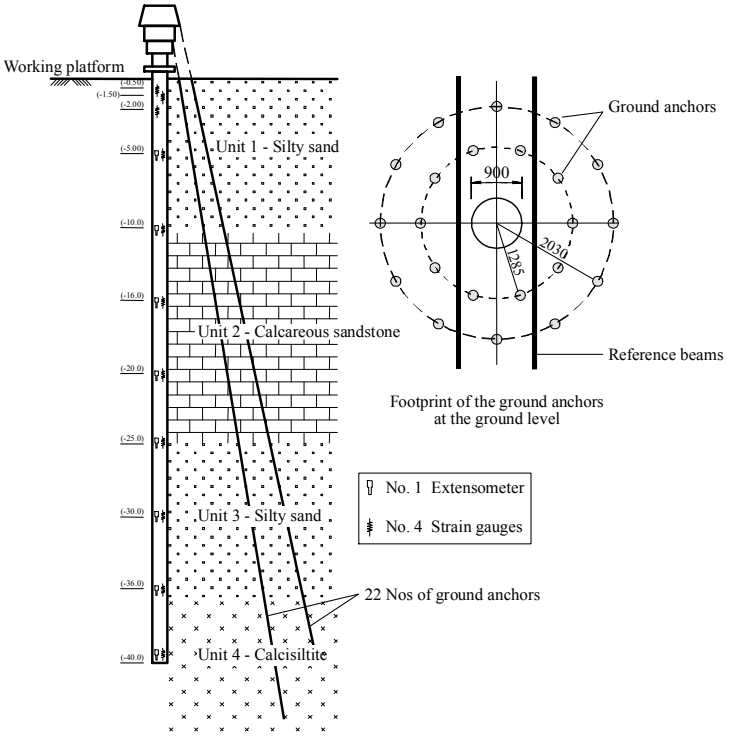

Figure 7: Setup for compression pile tests.

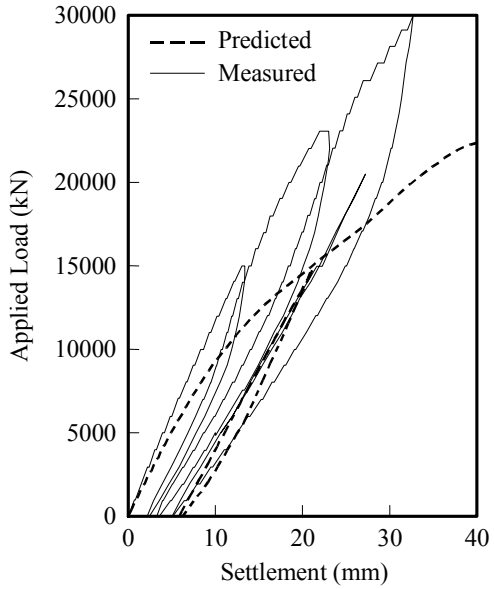

Figure 8: Predicted and measured load-settlement behaviour for pile P3(H).

10.3 Soil-Structure interaction aspects

In the final design, the piles were primarily 1.2 m diameter, and extended 40 or 45 m below the base of the raft. In general, the piles were located directly below 4.5 m deep walls which spanned between the raft and the Level 1 floor slab.

In additional to the conventional design analyses, more complete analyses of the settlement of the foundation system were undertaken with the computer program GARP (Poulos, 1994). GARP (Geotechnical Analysis of Raft with Piles) utilizes a simplified boundary element analysis to compute the behaviour of a rectangular piled raft when subjected to applied vertical loading, moment loading, and free-field vertical soil movements. The raft is represented by an elastic plate, the soil is modelled as a layered elastic continuum, and the piles are represented by hyperbolic springs which can interact with each other and with the raft. Beneath the raft, limiting values of contact pressure in compression and tension can be specified, so that some allowance can be made for non-linear raft behaviour. In addition to GARP, the program DEFPIG (Poulos and Davis, 1980) was used for the pile stiffness values and pile-pile interaction factors, and for computing the lateral response of the piles.

For the analysis of settlements under the design loads, the same values of Young's modulus were used as for the single piles, whose behavior had been quite well-predicted. For the non-linear GARP analysis, the unfactored values of estimated raft bearing capacity and ultimate pile load capacity were used.

Table 4 summarizes the computed maximum settlement and angular rotation under serviceability loading conditions. These computed values were relatively large, but were nevertheless acceptable for the project. It was found that the settlements showed a "dishing" pattern, with the settlements near the centre being significantly greater than those near the edge of the foundation. Fig. 9 shows contours of the computed long-term settlement of the Hotel tower.

Table 4: Computed Maximum Settlement and Angular Rotation Serviceability Limit State

Tower	Max. Settlement mm	Max. Angular Rotation
Office	134	1/384
Hotel	138	1/378

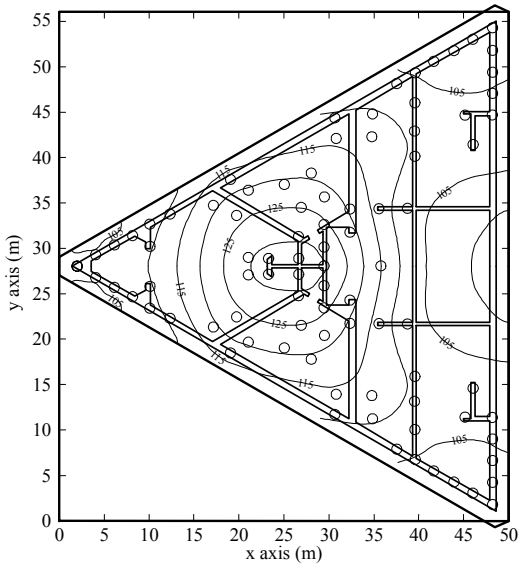

Figure 9: Foundation layout and computed settlement contours for Hotel Tower.

The generally good agreement between measured and predicted performance of the test piles gave rise to expectations of similar levels of agreement for the entire tower structure foundations. Unfortunately, this was not the case. Measurements were available only for a limited period during the construction process, and these are compared with the predicted time-settlement relationships in Fig. 10, for typical points within the Hotel Tower. The time-settlement predictions were based on the predicted final settlement, an assumed rate of construction, and a rate of settlement computed from three-dimensional consolidation theory.

Fig. 10 shows that the actual measured settlements were significantly smaller than those predicted, being only about 25% of the predicted values after 10-12 months. Figure 11 shows the contours of measured settlement at a particular time during construction for the hotel tower. Although the magnitude of the measured settlements was far smaller than predicted, the distribution was similar to that predicted. Thus, despite the considerable thickness of the raft and the apparent stiffness of the structure, the foundation experienced a "dishing" distribution of settlement more characteristic of a flexible foundation.

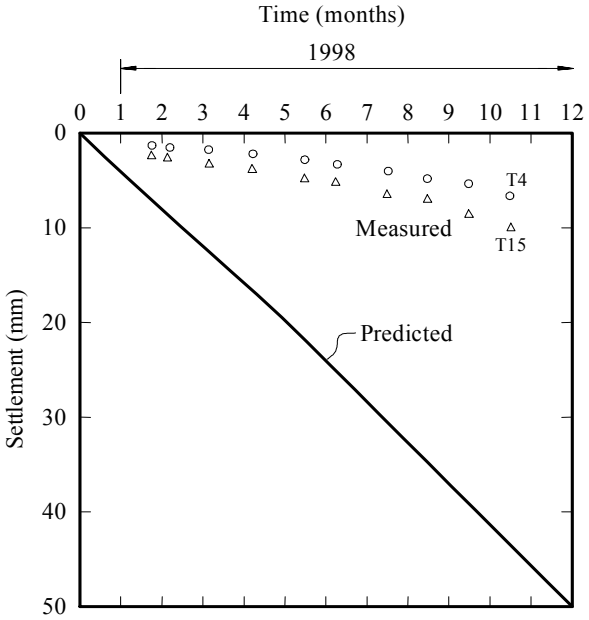

Figure 10: Predicted and measured settlement vs time – Hotel Tower.

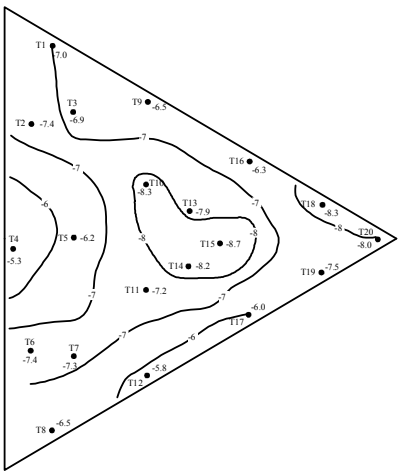

Figure 11: Measured settlement contours – Hotel Tower.

10.4 Assessment of predictions - possible reasons for discrepancies.

The disappointing lack of agreement between measured and predicted settlement of the towers prompted a "post-mortem" investigation of possible reasons for the poor predictions. At least four reasons were suggested:

1. Some settlements may have occurred prior to the commencement of measurements;
2. The assumed time-load pattern may have differed from that assumed;
3. The rate of consolidation may have been much slower than predicted;
4. The interaction effects among the piles within the piled raft foundation may have been over-estimated.

Of these, based on the information available during construction, the first two did not seem to be likely, and the last was considered to be the most likely cause. Calculations were therefore carried out to assess the sensitivity of the predicted settlements to the assumptions made in deriving interaction factors for the piled raft analysis with GARP. In deriving the interaction factors originally used, it had been assumed that the soil or rock between the piles had the same stiffness as that around the pile, and that the rock below the pile tips had a constant stiffness for a considerable depth. In reality, the ground between the piles is likely to be stiffer than near the piles, because of the lower levels of strain, and the rock below the pile tips is likely to increase significantly with depth, both because of the increasing level of overburden stress and the decreasing level of strain. The program DEFPIG was therefore used to compute the interaction factors for a series of alternative (but credible) assumptions regarding the distribution of stiffness both radially and with depth. The ratio of the soil modulus between the piles to that near the piles was increased to 5, while the modulus of the material below the pile tips was increased from the original 70 MPa to 600 MPa (the value assessed for the rock at depth). The various cases are summarized in Table 2.

Figure 12 shows the computed relationships between interaction factor and spacing for a variety of parameter assumptions. It can be seen that the original interaction curve used for the initial predictions lies considerably above those for more realistic assumptions. Since the foundations analyzed contained many piles, the potential for over-prediction of settlements is considerable, since small inaccuracies in the interaction factors can translate to large errors in the predicted group settlement (for example, Poulos, 1993).

Revised settlement calculations, on the basis of these interaction factors, gave the results shown in Table 5. The interaction factors used clearly have a great influence on the predicted foundation settlements, although they have almost no effect on the load sharing between the raft and the piles. The maximum settlement, for Case 4, is reduced to 29% of the value originally predicted, while the minimum settlement is only 25% of the original value. If this case was used for the calculation of the settlements during construction, the settlement at

Point T15 would be about 12 mm, which is in much closer agreement with the measured value of about 10 mm than the original predictions.

Curve No.	Modulus of Layer below MPa	Modulus of Soil between Piles to Near-Pile Values
1	90	1.0
2	90	5.0
3	200	5.0
4	700	5.0
5	700	1.0

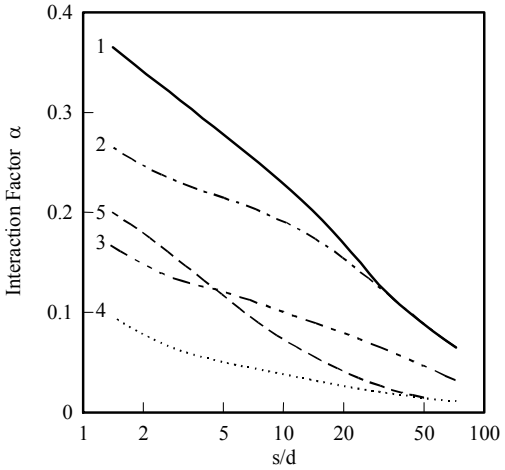

Figure 12: Sensitivity of computed interaction factors to analysis assumptions.

The importance of proper assessment of the geotechnical model and the pile interaction factors in order to compute the effects of group interaction has been emphasized by this case history. In addition, there was probably an inadequate appreciation of the potential problems of applying interaction factors to large pile groups, at the time of the predictions. In addition, in contrast to the single pile tests, the calculations were done for the purposes of design, rather than prediction, and consequently tended to be conservative.

Table 5: Summary of Revised Calculations for Hotel Tower

Case	Modulus below 53 m MPa	Ratio of max. to near-pile modulus	Max. Settlement mm	Min. Settlement mm	% Load on Piles
Original calcul-ations	80	1	138	91	93
Case 2	80	5	122	85	93
Case 3	200	5	74	50	92
Case 4	600	5	40	23	92
Case 5	600	1	58	32	92

11 THE BURJ KHALIFA, DUBAI

11.1 The project

The Burj Khalifa project in Dubai comprised the construction of a 160 storey high rise tower, with a podium development around the base of the tower, including a 4-6 storey garage. The Burj Khalifa Tower (originally denoted as the Burj Dubai prior to completion and opening) is currently the world's tallest building at 828m. It

is founded on a 3.7m thick raft supported on 196 bored piles, 1.5 m in diameter, extending approximately 47.5 m below the base of the raft. Figure 13 shows the completed tower.

The key challenges in this case were to undertake an economical foundation design for the world's tallest building, where the founding conditions were relatively weak rock and where significant wind loadings were to be resisted. The foundation design was undertaken by Hyder Consulting UK, with peer review by Coffey Geosciences. The final design involved the use of advanced three dimensional finite element analyses. A detailed description of this case is given by Poulos and Bunce (2008).

The geotechnical investigation was carried out in four phases and involved the drilling of 33 boreholes, with SPT testing, pressuremeter testing and geophysical testing being undertaken.

Figure 13: The Burj Khalifa

11.2 Load testing

Two programs of static load testing were undertaken for the Burj Khalifa project:

- Static load tests on seven trial piles prior to foundation construction.
- Static load tests on eight works piles, carried out during the foundation construction phase (i.e. on about 1% of the total number of piles constructed).

In addition, dynamic pile testing was carried out on 10 of the works piles for the tower and 31 of the 750 piles for the podium, i.e. on about 5% of the total works piles. Sonic integrity testing was also carried out on a number of the works piles.

Both the preliminary test piling program and the tests on the works piles provided very positive and encouraging information on the capacity and stiffness of the piles. The measured pile head stiffness values were well in excess of those predicted, and those expected on the basis of the experience with the nearby Emirates Towers. The capacity of the piles also appeared to be in excess of that predicted, and none of the tests appeared to have fully mobilized the available geotechnical resistance. The works piles performed even better than the preliminary trial piles, and demonstrated almost linear load-settlement behaviour up to the maximum test load of 1.5 times working load.

11.3 Soil-Structure interaction aspects

The original settlement prediction carried out by the author employed two analyses, one using an in-house program PIGS (Pile Group Settlement) and another using the commercially-available program FLAC (in axi-symmetric mode). The maximum settlement predicted from each analysis was almost identical (74mm and 73mm respectively), and these values also agreed with the values derived from an ABAQUS analysis carried out by the foundation designer, Hyder.

The measured maximum settlement towards the end of construction was around 43mm, indicating that the final long-term settlement would probably be in the order of 55 ± 5mm. Subsequently, a re-assessment of the settlements was undertaken in an attempt to understand the possible reasons for the (relatively modest) over-prediction of settlement (Russo et al, 2013). The majority of the foundation settlement re-assessment was carried out using linear elastic analyses with the computer program NAPRA, developed in Italy by Viggiani and Mandolini (1997). In developing the geotechnical model, lessons learned from the Emirates project were employed to try and avoid gross inaccuracy in the predicted foundation settlements.

The mesh adopted for the NAPRA analyses is shown in Figure 14, and in this mesh, the columns were spaced 1.7 m apart. Preliminary analyses indicated that using a finer mesh than this produced no change in the results. The actual shape of the raft was modelled by adopting a piecewise approximation. The majority of analyses were undertaken using the best-estimate modulus values derived from a careful interpretation of the load test data, taking into account the effects of pile-soil-pile interaction between the test piles and the reaction piles. Among the parameters investigated was the effect of the assumed loading pattern, and the effect of incorporating the stiffness of the superstructure.

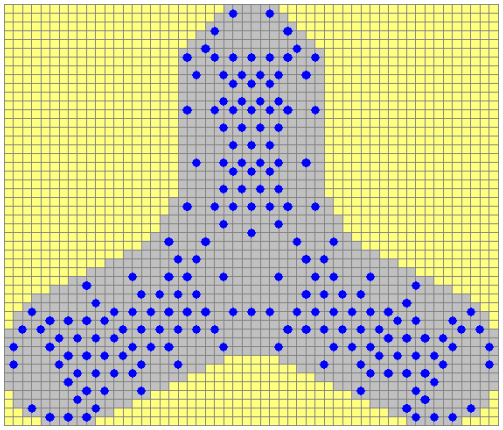

Fig.14: Model adopted in the NAPRA analyses

11.4 The influence of the loading pattern

The initial results were obtained by assuming that the average design load (32.21 MN) was applied to each pile location. In reality, the loads will be applied via wall and column locations, and consequently, NAPRA was used to examine the influence of the loading pattern on the computed settlement profile for two cases:

a. Equal loads on all the piles;
b. The actual design loadings are applied at the wall and column locations.

The computed settlement profiles along Wing C of the foundation system are shown in Figure 15, and reveal a difference in the computed settlement patterns, with the equal load assumption giving smaller maximum settlement than the other case. Thus, it would appear desirable to employ the actual load pattern in design calculations.

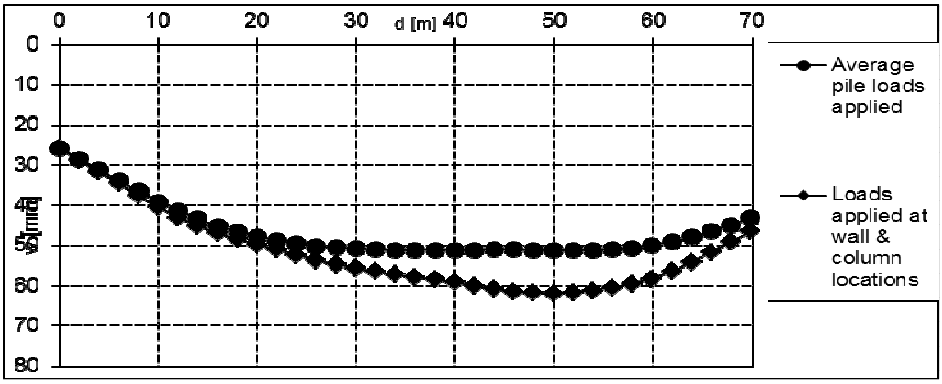

Figure 15: Influence of Assumed Loading Pattern on Computed Settlement Profile

In order to investigate the effect on the computed settlement and differential settlement, and to try and obtain a more accurate estimate of the pattern of settlement via a geotechnical analysis, the stiffening effect exerted by the superstructure on the raft was taken into account, in various ways, by increasing the bending stiffness of the raft in each wing (estimated by the structural designers to be equivalent to an increase of 25200 kNm^2 per wing). Six alternative methods of incorporating this increased bending stiffness were adopted:

a. Increasing the thickness of the whole raft to reflect the bending stiffness of the entire tower (Model 1);
b. Increasing the raft thickness over the central part of the wings and on the core, as shown in Figure 16, to reflect the bending stiffness of the entire tower. This is denoted as Model 2;
c. Increasing the raft thickness only below the shear walls (see Figure 17), to reflect the bending stiffness of the entire tower; this case is denoted as Model 3;
d. Model 1, with only 10% of the stiffness of the tower considered (Model 1M);
e. Model 2, with only 10% of the stiffness of the tower considered (Model 2M);
f. Model 3, with only 10% of the stiffness of the tower considered (Model 3M).

In each case, the actual pattern of loading via the columns and walls was applied, with only the dead load component considered

Figure 18 compares the various computed profiles of settlement across the tower, together with those in which no account is taken of superstructure stiffness. Also shown is the design profile developed by Poulos and Bunce (2008), which was for combined dead plus live load, and therefore not directly comparable. Clearly, there is a considerable difference between the extreme profiles, those taking all the superstructure stiffness into account, and that in which no account is taken of the superstructure stiffness. It would appear reasonable to assume that the profiles from Models 1M, 2M and 3M may be more reasonable approximations to reality, and this appears to be borne out by the comparisons with the measured settlements, as described below.

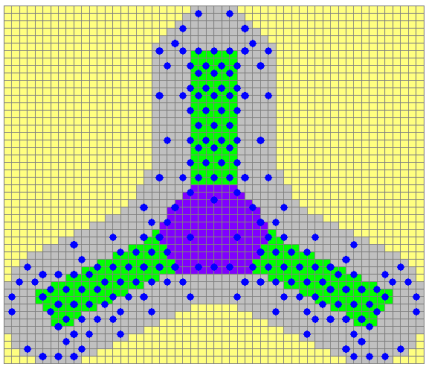

Figure 16: Raft model 2

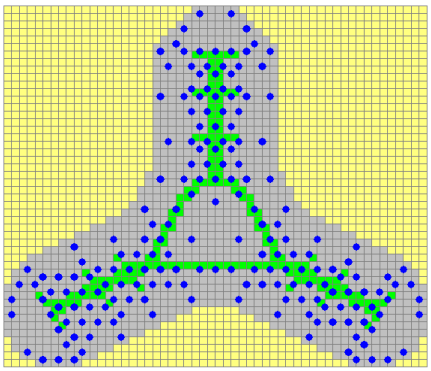

Figure 17: Raft Model 3

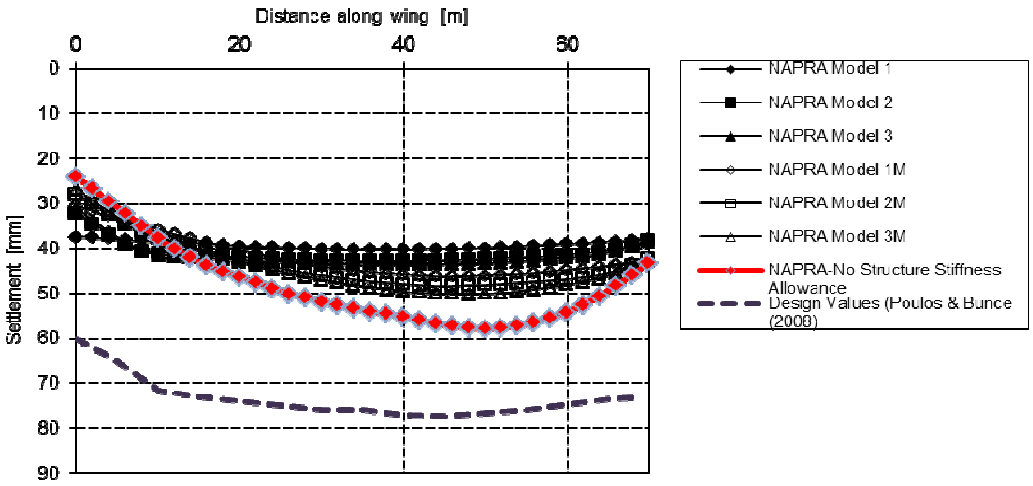

Figure 18: Comparison between Various Calculated Settlement Profiles

Detailed settlement measurements were only available up to February 2008, before the end of construction and well before the commissioning and occupation of the building in January 2010. Nevertheless, anectodal evidence indicated that the additional settlements between February 2008 and January 2010 were relatively small, of the order of 1-2mm.

Figure 19 shows comparisons between the latest available measured profile of settlement in February 2008, and the calculated settlement profiles from Models 1M, 2M and 3M. The following observations are made from an examination of Figures 18 and 19:

1. Without allowance for superstructure stiffness, the calculated maximum final differential settlement is about 23mm which is considerably larger than the measured value of about 14mm. The computed maximum settlement is also larger than the measured value, although some additional settlement would be expected after the building has been in operation for some years;
2. When allowance is made for the superstructure stiffness, the computed maximum settlement is similar in magnitude to the measured value. However, for Models 1, 2 and 3, in which the full superstructure stiffness is incorporated (albeit approximately), the computed settlement pattern differs somewhat from the measured pattern, and the computed differential settlements are significantly smaller than those measured. It seems clear that it is not appropriate to allow for the bending stiffness of the entire structure when trying to modify the foundation stiffness;
3. When the allowance for superstructure stiffness is reduced by a factor of 10 (Models 1M, 2M and 3M), there is better agreement between the computed and measured profiles, with a computed maximum differential settlement of about 22 mm, similar to the measured value. In this case, the stiffness of the raft is approximately 53 times its original value, and this latter value is much larger than the value of 10 times adopted by Hooper (1973) for the Hyde Park Barracks in London and by Sales et al. (2010) for the Skyper Building in Frankfurt. Interestingly, and almost certainly coincidentally, the profile for this case is rather similar to that obtained for the case when the average load is imposed on each pile;
4. There remain some differences between the measured and computed settlement profiles in the vicinity of the edge of the wing. There may well be scope to refine the method by which the superstructure is incorporated into the geotechnical foundation analysis;
5. The calculated settlements from the design phase are considerably greater than those obtained from the analyses in this paper. The main reason for these larger settlements is that the settlements were for both dead and live load acting, and in addition, conservative values of Young's modulus were used in these analyses, with a somewhat different distribution of ground stiffness with depth being adopted in those calculations. Once again, this comparison emphasises the importance of appropriate selection of the ground stiffness values if accurate foundation settlement predictions are to be made.

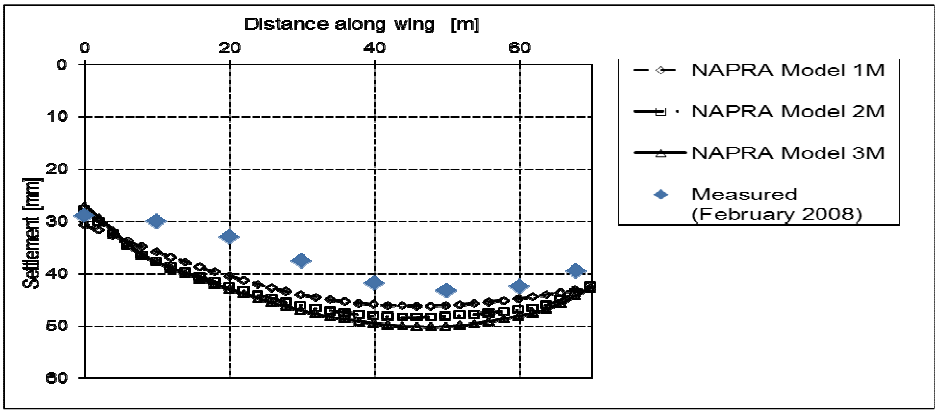

Figure 19: Measured and Computed Settlement Profiles along Wing C

The settlements measured during construction were consistent with, but comfortably smaller than, those originally predicted (between 70 and 80mm), with a maximum settlement of about 44mm being measured. Overall, the performance of the piled raft foundation system exceeded expectations.

As with other high-rise projects, the Burj Khalifa involved, as well as soil-structure interaction considerations, close interaction between the structural and geotechnical designers in designing piled raft foundations for the complex and significant high-rise structures. Such interaction has some major benefits in avoiding over-simplification of geotechnical matters by the structural engineer, and over-simplification of structural matters by the geotechnical engineer, thus promoting more effective and economical foundation and structural designs.

12 INCHEON 151 TOWER, SOUTH KOREA

12.1 The project

A 151 storey super high-rise building project is currently under design, to be located in reclaimed land constructed on soft marine clay in Songdo, South Korea. This building is illustrated in Figure 20, and is described in detail by Badelow et al (2009) and Abdelrazaq et al (2011). The challenges in this case relate to a very tall building, sensitive to differential settlements, to be constructed on a reclaimed site with very complex geological conditions.

The site lies entirely within an area of reclamation, and comprises approximately 8m of loose sand and sandy silt, over approximately 20m of soft to firm marine silty clay. These deposits are underlain by approximately 2m of medium dense to dense silty sand, which overlie residual soil and a profile of weathered ("soft") rock.

The footprint of the tower was divided into eight zones which were considered to be representative of the variation of ground conditions, and geotechnical models were developed for each zone. Appropriate geotechnical parameters were selected for the various strata based on the available field and laboratory test data, together with experience of similar soils on adjacent sites. One of the critical design issues for the tower foundation was the performance of the soft silty clay under lateral and vertical loading, and hence careful consideration was given to the selection of parameters for this stratum.

The foundation comprised a concrete raft 5.5m thick with 172 piles, 2.5m in diameter, with the number and layout of piles and the pile size being obtained from a series of trial analyses through collaboration between the geotechnical and structural designers. The piles were founded a minimum of 2 diameters into the "soft" rock, or below a minimum toes level of El -50m, which was deeper.

The use of a suite of commercially available and in-house computer programs allowed the detailed analysis of the large group of piles to be undertaken, incorporating pile-soil-pile interaction effects, varying pile lengths and varying ground conditions in the foundation design. During final design, an independent finite element analysis was used to include the effect of soil-structure interaction and to include the impact of the foundation system on the overall behaviour of the tower.

Figure 20: Incheon 151 Tower (artist's impression)

12.2 Load testing

A total of five pile load tests were undertaken, four on vertically loaded piles via the Osterberg cell (O-cell) procedure, and one on a laterally loaded pile jacked against one of the vertically loaded test piles. For the vertical pile test, two levels of O-cells were installed in each pile, one at the pile tip and another at between the weathered rock layer and the soft rock layer.

The vertical test piles were loaded up to a maximum one way load of 150MN in about 30 incremental stages, in accordance with ASTM recommended procedures. The lateral pile load test was performed after excavation of about 8m of the upper soil, to simulate a similar ground condition as for the tower foundation. The lateral test pile was subjected to a maximum lateral load of 2.7MN.

The results of pile load tests indicated that the actual performance, under both vertical and lateral loads, was superior to that predicted initially, thus providing scope for the development of a more cost-effective design.

Presently the tower site is fully reclaimed and fenced, and enabling works are being planned.

12.3 Soil-Structure interaction aspects

The overall settlement of the foundation system was estimated during all three stages of design, using the available data at that stage, and relevant calculation techniques. The predicted settlements ranged from 75mm from a simple equivalent pier analysis to 56mm from a PLAXIS 3D finite element analysis.

The detailed design analyses were carried out using an in-house computer program CLAP (Combined Load Analysis of Piles) for the ultimate limit state load cases (ULS) and the program GARP (Small and Poulos, 2007) for serviceability (SLS) loadings. As part of the design process, estimates were required of the maximum axial loads in each pile within the foundation system, and initially, the program CLAP was used. CLAP implicitly assumes that the raft supporting the piles is rigid, and as a consequence, the computed axial loads on some piles were found to be very large.

To investigate the effect of the rigid raft assumption, the foundation performance was re-assessed using GARP and taking the flexibility of the raft into account. The serviceability load case (i.e dead and live loads) was considered and the loads were applied at column and core locations.

Table 6 presents a summary of foundation settlement, axial loads and stiffness on the corner, centre edge and centre piles of the foundation (see Figure 21). The maximum predicted settlement occurs within the heavily loaded core area, while the computed pile stiffness values are greatest for the outer piles. As the analysis considered non-linear pile behaviour, therefore the higher stiffness (and hence larger loads) for the outer piles degrade more rapidly under loading than the central piles.

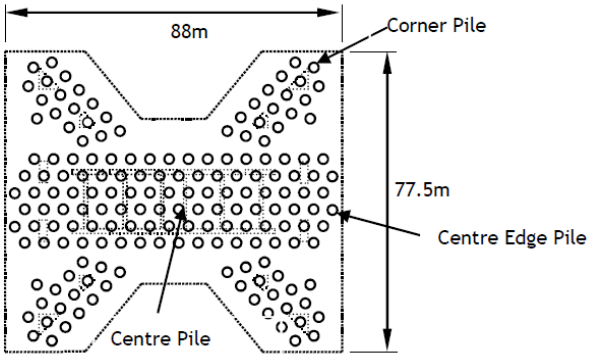

Figure 21: Foundation Layout for Incheon Tower

Considering a rigid raft for the foundation, the total and differential settlement was predicted to be smaller, with higher pile head loads for corner and centre-edge piles, thus resulting in higher vertical pile stiffness values, especially on the outer piles when compared with those for a flexible raft.

When the flexibility of the raft was incorporated, the pile load distribution was found to be fairly uniform, with slightly higher pile loads being predicted at the centre of the foundation where the heavily loaded core is located. The loads on piles for a rigid raft case are approximately two times the loads for a flexible raft, except for the centre piles.

Table 6: Summary of foundation performance

		Rigid Raft	Flexible Raft
Pile Load (MN)	Centre Pile	24	49
	Centre Edge Pile	65	33
	Corner Pile	85	43
Pile Stiffness (MN/m)	Centre Pile	511	726
	Centre Edge Pile	1418	932
	Corner Pile	1604	1292
Raft Settlement (mm)	Maximum	52	67
	Minimum	26	28

As the thickness of the raft (t) is 5.5m and the average centre-to–centre pile spacing (s) is approximately 5m, the ratio of t/s is greater than one, and the raft would be expected to behave as a semi-flexible raft (i.e. behavior in-between a flexible and rigid raft) with the loads on the outer piles then being significantly less than those for a perfectly rigid raft.

Based on the assessment, it is concluded that it is important to model the flexibility of the raft to avoid having to design for unrealistically large loads in the outer piles within the group.

13 CONCLUSIONS

This paper has outlined a process for the design of high-rise building foundations and has identified a number of soil-structure interaction aspects that need to be incorporated into this process. In particular, three aspects have been discussed in detail:

1. Pile-soil-pile interaction, i.e. the fact that a pile within a group environment is influenced by the loads and deformations of the other piles within the group and also, within a piled raft foundation, by the raft behaviour;
2. The stiffness of the superstructure and also the way in which the loads are represented in the analysis;
3. The flexibility of the raft.

The influence of these three aspects has been illustrated via three projects:

1. The Emirates twin towers in Dubai, for which over-simplification of the geotechnical model led to a significant over-estimate of the pile-soil-pile interactions and a consequent significant over-estimate of the foundation settlements;
2. The Burj Khalifa in Dubai – currently the world's tallest building, for which over-simplifying the representation of the loads and ignoring the superstructure stiffness led to some inaccuracy of the predicted distribution of settlement across the foundation;
3. The Incheon 151 Tower in Incheon, South Korea, for which the initial assumption of a rigid raft led to very large estimated axial loads in some of the outer piles. Inclusion of the effects of raft flexibility led to significantly smaller maximum pile loads and a more uniform distribution of pile loads.

It is clear that soil-structure interaction effects should be incorporated into the design of foundations for tall buildings. Failure to do so can lead to inaccurate assessments of foundation settlements and pile loads. In particular, failure to account for raft flexibility can lead to serious over-estimates of axial loads in some piles and to a consequent over-conservative structural design.

The value of pile load testing, in conjunction with advanced methods of analysis and design, has been emphasized, as has the importance of constructive interaction between the structural and geotechnical designers.

ACKNOWLEDGEMENTS

The author gratefully acknowledges the contributions of Frances Badelow, Tristan McWilliam, Helen Chow and Patrick Wong in relation to the analyses for the towers described in the paper. Grahame Bunce led the foundation design for the Burj Khalifa. S.H. Kim, Ahmad Abdelrazaq and their teams in Korea had a major involvement in the Incheon Tower foundation design. Professor John Small has been pivotal in developing the GARP program and implementing it in a user-friendly form.

REFERENCES

Abdelrazaq, A., Poulos, H.G., Badelow, F. and Sung-Ho Kim (2011). "Foundation Design and Pile Testing Program for the 151 Story Incheon Tower in a Reclamation Area, Incheon, Korea. *Paper TS21-02, Int. Conf. Tall Buildings & Urban Habitat (CTBUH*), Seoul, Korea.

Badelow, F., Kim, S., Poulos, H.G. and Abdelrazaq, A. (2009). "Foundation design for a tall tower in a reclamation area". *Proc. 7th Int. Conf. Tall Buildings*, Hong Kong, Ed. F.T.K. Au, Research Publishing, 815-823.

Brown, P.T. and K.R. Yu, 1986. "Load sequence and structure-foundation-interaction". *J. Struct. Eng.*, 112: 481-488.

CTBUH (2011). Council for Tall Buildings and the Urban Habitat, Press release, December 8, 2011.

Gazetas, G. (1983) "Analysis of Machine Foundation Vibrations: State of the Art". *Int. Jnl. Soil Dynamics & Earthquake Eng*., Vol. 2 (1): 2-42.

Gazetas, G. (1991). "Foundation Vibrations". Chapter 16 of Foundation Engineering Handbook, 2nd Ed., Edited H-Y Fang. Chapman & Hall, New York.

Gusmao Filho, J.A. and Guimaraes, L.J. (1997). "Limit Stiffness in Soil Structure Interaction in Buildings". *Proc. 14th Int. Conf. Soil Mechs. Found. Eng.*, Hamburg, Vol. 2, 807-808.

Haberfield, C.M. (2013). "Tall Tower Foundations – from concept to construction". *Advances in Foundation Engineering*, Ed. K.K. Phoon et al, Research Publishing Services, 33-65.

Hemsley, J.A. (2000)."*Design Applications of Raft Foundations*". Thomas Telford, London.

Horikoshi, K. and Randolph, M.F. (1998). "Optimum Design of Piled Rafts". *Geotechnique* 48(3): 301-317.

Katzenbach, R., Arslan, U. Moorman, C. and Reul, O. (1998). "Piled Raft Foundations: Interaction Between Piles and Raft". *Darmstadt Geotechnics*, Darmstadt University of Technology, 4: 279-296.

Lee, I.K. and Brown, P.T. "Structure-Foundation Interaction Analysis." *Journal of Structural Division, American Society of Civil Engineers,* Vol.98, No. 11, pp2413-2431.

Mandolini, A. and Viggiani, C. (1997). "Settlement of Piled Foundations". Geotechnique, 47(3): 791-816.

Poulos, H.G. (1975) "Settlement Analysis of Structural Foundation Systems". *Proc. 4th St.-East Asian Conf. Soil Eng*., Kuala Lumpur.

Poulos, H.G. (1993). "Settlement Prediction for Bored Pile Groups". Bored and Auger Piles, BAPIII, Ed W. van Impe, Balkema, Rotterdam, 103-118.

Poulos, H.G. (1994). "An Approximate Numerical Analysis of Pile-Raft Interaction". Int. Jnl. Num. Anal. Methods in Geomechs., Vol. 18, 73-92.

Poulos, H.G. (2001). "Piled Raft Foundations – Design and Applications". *Geotechnique*, 51(2): 95-113.

Poulos, H.G. (1994). "Settlement Prediction for Driven Piles and Pile Groups". *Vert. and Horizl. Deformns. of Foundns. and Embankments, Geotech. Spec. Publ. No. 40*, ASCE, New York, Vol. 2, 1629-1649.

Poulos, H.G. and Bunce, G. (2008). "Foundation design for the Burj Dubai – the world's tallest building". *Proc. 6th Int. Conf. Case Histories in Geot. Eng*., Arlington, VA, Paper 1.47, CD volume.

Poulos, H.G., Carter, J.P. and Small, J.C. (2001). "Foundations and Retaining Structures-Research and Practice". *Proc. 15th Int. Conf. Soil Mechs. Geot. Eng*., Istanbul, 4: 2527-2606.

Poulos, H.G. and Davis, E.H. (1980). "*Pile Foundation Analysis and Design*". John Wiley, New York.

Poulos, H.G**.,** Small, J.C. and Chow, H.S.W. (2013). "Foundation Design for High-Rise Towers in Karstic Ground". *ASCE GSP229, Foundation Engineering in the Face of Uncertainty*, Ed. J.L. Withiam, K-K. Phoon and M.H. Hussein, 720-731.

Randolph, M.F. (1994). "Design Methods for Pile Groups and Piled Rafts". *Proc. XIII Int. Conf. Soil Mechs. & Found. Eng.*, New Delhi, Vol.5, 61-82.

Russo, G., Abagnara, V., Poulos, H.G. and Small, J.C. (2013). "Re-Assessment of Foundation Settlements for the Burj Khalifa, Dubai". *Acta Geotecnica*, 8(1): 3-15.

Small, J.C. and Poulos, H.G. (2007). "A Method of Analysis of Piled Rafts". Proc. 10th Australia-New Zealand Conf. Geomechs., Aust. Geomechs. Society, 1: 550-555.

Zhang, L. and Ng, A.M.Y.(2006). "Limiting tolerable settlement and angular distortion for building foundations". *Geotech. Special Publication No. 170, Probabilistic Applications in Geotechnical Engineering*, ASCE (on CD Rom**).**

Zhang, and Small, J.C. (1994). "Finite layer analysis of soil-raft-*structure interaction*." *Proc. 13th Int. Conf. Soil Mech. Foundn Engng,* New Delhi. India. Jan. *1994*. 2, 587-590. A. A. Balkema. Rotterdam. *1994*.

The Role of Pile Structural Capacity in Pile Lateral Load Effect on Slope Stability

B.K.L. Ieong, R.K.Y. Leung & R.N.N. Keung
Hyder Consulting Limited, Hong Kong

ABSTRACT

Piles under lateral load and embedded within a slope are often considered to have a load effect on the slope and hence affect its stability. As a common design approach, soil-structure analysis with piles modelled as beams and lateral soil resistance as elastic springs is undertaken to work out the distribution of soil resistance along pile shafts. Limit state equilibrium analysis is then undertaken for the slope to ensure that, with the lateral load action on the soil mass considered, the slope still achieves the required factor of safety. The intrinsic inconsistence of this approach, however, is that the forces from an elastic analysis are assumed to apply continuously into the plastic deformation stage of the slope when the slope fails, i.e. the increase in resistance to the lateral load applied to the pile group through internal forces of the piles (shear and, in case of raking piles, axial forces) associated with increase in deflection has not been taken into account.

This paper serves, with the aid of numerical modelling of a typical problem of pile lateral load effect on slope, to present a design approach taking into account the available soil resistance, without jeopardizing slope stability, and the pile structural capacity. It also aims to demonstrate that, though it is a common practice to provide pile sleeves to reduce pile lateral load effect on slopes, the pile sleeves can actually be eliminated for the benefit of reducing pile deflection while not sacrificing slope stability, provided the piles are designed properly.

1 INTRODUCTION

In Hong Kong, many buildings are constructed on slopes and most of these buildings are supported by piles. The stability of the slopes under the effect of piles under lateral load needs to be assessed by the geotechnical engineers. Limit-equilibrium methods are the most commonly used approach for analyzing the stability of slopes. The popularity of limit equilibrium methods is primarily due to their relative simplicity, ready ability to evaluate the sensitivity of stability to various input parameters, and the experience that geotechnical engineers have acquired over the years in interpreting calculated factor of safety values. The factors of safety given by the limit equilibrium analyses help geotechnical engineers to guard against uncertainties associated with geological model, soil strength parameters and loadings, etc., and the possibility that identified failure mechanisms differ from actual behavior. Also, the recommended factor of safety values for slopes generally ensures that deformations are within acceptable range.

For calculating the minimum factor of safety of slopes in Hong Kong under the effect of laterally loaded piles, it is a common practice to adopt limit equilibrium approach using of method of slides. Using this approach, the distribution along the pile of lateral load transfer from the pile to the soil mass is first calculated. The lateral load transfer distribution is then modeled as horizontal load, either in the form of a series of point loads or line loads, acting in the soil mass in the limit equilibrium slope stability analysis programme. Loads above any defined slip surface are taken onto account in calculating the factor of safety against failure of the slip surface. By adopting this approach, the calculated minimum factor of safety of the slope is destined to decrease with a pile under lateral load in place. This approach, however, is conservative since the increase in structural resistance of the pile to the applied lateral load through bending and shear associated with increase in deflection is not taken into account. As a result, either pile sleeving, aiming at minimizing the transfer of lateral load from the pile to the slope, particularly at shallow depth, or raking piles are required to be adopted in order to avoid rendering the factor of safety of the slope below the acceptable limit.

Advances in computer technology have pushed the finite element method (FEM) and other numerical analysis approaches to the forefront of geotechnical practice. It can accommodate practically all kinds of geometry and can model elasto-plastic behaviour typical of soil materials. FEM is increasingly being applied to slope stability analysis. One of the most popular techniques for performing FEM slope analysis is the shear strength reduction approach. The shear strength reduction approach is simple in concept - systematically reducing the shear strength parameters of materials by a factor and carrying out FEM analysis of the slope until deformations are unacceptably large or the analysis does not converge due to the formation of a global failure mechanism. In this paper, the shear strength reduction method is adopted to assess the factor of safety of a slope under the same lateral load for different pile types in order to offer some insight into the behaviour of laterally loaded piles on slopes.

2 SHEAR STRENGTH REDUCTION (SSR) APPROACH

By definition, the factor of safety of a slope is the "ratio of actual soil shear strength to the minimum shear strength required to prevent failure," or the factor by which soil shear strength must be reduced to bring a slope to the verge of failure. In the SSR finite element technique, elasto-plastic behavior, such as Mohr-Coulomb model, is assumed for slope materials. The material shear strengths are progressively reduced until collapse occurs. The SSR technique for slope stability analysis involves systematic use of finite element analysis to determine a stress reduction factor (R) that brings a slope to the verge of failure. The shear strengths of all the materials in a FE model of a slope are reduced by dividing them with R, starting from unity and then progressively increased or decreased. FE analysis of this model is repeated until a critical R value that induces instability is attained. A slope is considered unstable in the SSR technique when its FE model does not converge to a solution (within a specified tolerance). The key advantage of SSR method over traditional limit-equilibrium analysis for investigating slopes stability is that there is no need to pre-define potential slip surfaces as the SSR technique automatically establishes the critical failure mechanism.

Typical to slope stability problems where the Mohr-Coulomb soil model is used, the SSR method involves reducing the cohesion, c' and friction angle, ϕ', of soil materials by a strength reduction factor, R, using Equations (1) and (2) below until the slope fails quasi-naturally:

$$c_d = \frac{c}{R} \tag{1}$$

$$\tan(\phi_d) = \frac{\tan(\phi)}{R} \tag{2}$$

The highest value of the strength reduction factor that still satisfies equilibrium and is kinematically acceptable is the Factor of Safety, FOS, of the slope:

$$R_{max} = FOS \tag{3}$$

Figure 1 extracted from Ng et al. (2001) shows a typical relationship between the strength reduction factor and the displacement at a nodal point adjacent to the pile from an analysis using an elasto-plastic model. When the strength parameters are factored down continuously, the stress state of the slope would arrive at the critical point A, beyond which isolated plastic zones would merge and expand rapidly. Plastic deformations would then start to accelerate upon a further increase in the strength reduction factor. This critical point A symbolizes initiation of slope instability, whereas Point B signifies global failure of the slope and the strength reduction factor corresponding to this point is taken as the slope stability factor of safety.

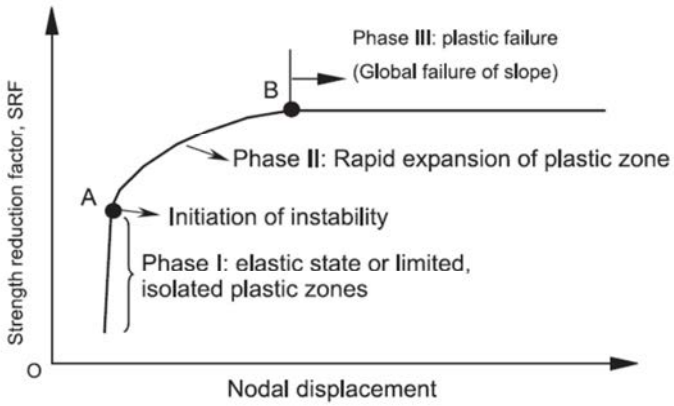

Figure 1 – Identification of Slope Failure from Calculated Nodal Displacement, Ng et al. (2001)

3 STUDY MODEL

In this paper, a single pile-slope system in an idealized elastic, perfectly plastic soil is investigated using the commonly used finite element program PLAXIS 2D. A 10-m high soil cut slope with slope angle of 35° is modelled. A pile is assumed to be of 20 m long to installed at 2 m setback away from the slope crest line. An inclined bedrock is assumed to be located at 20m below the pile head at ground level of the slope crest. For simplicity, the slope is assumed to be dry. The slope-forming material is modelled using the Mohr-Coulomb soil model and assumed to possess a Young's Modulus E of 50MPa, typical of dense Completely Decomposed Granite encountered locally in Hong Kong. Apparent cohesion c' and friction angle ϕ' of the soil are assumed to be 5 kPa and 35° respectively. The pile material is assumed to be linearly elastic. In PLAXIS 2D, the SSR method is called "Phi/C" Reduction and the strength reduction factor, R, takes the notion of Msf (the Total Multiplier Summation).

The factor of safety of the slope before pile installation, determined by limit equilibrium method with the analysis programme SLOPE/W, is 1.471. Using SSR with PLAXIS 2D, the factor of safety of the slope is found to be 1.502, which is 2% from that giving by SLOPE/W, thus confirming the two approaches give consistent results. The SLOPE/W analysis and PLAXIS 2D analysis are presented in Figure 2 and Figure 3 respectively.

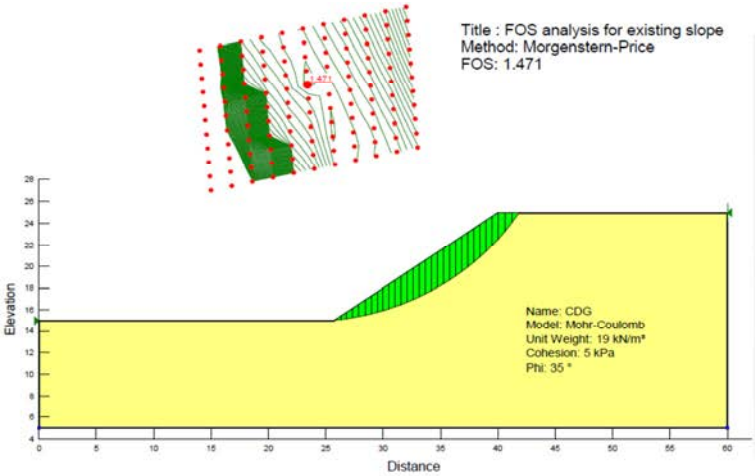

Figure 2 – SLOPE/W analysis for slope without pile

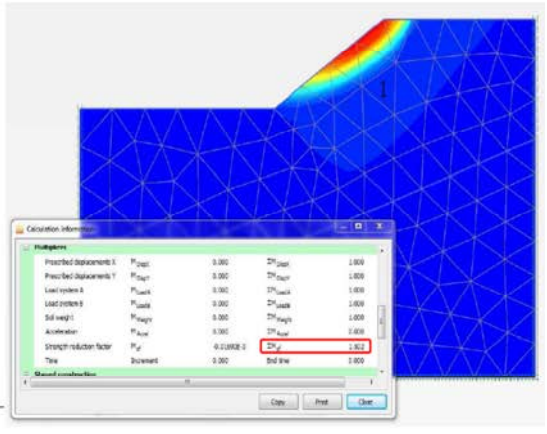

Figure 3 – PLAXIS analysis for slope without pile

Four types of pile under an assumed lateral load of 200kN at pile head as below are considered for the SSR analysis:

a) 1m dia. bored pile with 2 m rock socket;
b) 1m dia. bored pile with pile base on bedrock level;
c) Socketted H-pile (305 x 305 x 223 kg/m UBP in 610-mm dia. grouted hole with 5 m socket into rock; and
d) Driven H-pile of 305 x 305 x 223 kg/m UBP terminating at bedrock level.

Sectional properties for the 3 types piles are presented in Table 1 below:

Table 1 – Sectional properties of piles

	EA(kN/m)	EI (kNm^2/m)
1m dia. bored pile (Grade 45 concrete)	20734511.5	1295907.0
Socketted H-pile	11679395.8	247217.4
Driven H-pile	5822000.0	108033.0

For simplicity, the pile stiffness and lateral load are applied directly into the plain strain FE model without consideration of 3D load spread effect. The pile is modelled as a continuous wall into-the-plane. Figure 4 shows the finite element model of Case (a)

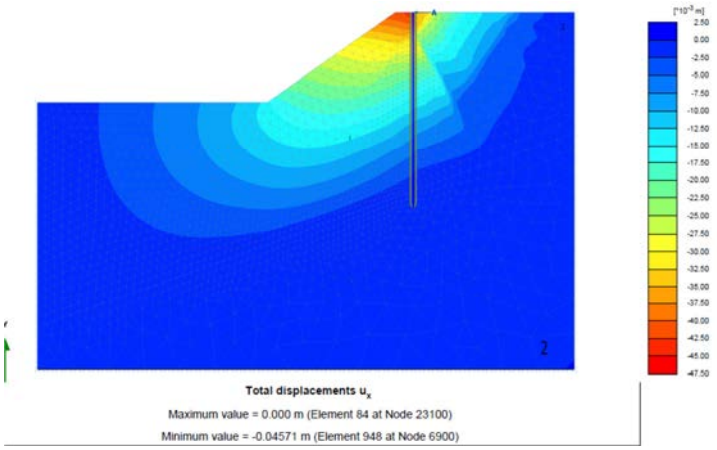

Figure 4 – PLAXIS Model of Case (a)

4 RESULTS OF ANALYSES

The calculated factor of safety of the slope is around 1.5 for Case (a), as presented in Figure 5 below. Similar result is given by analyses of the other cases.

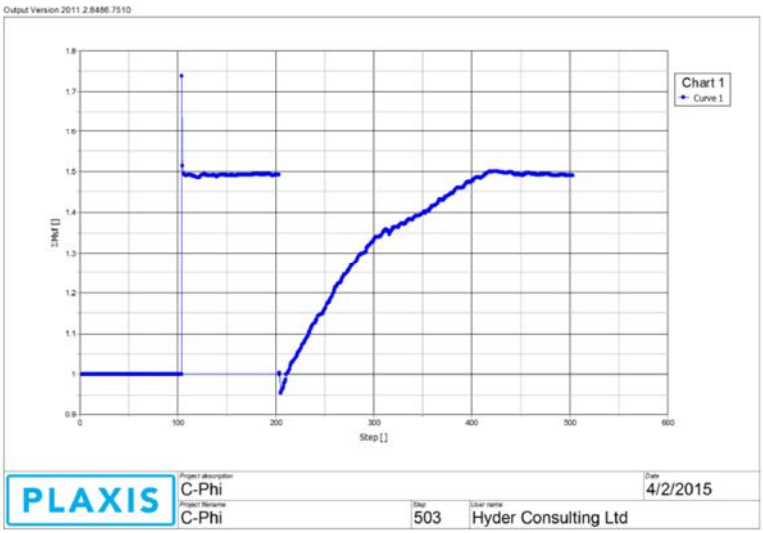

Figure 5 – Calculation of FoS of Slope under Case (a)

The predicted slope movement mechanism under Case (a) after SSR to FoS of 1.4 is presented in Figure 6 below.

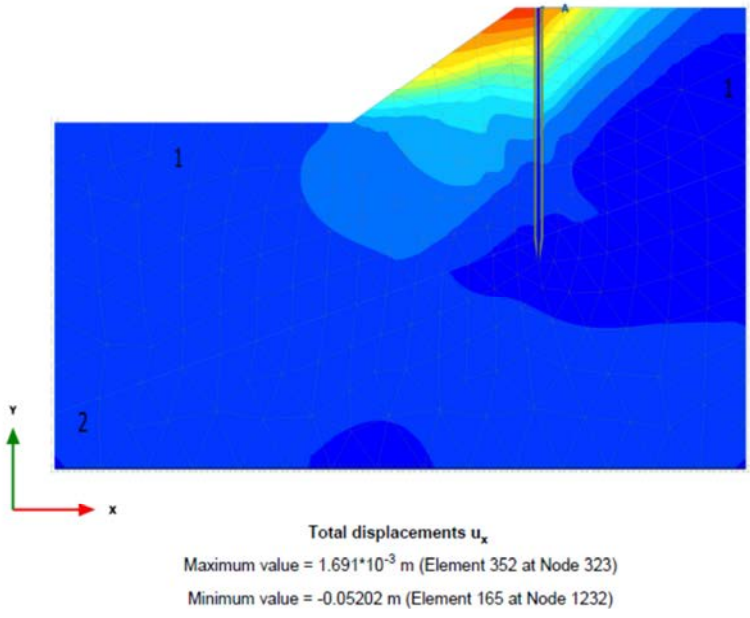

Figure 6 – Predicted Slope Movement Mechanism under Case (a) after SSR

Figures 7 and 8 show the pile bending moment diagram of Case (a) respectively before strength reduction process, i.e. with R equals 1, and after strength reduction process, with R equals 1.5. Comparing the two bending moment diagrams, the one with soil strength parameters reduced by a factor of 1.5 shows at a greater

depth below pile head a higher maximum bending moment, implying there is less transfer of lateral load to the soil mass at shallower depth and more lateral load is carried down the pile shaft through shear in the pile.

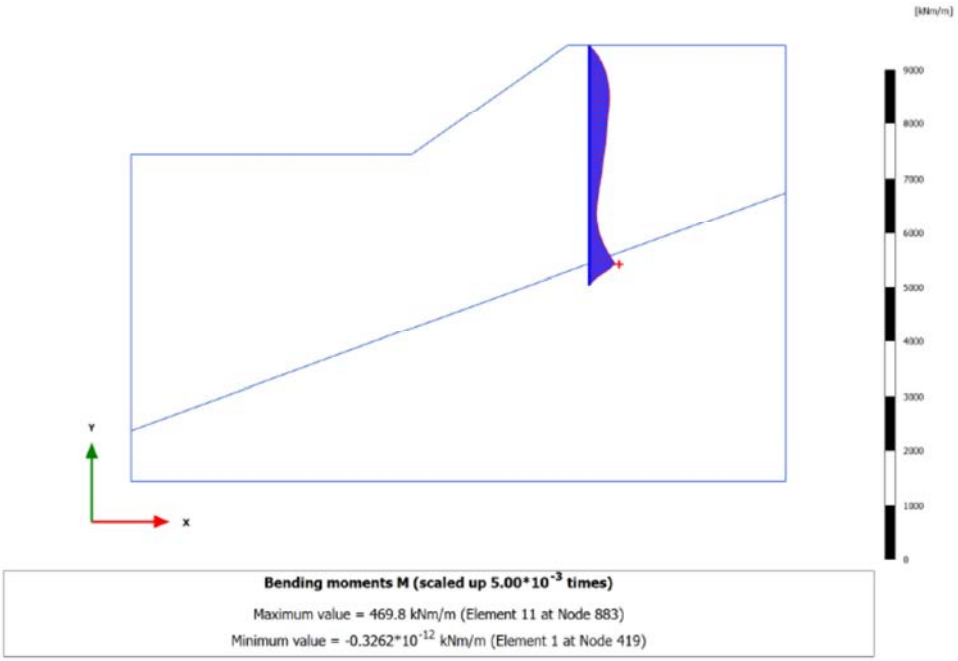

Figure 7 – Pile Bending Moment Diagram for Case (a) before SSR

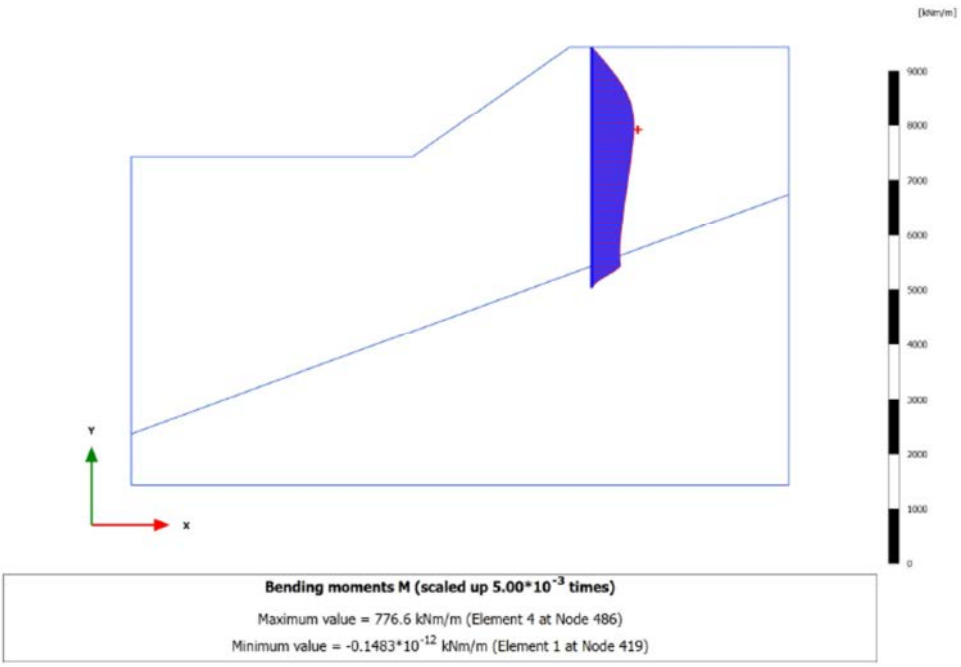

Figure 8 – Pile Bending Moment Diagram for Case (a) after SSR

A plot of strength reduction factor against the calculated lateral displacement of soil immediately in front of the pile head under Case (a) is presented in Figure 9. It shows that as R approaches R_{max} = 1.5, displacements become very large, meaning that the slope is yielding.

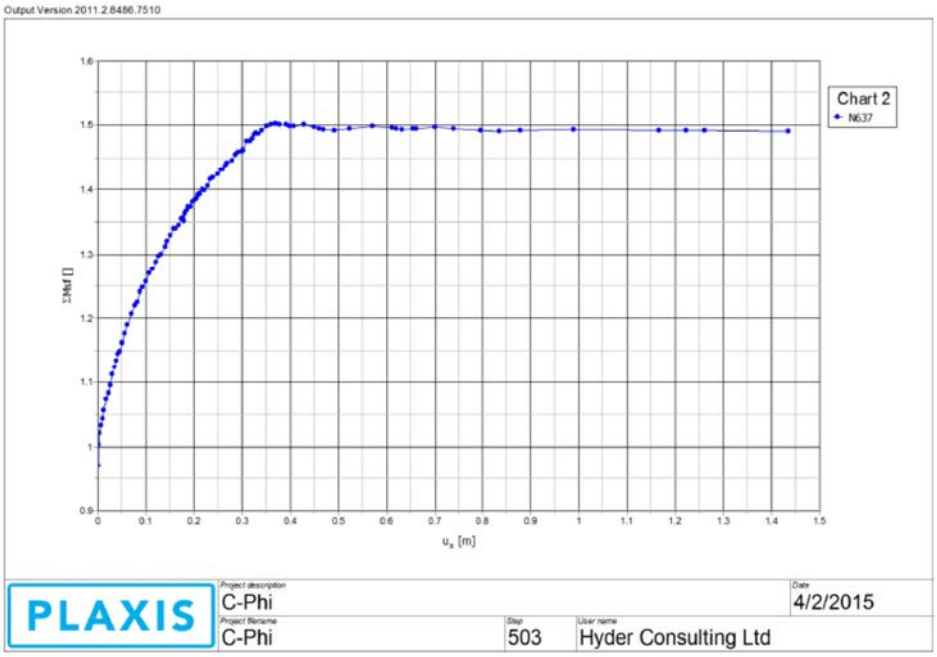

Figure 9 - Plot of Strength Reduction Factor against the Calculated Lateral Displacement of Soil Immediately in front of the Pile Head under Case (a)

The bending moment and shear force diagrams of the pile in Case (a) for R from 1.0 to 1.5 are shown in Figure 10. The plots further demonstrate that with and increasing R, lateral load transfer from the pile to the soil mass takes place at greater depth and the pile bending moment becomes greater.

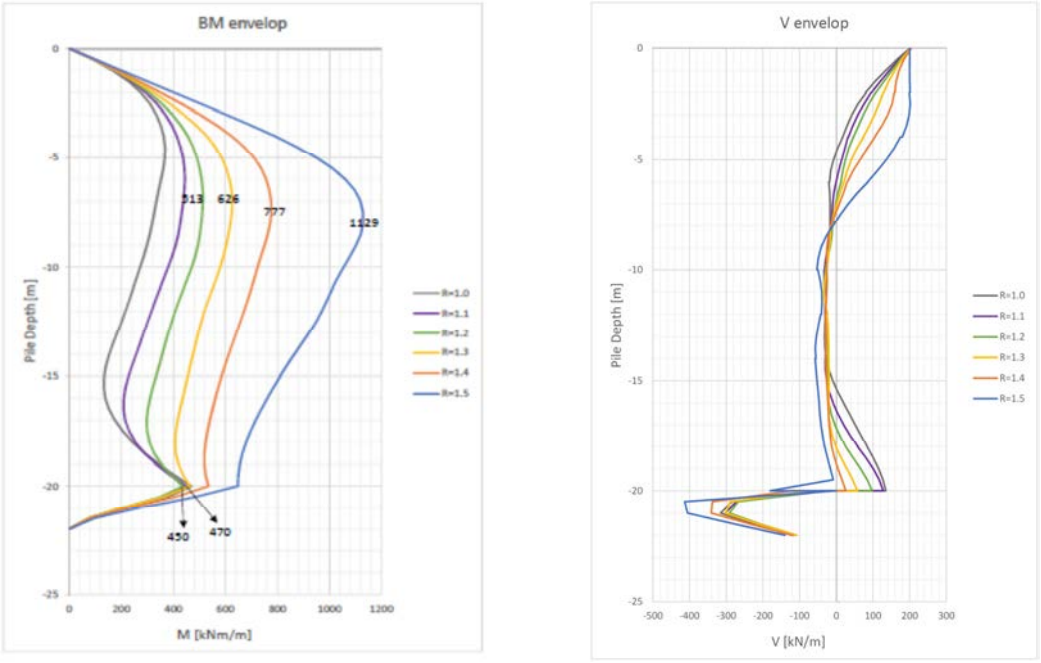

Figure 10 - Plots of Pile Bending Moment and Shear Force in Case (a)

Table 2 summarises the pile head displacement and maximum pile bending moment from the FE model based on design strength parameters (i.e. R=1.0) and the maximum pile bending moment from the FE model when R=1.4 is applied for the four cases.

Table 2 – Summary of FE Analyses Results for the Four Study Cases

Case	Pile Head Displ. for R=1.0 (mm)	Max M for R=1.0 (kNm)	Max M for R=1.4 (kNm)
Case (a) – Bored pile with rock socket	45.7	368/470*	777
Case (b) – Bored pile on rock	46.4	365	758
Case (c) – Socketted H-pile	62.5	291	703
Case (d) – Driven H pile	86.0	284	700

*M at top of rock socket

For verification purpose, the bored pile in Case (a) is re-modelled as elasto-plastic element and the required bending moment capacity of bored pile for Case (a) (i.e. 777 kNm) corresponding to that of FOS =1.4 is inputted as strength properties. After SSR, the FoS is found to be 1.4 as presented in Figure 11 below and which is consistent with the result presented in Figure 5.

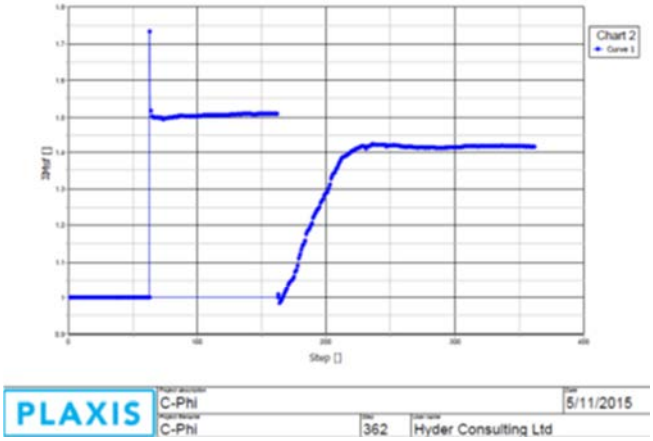

Figure 11 – Calculation of FoS for Slope under Case (a) with Moment and Axial Strength Properties as Input

5 OBSERVATIONS

From the analysis results as shown above, the following observations can be made:

a) The stability of a slope, i.e. its factor of safety, is not impaired by a pile installed in it and subjected to lateral load, provided the pile has sufficient embedment to carry the load to deeper soil stratum and does not fail structurally.
b) With progressive reduction of soil strength, the pile bending moment increases and hence the required pile structural capacity. Hence, the pile can be designed to a lower structural capacity if a lower slope stability FoS (i.e. R) is required to be achieved. The study model has a factor of safety of 1.5, if 1.4 is adopted as the design factor of safety, then the pile is only required to be designed to resist the bending moment corresponding to an R of 1.4. The soil resistance provided to the pile will have intrinsically a factor of safety of 1.4.
c) Whilst the four cases studied show the slope stability is not impaired provided the pile has the adequate structural and geotechnical capacity, the pile and slope movements differs according to the pile stiffness in the four cases. This has to be taken into account in serviceability consideration.

6 SUGGESTED DESIGN APPROACH

It is suggested for the classical problem of pile under lateral load embedded within a slope, the following approach based on the Shear Strength Reduction (SSR) Method be adopted:

a) Carry out slope stability analysis taking into account the pile and pile lateral load using SSR.
b) Check that the pile has sufficient embedment that Rmax is greater than the required FoS of the slope.
c) Check serviceability limits are complied with, e.g. that the pile head movement is within allowable limit under the analysis of R=1.0. If not, the pile design has to be revised by, say, increasing pile stiffness or reducing pile lateral load.
d) Carry out structural design for the pile based on the shear force and bending moment corresponding to the R equaling to the required slope FoS, typically 1.4 in most cases of slope stability problems in Hong Kong.

ACKNOWLEDGEMENTS

The authors would like to thank Mr. Ellis Lam, also of Hyder Consulting Limited for his assistance in the numerical analyses described in this paper.

REFERENCES

PLAXIS 2D (2015) – PLAXIS 2D Manual

Ng, C. W. W, Zhang, L.M. & Ho, K.K.S. (2001) – Influence of laterally loaded sleeved piles and pile groups on slope stability, *Canadian Geotech. J.*, 38, 553-566.

Lateral Load Tests on Four Large Diameter Piles in Hong Kong

J.M. Shen
Geotech Engineering Ltd, Hong Kong

ABSTRACT

This paper describes the test arrangements, the test results and the associated analysis for lateral load tests carried out on two pairs of large diameter (1.2m and 1.8m) bored piles during the construction of the Extension of Hung Hom Railway Terminus in the 1980s. The top soil stratum which dominated the pile behaviour during test is CDG fill in a typical reclaimation. One important feature of the tests is that besides deflection, rotation was also measured. This permits two parameters of soil stiffness to be back calculated instead of one, and the distribution of subgrade reaction with depth can thus be investigated. The method of analysis is described and observations on the test results are discussed. Conclusions are drawn and recommendations made.

1 INTRODUCTION

During the construction of the Extension of Hung Hom Railway Terminus in the 1980s under the management of the then Railway Development Office, lateral load tests were carried out on two pairs of large diameter bored piles (of 1.2m and 1.8m diameter respectively). The author was with the GEO then and was not directly involved in the project, but played an advisory role through a colleague, Mr W.K. Lai. He was then a Civil Engineering Graduate. He had been posted to the GEO for training under the author before being posted to the Railway Development Office working on the project under his supervisor Ir Y.C. Wong. This paper describes the site in general, the test arrangements, the test results obtained and the associated analysis by the author.

2 DESCRIPTION OF THE LATERAL LOAD TEST.

2.1 Geology of the site

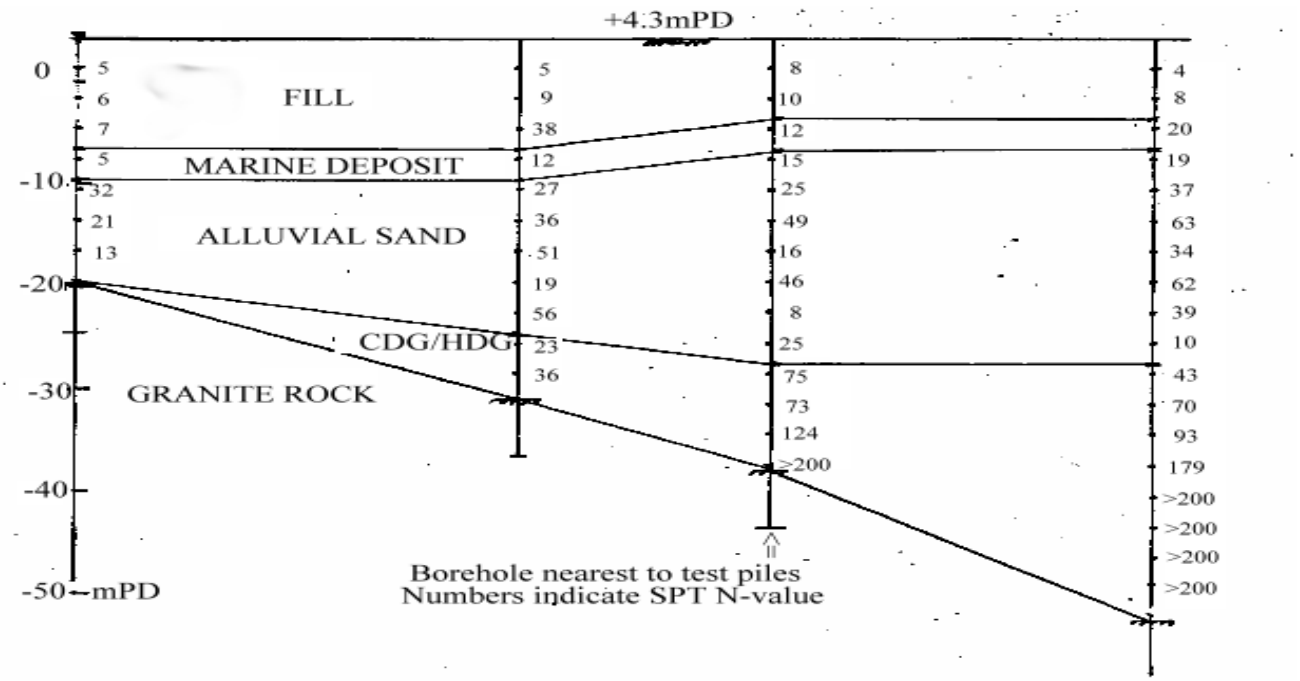

Figure 1: Geological Section of the Site

Typical reclaimation geology existed in the site, consisting of CDG fill overlaying marine clay, alluvium, in-situ CDG and finally bedrock, which was encountered at depths varying from 20m to over 40m. The thickness of various strata also varied greatly over the site. Figure 1 shows a typical geological section of the test site. The top 6 to 10m was CDG fill with SPT values in the range of 4 to10 (with one exception at 38, probably caused by boulder). As the soil near the ground surface has dominant effect over the stiffness of the pile soil system in this test, the results would reflect mainly the stiffness of the top fill layer.

2.2 Details of the piles

Piles in the project are either 1.2m or 1.8m diameter bored piles with 8mm steel casings left in place. For the purpose of calculating the EI of the pile in this analysis, it is assumed that the casing and the pile act as composite section without shear slip. The piles are spaced at about 8 diameters centre to centre, and the piles under test are about 40m long.

2.3 Test arrangement

Two piles were pulled towards each other using steel strand and hydraulic jack as shown schematically in Figure 2. The line of force was set at ground level. Vertical extension rods about 3 meters long were fixed at the top of the test piles. Horizontal deflection of the extension rods were measured with dial gauges against fixed datum at heights of 825 and 2825 mm above ground. As the extension rods are not under any load and remained straight, the deflection and rotation at the pile head at ground level can be calculated by linear extrapolation.

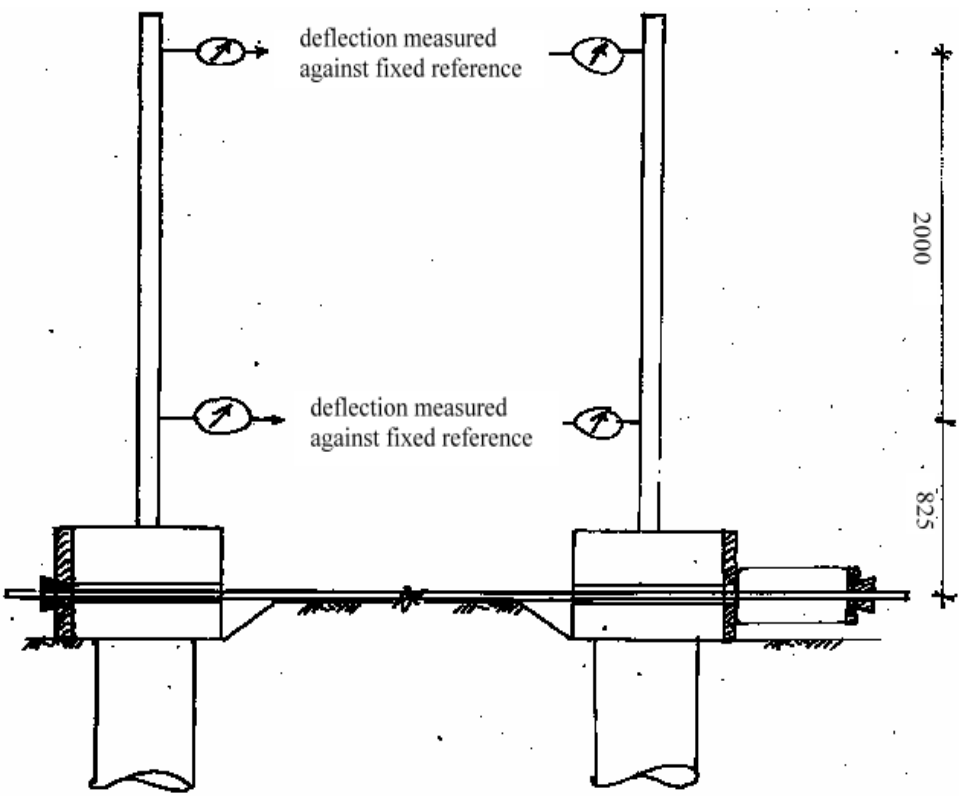

Figure 2: Test Arrangement

Loadings were applied at 100 kN increments until a load of 800 kN was reached for the 1.2m diameter piles, and at 200 kN increments until 1400 kN is reached for the 1.8 diameter piles. Loads were then

decreased at the same intervals to zero. Only one cycle of loading was carried out. Both the deflection and the rotation at the top of the 4 piles were measured for each load increment and decrement.

2.4 Test results

The deformations of the four piles at the end of each loading/unloading stage are presented in Figure 3 (deflection) and Figure 4 (rotation).

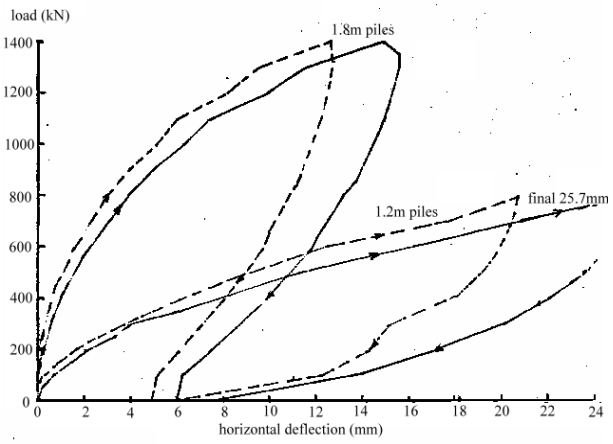

Figure 3: Load-deflection Relationship

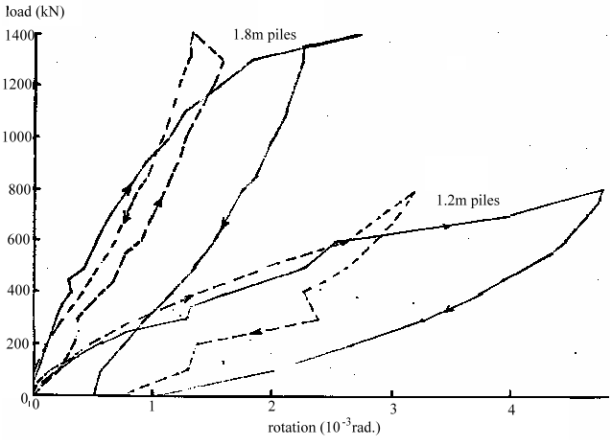

Figure 4: Load-rotation Relationship

3 ANALYSIS OF THE TEST RESULTS

3.1 Theoretical model

The secant modulus approach was adopted to handle the highly non-linear load-deflection/rotation relationship. Two popular model used for analysis of laterally loaded piles are the subgrade reaction approach and the elastic solution approach. The subgrade reaction approach is simpler to use, and does not involve L/D ratio of the pile. Complete solutions in table form were published, for example, in Sheriff (1974). Complete elastic solutions were also published for piles of selected L/D ratio, for example, in Poulos and Davies (1974). Test piles described in this paper has a L/D ratio close to 25, and this solution is used for analysis.

3.2 Basic approach

Normally only deflections are measured in lateral load tests on piles (sometimes as the only acceptance criterion) and hence only one stiffness parameter can be back calculated to fit the observed result. Assumptions are usually made on the distribution of horizontal subgrade reaction with depth so that it can be defined with one parameter, being constant with depth for hard clays or soft rock, and increasing linearly with depth with zero stiffness at the ground surface for sand and normally consolidated clays. Since two parameters (rotation and deflection) are observed this time, it is possible to back calculate two soil stiffness parameters. The first step is to suggest a soil stiffness model so that it can be defined with 2 parameters. There are many ways to do this, depending on the sophistication of the analytical tools and quality of soil data available. For example, one can assume the SPT N-value to reflect the spring stiffness through a scale factor (first parameter) and a depth influence factor (second parameter) to be back calculated. To do this, the analytical tool need to be able to assign spring stiffness along pile depth according to SPT values, and SPT data at the pile location have to be available.

In this analysis, it is assumed that the coefficient of horizontal subgrade reaction varies linearly from a value of K_0 at the pile top to K_1 at the pile bottom, where K_0 and K_1 are to be back-calculated for each load increment from the rotation and deflection observed. This is a simple extension of the conventional approach,

and can be carried out with published solutions. To facilitate repeated analysis, dimensionless charts are prepared. The test results are then superposed on the chart to read off the required parameters of stiffness. Elastic solutions for piles with a L/B ratio of 25 were also included in the chart for comparison.

3.3 Dimensionless parameters

The following dimensionless parameters are adopted for analysis:

i) Distribution Shape Factor $\alpha = K_0/K_1$ (subgrade reaction) or Es_0/Es_1 (elastic solution)

ii) System Rigidity $KC = 12EI/(K_1.B.L^4)$ for subgrade reaction solution and $KR = EI/(Es_1L^4)$ for elastic solution

iii) Rotation Factor $RF = \delta/(L.\theta)$

iv) Deflection Factor $DF = 12EI\,\delta/(L^3.P)$ where P is the applied force.

Charts were prepared with DF and RF as x and y axis respectively. Contours of constant α and constant KC/KR obtained from theoretical solutions are then plotted on the chart. This is the master chart for analysis of real test results. The test results shown in Figures 3 and 4 were then transformed into dimensionless form RF and DF and superposed on to the chart, as shown in Figures 5 and 6. Only the loading results are presented.

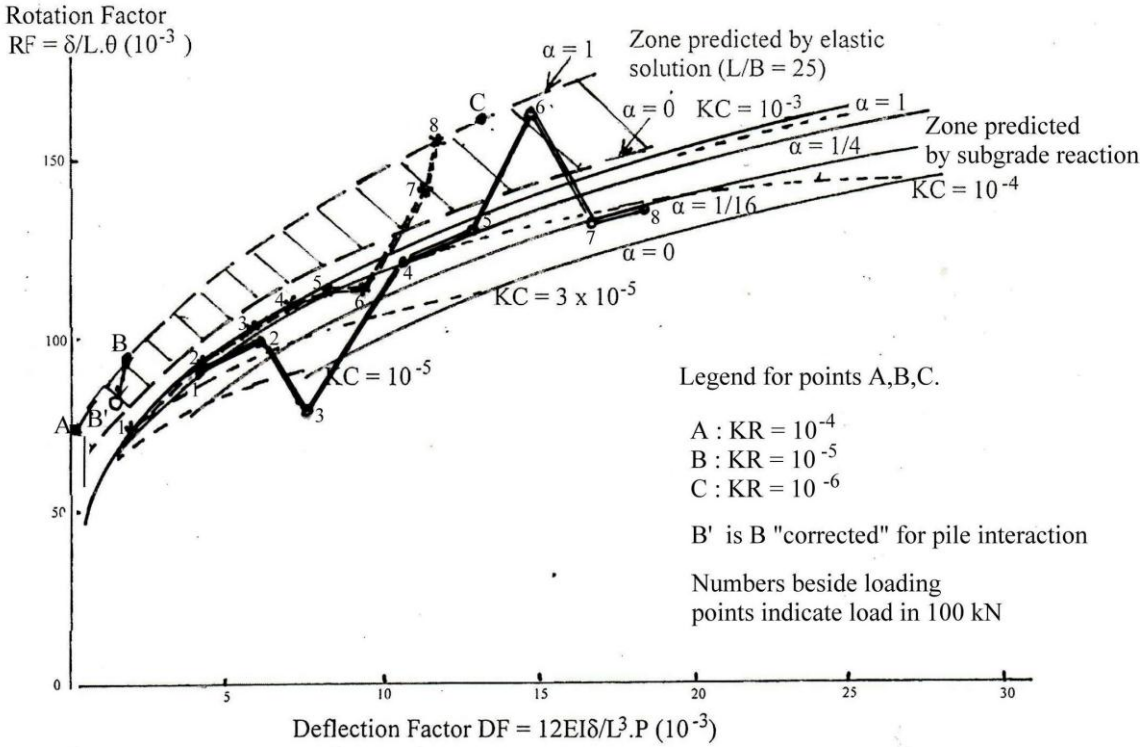

Figure 5: Chart with Results of 1.2m Piles Superposed

3.4 Results

As shown in Figure 5, the results of the 1.2m diameter piles followed closely the trend predicted by the subgrade reaction model, except for points at 300 kN and 600 kN for one of the piles. The results then entered the zone of elastic solutions at 700 and 800 kN. On the contrary, the results of the 1.8m diameter piles (Figure 6) did not follow the trend predicted by the model initially, the rotation being much smaller then predicted for a given deflection. However, as deflection (and therefore loading) increased, the test results entered (at 600 kN for one pile and 1200 kN for the other) into the zone predicted by the subgrade reaction model. They finally entered the zone predicted by the elastic solution model.

When the test results fall within the predicted zone, it is possible to back calculate the values of the two parameters α and KC/KR defining the distribution of subgrade reaction with depth. Three pairs of such results are presented in Table 1.

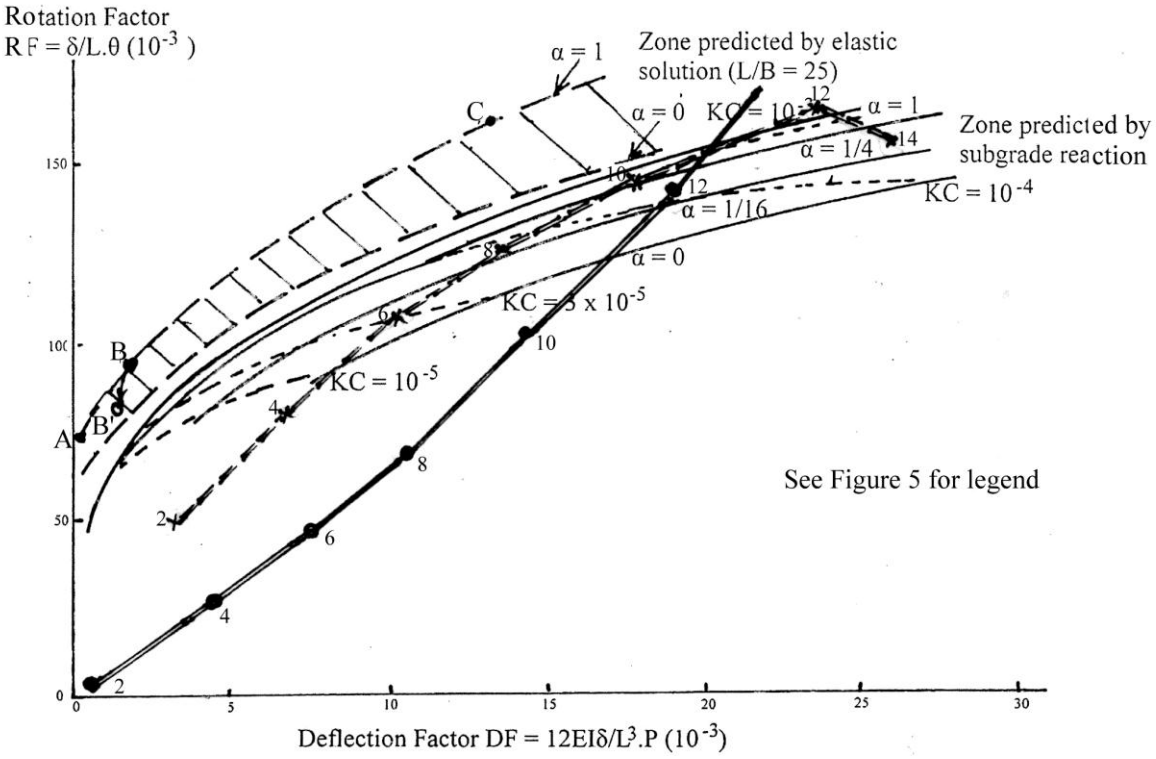

Figure 6: Chart with Results of 1.8m Piles Superposed

Table 1 Subgrade Reaction Back Calculated From Pile Test Results

	1.2m pile			1.8m pile		
Load P (kN)	200	400	800	600	800	1000
K_0 (MN/m^3)	31	25	8	46	43	22
K_1 (MN/m^3)	170	114	127	1150	434	87
m (MN/m^4)	3.5	2.2	3.0	27.5	9.8	1.6

3.5 Observations and discussions

Two observations, which are not related to the test results, are made on the theoretical model. The first observation is that the $\alpha = 0$ contour of elastic solution lies very close to the $\alpha = 1$ contour of the subgrade reaction model. If test results fall on this region (and they do), there may be heated arguments on whether α should be 0 or 1, depending on the model used. This at first sight may seem to be an inconsistency between the two models, but it is actually not. Shen (2015) shows that for the case of a smooth rigid wall embedded in a uniform elastic half space (and therefore $\alpha = 1$), the corresponding subgrade reaction distribution is close to $\alpha = 0$. This is a similar situation.

The second observation relates to how pile interaction would affect the single pile solution. The pile interaction factors (this time with opposing load) given in Poulos and Davies (1974, Figures 14.22 and 14.26) were used to modify the single pile solution for KR = 10^{-5}. As a result, the point B in Figures 5 and 6 are shifted to B'. Apparently this would not significantly affect the analysis

As for the test results, those of the 1.2m diameter piles fit in generally with the models, but not those of the 1.8m piles. In the initial (stiff) stage of the loading, the relative value of rotation and deflection is not compatible with the prediction of models assumed, and values of K_0 and K_1 cannot be back calculated. This

observation applies to both piles, although more pronounced in one of them. The author cannot offer any explanation, but is interested to know whether others have similar experience. When the loading exceeds about 50% of the final load, the results start to fall into the zone predicted by the subgrade reaction model, and values of K_0 and K_1 can then be obtained and found to be much higher than conventionally associated with DG fill.

As can be seen from Table 1, there is a drastic decrease in soil stiffness at depth (K_1) for the 1.8m pile and the author tried to seek an explanation. The elastic curves of the pile at 600 kN and 1000 kN are plotted out according to the subgrade reaction model. It is found that, although having a diameter of 1.8m, it actually behaves as a flexible structure when it is 40m long. At 600 kN, the soil is very stiff and the elastic curve consists of over 5 half waves. At 1000 kN, the soil is less stiff and the elastic curve consists of less than 4 half waves. As a consequence, the soil at the bottom 40% of the pile has undergone stress reversal, even though the loading was monotonic increasing. Since the soil on unloading would not provide the same support as loading as assumed by the subgrade reaction model, there would be a drastic drop in soil support at depth, as observed in Table 1. This explanation is, of course, based on the subgrade reaction model. When most of the results do not fit in with the model, one may consider any explanation based on the model superfluous.

Other factor that may cause results to deviate from the model include soil variability near the ground surface, such as a rigid inclusion in the form of a boulder in the fill near the pile.

4 CONCLUSIONS AND RECOMMENDATIONS

Lateral load tests and the associated analysis carried out on two pairs of large diameter bored piles have been described in this paper. The measurement of both deflection and rotation enables 2 parameters on soil stiffness to be back calculated instead of one, and permitted a more in depth analysis of the results. It may also expose the deficiency of existing models, such as those shown in this paper. If only deflections were measured, one would be happy to back calculate one soil stiffness parameter without knowing the deficiency of the model. As the measurement of rotation is relatively simple and would enable more in-depth analysis, it is recommended that it be done routinely for lateral load test on piles through the test specification, even if it is not part of the acceptance criteria.

Information on the pile top only does not provide sufficient data to thoroughly analyse the situation and the case in this paper is an example. For research projects, instrumentation should be provided to monitor the pile behaviour at depth.

The method of analysis and the dimensionless charts presented in this paper can be used to analyze other lateral load tests where rotation as well as deflection is measured.

Even 1.8 diameter piles would behave as flexible structures in CDG fill, if it is 40m long, and stress and contact pressure reversal may occur at depth, even though the load is monotonic increasing.

Many test results, such as those shown in this paper, are hidden in project files and never made known to the public. The author appeals to project engineers to publish them.

ACKNOWLEDGEMENTS

The author is grateful to the project team of the Railway Development Office for making the test results available, without which this paper could not have been written. Opinions expressed in this paper are those of the author only.

REFERENCES

Poulos, H.G. & Davis, E.H. 1974. *Elastic solutions for soil and rock mechanics.* John Wiley & Sons.

Shen, J.M. 2015. Subgrade reaction vs elastic solutions – theoretical considerations. *Proceedings of the 35th HKIE Geotechnical Division Geotechnical Division Annual Seminar,* May, Hong Kong, pp.

Sherif, A. 1974. *Elatically fixed structures.* Earnest & Sohn, Berlin.

Subgrade Reaction vs Elastic Solutions Theoretical Considerations

J.M. Shen
Geotech Engineering Ltd, Hong Kong

ABSTRACT

In this paper comparisons are made between the subgrade reaction approach and the elastic solution approach in solving soil structure interaction problems. Based on theoretical solutions obtained from theory of elasticity, inferences are made on the magnitude and distribution of subgrade reaction which would render the two approaches compatible. Both vertical subgrade reaction and horizontal subgrade reaction problems are studied and cases with particular interest (such as Gibson soil) are highlighted. It is concluded that if educated assumptions on the magnitude and distribution of the subgrade reaction is made according to the size, shape and rigidity of the structure, as well as the nature of the soil, realistic solutions similar to those in elastic solutions could be obtained with the simple subgrade reaction approach.

1 INTRODUCTION

Subgrade Reaction and Elastic Solution are two popular tools for handling soil structure interaction problems. Those in favour of one approach often criticize the other. This paper tries to point out, from a practical point of view based on theoretical solutions, the similarities rather than the differences between the two approaches, hoping to bridge the gap between the two sides. The reader is assumed to be familiar with the fundamental assumptions of the two approaches, which are mentioned only very briefly below. Also the term "subgrade reaction" is used interchangeably with the term "coefficient of subgrade reaction" to facilitate reading.

In the subgrade reaction approach, the soil reactions are modeled as independent springs. This makes the formulation of the problem as well as its solution relatively simple. Soil variability can be handled readily as different spring stiffness can be assigned to different soils without affecting one another. However, the stiffness of these springs are not true soil properties, and depend on the size and rigidity of the structure. On the other hand, soils are modeled as coupled continuum in elastic solutions in theory of elasticity, in which the Young's modulus E_s and Poisson's ratio μ are true soil properties independent of the structure. This is obviously a great advantage over the subgrade reaction approach. The costs of these advantages are more complicated problem formulation and solution, and less versatility in handling soil variability.

Terzaghi (1955) provided classical guidelines on the evaluation of coefficient of subgrade reaction, usually in terms of semi-empirical formulae based on his vast experience and in-depth analysis. He pointed out, using the zone of influence of the stress bulk, the effect of foundation size on clay is different from that in sand, due to the increase soil stiffness with depth for sand, and gave empirical formula for the effect in sand. Many elastic solutions have emerged since that time, providing further theoretical bases for the evaluation of the "correct" sub-grade reaction. Some are discussed in this paper.

2 VERTICAL SUBGRADE REACTION

2.1 Particular cases of similarity

There are at least two particular cases where the two approaches are compatible. The first case is the elastic solution for a surface load on a semi-infinite mass of Gibson soil (one with modulus increasing linearly with depth) with Poisson ratio $\mu = 0.5$ and zero Young's modulus E_s at the surface. In this case the two approaches are entirely compatible for any size and shape of vertical surface load, with the value of the vertical subgrade reaction k_v given by:

$$k_v = 2m/3 \quad (1)$$

where m is the rate of increase in Young's modulus E_s with depth.

The second case involves a point load on an infinitely long structural strip with bending stiffness E_pI_p resting on a finite layer of uniform soil with Young's modulus E_s (situation often used to simulate a railway track under the wheel load of the train). Vesic (1961) showed that the two approaches are practically equivalent (some numerical approximations involved) provided that the value of subgrade reaction is calculated with the following formula:

$$k_v.B = 0.65\ E_s.\sqrt[12]{(E_s.B^4/E_pI_p)/(1-\mu^2)} \quad (2)$$

where B is the breadth of the structural strip.

This time k_v is affected by the size and rigidity of the structural strip.

2.2 General Cases

Information in general can be obtained by considering the two limiting cases of loading stiffness on a soil : flexible loading (constant pressure independent of deformation) and rigid loading (imposed deformation irrespective of soil reaction). Actual loading would lie between these two limits. If a uniform k_v is assumed for the design of a flexible loading such as a large water tank, it will result in uniform settlement without any bending on the floor slab, while in reality the centre of the tank will settle more, leading to bending. This is the usual criticism on the subgrade reaction approach. The settlement profile predicted by elastic solutions for a flexible load will give indication on the "correct" distribution of subgrade reaction that would make the two approaches compatible. On the other limit, the contact pressure distribution of a rigid loading would reflect the value of subgrade reaction that need to be used to make the two approaches compatible, based on the definition of subgrade reaction.

The case of a circular raft resting on a semi-infinite mass under a uniform load will be used for illustration. The system rigidity in this case is defined by a dimensionless parameter K given by

$$K = (Ep/Es)(t/a)^3(1-\mu^2) \quad (3)$$

Where t and a are thickness and radius of the raft respectively.

Figures 1 to 3 below are reproduced respectively from Figures 12.22, 12.26 and 12.23 of Poulos & Davis (1974). Figure 1 gives the settlement at the centre; Figure 2 gives the maximum differential settlement (between centre and edge) and Figure 3 gives the contact pressure for a range of values of K. From these figures the following observations can be made:

i) Practically $K = 10^{-2}$ can be considered as flexible load and $K = 10^2$ rigid load (figure 1).
ii) The centre of a flexible raft settles 27% more than that of a rigid raft under the same load (figure 1).
iii) For flexible load, the settlement at the edge is 0.32 of that at the centre (figure 2), implying the subgrade reaction at the edge should be about 3 times that at the centre in order to produce such result.
iv) There is good consistency of contact pressure at 0.8 radius despite the large range of K. This contact pressure is 83% of the applied pressure (figure 3).
v) Poisson's ratio has little effect on differential settlement (figure 2).

From the elastic solution for a rigid loading, the contact pressure is given by

$$\sigma_z = p_{av}/\{2.\sqrt{(1 - r^2/a^2)}\} \quad (4)$$

where σ_z is the contact stress, p_{av} the average applied pressure, a the radius and r the distance from the centre.

The contact stress at the centre is 50% of the average contact stress and the contact stress at the edge is theoretically at infinity. The contact stress is 3 times that at the centre at a distance of 94.3% of the radius

from the centre (or 5.7% from the edge). It seems surprising that an edge/centre ratio of 3 for spring stiffness would seem appropriate for both a flexible and a rigid loading.

For intermediate values of K shown in Figure 3, both the settlement and the contact pressure have to be evaluated in order to arrive at an edge/centre spring stiffness ratio. Using the results of Figures 2 and 3, calculation revealed a ratio of 2.7 (at 5% radius from edge) for K = 1. This is close to 3 found for the two extremes. Absolute value of spring stiffness at the centre can be evaluated to complete the picture of subgrade reaction distribution.

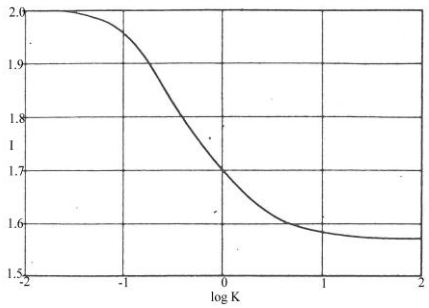

Figure 1: Central Vertical Displacement

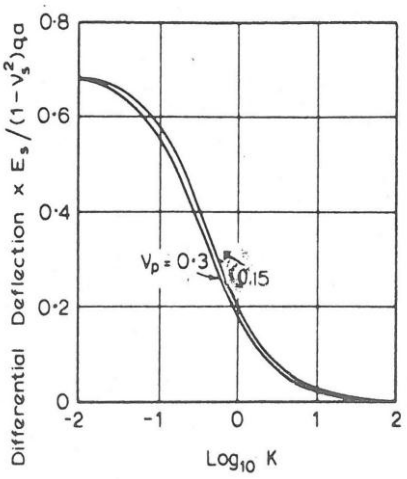

Figure 2: Differential Settlement

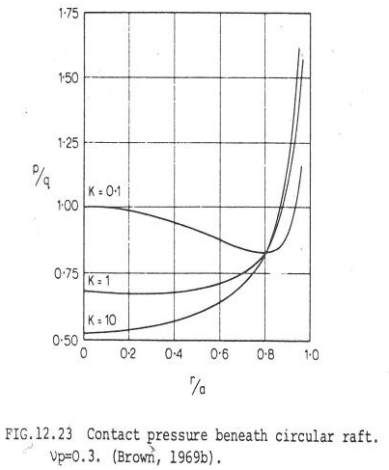

Figure 3: Contact Pressure

2.3 Observations

The above paragraphs indicate that provided the value of subgrade reaction is chosen properly, the two approaches can be highly compatible. For the circular raft, the edge/centre spring stiffness ratio is surprisingly consistent for a wide range of K. The case of Gibson soil shown in paragraph 2.2, although academic and unrealistic in real life, is particularly interesting in that it demonstrates complete compatibility between these two concepts is possible.

3 HORIZONTAL SUBGRADE REACTION

3.1 Distribution with depth

In the case of vertical subgrade reaction, one is not directly involved in distribution of stiffness with depth as only surface loading is involved, although it has effect indirectly on the soil stiffness or subgrade reaction as shown in paragraph 2.1 above, or pointed out in Terzaghi (1955). However, when horizontal subgrade is considered, one need to know the distribution of subgrade reaction with depth, as it has profound influence on the results. For piles, where the critical dimension is the breadth B, it is conventionally assumed that the stiffness is constant with depth in stiff clays and increasing linearly with depth for sands. For walls where the critical dimension is the height L, it is conventionally assumed as suggested in Terzaghi (1955) that the distribution of subgrade reaction is increasing linearly with depth, somewhat like earth pressure. One can apply the rigid loading approach described in paragraph 2.2 to see what would be the "correct" distribution with depth according to elastic solutions in these cases.

3.2 Rigid loading approach

Various elastic solutions have been collected and published in Poulos & Davis (1974). Solutions for practically rigid piles, plates and wall (mainly defined by the L/B ratio) are selected. By superposing the right combination of force and moment at the top of the rigid structure, the structure can be made to cast a uniform

displacement into the soil, and the resultant pressure distribution would represent the subgrade reaction, by definition. Such solutions were worked out for a pile (L/B = 25), a plate (L/B = 2/3) and a wall (L/B = 0) embedded in a semi-infinite mass. These are shown in Figures 4, 5 and 6 respectively.

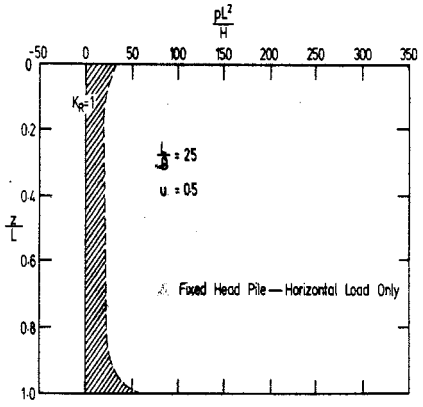

Figure 4: Pile (L/B = 25)

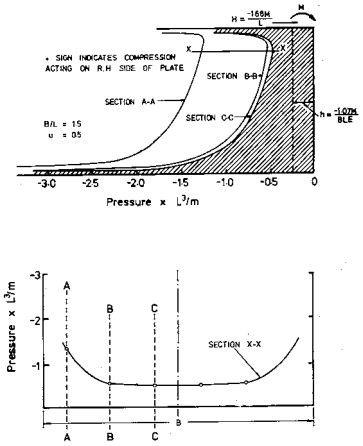

Figure 5: Plate (L/B = 2/3)

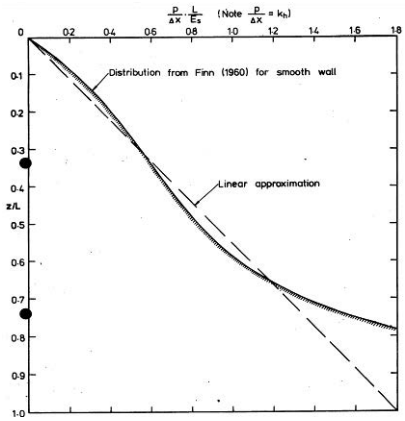

Figure 6: Wall (L/B = 0)

3.3 Observations

From the above analysis and Figures 4 to 6, it is seen that for a uniform soil, the distribution of subgrade reaction with depth is approximately constant with depth for a pile (with slight deviation at the two ends) and increasing linearly with depth like earth pressure for a wall ($K_h.L = 1.8\ E_s$ is a good approximation over top 70% of the wall height). A rigid plate is somewhere in between, with a finite value at the top and increasing linearly with depth. Thus although the soil is uniform, the subgrade reaction is not necessarily uniform, but depend on the shape of the rigid structure. If the soil has inherent trend of stiffness increasing with depth (most soils do), the subgrade reaction may be expected to further increase with depth accordingly.

4 CONCLUSIONS

Subgrade Reaction and Elastic Solution are two popular tools for handling soil structure interaction problems. Some comparisons between the two approaches are made in this paper. Elastic solutions are used to work out the "correct" distribution and magnitude of the subgrade reaction to render the two approaches compatible. By making an educated assumption on the distribution of subgrade reaction, one can then make use of the simplicity of the subgrade reaction approach to solve the problem, without deviating too far from the more sophisticated elastic solution approach.

REFERENCES

Poulos, H.G. & Davis, E.H. 1974. *Elastic solutions for soil and rock mechanics.* John Wiley & Sons, New York.

Terzaghi, K. 1955. Evaluation of coefficient of subgrade reaction. *Geotechnique,* 5(4): 297-326.

Vesic, A.S. 1961. Bending of beams resting on isotropic elastic solid. *Journal of Engineering Mechanics Division, ASCE,* 87(2): 35-53.

Piled Raft Foundation Design for a Supertall Tower

J.W.C. Sze and A.K.M. Lam
Ove Arup and Partners Hong Kong Limited

ABSTRACT

High-rise or super high-rise buildings usually accompanied by a deep basement to accommodate car park spaces and plant rooms. With favorable ground condition, the basement may already be rested onto rock and a raft foundation can simply be adopted. In contrast, some project sites may be located in alluvial plain area where excessive weak deposits are encountered. In such case, pile foundation is demanded and common pile design process is followed which may not require significant geotechnical input.

A special case could be that the underlying soil or rock is marginally competent to support the tower load or to assure that the movement performance of the tower can be met. In such situation, a piled raft foundation might be the best option to pursue in order to achieve cost effectiveness. However, the design of a piled raft foundation is somewhat different from the traditional way of designing building foundation as it involves soil-structural interactions amongst the raft, piles, soil and/or rock.

This Paper uses a supertall tower in South Korea resting on soft rock with complex geological setting as a case history to illustrate the geotechnical design process of a piled raft foundation. The specialties are attributed by the way in establishing the possible geological models, three dimensional soil-structural interaction analyses and non-linear stiffness were adopted in the analyses to better represent the non-linearity of the ground response under the tower loads. The findings of the three dimensional soil-structural interaction analyses using Arup in-house program GSRaft computer models and a cross-checking exercise using PLAXIS 3-D model will be discussed. Another critical element during the design process is the active input from the designer during the construction phase apart from the routine supervision by the construction supervisor. Instrumentation for monitoring the performance of the foundation and hence the tower will also be highlighted.

1 INTRODUCTION

The combination of raft and pile foundations as a unified supporting system to support super high-rises involves soil-structure interactions amongst the raft, piles and the underlying soil. The estimation of the load sharing among the raft and the piles and the degree of mobilization of the pile capacity are the key challenges for a piled raft design. Normally, a safety factor of 2 and 3 are applied to the design of the pile and the raft foundations respectively. When the raft alone does not possess adequate safety factor, the piles are introduced to reduce the bearing pressure of the raft. However, as the piles are much stiffer than the soil, if the conventional safety factor is adopted, most of the load will be taken by the piles and the contribution from the raft under the piled raft system is substantially decreased to less than 15 to 25% of the total load based on the past experience. Although the raft has a lot more spare capacity in this situation, the use of a lower safety factor for the pile in the piled raft system is not widely accepted.

An alternative is to design the piles as settlement reducers to control the settlement and/or differential settlements of the raft. This Paper uses a supertall tower in South Korea resting on soft rock with complex geological setting as a case history to illustrate the geotechnical design process of a piled raft foundation using the concept of piles as settlement reducers.

2 DESIGN PHILOSOPHIES

The design philosophies with respect to piled raft foundation have been clearly defined by Randolph (1994) and summarized by Poulos (2001a) as follows: -

(a) the "conventional approach", in which the piles are designed as a group to carry the major part of the load, while making some allowance for the contribution of the raft, primarily to ultimate load capacity;
(b) "creep piling", in which the piles are designed to operate at a working load at which significant creep starts to occur, typically 70 to 80% of the ultimate load capacity; sufficient piles are included to reduce the net contact pressure between the raft and the soil to below the pre-consolidation pressure of the soil.
(c) differential settlement control, in which the piles are located strategically in order to reduce the differential settlements, rather than to reduce the overall average settlement substantially.

Design philosophy (a) is predominately governed by the pile group behavior. Design philosophy (b) is considered to be effective to control the raft settlement with piles designed with a lower safety factor. Design philosophy (c) is believed to be the most cost effective piled raft system as the piles are designed to fully utilize their ultimate capacity. It is however difficult to precisely predict the load sharing between the piles and the raft in view of the complex soil-structural interaction of a pile group, the non-linear stiffness behavior of the soil and the actual pile deformation behavior in practice.

As far as the overall stability of a piled raft system is concerned, the most effective application of such system is that the raft alone can provide adequate load bearing capacity and the piles are only designed to control the settlement and/or differential settlements of the raft. In this regard, the piles can be treated as settlement reducers or part of the ground stiffening element and a lower safety factor can be adopted. This design concept is acceptable to most design engineers as the overall stability is also increased in associated with the introduction of the piles. Nevertheless, the structural design of the piles shall comply with the respective design code in order to prevent any structural damage. Taking the design philosophy (b) as discussed above but with the raft alone being capable to provide adequate safety factor against bearing failure, piles are designed with factor of safety of about 1.3 to 1.4 against the geotechnical capacity. With this design concept, Davies et al (2009) applied the piled raft system to control the settlement and the differential settlement for a high-rise development and discussed its financial benefits.

3 DESIGN PROCESS AND METHOD

The design process of piles as settlement reducers or ground stiffening element and the geotechnical design of the raft foundation is shown in Figure 1. For the case of raft foundation bearing on rock (i.e. soft rock) with complex geological setting, phased rock face mapping is essential to establish a credible geological model. Sometimes, several geological models are developed for design in respond to the variability of the ground.

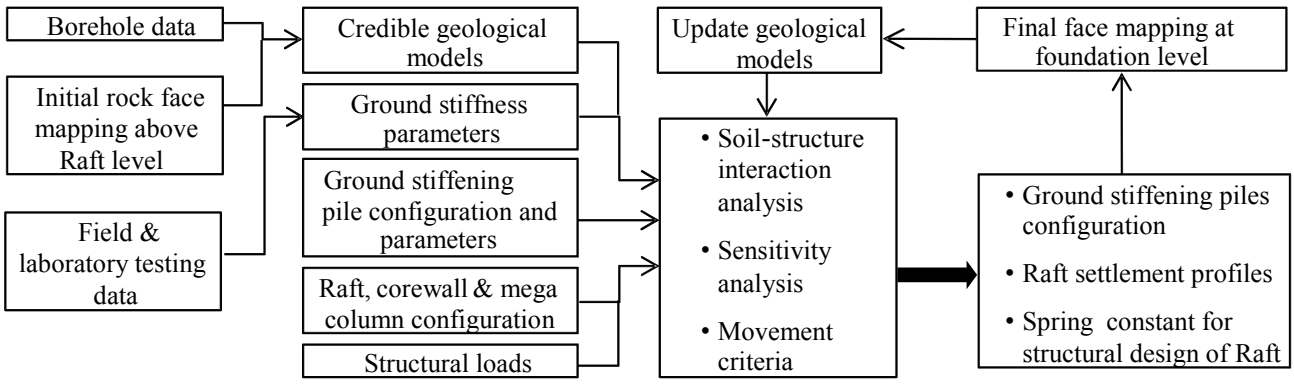

Figure 1: Geotechnical Design Process of the Raft Foundation with Ground Stiffening Piles

Apart from the geological model, the stiffness of the ground is another critical factor that influences the analysis results. Soil and soft rock are well known as non-linear materials but in routine foundation designs they are usually treated as elastic material to facilitate an easier computational analysis. However, the ground with complex geological setting renders difficult estimation of a reasonable average stiffness of the ground. In

addition, the use of non-linear soil and/or rock stiffness do not require a well-defined rigid boundary beyond which the settlement becomes minimal. The degradation curve of the non-linear modulus for sandy soils can be referred to Seed & Idriss (1970) and Pappin et al (1989). The initial modulus at very small strain (i.e. about 0.0001%) can be correlated with the in-situ shear wave velocities measurement whilst the modulus at higher strain values (i.e. about 0.01% to greater than 1%) can be correlated with the deformation modulus obtained from the small strain triaxial tests or Pressuremeter tests for soil and Goodman Jack tests for rock. The radial strain measured from these tests were converted into axial strain based on the relationship of $\varepsilon_{axial} = 2\ \varepsilon_{radial} / \sqrt{3}$ as proposed by Jardine (1992).

The essential part of a piled raft design is soil-structure interaction. Katzenbach et al (1999) described the interactions amongst different elements of a piled raft design, which is much more complex than the traditional raft foundation design. These included raft-pile interaction, raft-soil interaction, pile-soil interaction and pile-pile interaction. Poulos (2001b) described different methods of analysis for piled raft foundations. Amongst these methods, numerical analysis using the plate-on-springs approach and 3D finite element analysis are potentially the most accurate method available. It is however very time consuming to carry out a 3D finite element analysis. Arup has developed an in-house program namely GSRaft, which is part of the General Structural Analysis (GSA) program, using similar concept of plate-on-springs approach with consideration of the soil-structure interaction by conducting iterative process to achieve the compatibility of settlement between the structural elements and the underlying soil elements. The program takes into account the structural stiffness of the raft, piles as well as the stiffness of the underlying soils. The interaction between the raft and the soil is simulated by a group of springs at the base of the raft while the interaction between the pile and the soil is simulated by a group of soil interaction springs as illustrated in Figure 2 and the level of these springs can be defined as the base of an equivalent raft level of the piles, which is usually taken as two-third of the pile depth for pile friction developed linearly with depth or half of the pile depth for constant pile friction. Since the pile in GSRaft is modeled as elastic beam element, when the pile approaches its ultimate capacity, the pile spring stiffness may be overestimated. Therefore, GSRaft is primarily applicable for design philosophies (a) & (b). Furthermore, the assigned equivalent raft level of the piles will affect the results and in layered soil strata and soil with varying stiffness, it is not easy to determine the appropriate level.

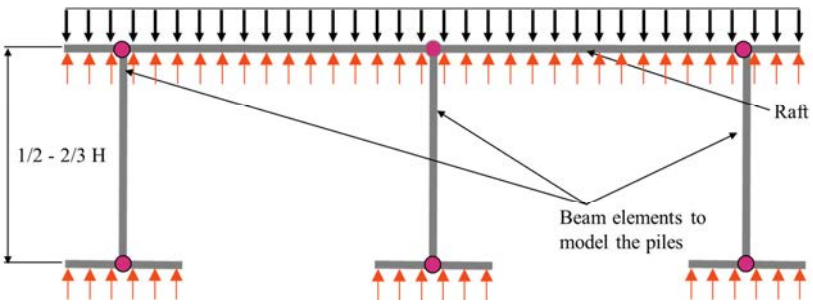

Figure 2: GSRaft Conceptual Model

4 CASE HISTORY

4.1 The project

The site is located at Jamsil-dong of Seoul, South Korea with a footprint of 87,000m^2 and to be developed into an integrated commercial, residential and entertainment complex. As a landmark of development as well as Seoul, a 123-storey, 555m high supertall tower with a 6-level basement is situated at the western end of the site. The initial ground investigation boreholes at the Tower were sunk in early 2006 to provide the basic geotechnical information for the design of the Tower foundation. The Tower was subsequently replanned and Arup was appointed as the geotechnical engineer of the international design team to provide the geotechnical designs for the newly planned tower in view of the suspected complex ground condition as revealed from the initial boreholes.

4.2 Structural form

The Tower has a footprint of approximately 72m x 72m. The structural form comprises concrete core wall with 8 peripheral mega columns to resist both the gravity and lateral forces. To enhance the structural rigidity, two belt trusses are positioned at 218m and 347m from the base of the raft. The total serviceability gravity load is around 6,700MN.

4.3 Ground investigations & geological conditions

There were three phases of borehole investigation carried out at the Tower location. The first phase was carried out in early 2006 and consisted of 16 boreholes accompanied by in-situ Pressuremeter/Goodman Jack tests and laboratory strength tests. Most of these boreholes were terminated at around 20m below the foundation level, which were relatively short comparing to the Tower footprint. Additional ground investigation consisted of 7 numbers of deep boreholes were sunk in mid 2009 with depth as deep as 80m and signs of faults running underneath the Tower were identified. With the mega-column locations and the corewall dimensions became more certain, the third phase boreholes, which consisted of 10 numbers of boreholes, was carried out in late 2009 accompanied by additional in-situ Pressuremeter tests and Goodman Jack tests to further supplement the existing borehole information. Figure 3 illustrates the variability of the rock quality and strength at distances underneath the foundation level.

The ground investigation works revealed that the bedrock at the Tower consisted of Gyeonggi Gneiss complex overlaid by Quaternary colluvium and alluvium deposits. The Gneiss had banded structures and medium grain to coarse grained texture. Hydrothermal intrusions were observed along fractures resulted from faulting. Due to the variability of the rock strength over the depths underneath the Tower, for engineering purpose, the rockmass could be classified into several categories using Geological Strength Index (GSI) classification suggested by Hoek et al (1995) and the corresponding rockmass modulus could be estimated as shown in Table 1. The rock condition at the excavation face of around 10m above the foundation level was also inspected and mapped by the Korea Society of Engineering Geology (KSEG) in late 2009 and reviewed by Arup, in order to better infer the extent of the individual rockmass over the footprint of the Tower. The final rock face mapping at final formation level is illustrated in Figure 4.

Figure 3: A Sample Rock Core

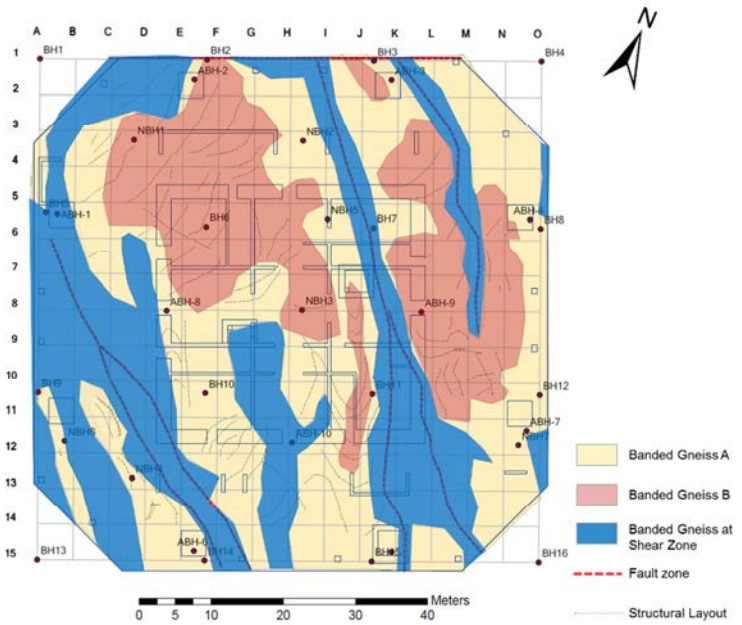

Figure 4: Final Rock Face Mapping Results

Table 1: GSI Classification of the Rockmass

Rockmass Category	GSI/Em (GPa)		
	upper bound	lower bound	average
Banded Gneiss A	50/8.7	35/3.7	42/5.5
Banded Gneiss B	36/3.2	21/1.3	30/2.2
Banded Gneiss at Shear Zone	31/2.1	13/0.8	23/1.3
Fault zone	18/0.5	5/0.3	13/0.4

4.4 Proposed foundation system

In view of the loading condition of the Tower and the bearing capacity of the ground even assuming lower conservative parameters, a single raft foundation was considered to be a technically feasible after an initial assessment. Compared to individual footings, a single 6.5m thick raft foundation over the Tower footprint was more robust in tolerating local weak spots due to its high stiffness. However, the presence of faults, shear zones and highly foliated soft to hard rock would have a significant influence on the total and differential settlements of the raft, which were carefully considered in order not to impair the Tower performance. The uncertainties associated with the estimation of raft foundation settlement included: -

1. The rock conditions were highly variable. The stress and strain levels were concentrated locally at the good rock areas under the core and mega columns. According to the Pressuremeter test results, the difference of elastic modulus between good and poor rocks could be varied by a factor greater than 20. The risk of unacceptable differential settlement would be high especially under lateral forces.
2. The geology condition beneath the formation level was highly complex. It would be difficult to develop a full or complete geological model to represent the ground. The uncertainty of the geological model would impose a high risk in predicting the actual response of the ground under the applied pressure.
3. Computation analysis, irrespective to the degree of sophistication, involved simplifications and the inferred geological models could not be fully reflected in the analysis.

To mitigate such ground risk and enhance the performance of the raft foundation, ground stiffening piles were placed at strategic locations to balance the foundation cost, ground variation and the building performance. Using different credible geological models and after several rounds of studies, a total of 108 nos. 1m diameter Percussion Rotary Drilling (PRD) piles were designed to be positioned underneath the perimeter corewall and inner zones to maximize the benefit. PRD pile was selected due to its readily easy maneuvering and quick installation upon bulk excavation had reached 1 to 2m above the foundation level. The piles did not require a temporary steel casing to be used and the down-the-hole hammer drilling could be applied directly to

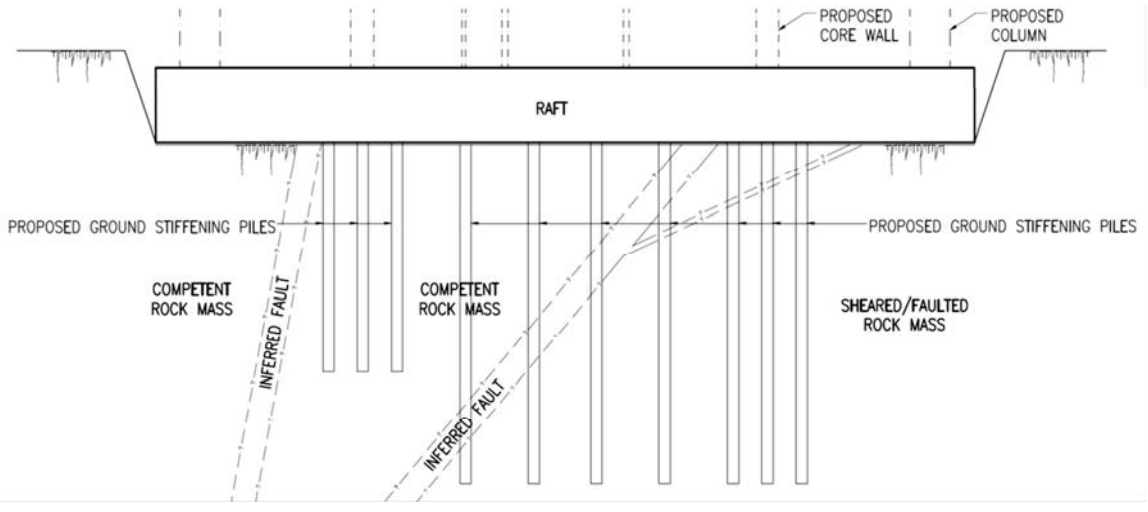

Figure 5: Typical Section

enable a fast construction. These piles had a net length of 20m and 30m located at the highly stressed influence zone and distributed based on the inferred geological setting. Figure 5 shows a typical section showing the extent and depth of the proposed ground stiffening piles across the Tower footprint.

4.5 Design parameters & models

Non-linear stiffness of the banded Gneiss and brecciated Gneiss (shear zone) were applied in order to better reflect the strain dependent behavior of these rockmasses, as shown in Figure 6. The initial moduli at very small strain was correlated with the in-situ shear wave velocities measurement whilst the moduli at higher strain values were correlated with the deformation moduli obtained from the Pressuremeter and Goodman Jack tests. In view of the ground variation risk, a lower bound design line was adopted for design and prediction of the Tower performance. For fault zones, since the long term creeping of the highly weathered soil dominated the non-linear behavior rock, linear deformation modulus was adopted in the design.

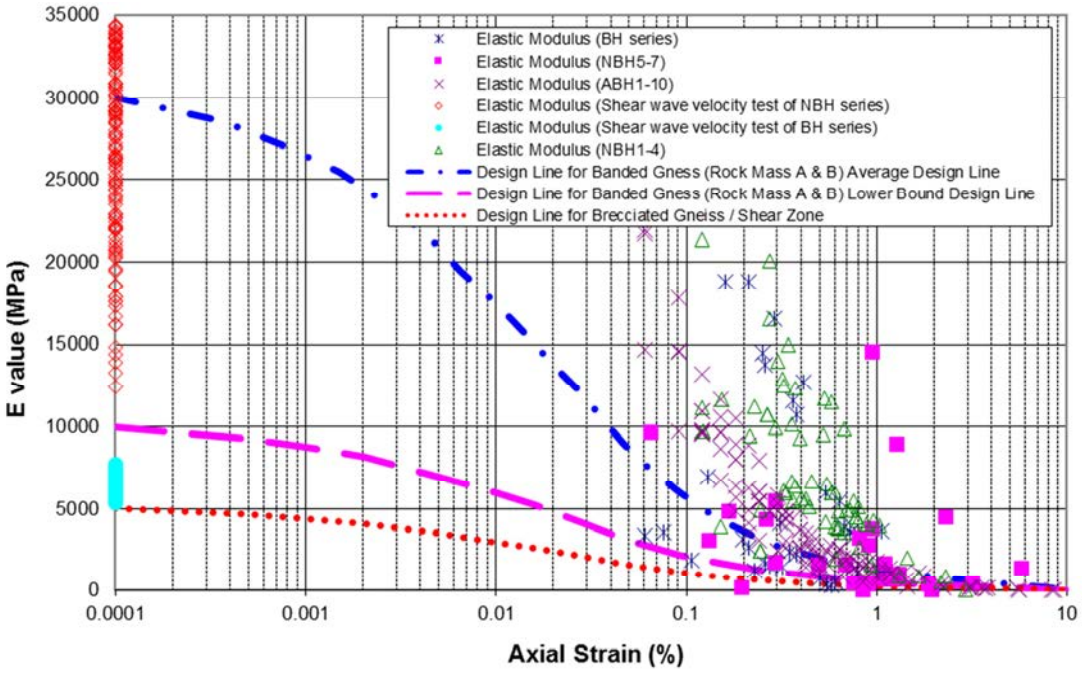

Figure 6: Non-linear Modulus Design Curves

With different phases of borehole information and the rock face mapping at 10m above the foundation level during the bulk excavation, two possible geological models were established to be the most credible for the design purpose. One of the simplified geological models is shown in Figure 7.

In the GSRaft analysis, the raft was modeled as grillage and the cross points formed the common nodes to iterate with the soil model. Piles could also be attached to these nodes. The piles were modeled as bar elements with axial stiffness only and the top of the piles were pin-jointed to the raft. Soil-pile interaction springs were placed at the end of the equivalent length of the piles. The loads were simulated as patches of pressure loading over the mega columns and core walls footprint. A number of GSRaft models were set up to carry out sensitivity check based on a range of design parameters and different load cases. A GSRaft model is shown in Figure 8, which was coupled with the soil model as shown in Figure 7 during the analysis.

The result of analysis along one section at a particular load case of the proposed raft is shown in Figure 11. The maximum and differential settlements can be derived accordingly from the displacement at individual node. The corresponding spring constant could also be derived by dividing the reaction by the displacement at each node for individual load case and a spring contour map could be produced for the use of the Project Structural Engineer for the detailed structural analysis and design of the raft foundation.

In addition, from the GSRaft models, the envelope of reaction forces at individual ground stiffening piles could be obtained. As discussed above, the raft foundation alone could sustain the total tower load. The inclusion of the ground stiffening piles was to reduce the raft settlement and to bridge over fault zones or localized weak zones. In this regard, these piles were allowed to settle plastically relative to the surrounding soil (i.e. creeping) such that the exceptionally high load could not be developed in piles. In order to allow the pile settled plastically relative to the surrounding soil/rock following the design philosophy (b) as mentioned in Section 2, a factor of safety of 1.3 was adopted for the derivation of allowable geotechnical capacity of the ground stiffening pile. A trial pile with load testing was carried out prior to the commencement of the working pile construction and a bond capacity between the concrete and the brecciated Gneiss was proven to be 400kPa. Since the piles were generally socketed into banded Gneiss and/or brecciated Gneiss, with such a high bond capacity, the pile capacity was not governed by the geotechnical capacity. Instead, the structural design governed the pile capacity. The structural design of the pile complied with the Korean Building Code (KBC) - Structural 2009. The ground stiffening piles had a concrete cylinder strength of 60MPa, which had the same concrete strength as the raft after considering a tremie factor of 0.85.

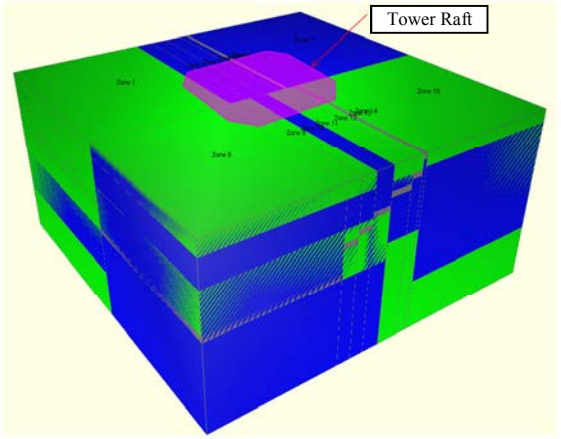

Soil Zone		Initial Modulus	Soil Profile
	Fault Zone	0.5GPa	Linear
	Banded Gneiss	10GPa	Non-linear
	Brecciated Gneiss	5GPa	Non-linear

Figure 7: Geological Model for Input into Computer Analysis

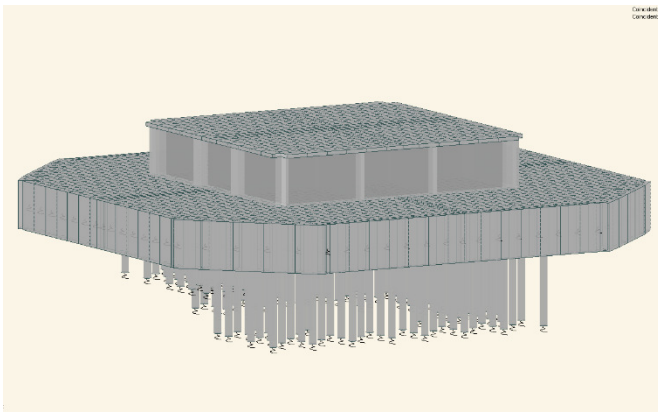

Remark: Half-length of piles modelled in GSRaft to reflect the pile-soil interaction level

Figure 8: Raft and Piles in GSRaft Model

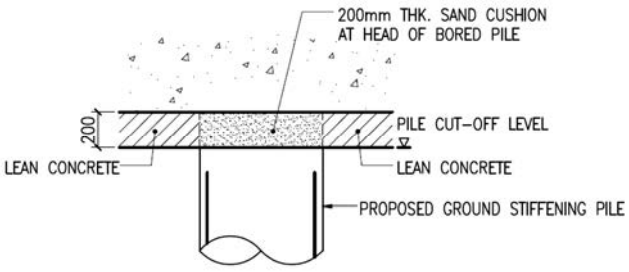

Figure 9: Pile Head Soil Cushion

A key feature of these piles was the pile heads being disconnected from the raft, with a 200mm soil cushion as shown in Figure 9, which separates the piles entirely as part of the ground. This also reduced the maximum pile reaction by 30% as the load from the raft was transferred to the ground before reaching the

pile. This allowed the load from the raft to transfer more uniformly into the ground instead of forming extremely hard spots at the individual pile locations.

When the excavation approached around 1 to 2m above the foundation level, a final rock mapping was carried out and the geological model was finalized.

The GSRaft analysis was then refined and further compared with a 3-D Plaxis model.The mesh set-up, the ground model and the raft simulation are shown in Figure 10. Non-linear moduli of the rockmass were also adopted in the Plaxis model. Based on the results of the analysis, similar peak settlement was found in both 3-D Plaxis and GSRaft models but the predicted differential settlement by 3-D Plaxis was about 17% smaller than that predicted by GSRaft model. It might be explained by the fact that the raft in Plaxis was modeled as "solid continuum" element, which allowed dispersion of load through the physical dimension of the elements resulting in more uniform load distribution beneath the raft while the raft in GSRaft was modeled as "shell" element with no physical thickness despite the stiffness equivalent to the raft was incorporated.

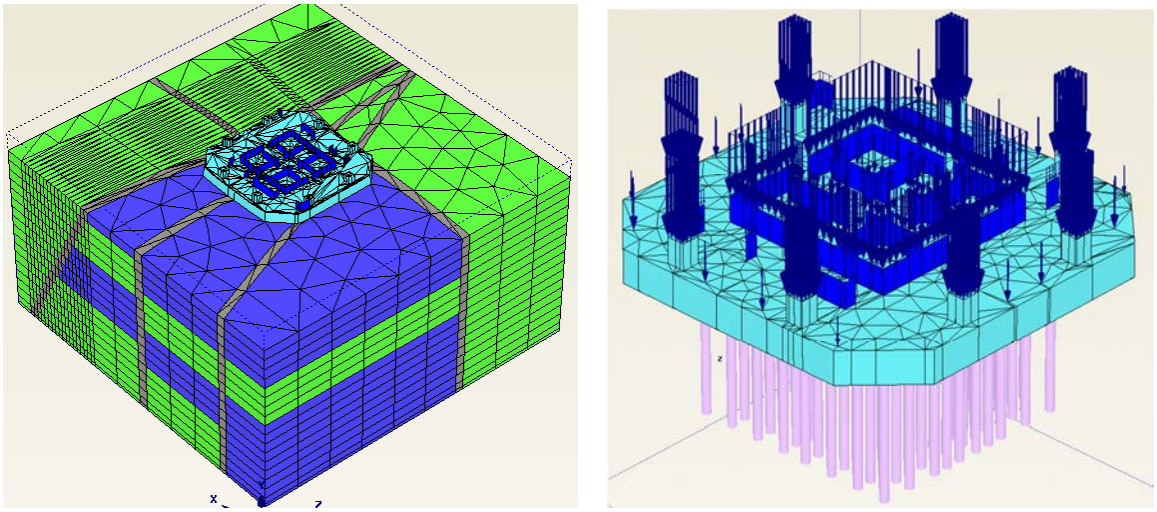

Figure 10: 3-D Plaxis Model to Cross-check GSRaft Analysis

4.6 Construction stage support

It is a common practice in South Korea that the construction supervisor was independent from the design team and the supervision team might have limited knowledge on the geotechnical design. In view of the variability of the rock condition, the active input from the Designers during the construction phase apart from the routine supervision by the Construction Supervisor is a critical element to promptly review if the actual ground condition matches with the design assumptions. Periodic site supervisions were conducted by Arup's designer and engineering geologist to carry out rock face mapping and to verify or update the geological models at the interim stages of excavation and before the final formation level was reached. Another important issue is the potential blast induced damage to the rockmass immediately beneath the raft, which may result in undue settlement during recompression of the opened joints under the imposition of the building loads. It is therefore advised that no blasting shall be applied to the rockmass within 1m above the foundation level.

4.7 Design performance

Monitoring of the raft response during the imposition of loads throughout the construction phase is important to verify the design assumptions and hence to secure the Tower performance. Instrumentations at raft foundation level included the strain gauges in selected ground strengthening piles, earth pressure cells underneath the raft, extensometers in rockmasses and settlement markers at the top of the raft. The bearing stress, settlements and hence the differential settlements obtained from the site were compared to the prediction at different stages of the Tower construction. The Tower is still under construction at the time of

preparing this Paper. Figure 11 shows the measured settlement of the raft when the Tower construction was up to about three quarter of the total building height comparing with the design prediction. The projected settlement when the total building load is applied is also estimated and is well within the design prediction. This reflects that the assumed ground stiffnesses are reasonably conservative and the actual ground stiffness may be close to the average ground stiffness as shown in Figure 6.

Besides, the bearing stress measured by the earth pressure cells underneath the mega column was found to be slightly less than the theoretical value. This may be due to the actual concrete stiffness of the raft being higher than the design prediction to spread the column load.

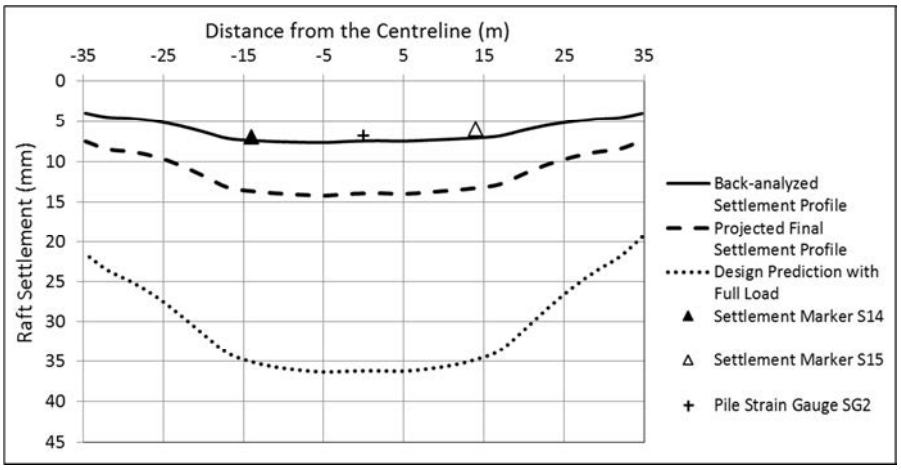

Figure 11: Comparison of Measured, Predicted and Projected Settlement of the Tower

5 CONCLUSIONS

The use of piles as settlement reducers (i.e. ground stiffening pile) to control the settlement and/or differential settlement of a raft foundation is geotechnically viable. Using the modern computer modeling tools, the soil-structural interaction among the raft foundation, the ground stiffening piles and the ground can be efficiently analysed. Furthermore, with the consideration of non-linear ground stiffness, a cost-effective piled raft foundation solution can be derived. The case history presented in the paper has demonstrated the successful application of ground stiffening piles for the raft foundation design in a complex ground condition to support a high super tall landmark tower in Seoul. The Designers' involvement to calibrate the ground models throughout the construction process is one of the essential elements for the success of the project.

ACKNOWLEDGEMENTS

The authors would like to express gratitude towards the client Lotte Moolsan in allowing the publication of this Paper. The authors would also like to express thanks to the project design team in particular the Structural Engineer Lesile Robertson Associates and the local geotechnical consultant Jin Young Consultants for the collaborated effort in pursuing this foundation design approach.

REFERENCES

Davies J., Lam K.L.A. & Junaideen S.M. 2009. Piled Rafts to Support High Rise Developments, *Proceedings of The 3rd Asian Seminar on ATC 18 Mega Foundation: "Recent Advance of Deep Excavation and Foundations"*, Bangkok, Thailand.

Hoek E., Kaiser P.K. and Bawden W.F. 1995. Support of underground excavations in hard rock, *Rotterdam, Balkema*, 213pp.

Jardine R.J. 1992. Nonlinear stiffness parameters from undrained pressuremeter tests, *Canadian Geotechnical Journal,* Vol. 29, pp. 436-446.

Katzenbach R., Schmitt A. and Turek, J. 1999. Co-operation Between Geotechnical and Structural Engineers – Experience Gained from Projects in Frankfurt, *COST Action C7, Soil-Structure interaction in urban civil engineering Proceedings of the Workshop in Thessaloniki*, 1./2. Oct. 1999

Pappin J.W., Heidenbrecht A.C., Henderson P. and Naumoski N. 1989. Site response study – soil modeling, *McMaster University*, EERG Report 89-02, 52pp.

Poulos, H.G. 2001a. Piled Raft Foundations – Design and Applications. *Geotechnique*, Vol. 50, (2): 95-113.

Poulos, H.G. 2001b. Methods of Analysis of Piled Raft Foundations. *A Report Prepared on Behalf of Technical Committee TC18 on Piled Foundations.*

Randolph, M.F. 1994. Design Methods for Pile Groups and Piled Rafts. *S.O.A. Report, 13 ICSMFE*, New Delhi, 5: 61-82.

Seed H.B. and Idriss I.M. 1970. Soil moduli and damping response analysis. *EERC Report No. 70-10*, Berkeley, California.

Does 3D Finite Element Analysis Allow Better Design of Piles? – A Case Study for Temporary Marine Pile Design

Gavin S.H. Toh & Chao Li
Lambeth Associates Limited, Hong Kong

ABSTRACT

Large diameter steel tubular piles have been widely used by contractors in Hong Kong as temporary support to working platform for construction of permanent bridge bored piles. In Hong Kong design of piles has been normally practiced according to GEO Publication No. 1/2006 (GEO, 2006), which reflects a combination of local experience with state-of-the practice design philosophy. In general, GEO 1/2006 has been a very useful design manual for practitioners and has been widely used in Hong Kong successfully. However it does not particularly differentiate the design according to the expected function/nature of the piles. Particularly temporary steel tubular piles have not been explicitly dealt with in sufficient details. This paper uses PLAXIS 3D as an analytical tool and to investigate the pile behaviours with soil-structure interaction and its implication in design. Sensitivity analyses regarding drained/undrained behaviour of alluvium as well as R_{int} (Interface Factor) were also carried out. For temporary works, the authors recommend the use of observation method, with the aid of advanced finite element analysis. General observations and recommendations on the practicality of using advanced method in design are also provided.

1 INTRODUCTION

A series of temporary steel tubular piles has been designed/constructed as part of some bridge foundation project carried out by Gammon Construction Limited. The function of these piles is mainly for support of a working platform used for permanent works, which includes both installation of permanent bored pile and construction of bridge piers. This paper presents a series of 3D finite element modelling works which were used as basis for temporary tubular pile design considering the intended function of these piles. For simplicity and clarity, only axial loadings are of concern in this paper.

GEO Publication 1/2006 has been routinely used in checking pile capacity. For drained soils, Equations 6.3 to 6.5 are frequently used (GEO, 2006). The shaft resistance equation based on semi-empirical method is repeated as below

$$\tau_s = \beta\sigma_v^{'} \qquad (1)$$

where β is the shaft resistance coefficient.

It is noticed that according to Table 6.3 (GEO, 2006), β value can have a large spread. For driven small displacement piles, the value varies from 0.1 to 0.5. For driven large displacement piles, the range is 0.2 – 1.5. This large spread simply means that the shaft resistance can vary up to 5 times for small displacement piles and 7.5 times for large displacement piles. Local experience is therefore critically important for establishment of the shaft resistance coefficient β.

The local experience for temporary steel tubular piles has not been fully established. To help to understand the implications of β value, a series of 3D simulation were carried out to investigate the performance of the large steel tubular piles under axial loadings. The results appear to point to a more efficient way of doing temporary steel tubular pile design, which, if implemented in full detail, can lead to more efficient design, improved performance prediction and establishing local experience in steel tubular pile as temporary pile foundation.

2 THE PROBLEM SETUP

2.1 Geological profile and pipe pile modelling

For the concerned project, the soil deposit mainly consists of Marine Deposit (MD) and Alluvium. Alluvium can be either Alluvium Clay or Alluvium Sand. The design shear parameters for the Marine Deposit and Alluvium adopted in the 3D FE model is presented in Table 1. Mohr Coulomb model has been used as the material constitutive model.

Table 1: Soil Parameters Adopted in FEM Analysis for Location A

Soil Type	Elevation (mPD)		Density (kN/m^3)	Young's Modulus	Friction Angle (θ')	c' (kPa)	Cu (kPa)	dCu/dz (kPa/m)
Marine Deposit	-5	-15	15	Eu = 400 Cu	---	---	5	1.1
Alluvium	-15	-50	19	E = 1N (MPa)	30	4	50	2.5

* N is the SPT N-value

Dimension and parameters of the pile is given as following:

- Pipe pile diameter D = 1.2m
- Pipe pile thickness = 16 mm
- Material: Steel,
- Elastic properties of steel: E = 205GPa, v = 0.2

2.2 Model geometry and analysis settings

The photograph in Plate 1 shows a picture of the construction project during the installation of the 1.2m diameter steel tubular pile. Figure 1 illustrates the associated application of this problem – the investigation was started with a real construction problem where the steel tubular pile has been installed to refusal but is not able to reach the design toe level. To verify the load capacity of the tubular pile, loading test is commonly adopted. However, under the marine condition physical loading test is difficult with safety concern. PLAXIS 3D is therefore adopted as a simulation tool to model the soil-structure loading behaviour of the tubular pile with the following considerations:

- Soil parameters including drained/undrained alluvium and the interface factor;
- The open tubular pile behaves as plugged or unplugged mode; and
- The allowable settlement of the tubular pile that will provide a safe temporary platform for the permanent piling work.

Given the complexity of soil pile interaction, this paper primarily focuses piles under static axial loading and the driven process is not simulated.

Plate 1: Installation of the Steel Tubular Pile

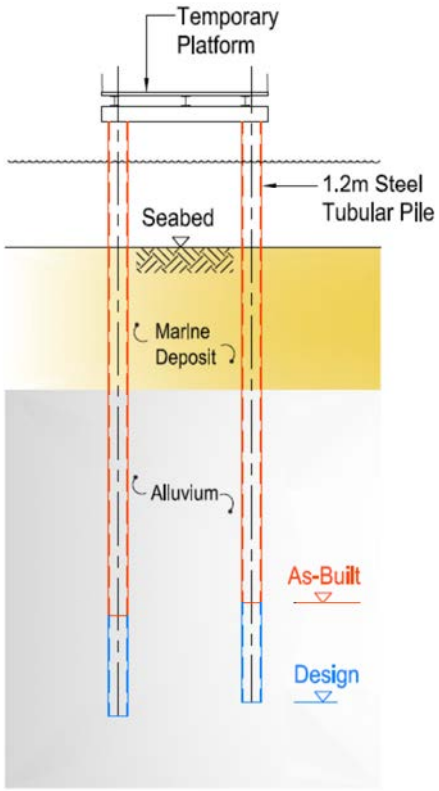

Figure 1: Configuration of the Temporary Platform

3 RESULTS OF PLAXIS 3D MODELS

3.1 Analysis cases

Four cases of the PLAXIS 3D model representing different assumptions is summarized in Table 2. Case 1 considers the alluvium as "undrained" and no "reduction" of interface strength (which means the interface has the same properties as the surrounding soils). This case is considered as the base design condition for comparison. The model predicts a settlement of around 10mm at top of the steel tubular pile. In Case 2, the alluvium as "drained" material is considered. In Case 3 a reduction of 50% on the interface material properties was performed. In Case 4, an artificial steel plate is set at the pile base to verify the result of Case 3 where the

tubular pile is expecting to behave as a plugged mode. The vertical displacements at the top of the tubular pile is presented in Table 2.

Loading displacement curves up to 50mm settlement of four cases is shown in Figure 2. A typical result of the PLAXIS 3D model showing the vertical displacement contour is presented in Figure 3.

Table 2: Summary of PLAXIS 3D Models and Predicted Settlements

CASE No.	Interface factor	Interface Factor, R_{int}	Length of Pile (m)	Alluvium	Pile Settlement (mm)
1	1	1	25	Undrained	10.0
2	1	1	25	Drained	11.6
3	0.5	0.5	25	Undrained	15.5
4*	0.5	0.5	25	Undrained	14.3

* The soil-plug condition is simulated by including an artificial steel plate at the bottom of the tubular pile (this case is for reference only).

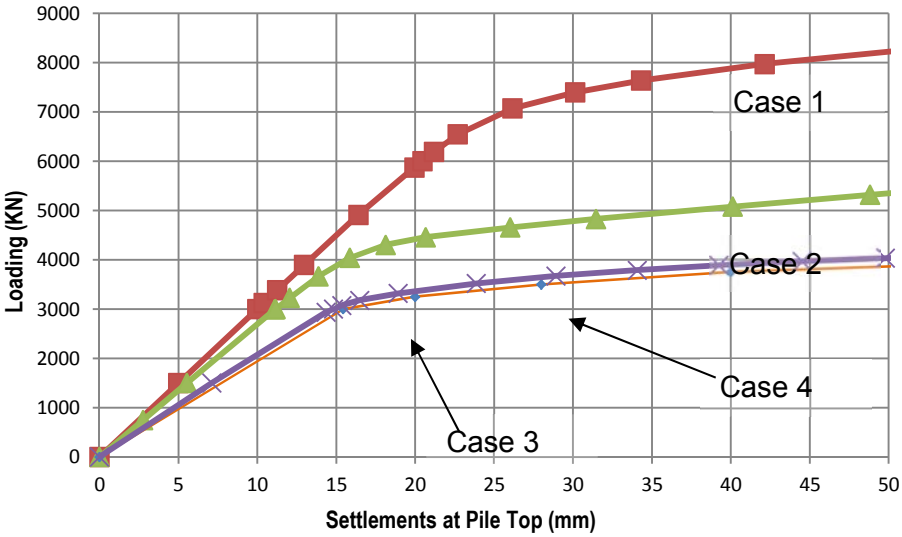

Figure 2: Load-displacement Curves for Cases 1 to 4

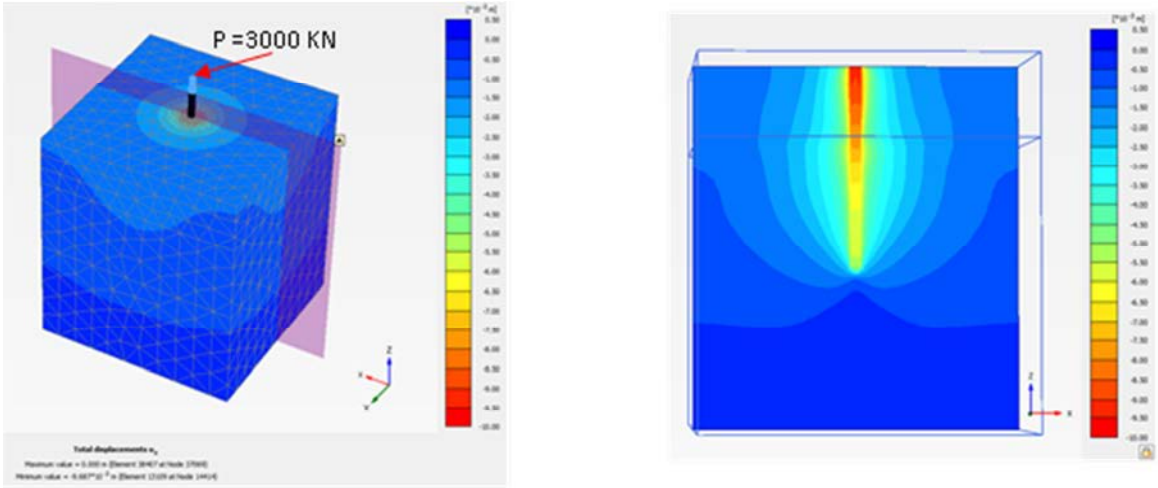

Figure 3: Vertical Displacement Contour under Working Load, P = 3000kN

3.2 Discussion on soil parameters

The difference of the load-displacement curve between drained and undrained of alluvium by comparing Case 1 and Case 2 is notable in Figure 3. However, the differences of the predicted displacement between two sets are still rather small at the working load, P of 3000kN (only 1.6mm difference). This set of sensitivity analysis is not to make judgment about whether drained or undrained behaviour actually shall take place, particularly considering the uncertainties and variations in actual soil conditions.

In this paper, however, the computer model is mainly used as a simulation tool which can fit with the observed data and provide guidance to future performance. For this purpose either drained or undrained load-displacement curves satisfies the purposes. For simplicity, the set of analysis which fit with the observed monitoring data is considered. It should be noted that the general trend between drained and undrained analyses are similar.

In the PLAXIS 3D model the interface elements are used to model the soil-structure interaction behaviour where the material properties of the interface is in-general follows the adjacent soils with a reduction factor (PLAXIS, 2012). It is important to realize that R_{int} (Interface Factor) in PLAXIS 3D is not strictly a physical material property. Rather it is the proportion of strength reduction to the strength of adjacent soil clusters (PLAXIS, 2012). The comparison between Cases 1 and 3 suggests that R_{int} can change the load-displacement relationship significantly. It is noted that when interface factor R_{int} drops from 1.0 to 0.5, pile top settlement increase 50%. The comparison between prediction model and observation suggests that modelling assumptions in Cases 1 and 2 are closer to observed behaviour. However, this should not be interpreted that the analyses has confirmed that the R_{int} should take the value 1.0; but on the other hand, it has confirmed that the interfaces properties are close to c'/c_u or phi' values as presented in Table 1.

3.3 Discussion on formation of soil plug

GEO 1/2006 has make references to the idea of formation of soil plug when making difference between small displacement and large displacement driven piles type. If the open-ended tubular pile behaves in a plugged mode the pile will effectively become large displacement pile type. It has therefore drawn special interest from the authors to investigate whether the performance of the open-ended pile is close to the plugged or unplugged mode. The comparison between Cases 3 and 4 has confirmed that the plugged assumption is valid.

3.4 Choice of prediction model based on comparison with measured settlements

Figure 4 shows the following measured settlement at the working platform under a design loading of 3000kN. It is noted that Case 2 prediction is closest to the measured value. Therefore it is considered most appropriate to adopt Case 2 as the prediction model.

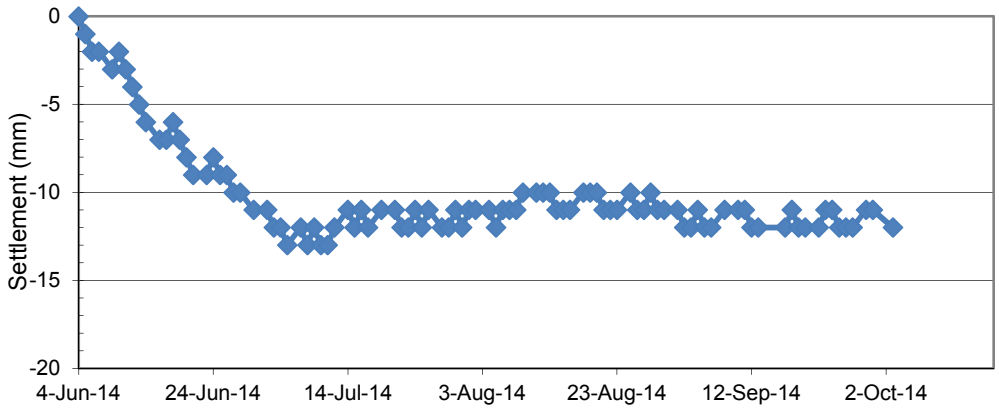

Figure 4: Measured Vertical Settlement at the Temporary Platform Near to the Concerned Pile

4 REVIEW OF PILE ULTIMATE LOAD AND SHAFT RESISTANCE

Using Case 2 as the preferred model, Figure 5 shows the load-displacement curve of the pile loaded up to 12,000kN with unloading-reloading at 6000kN, 9000kN. The tubular pile did not reach a physical failure load, beyond which the load cannot be further increased. However, it should be noted that the displacements has become more than 500mm under the axial loading of 12000kN.

For normal design purpose, GEO 1/2006 made reference to BSI (1986), in which the ultimate pile load is defined as the loading mobilized when the settlement has reached about 10% pile diameter. From the load-displacement curve in Figure 5, the ultimate pile load is determined as 6800kN at 120mm settlement. The axial load distribution along the pile shaft from the PLAXIS 3D model is shown in Figure 6 for different loading magnitude. The results indicate that the load bearing at the pile base varies from 10% to 25% (summarized in Table 3) depending on the magnitude of the pile load at the top.

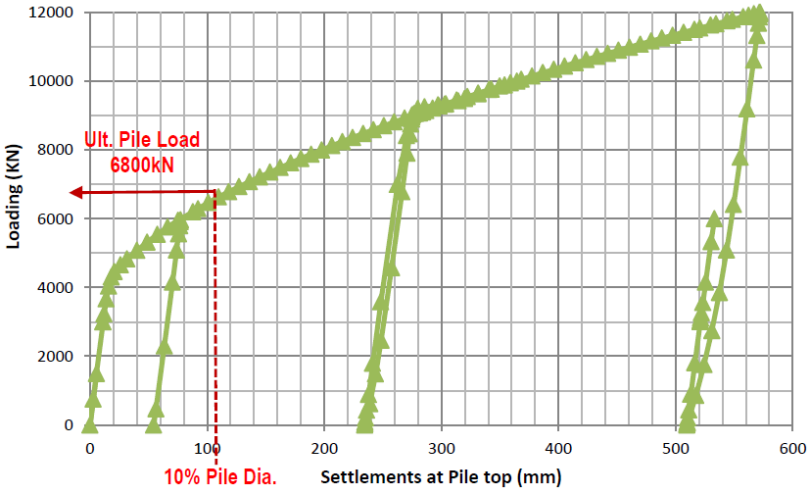

Figure 5: Load-displacement Curve of the Pile (Case 2)

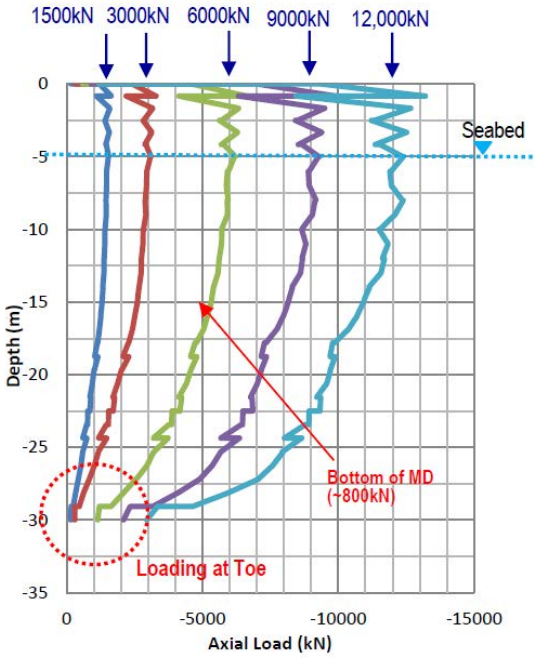

Figure 6: Pile Load Distribution with Depth (Case 2)

Table 3: Percentage of Load Bearing at Pile Base (Case 2)

Total Load (kN)	End bearing (kN)	Percentage (%)
12000	2950	25%
9000	2100	23%
6000	1145	19%
3000	295	10%
1500	155	10%

Since PLAXIS provides a detailed distribution of axial loading along the pile shaft, it is possible to back calculate β value of Equation (1) at the alluvium layer. For the ultimate load of 6800kN, the distribution of the shaft loading at the marine deposit, alluvium and end bearing is summarized in Table 4. For alluvium, the back-calculated value of $\beta = 0.78$, which falls within the large displacement driven pile range of 0.2 – 1.5 (GEO 1/2006). This is consistent with the observation of a plugged mode behaviour discussed earlier.

Table 4: Distribution of Loading along the Pile (Case 2 with 68000kN)

Load Type	Load Value (kN)	Percentage (%)
Ultimate Load	6800	-
Shaft Load in MD	800	12%
Shaft Load in Alluvium	4640	68%
End Bearing	1360	20%

The analysis approach using PLAXIS 3D presented in this paper has been used to investigate the tubular piles at other temporary platforms of the project. Summary of the piles details, the average modulus of the alluvium, depth of rock head beneath the pile toe and back-calculated β values are tabulated in Table 5. The ultimate load is taken as load at a displacement 10% of pile diameter. The results of the pile at location A have been described in detail in this paper. The β value around 0.4 at location B is smaller than the value at A is likely due to the lower modulus of the alluvium at B. When the rock head is closer to the pile toe at location D, the lower β value compare to A suggests a higher distribution of load at pile toe due a stiffer bearing material. However, the β value at location C is notably high despite a lower modulus and higher rock head. It is likely due to a higher mobilised shaft friction at the alluvium layer. Nonetheless, the back-calculated β values are within the large displacement driven pile range indicating a plugged mode behaviour.

Table 5: Summary of PLAXIS 3D and Back-calculated β Values

Location ref.	Tubular pile ref.	Ultimate load (kN)	Pile Length in soils (m)	Pile length in alluvium (m)	Rock head depth below pile toe (m)	Ave. E of alluvium (MPa)	Back-calculated β
A	A_1	6800	24.0	14.0	30	26.3	0.78
B	B_1	6200	35.5	16.0	15	12.2	0.41
	B_2	6400	36.0	16.5	15	12.5	0.40
	B_3	5400	34.0	14.0	15	11.4	0.43
	B_4	5700	34.5	15.0	15	11.8	0.41
C	C_1	3500	19.0	10.0	7	18.0	0.80
D	D_1	5000	23.5	15.0	8	28.6	0.52

5 CONCLUSIONS

It is possible to directly determine an acceptable working load of temporary tubular piles from finite element PLAXIS 3D. With the load-displacement relationship from PLAXIS 3D, one would be able to estimate the behaviour of the piles. However, careful calibration with observed settlements must be carried out in view of variations in the input parameters. Alert, action, alarm (AAA) levels need to be set up in case of unforeseeable ground conditions. The level of AAA levels, however, will depend on the acceptable settlement of the temporary work.

From design point of view, direct use of GEO 1/2006 is preferable because of its simplicity in calculation. However, since the β value has a relatively large spread, the variation of working loading is also very large. A conservative design may result from the simplified calculation based on GEO 1/2006 requiring a deeper pile toe. Verification of the load capacity of the pile using physical loading test is a challenge in a marine condition. PLAXIS 3D can be an alternative method for verification of the pile load.

It can be concluded that finite element using PLAXIS 3D together with site observation can help to review the behaviour of temporary tubular piles with consideration of soil-structure and geological variations, to assess the observed displacement and to predict future movement as the construction progress.

REFERENCES

BSI, 1986. *British Standard Code of Practice for Foundations (BS 8004: 1986).* British Standards Institution, London.

GEO. 2006. *Foundation design and construction* (*GEO publication No. 1/2006)*. Geotechnical Engineering Office, Civil Engineering and Development Department, The Government of Hong Kong SAR

PLAXIS 3D, 2013. *PLAXIS Reference Manual 3D-Version 2013.* Delft.

Application of Modern Analytical Tools to a Four Decade Old Metro Rail Station

S.P. Chin, A.K.L. Ng, L.J. Endicott & M. Ramanathan
AECOM Asia Co. Ltd., Hong Kong

ABSTRACT

The existing Diamond Hill Station in Kwun Tong Line (KTL-DIH) was built in mid-seventies with provision for future expansion to either side. Thus a special form of external wall comprising 1500mm diameter hand dug caisson shafts with steel king posts and concrete jack arch panels were adopted, which could facilitate removal of the walls for future expansion. However, the KTL-DIH station does not expand sideways as originally planned. Now, the station in its fourth decade is being linked to a new Diamond Hill Station (SCL-DIH) as a part of the Shatin to Central Link expansion. When SCL commences its service DIH Station will be transformed into a major railway hub for East Kowloon. The new and old DIH stations will be interconnected with adits and unpaid links, and at these locations jack arch panels and kingposts would be removed. Also, lifts and escalators would be added to KTL-DIH and existing entrances modified to connect with SCL-DIH.

To carry out these modifications and to assess the impact due to deep excavation and construction SCL-DIH structure in close proximity, the designers need to review and understand the design principles and behaviour of the KTL-DIH structure. Back in the seventies, there were few computers in use and hand calculations adopted. The Terzaghi and Peck envelopes were used to determine the strut forces. A plastic design method, which was not recognised in any Code of Practice until 1990, was adopted taking each stage of loading independently. The main walls comprising king posts with external lagging are still in use today. PLAXIS, a modern-day geotechnical software based on the finite element method has been used to replicate and back-calculate the conditions that were encountered during construction of KTL-DIH and establish the locked-in-stresses considering the soil-structure interaction. SAP2000, state-of-art structural design software has been used to evaluate the transition stresses from the transient active stage to a permanent static stage. The forces and deformations from these two analyses are combined and the walls as built are found acceptable based on the then prevailing codes. This method paved way for further design leading to modification and adjacent excavation works, and has made the connection from Shatin to Central Link possible.

1 INTRODUCTION

1.1 Diamond Hill Stations - old and new

In the year 1975, Mass Transit Railway (MTR) commenced the construction of the then called Modified Initial System from Hong Kong Island, under the harbour, through Kowloon and outlying suburbs to terminate at Kwun Tong: a distance of about 16km with 15 stations. The Modified Initial System (now part of the Kwun Tong Line(KTL) and Tsuen Wan Line) comprised of 12 underground stations linked by bored and cut-and-cover tunnels, and three elevated stations connected to 2.4km of viaducts. MTR decided that the initial system should be let on a multi-contract basis, of which 25 were civil engineering works. The individual contracts for the underground works were let on a design and construct basis and for a lump sum. Paul Y. Construction Co. Ltd., Hong Kong was successful in bagging four civil engineering tenders which formed a continuous site of 2km with two major stations, a cut-and-cover tunnel and a bored tunnel. Choi Hung and Diamond Hill are the two stations built by Paul Y (Benjamin et al. 1978). The detailed design of these works was carried out by Maunsell Consultants Asia Ltd. (During the year 2009 Maunsell merged with AECOM).

Diamond Hill Station in Kwun Tong Line (KTL-DIH) which began its operation in the year 1979 was built with provision for future expansion to either side (MTR 1974). However, the KTL-DIH station does not expand sideways as originally planned, as a better alignment has now been planned to suit future transport integration, and also to respect subsequent cityscape developments.

Shatin to Central Link (SCL) was gazetted in the year 2010 and construction commenced in 2012. It comprises of two sections, namely 'Tai Wai to Hung Hom Section' and 'Hung Hom to Admiralty Section'. The former Section will extend the existing Ma On Shan Line from Tai Wai to the West Rail Line via East Kowloon to form the 'East West Corridor' with the following stations: Tai Wai, Hin Keng, new Diamond Hill, Kai Tak, To Kwa Wan, Ma Tau Wai, Ho Man Tin and Hung Hom. Refer to Figure 1.

Diamond Hill Station will be transformed into a major railway hub for East Kowloon when 'Tai Wai to Hung Hom Section' is completed. Modification works began in 2013 to upgrade Diamond Hill Station to serve as the future interchange between the SCL and the KTL. A new Diamond Hill station (SCL-DIH) with separate concourse and platforms would be built and a wide array of enhanced facilities added there including the installation of three new lifts, 12 escalators, additional ticket issuing machines, automatic teller machines, shops, and new public toilet facilities. Upon completion of SCL, passengers will be able to travel directly from Diamond Hill Station to the East and West New Territories, Kai Tak, Kowloon City, and Hung Hom without needing to change trains.

The MTR Corporation Ltd. appointed AECOM among other consultants to provide design services for SCL. AECOM's work involves civil, structural and building services engineering design of a new interchange station at Diamond Hill, and also upgrade of an existing rail depot and an extensive footbridge network. Unlike KTL-DIH Station which was a design and construct contract, the new SCL-DIH Station is an Engineer's Design contract. Whilst AECOM (formerly Maunsell) worked as the detailed design consultant for the contractor for KTL-DIH station, it is servicing as the client's detailed design consultant for SCL-DIH station.

Figure 1: MTR Part Route Plan

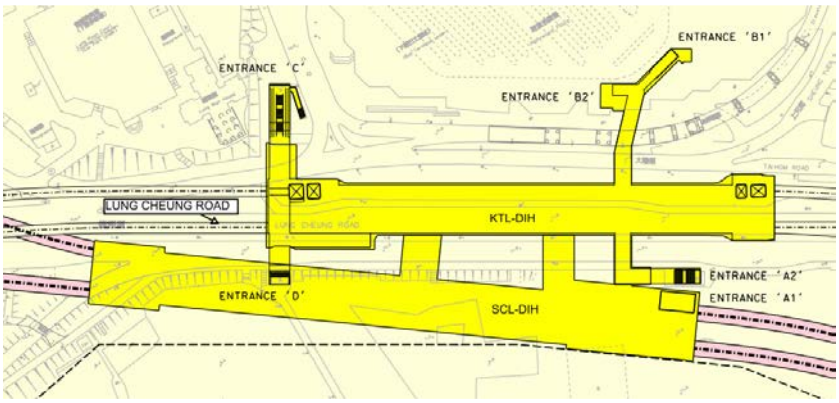

Figure 2: Diamond Hill Stations-Location Plan

2 DESIGN OF OLD KTL-DIH STATION

2.1 Station box

KTL-DIH station is located under the carriageway of Lung Cheung Road (Figure 2). The existing roof, concourse and track slabs are approximately 4m, 10m and 16.6m lower than the road level (Figure 4). Lung Cheung Road dips from +12.8mPD (west) to 10.6mPD (east)

In the original design, provision was made to expand the station to either sides to accommodate an additional track to the north and one to the south of the existing tracks. For such a future expansion main walls along the sides of the station box were required to be removed with trains in service.

2.2 Tender design

The engineer's notional tender design scheme was to drive steel sheet piling to a cut-off below the station, then excavate and build the station from the bottom upwards. Sheet piles as a semi-permanent wall could be readily dismantled at a later date when the station widened. However, this scheme was later discarded as hard ground conditions would result in damage to the sheet piles during driving with a corresponding loss of strength and water-tightness. Also, sheet piles with limited structural depth are inefficient in bending over large spans. The diaphragm wall option was also found unsuitable as it would have been difficult to break open at a later date.

The contractor had access to some 1500 hand dug caisson workers. Typically shafts of about 1.5m diameter were excavated, if a boulder or bed rock was encountered it could be excavated by pneumatic tools. Following exchange of ideas with the Contractor's site staff, it was decided to use hand dug caissons extensively. For the external walls, primary shafts sunk at 2.8m centres were used to place steel beams vertically to act as king posts. Steel beams 911 x 418 x 342kg/m in Grade 43A in general were set to form the main structural element, spanning vertically between the slabs. Between king posts, intervening soil excavated and concrete jack arches spanning horizontally were provided extending from the level of the top of the roof of the station to the underside of the track slab. Similar inner lining were also provided, but only as a temporary support of the soil until the main excavation was done. Refer to Figure 3.

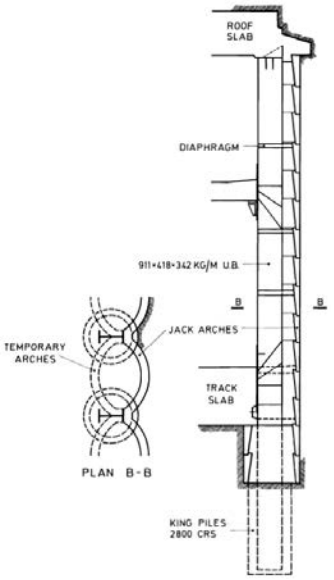

Figure 3: Outer Wall of KTL-DIH Station

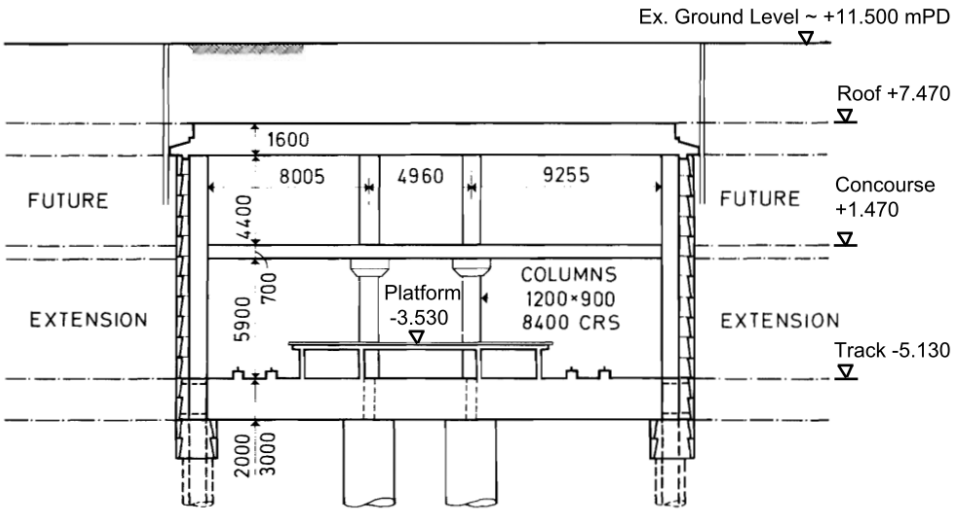

Figure 4: Typical Cross Section of KTL-DIH Station

Hand dug caissons were also used for the end walls where all the caissons were completely filled with reinforced concrete to construct permanent walls. However, these caissons were not founded on bedrock and the station box in effect is a floating structure. The station box is also supported by two rows of 900 x 1200mm internal columns at every 8.4m grid.

With the walls and columns in place top down construction commenced with casting the roof slab and then excavating underneath the roof slab down to the level of the concourse and so on. This process was then novel to Hong Kong. At the time there was only one deep excavation which was for the basement of the New World Hotel which used diaphragm walls and tie back anchors for bottom up construction.

In 1975 there were few computers in use in the industry and very few engineering programs. Hand calculations were commonly in use. For excavations with several strutting levels it was common to use Terzaghi and Peck envelopes to determine strut forces. Moreover designers tended to determine bending moments in the walls by using the same envelope but not taking into account the built in deformations resulting from the staged construction.

In order to minimise costs, the tender design attempted to consider soil/structure interaction and to consider the built in deformations. Instead of adopting the Terzaghi and Peck envelope, the active and passive soil pressures were determined for each stratum on the site and the displacements needed to reduce the external soil pressure from the at rest pressure to the active pressure and on the inside the forwards movement required to develop the passive were included in the design calculations. This was a novel approach at the time. However the approach was not readily accepted by the checkers and, for the detailed design for construction, the Terzaghi and Peck envelope method was adopted.

Detailed design by traditional methods led to an estimated overstress which was overcome by adopting a plastic design method (Horne 1968). Plastic design permitted assumptions of plastic hinges which resulted in redistribution of bending moments. To accommodate shear stresses it was necessary to stiffen the webs of the steel beams at the level of the concourse. By this means the design was approved for construction. Plastic design was not recognised in a Code of Practice in U.K. until 1990, some 15 years later (BS5950-1990).

2.3 Geology and ground conditions

The area typically comprises 2m to 10m thick fill, underlain by 2m to 7m thick alluvium, in turn underlain by saprolite, a completely decomposed granite ranging from 22m to 57m in thickness. Isolated pockets of colluvium up to 9m in thickness were also identified locally. Level of bedrock (i.e. moderately decomposed rock or better) is variable, between -25mPD to -40mPD.

2.4 Inspection

To verify the jack arch wall system the station was inspected during 2010. King posts are found to be well covered by fire protection cement, no spalling noted, no significant rust identified, no excessive deflection found nor no sign of distress. Jack arch panels are found dry in general, no major seepage or cracks identified, and found generally in good condition. The RC diaphragms used as a tie member for king posts are also found without any sign of cracks or distress. The station is well maintained.

3 IMPACT OF NEW WORKS TO KTL-DIH

3.1 Modification works

Two new interchange adits in the middle and an unpaid link in the western side KTL-DIH would be added to serve the concourses of both SCL-DIH and KTL-DIH stations. The adits will be integrated with KTL-DIH, and with movement joints at the interface with SCL-DIH. The existing jack arch walls and king posts on the south side between roof and concourse would be removed at adit locations, and its impact should be assessed.

The existing public subway above KTL-DIH serves Entrances A1 & A2 and also provides entry down to the KTL-DIH concourse. Entrance A2 would now be extended and configured to suit the layout at SCL-DIH. A new lift will be provided at Entrance A1. A new shaft will be built and breakthrough of the subway wall is necessary for entry at the public subway level.

3.2 Excavation of SCL-DIH

Owing to deep excavation of SCL-DIH structure, KTL-DIH, as a floating structure, will be subjected to lateral movements and settlement. There will also be changes in forces acting by the surrounding soils to the structure. In order to assess the structural adequacy of KTL-DIH when subjected to these movements and changes in forces, it is first necessary to establish the current utilization of the structural members of KTL-DIH, predict its future movements due to the excavation of SCL-DIH station and then estimate the corresponding impact to the KTL-DIH structure.

As the KTL-DIH structure was built by top down method, the assessment of locked in stresses during its construction stages plays a vital role. To assess the impacts of modification and new works, the existing station has to be reassessed by modern computing methods. It was decided to adopt a two-computer software approach and the outputs were ‘coupled’. More details are given in the following section.

4 DESIGN CHECK OF KTL-DIH USING MODERN TOOLS

PLAXIS (2D), a modern-day geotechnical software based on the finite element method has been used to replicate and back-calculate the conditions that were encountered during the construction of KTL-DIH structure and establish the locked-in-stresses considering the soil-structure interaction. The top-down construction sequence of KTL-DIH structure and groundwater drawdown were simulated using PLAXIS to find out the stresses and deformations locked-in the structural members at each key construction stage. This analysis can determine the stresses and deformations induced by all temporary works, and provide the conditions of the structural members at several critical sections at every stage of construction. The lateral stress from the surrounding soil can be denoted as Kplaxis, which may be close to Ka conditions depending on how much movement the soil has experienced.

SAP2000, state-of-art structural design software, on the other hand was then used to further replicate the station structure by applying the increment of loading from the surrounding soils (Kplaxis) to the final loading in permanent (Ko) condition. Simple two dimensional models are generated from the as-built records at various sections. The models provide the current utilization of the structural members of the KTL-DIH structure, setting a bench mark for the subsequent analyses for investigation impact to the structure due to SCL DIH construction. Table 1 summaries the methods adopted for analysing the KTL-DIH structure in the original design and present methodology.

Table 1: Comparison of Verification Methods

	1970s	Present
Water Drawdown Analysis	Seepage Analysis Using Flow –net	PLAXIS
ELS/Construction Sequence Analysis	Beam Frame Analysis by Stage by Stage approach	PLAXIS
Permanent Case Analysis	Plastic Analysis	(PLAXIS + SAP2000)

The superposition of stresses, namely Kplaxis and (Ko-plaxis) and the forces derived from the two software are illustrated in Figure 5. The design checks in accordance with BS449-1969 (elastic design) indicated that the structural capacity of the king posts estimated in terms of P/A + M/Z is close to the unity. However, in order to further compare with the modern codes, king posts when checked against BS5950:1990 (limit state design), have been found well within the limit. Nevertheless, before application of further forces to KTL-DIH structure, by modification and adjoining new works, it was decided to strengthen the kingposts based on the then prevailing elastic design (AECOM 2011).

5 EXTENDING THE FINDINGS

Reassessing the adequacy of the existing station by the above mentioned two-fold method has led the designers to understand the behaviour and the conditions of the structural members; the application is further extended into stimulating the global and local effect from the new SCL-DIH construction.

To assess the impact of the KTL-DIH structure due to SCL-DIH construction, PLAXIS models comprising KTL-DIH and SCL-DIH structures would be set up at critical sections, and the excavation of the SCL-DIH to its formation level, including installation of lateral supports would be modeled. Excavation of interconnecting adits, removal of king posts and jack arch walls of KTL-DIH, construction of adits and back filling would also be modeled. These PLAXIS models would provide predictions on the movement of the KTL-DIH structure at each critical stage of SCL-DIH and adit construction, and respective changes to the soil pressures acting on the KTL-DIH structure.

The predicted movements of the KTL-DIH from PLAXIS would then be fed into the SAP2000's three dimensional model of KTL-DIH structure to study its structural behavior. Furthermore, multiple stage-construction analyses of SAP2000 model of KTL-DIH simulating with strut propping forces and soil pressures from PLAXIS model would be carried out. By looping the above process, several iterations would be required to achieve converged movements of the KTL DIH station as well as soil pressures acting on the station. While the iteration is a lengthy process, it would capture the soil-structure interaction in a more rigorous way where the changes in the soil pressures acting on the station can be modeled more realistically.

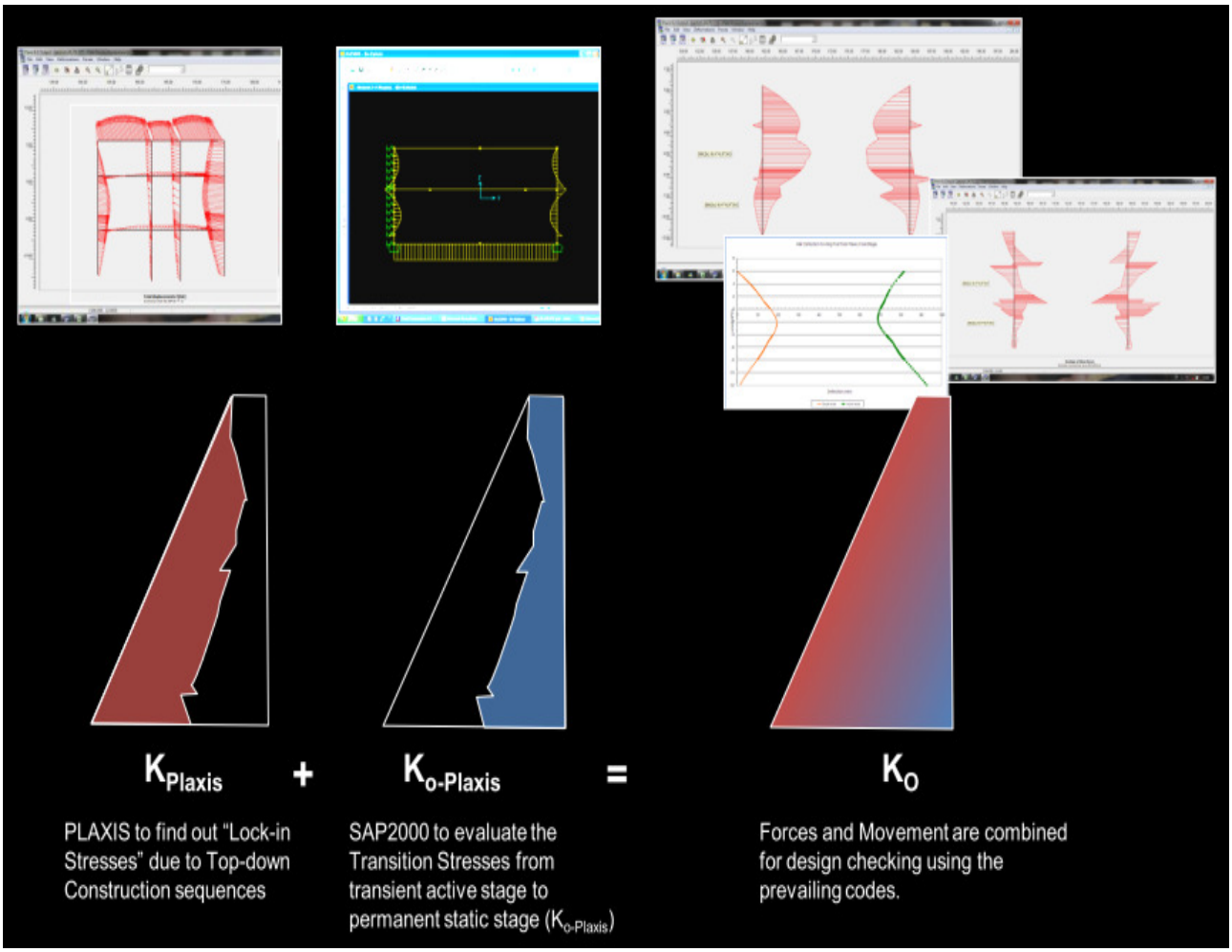

Figure 5: Superposition of Results from Two Softwares

6 CONCLUSIONS

The condition of the walls, both steel and concrete was found to be well maintained and in good conditions. The check would have been very difficult if it were not for the detailed records held by the MTR Corporation Ltd. including design calculations dating from 1976 and as-built drawings dating from 1978. The check determined that the walls as built are acceptable when checked to current design standards. To be compatible with present day design and construction methods, and to meet the challenge of construction a new station and interconnecting adits next to the old one, two different computer software have been used to model the old structure; and this would be extended for assessing the impact on old structure owing to new construction.

ACKNOWLEDGEMENTS

The authors wish to thank the MTR Corporation Ltd. for providing them an opportunity to be part of this project and also permitting to publish this paper. The authors are grateful to Clement Ngai, Chief Design Manager and Jason Wong, Project Manager of the SCL project team of the MTR Corporation Ltd. for their support and guidance. The authors are indebted to AECOM's Jacky Wong, Managing Director, Building Engineering and Ian Whitton, Sector Director-Railways for their encouragement.

REFERENCES

AECOM. 2011. Shatin to Central Link, Consultancy Agreement C1103 – Diamond Hill Station and Stabling Sidings, Works Contract 1106 – A3.13A2 BD and RDO Consultation Submission for KTL DIH Structural – Calculation, Rev.B, December 2011.

Benjamin, A.L., Endicott, J.L. & Blake, R.J. 1978. The design and construction of some underground stations for the Hong Kong mass transit railway system. *The Structural Engineer*, January 1978/No. l/Volume 56A, pp11-20.

Horne, M.R. 1968. The Full Plastic Moments of Sections Subjected to Shear Forces and Axial Forces. *British Welding Journal*.

Mass Transit Railway. 1974. Contract 207, Diamond Hill Station, Tender Design Statement.

Geotechnical Challenges in Construction of an Underground Stormwater Storage Scheme in Happy Valley

W.H. Luk, C.L. Leung & C.Y. Lam
Drainage Services Department, the Government of Hong Kong SAR

M.S. Hendy, S.S. Fang & J. Premchitt
ONLYgeotechnics Limited, Hong Kong

K.H. Lum
Black & Veatch Hong Kong Limited, Hong Kong

ABSTRACT

Happy Valley Underground Stormwater Storage Scheme (HVUSSS) is under construction by Chun Wo Construction and Engineering Company Limited and supervised by the Drainage Projects Division of the Drainage Services Department, the Government of the HKSAR, supported by an Independent Geotechnical Engineer. The Scheme includes construction of a storage tank, which is located below the existing football pitches at Happy Valley. Phase One work including the southern portion of the scheme was constructed to a very tight programme. As a part of this work, temporary excavations supported by strutted sheet pile wall have been carried out in close proximity to sensitive structures. Soil-Structure Interaction modelling was conducted as a part of the design of temporary support for sheet pile wall. The project requires extensive geotechnical instruments monitoring with daily feedback to the Project Manager, Contractor, temporary works designer and the IGE. This paper presents the geotechnical challenges of the Excavation and Lateral Support works of the Phase One project (include 30,000 m^3 storage tank, pump house, box culvert, etc.) together with description of notable events during construction.

1 INTRODUCTION

Happy Valley was first developed as a race-course in 1846 on a piece of 'swampy land in a valley' and was 'often affected by floodwater.' The area around Happy Valley has long been prone to flooding problems. During the major rainstorms in August 2000, April 2006 and June 2008, severe flooding occurred in Happy Valley and adjacent areas including Sing Woo Road, Wong Nai Chung Road, Morrison Hill Road, Lap Tak Lane and the Happy Valley Racecourse and the Recreation Ground.

In this area drainage improvement by upgrading the existing major stormwater drains is disruptive and very difficult. It would involve open trenching in the busy main roads. To avoid serious disruption to the public and to minimize complicated diversion of the underground utilities, an underground storage tank was proposed.

The underground storage tank will temporarily store part of the stormwater collected from the upstream catchment. The addition of the storage tank would enable the drainage system to handle major rainstorm events effectively, thus minimizing flooding problems in the area. The stormwater will subsequently be discharged via pumps and gravity drains to the outfall once the stormwater flow volume in the existing drains has subsided.

The Contract was awarded to Chun Wo Construction & Engineering Co., Ltd. (Chun Wo) in September 2012 who submitted, and obtained approval for a cost-saving design with raft foundations and under-drainage system. The permanent and temporary works design is by Black & Veatch Hong Kong Limited (BV HK). This contract is one in the initial batch of Government contracts to use New Engineering Contract (NEC) instead of the traditional General Conditions of Contract (GCC). As a part of this contract, an Independent Geotechnical Engineer (IGE), ONLYgeotechnics Ltd, was appointed to provide advice and assistance to the Client, DSD, in their supervision and control with regard to geotechnical aspects of the contractor's work. To

ensure timely control and minimizing any damages during Excavation and Lateral Support works, geotechnical instruments monitoring was carried out with daily feedback to the Project Manager (the Engineer as referred in GCC), Contractor, temporary works designer and the IGE.

2 SITE LOCATION

The site is situated on the estuary area downstream of the Wong Nai Chung Valley (ERM, 2010). An old map, Figure 1, indicated that villages including Wong Nai Chung Village had been established on the valley upstream of the estuary area. The original swampy ground was infilled over 150 years ago to form the race course with filling probably sourced from the surrounding hills. The infield area of the race course was mainly used as a resting area for recreation and leisure, up to the present. As revealed in old maps and aerial photographs, there have been no significant earthworks within the infield area since then. Happy Valley Underground Stormwater Storage Scheme (HVUSSS) is located beneath the infield area (football pitches) in the centre of the Hong Kong Jockey Club's Happy Valley Racecourse – Figure 2.

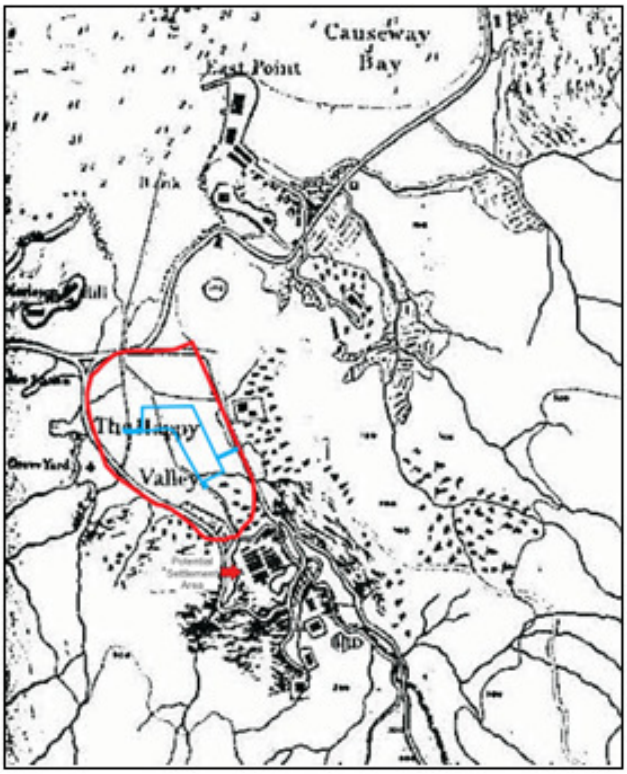

Figure 1: Old map of Happy Valley Area

3 THE SCHEME

The project (two phases) involves the construction of a 60,000 m^3 stormwater storage tank, an inlet structure, a twin cell box culvert and a movable crest overflow side-weir system, see Figure 2. It also includes the construction of a pump house with a discharge rate of 5,400m^3 per hour. At the southern end of the scheme, towards the hills, at the stilling basin, is a short length of hand-excavated tunnel which carries the new culvert. The culvert then passes under the race-course and through the centre of the football pitches area, and exits at the north western end of the race-course. The catchment area served by this scheme is about 130 hectares. The infield area of the Happy Valley Racecourse is the lowest spot in the area, therefore it provides an ideal location for the scheme from the hydraulic point of view.

The design calls for the use of a movable crest overflow side weir system incorporating supervisory control and data acquisition (SCADA) for real time monitoring of water levels at the existing drainage system and the

tidal levels at the outfall to control up and down movement of the weir automatically. This innovative and intelligent design would reduce the volume of the storage tank by 30% and save electricity consumption up to 60%. The pumping station will be remotely monitored and controlled, with outgoing data stream of water levels, status of pumps and penstocks, any equipment failure etc.

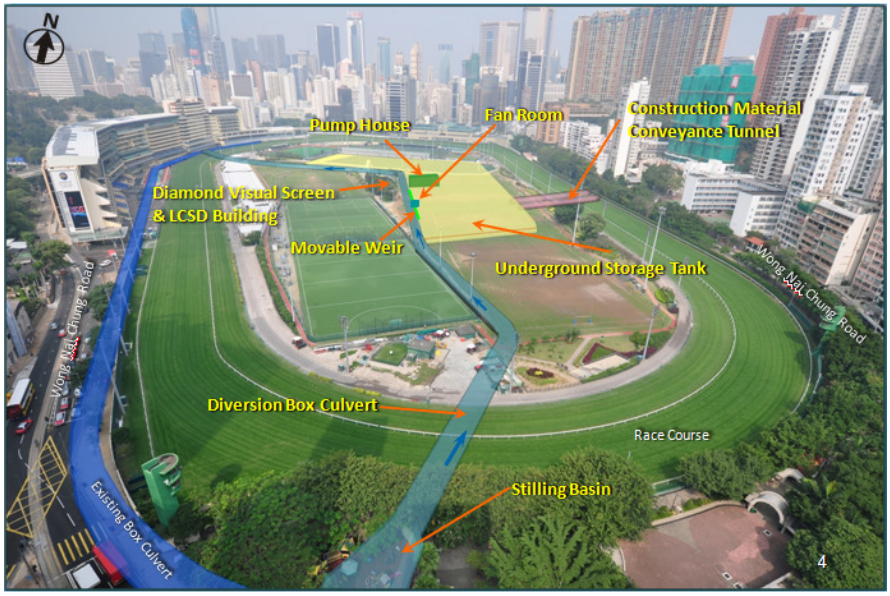

Figure 2: Key features of the HVUSS

4 DESIGN SCHEME

The original design for foundations of the scheme indicated that pre-bored H-piles socketed into bed rock would be required. Due to the lighter unit weight of the storage tank than that of the existing ground, the foundation was designed to be capable of resisting the buoyant force. The Contractor proposed a cost saving design using a raft foundation with subsoil drainage system including a cut-off wall (BV, 2012). The system would maintain groundwater level to below a limit by conveying any excess groundwater through a drainage blanket to be discharged or re-used. A series of groundwater monitoring points was installed along the perimeter of the storage tank within the groundwater cut-off wall. An array of pressure relief wells was constructed at the base slab of the storage tank as a part of emergency relief of any high groundwater pressure within the groundwater cut-off wall. This alternative design was agreed and adopted.

The storage tank itself is a large concrete structure, L-shaped in the overall layout plan as viewed from above, see Figure 3. The structure is some 7 metres deep. It is built in two phases according to the layout of the existing football pitches in order to maintain the use of some of the football pitches throughout the construction duration. The design allowed for soil cover of up to 800 mm thick on top of the storage tank for re-turfing works, which would enhance the resistance to the uplifting force.

The alignment for the stormwater culvert (Figure 3) runs parallel to the storage tank and lies between the "LCSD building" and the main excavation. The building is 2-storey LCSD changing rooms building for the users of the infield's sports facilities, with the large Diamond Vision Screen mounted on its roof. In order to minimize disturbances to nearby sensitive structures, the construction sequence required early completion of the stormwater culvert, before the start of the excavation for the adjacent storage tank. This would minimise the effect of the main excavation on ground movements at the LCSD building.

5 GROUND CONDITIONS

Ground investigations were conducted in the 1990's associated with development of the Hong Kong Jockey Club. Later, a two phased ground investigation was carried out in 2010 for USSS by DRILTECH comprising 36 drillholes, 1 trial pit, 30 inspection pits and 6 trial trenches and 8 GCO probes. A third phase of

investigation was undertaken following award of the contract to verify the design parameters for the cost saving design. This included an additional 10 boreholes and 10 Cone Penetration Tests (CPTs).

Overall the investigation showed the ground conditions comprise several metres of sandy clayey Fill underlain locally by Pond/Marine Deposits (soft clays) up to 5 metres thick. Below the soft clays is Alluvium of predominantly sandy silty CLAY but locally clayey silty SAND up to 17m thick. The underlying bedrock is Granite. Figure 4 is a summary of soil strata, and a section through the site is shown in Figure 5. Geotechnical properties of the strata are summarized in Figure 6.

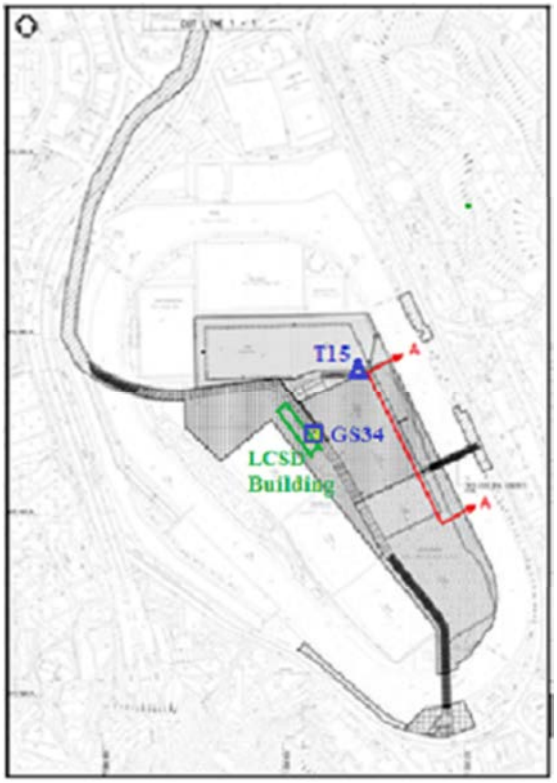

Figure 3: Underground Tank and Culvert Alignment

Soil Strata	Thickness (m)	Depth (mbgl)	Description / Remarks
Fill	1.0 – 3.3 (Paving: 3.6 – 5.0)	0.0 – 5.1	• Clayey silty SAND/Sandy clayey SILT
Alluvium (ALL)	8.6 – 16.5 (Clay: 0.5 – 5.5)	0.3 – 17.5 (Clay: 0.6 –14.5)	• Sandy silty CLAY/clayey silty SAND • Interbedded with MD/ED • Cobbles (up to 2.9m thick)
Marine Deposits/ Estuary Deposits (MD/ED)	1.0 – 5.2 (Clay: 1.0 – 4.5)	3.6 – 11.7 (Clay: 5.0 – 11.7)	• Soft to firm • Sandy silty CLAY/Clayey silty SAND/SAND
Saprolite & Corestone	9.9 – 51.6 (Corestone: 1.1 – 19.4)	11.1 – 64.3 (Corestone: 14.2 – 64.3)	Average depth of Corestone & IV/III Layer above bedrock ~ 4.3m (Based on relevant boreholes in Phase I)
Bedrock	Rockhead : -19.4mPD to -59.2mPD (22.5mbgl to 64.3mbgl)		Fault zone encountered locally at BH22 (43.2mbgl to 51.1mbgl)

Figure 4: Summary of Soil Strata Extracted from GEO (2012)

Review of the Phase I ground investigation results indicated that the superficial deposit comprises fill, pond deposit, estuary deposit, marine deposit, alluvium and colluvium. The fill layer is found in all drillholes and the trial pit/trial trenches with a maximum thickness of 4.20m in drillhole BH15, which composed mainly of clayey silty sand and sandy clayey silt with some angular gravel and occasional cobbles of rock fragments

materials. Alluvium is found in all drillholes with a maximum thickness of 16.20m in drillhole BH1, locally interbedded with pond deposit in BH3 and IBH2, interbedded with estuary deposit in BH6 to BH8, BH11 and IBH2 and interbedded with marine deposit in BH10 and IBH2, which composed mainly of sandy silty clay and clayey silty sand with gravel materials. Colluvium is found in drillhole BH4 only with a thickness of approximately 9.20m, which composed mainly of clayey silty sand with gravel materials. The distribution of subsoil strata is rather complex, hence in model simulation a large number of different strata has to be included and their thicknesses vary greatly in different vertical sections.

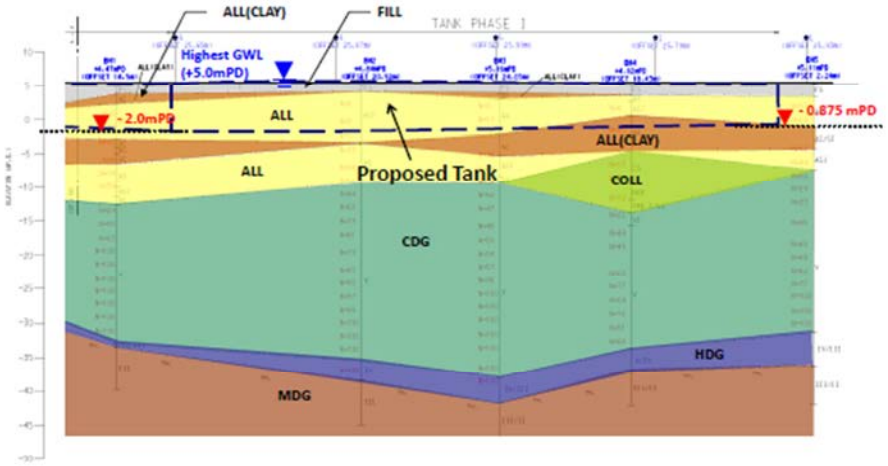

Figure 5: Ground Profile at Section A-A of Figure 3

Soil Strata	γ (kN/m^3)	c' (kPa)	ϕ' (deg)	S_u (kPa)	SPT-N	E' (MPa)	E_u (MPa)	k (field test) (m/s)	m_v (m^2/MN)	Cr	Cc
Fill	18	0	35	/	/	10	/	No Test	/	/	/
ALL	19	3	35	/	2 – 100	10, z≤5m 2z, z>5m	/	2.62 x 10^{-05} to 1.68 x 10^{-06}	/	/	/
ALL (Clay)	18	3	35	30 (17.5 – 51)	5 – 41	/	8, z≤5m Z+3, z>5m	1.77 x 10^{-05} to 1.74 x 10^{-07}	0.092 – 1.99	0.011 – 0.06 [0.029]	0.115 – 0.386 [0.211]
MD/ ED	18	1	32	20 (9 – 48.7)	/	/	9.45	1.73 x 10^{-06} to 1.79 x 10^{-08}	0.066 – 2.72	0.01 – 0.029 [0.018]	0.126 – 0.291 [0.199]
CDG/ HDG	19	5	37	/	8 – 100	6z-26, z>11m	/	1.18 x 10^{-04} to 1.38 x 10^{-07}	/	/	/

Figure 6: Geotechnical Properties of Various Soil Strata Extracted from GEO (2012)

Groundwater monitoring records show the highest level of groundwater to be close to ground level ~ +5mPD with a lower level at around +2.9mPD. The water table generally follows the ground profile which falls gently towards the north west.

6 SOIL-STRUCTURE INTERACTION MODELLING

As a part of the design for the Excavation and Lateral Support system, extensive Soil-Structure Interaction modelling was carried out. Two dimensional finite element analyses were conducted using the BD approved program PLAXIS version 9.02. Plane strain conditions are assumed. The analyses' results were used to assess the ground movements at and around the excavation face, the sheet pile and the nearby sensitive structures. Initial analyses were conducted from early 2013. Five vertical sections within the area under construction were analysed, see Table 1. The analysis for each of the sections was performed through all the construction stages (phases) relevant to section from start to finish in a step by step procedure. The number of

ground strata included in the analysis varied from 24 to 10 depending on the section considered. Additionally, relevant structural elements were also included, such as sheet pile wall, concrete walls and slabs of storage tank, box culvert and LCSD Building. The total numbers of construction stages, time steps, ground strata and structural elements for each of the sections analysed are presented in Table 1. Examples of the finite element grid used for Section 10-10 are shown in Figure 7 for the initial ground condition before construction work and in Figure 8 for near completion stage with strutted support to the sheet pile wall.

Table 1 Summary of the Sections for PLAXIS Analyses Carried Out Initially

Section No.	Total Construction Stages	Total time steps	Ground Strata[1]	Structural Elements[2]
8-8	37	717	24	14
10-10	23	343	19	12
11-11	25	304	22	10
12-12	24	634	24	10
X	15	303	10	2

Note 1. Ground strata such as Marine Clay, Alluvial Clay, CDG each has assigned engineering properties such as unit weight, permeability, Young's Modulus, etc.
Note 2. Structural elements such as sheet pile wall, concrete walls and slabs of storage tank, box culvert, LCSD Building, etc and elements acting as anchors.

For finite element analysis, the important values of Young Modulus for soils were derived from relevant considerations including initial values from early studies (Figure 6) and those estimated from later investigation as a part of the design including CPT results for soil layers above CDG and SPT "N" values from the tests on CDG and HDG layers. It is generally recognized that the Young's Modulus for unloading and reloading could be much higher than that for the virgin loading. In the ground movement analysis, the Young's Moduli for soil within the excavated area of the storage tank, where effective stress would be reduced, were taken to be 2 times the respective virgin moduli (unloading & reloading E' = 2 x virgin E). However, for determination of member forces and moments for structural design (under ULS) the virgin values were used.

Supplementary PLAXIS simulation was carried out and reported in early 2014 after initial part of the work has been done. This is to take account of the agreed change in the strut support arrangement in view of the much smaller measured ground movements than expected. This included further analyses on Sections 10-10, 11-11 and 12-12.

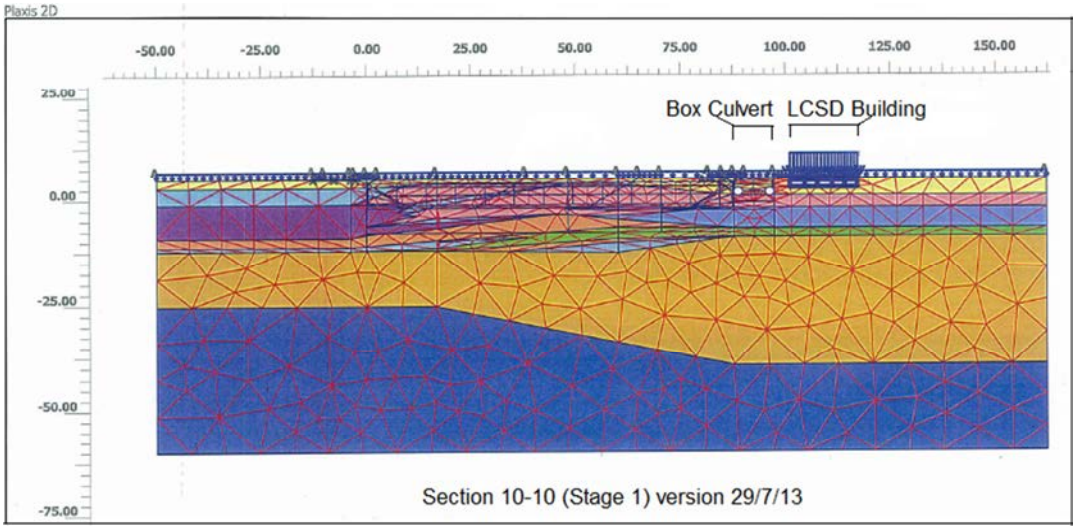

Figure 7: The PLAXIS Finite Element Grid for the Ground Before Excavation

The total ground settlement around an excavation comprises two part, settlement due to wall deflection and that due to groundwater drawdown. PLAXIS analysis was able to simulate the wall deflection and the associated ground settlement as well as the groundwater drawdown and the related settlement. For the area around the LCSD Building the results from PLAXIS for the maximum total ground settlement is 26 mm. The maximum estimated at the most critical high mast for lighting (out of the 10 masts) is about 22 mm. The range of possible maximum settlements at the edge of race track was estimated to be from 5 to 14 mm. For 10 m wide zone surrounding the outside of the sheet pile cut-off wall, the estimated ground settlement is more than 25 mm. Part of the jogging path and part of paved area at the east of the LCSD Building are in this zone and could be affected. It is considered that the impact to the race track and the area east of LCSD Building are much less critical than the impact to LCSD Building itself and the high masts.

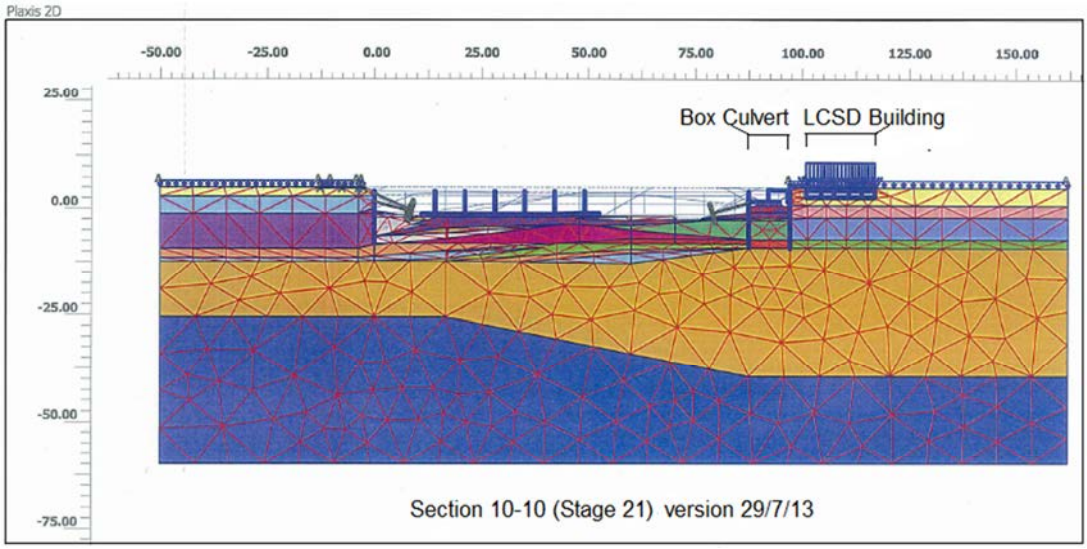

Figure 8: The PLAXIS Finite Element Grid for the Excavated Ground with Strutted Support (Stage 21)

It is considered that the results from PLAXIS simulation are within the settlement limit generally adopted for settlement control at or near structures. Therefore the Action Level was set at 25 mm, with Alarm and Alert Levels set at 20 and 10 mm respectively.

7 GEOTECHNICAL CHALLENGES

The construction works started from September 2012, and reached substantial completion of Phase One by March 2015. The works commenced with construction of the pump house followed by excavation for the storage tank. As the excavation progressed, temporary support is provided by installation of sheet piles using a "silent piler" to minimize any noise impact to the public in the vicinity. Thickness of the soft layer is critical in the control of movements during the work, and the thickness contour is shown in Figure 9. The progress of work up to May 2014 is illustrated in Figure 10.

The cost saving design requires the sheetpile wall around the storage tank to act as groundwater cut-off wall as a part of permanent work to minimize the water pressure under the tank. The sheetpile wall has to perform this function well or else there could be a high uplift force, nevertheless there is a contingency measure for such an event by activating the relief wells. Pumping test for demonstrating water tightness of the sheetpile wall was conducted. Although some seepage was observed from the sheetpile wall, the amount is considered small and well below the limit allowed for in the design.

The design also requires excavation of about 7 metres of the superficial deposits, with much of it below the level of the ground water table. The LCSD building with Diamond Vision Screen on top, and the high mast supporting the flood lighting (> 20 m high) are both quite close to the excavation. According to ArchSD as-built drawings, the building is founded on a raft footing, a hollow box structure embedded about 1.6m below ground (BV, 2012). The hollow box reduced the load on the soil strata below. The high mast (visible in

Figure 12) poses a particular challenge. It is founded on shallow spread footing, size 4.3m x 4.3 m at about 1.6 m depth, and only a few metres from the excavation. Local softening due to heavy rain exacerbated the potential movement and will be discussed later. The challenge for the construction was to have adequate excavation support system, with control on construction sequence, and continuous monitoring / alert system for on-going detection of any excessive movement and timely remedial action.

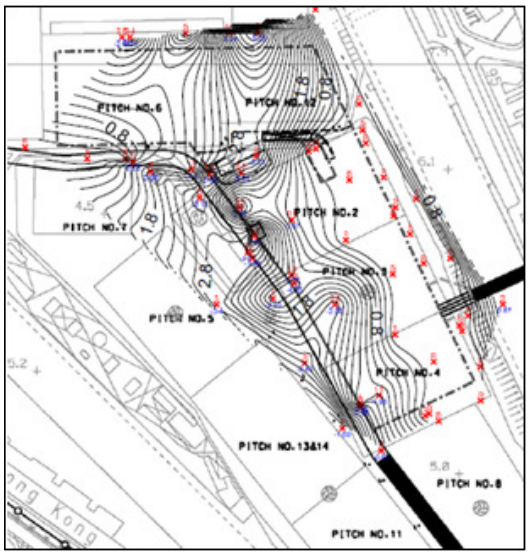

Figure 9: Contours of Soft Deposits

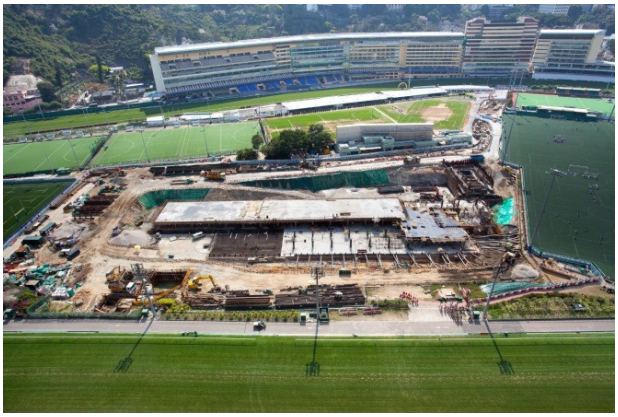

Figure 10: Phase One Construction in Progress May 2014

The design of the Excavation and Lateral Support is a typical arrangement with multiple struts required as excavation proceeds. One of the particular challenges arose at the sheet pile wall immediately in front of the LCSD building. This is the most sensitive area but made more complex because of the location of the box culvert between the storage tank and the building. Programme requirements dictated early construction of the box culvert between the pair of sheet piles shown in Figure 11. The design indicated that some movement of the LCSD building and area to the east of the building would occur during trenching and installation of the box culvert and this movement would be further developed during excavation for the adjacent stormwater storage tank. As a cost-effective alternative for extensive ground treatment works, pre-loading of the struts was introduced to mitigate the predicted movement of the building. The lateral support work in progress is shown in Figure 10.

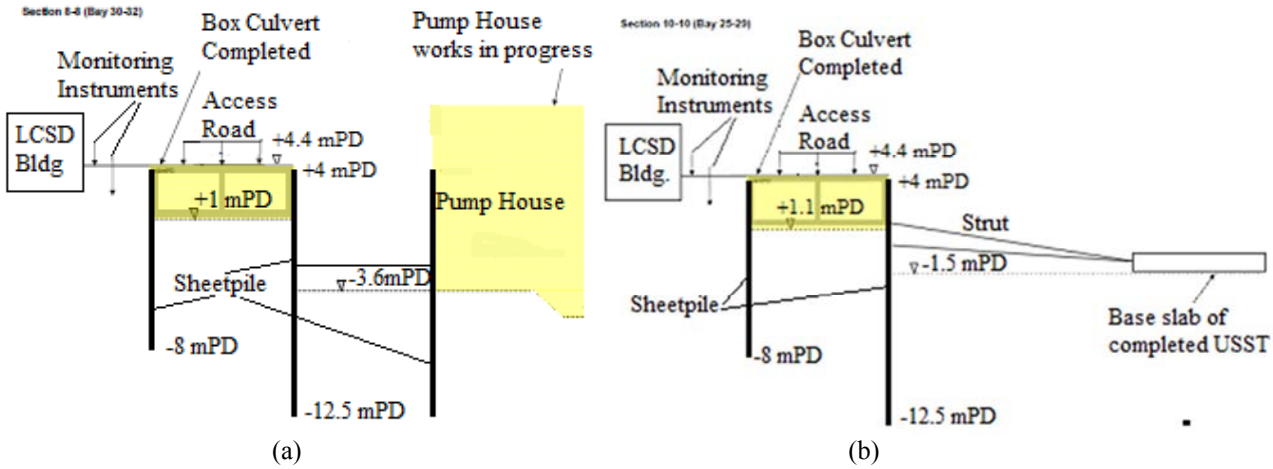

Figure 11: The Arrangement for Excavation and Support in Two Areas

8 INSTRUMENTATION AND MONITORING

Assessment of the results from the finite element modelling could be made by comparing the results with the measured movements from instrument monitoring including those on sensitive facilities located close to the race course compound. This was done based on the monitoring report of cumulative readings of all instruments up to the end of February 2015. For ground settlement, it is mostly below Action Level of 25 mm, with only about 10% of ground settlement markers (19/189) having settlement readings exceeded the level. The percentage is also relatively low, about 18%, for building settlement markers (12/68), and 5% for tilt markers (4/83). Most other readings show little movements. Apart from SSI modelling, other factors during construction have to be taken account of, such as the mis-match in the sequences of excavation work and lateral support work, and heavy rainfall at vulnerable stages of work. For the exceedance cases, all parties were aware and take appropriate actions since after Alert Level has been reached. Some minor damages such as cracked paving and surface drainage channels did occur and were immediately rectified but no major damages were observed. Two cases of exceedance are presented below to show the geotechnical challenges encountered in actual construction work.

Figure 12: Excavation and Lateral Support Woks in Progress

The contour plan in Figure 9 shows the clay is up to 3 metres thick below the building. The LCSD building is on a spread raft foundation with the existence of soft clay layer below it. Geotechnical instruments installed around LCSD Building are summarized in Table 2.

In the area near LCSD Building, up to 4mm of ground settlement was recorded on by October 2013 due to nearby excavation for the box culvert. Settlement continued but gradually reduced, stabilizing from end of 2013 to June 2014, see Figure 15(a) for ground settlement marker GS34, the location of which is shown in Figures 3 & 13. This marker is located near a surface u-channel in the area east of LCSD Building. Starting from July 2014 substantial settlement occurred and progressed at a high rate concurrent with the rapid excavation in the area, while strutting support work was not yet catching up. The settlement also appeared to be accelerated at times of heavy rainfall. High ground settlement (26mm) in this area is anticipated according to PLAXIS results discussed earlier. During this period, the building settlement markers at LCSD Buildings recorded fairly uniform settlements along the edge parallel to the excavation indicating very small tilting and distortion of the building. Immediate response to readings included increasing the monitoring rate, reviewing the construction sequence and immediately repairing gaps between the LCSD building and the adjacent ground to avoid water ingress. It became apparent during the review that the building itself was not subject to significant movement but that adjacent channels at ground level had moved during excavation. This movement was not critical to the building and was resolved by an adjustment to the construction sequence.

Table 2 Summary of Instrumentation around LCSD Building

Instruments	Purpose	Ground Level, mPD
Ground Settlement Marker		
GS33 – GS41 (10 Nos.)	To monitor the ground settlement around LCSD Building	+4.371 - +4.796
Building Settlement Marker		
BS1 – BS15A(15 Nos.)	To monitor the building deformation/tilting	+4.862 - +6.530
Inclinometer		
IN8 - IN9	To monitor the deformation profile inside soils	+4.362 - +4.450
Piezometer		
SP4	To monitor the ground water level and pore water pressure around the LCSD building	+4.45
Extensometer		
E1 - E2	To monitor the deformation between soil layers	+4.473 - +4.535
Tilt Marker		
T9 – T20	To monitor LCSD light mast	-

The teams involved were alerted to the situation and the increased observation and rectification of existing facilities and newly built structures (e.g. box culvert) were carried out. No significant damage was observed on the newly built structures and the LCSD building while there was localised damage to the drainage channel near the building. The settlement stabilized by the end of August and during September 2014, as the full strut supporting work was completed. There have been no significant settlements since September 2014. The progress and magnitude of ground settlements around the LCSD Building (see also Figure 14) at three settlement markers can be seen in Figure 15(a).

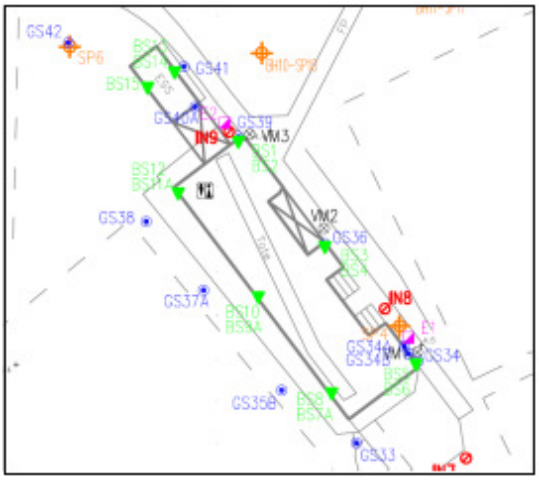

Figure 13: Instruments around LCSD Building

Figure 14: The Diamond Visual Screen on top of LCSD Changing Rooms Building

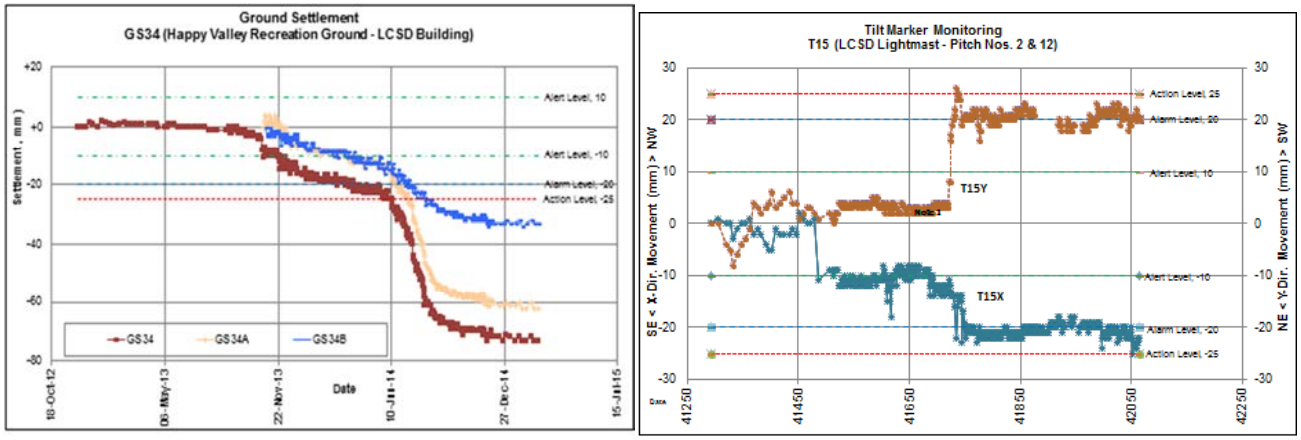

(a) (b)

Figure 15: Monitoring Results (a) Ground Settlement at LCSD Building (b) Tilt Marker at the High Lighting Mast

Close attention was paid to the high mast for lighting T15 as it is located near the construction area as shown in Figure 3. The data from the reading of tilt marker T15 are shown in Figure 15(b). The tilt marker T15 is of the type recommended by GEO (2012) with a vertical distance of 5 m between the two marker-points. The location of T15 is indicated in Figure 3. The first significant movement of about 12 mm occurred in August 2013, related to the excavation for underground storage tank, possibly also included unknown measurement anomaly due to the change in monitoring team at the time. Responses to rainfall events similar to that at GS34 were also observed for T15. The most significant movement of up to 20 mm was observed in April 2014 during the construction work of the storage tank in the vicinity. The relevant teams were alerted and prompt attention and collaboration was initiated. The movements were quickly stabilized within about a month (Figure 15 (b)) at the completion of base slab of the tank and the lateral support system nearby.

The construction of HVUSSS is well on the way to completion on schedule for both Phases One and Two.

9 CONCLUSIONS

An innovative project to alleviate the serious flooding problems in Wan Chai – Happy Valley area is in progress with Phase One substantially completed. Temporary excavations had been carried out in close proximity to existing sensitive structures. A plan of continuous monitoring and construction control has been implemented from the start within the frame work of the newly introduced NEC Conditions of Contract. The monitoring and control work has been well conducted with effective co-operation among the Project Manager, Contractor, Temporary Works Designer and the Independent Geotechnical Engineer (IGE). Analyses to determine ground movement, using PLAXIS finite element simulation as a Soil-Structure Interaction modelling, was carried out from the design stage and well into the construction stage so that adjustments can be made for the modelling to be more representative of the actual conditions. The simulation results compared with the actual measured movements showed that only 5% to 18% of all instrumented locations have readings exceeding the maximum limit specified. Two exceedance cases are described. They showed that compliance with the designed construction sequences in all stages is important in reducing any potential problems during the work. The presented cases illustrate the vital role and effectiveness of continuous instrument monitoring and reporting in the control and management of geotechnical works, so that any possible problems are detected early and prompt co-ordination of actions can be carried out to prevent more serious problems from occurring.

ACKNOWLEDGEMENTS

This paper is published with the permission of Drainage Services Department, the Government of the Hong Kong Special Administrative Region (HKSAR).

REFERENCES

BV(2012), Happy Valley Underground Stormwater Storage Scheme Innovative Design Enhancement, No. 382903/B&V/GDR/001, Dec 2012, Black & Veath Hong Kong Ltd., produced for Chun Wo Construction & Engineering Co. Ltd.

ERM (2010), Archaeological Impact Assessment for Happy Valley Underground Stormwater Storage Scheme – Phase A – Desktop Research Report, Ref.0122176, Nov 2010, Environmental Resources Management, produced for DSD

GEO (2012), Item No. 160CD Happy Valley Underground Stormwater Storage Scheme (HVUSSS) Foundation Design, ADR 5/2012, Aug 2012, Geotechnical Engineering Office, produced for DSD.

Recent Experiences of Numerical Prediction & Assessment – Excavation over a Tunnel of Unbolted Segmental Tunnel Lining

J.B. Wang & L. Swann
Jacobs (China) limited

S. Reynolds
Jacobs (UK) limited

ABSTRACT

A 700 m long Grade Separated Road (GSR) was proposed to link the new Terminals and on to a new set of remote stands at an Airport in UK. Construction of the GSR involved excavation adjacent to and over the existing live underground tunnels. The excavation had a depth upto 11m, and was only 6m above the crown of existing tunnel. To investigate the impacts on the unbolted concrete segmental tunnel lining from the proposed GSR work, a 3D model together with a series of 2D models were developed considering the site history and construction sequences proposed. Both short and long term behaviour of the existing underground tunnels during and after the GSR construction was investigated, showing the proposed GSR construction method was a viable solution to minimise the impacts on the existing tunnels.

1 INTRODUCTION

As part of the airport development, a Grade Separated Road (GSR) is proposed to link new Terminals and on to a new set of remote stands. The road has an overall length of 700 m and comprises two taxilane underpasses to avoid conflict between road vehicles and aircraft. Construction of the proposed GSR involves the installation of embedded secant pile retaining walls, casting bridge decks across the underpass sections, and subsequent excavation within the walls to depths of up to 11m with temporary propping, in places, to reach formation level for casting the base slab.

The GSR passes over and runs sub-parallel to the existing underground tunnels which were built in the 1970s using an unbolted concrete segmental tunnel lining. The excavation for the GSR, over and adjacent to the live tunnels, causes great concern over safe operation of the trains. ELS scheme was developed to limit the impacts on the existing tunnels associated with the GSR construction consisting of installing 900mm diameter secant pile walls as temporary retaining walls during the excavation stage and also as permanent retaining walls for the GSR.

FEM 2D software Plaxis 2-D Numerical analyses were carried out at selected critical sections to estimate the associated ground movements and to assess the impacts to the underground line. The Plaxis 2D was adopted at locations where excavation is along / parallel to the existing tunnels, hence a plain strain condition is generally applicable. A 3Dmodel was established to investigate the impacts where the proposed GSR crosses over the existing tunnels at a skew direction. In addition, a Plaxis 2D analysis was also performed at the 3D region to illustrate the inaccuracy of 2D analysis for solving such 3D problem. The 3D model was analysed using 3D software FLAC ^{3D} which adopts finite difference method for its lower computation memory demand.

This paper presents the case study from the numerical modelling aspect, concentrating on the 3-D analysis in particular. Compared with 2-D analysis, the benefits of the 3-D modelling for prediction with higher accuracy are highlighted.

2 SITE AND GROUND CONDITIONS

Ground conditions at the site, comprise Made Ground, underlain by River Terrace Deposits overlying London Clay. The existing ground level is generally flat, approximately at 23.1 m AOD. Groundwater levels recorded on site were typically at 3m below ground level.

The Made Ground is relatively thin having a thickness of 0.8m to 1.6m, and is generally described as medium dense silty sand with a base level at 21.65 to 22.25 m AOD. The thickness of the River Terrace Deposits varied between 3.5 m and 4.7 m, and are described as medium dense to very dense sandy gravel with occasional cobbles. London Clay has typically been described as firm to stiff, grey extremely closely to closely fissured clay with occasional silt laminate and partings and occasional medium sand to fine gravel size shell fragments and is heavily overconsolidated. The ground conditions on site are illustrated below:

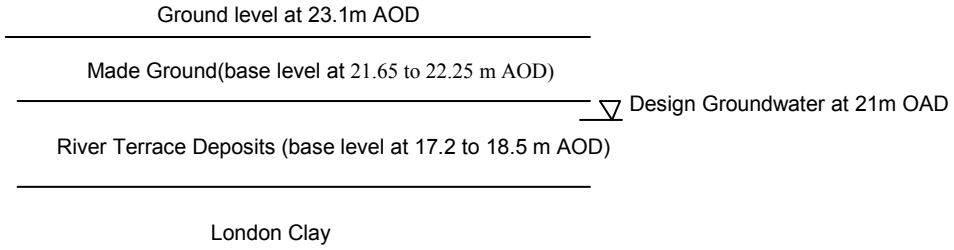

The GSR is about 700 m in length and 12 m wide, lying above the existing live tunnels. The GSR ramp crosses over the tunnels at an angle of 57 degrees and then runs approximately parallel to the tunnels with a minimum 4.3 m spacing. At the crossing area, the GSR ramp is about 3 m deep and is approximately 8 m above the tunnels. The depth of the GSR increases to about 8 m at the down ramp near the proposed left taxilane underpass. The internal diameter of the Piccadilly Line tunnels is 3.81 m, formed by 22 numbers of precast concrete segments. The tunnel rings are approximately 0.6 m long and 152.5 mm thick. Airbus A380 / Boeing 747 aircraft loading of total 9000 kN is considered in the design of the bridge and retaining walls.

3 METHOD AND SEQUENCE OF CONSTRUCTION

It is proposed that the excavation for the GSR be supported by secant pile walls and that the secant pile walls will also form the permanent walls of the GSR. The secant piles above the tunnels will terminate at approximately 6 m above the tunnels and the piles shall also be a minimum of 3 m away from the tunnel structure as required by the tunnel exclusion zone.

One to two layers of temporary props are proposed to support the secant pile walls during GSR construction. At the underpass area, with a bridge deck at the top, no props are proposed during excavation. Construction of the GSR shall adopt top-down method under the bridge deck and bottom-up construction sequence for other parts. The typical construction sequence using bottom up sequence for the GSR sections outside the Taxilane Underpass is presented below:

(1) Install secant piles
(2) Excavate to 0.5m below bridge deck
(3) Install /casting bridge deck
(4) Excavate to final excavation level
(5) Cast base slab and skin walls and connect it with the secant pile walls

4 3-D NUMERICAL MODELLING

Excavation for the construction of the GSR will change the stresses and induce ground movement around the existing tunnels. The western ramp of the GSR crosses over the existing tunnels at a skew, which requires a more sophisticated study on the likely impacts on the existing tunnels. A three-dimensional numerical model was developed and analysed with Finite difference software FLAC ^{3D} version 3.1.

4.1 Modelling domain and boundary conditions

The 3D model developed is a rectangular block of 102 m long x 100 m wide x 63 m deep comprising a total of around 60,000 soil zones. A general view of the domain is presented in Figures 1 & 2 below.

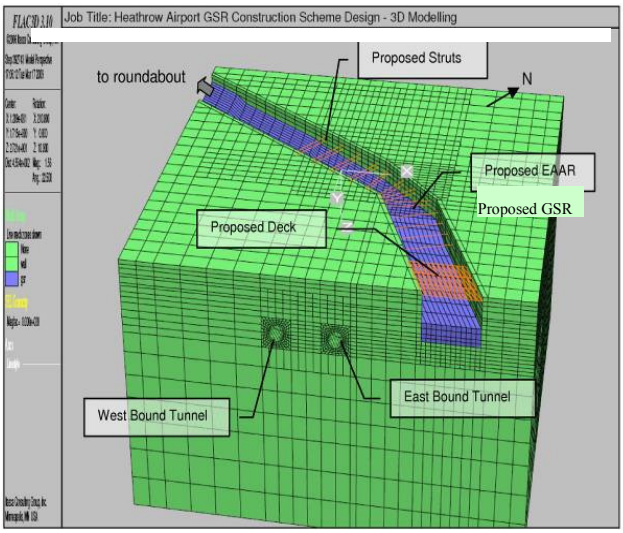

Figure 1: General View of FLAC ^{3D} Model

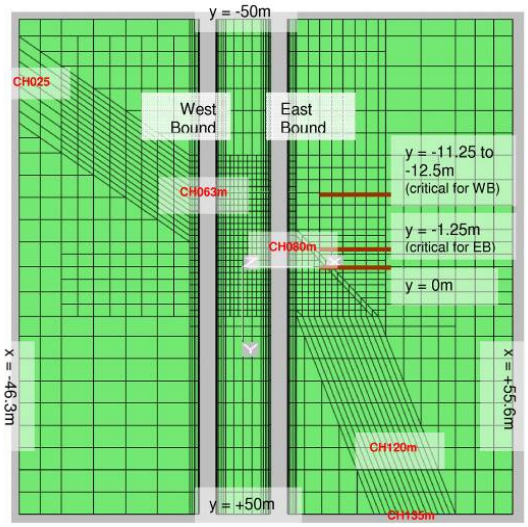

Figure 2: Plan View at 13.9 mbgl

The model simulates the western portion of the proposed GSR which runs above the existing twin tunnels at an acute angle, between chainage of 25 m and 135 m as shown in Figure 2. A 100 m length of the twin tunnels are covered in the model, running parallel to the y-axis from y = -50 m to y = +50 m.

For the four vertical external boundaries, horizontal movement perpendicular to the plane is restricted while movement in the plane of the vertical boundary is allowed. The vertical movement is not permitted at the base boundary of the 3D model.

4.2 Soil elements and soil properties in the model

The ground under consideration comprises London Clay overlain by Made Ground (MG) and River Terrace Deposit (RTD). The ground model has been simplified to combine the thin layer of MG and RTD into a single stratum of drained soil in the 3D model since the thin layer MG has similar granular material properties to the RTD. A constitutive model of liner elastic perfectly-plastic with Mohr-Coulomb failure criterion was adopted for the Made Ground and the River Terrace Deposit. The nonlinear elastic properties of the London Clay shows a strong dependency of the soil stiffness on the strain levels experienced, i.e. higher stiffness at lower strains. The nonlinear tangent elastic properties of the London Clay can be described by the following equations, given by Jardine et al (1986):

$$E_u = c_u \left\{ A + B\cos\left(\alpha I^{\gamma}\right) - \frac{B\alpha\gamma I^{\gamma-1}}{\ln(10)}\sin\left(\alpha I^{\gamma}\right) \right\} \quad (1)$$

where:

c_u = undrained shear strength , $I = \log_{10}(\varepsilon_\alpha / C)$, A, B, C, α, γ = material-specific constants,

$\varepsilon_a = \frac{\sqrt{2}}{3}\left\{(\varepsilon_1-\varepsilon_2)^2+(\varepsilon_2-\varepsilon_3)^2+(\varepsilon_3-\varepsilon_1)^2\right\}^{0.5}$, ε_1 , ε_2, ε_3 = principal strains (or principal deviatoric strains)

The soil parameters adopted in the 3D model are summarized in Tables 4.1 and 4.2 below:

Table 4.1: Soil Parameters

Soil Type	γ (kN/m^3)	υ' / υ	k_o	c' /c_u (kPa)	ϕ' (°)	E' (kPa)	k (m/s)
Made Ground & River Terrace Deposits	20	0.2	0 – 5.5mbgl: 0.4	0	36	37,500	2 x 10^{-4}
London Clay	20	0.49	5.50 – 11.25mbgl: 2.6 11.25 – 31.75mbgl: 2.2 31.75 – 63.00mbgl: 1.2	Increase with depth (86 kPa at London Clay top	-	-	2 x 10^{-9}

Table 4.2: Jardine Model Parameters for London Clay

A	B	C (%)	α	γ	ε_{min} (%)	ε_{max} (%)
1350	1350	0.001	1.319146	0.66336	0.0011	0.3

4.3 Tunnel lining in the model

The existing tunnel lining comprises 22 unbolted pre-cast concrete segments with a ring length of 600mm. Since it is impractical and unnecessary to build a 3D model with those lining segments modelled precisely, an "equivalent stiffness method" by Muir Wood (1975) is adopted, which suggests:

$$I_e = I_{joint} + (4 / n)^2 \, x \, I_{segment} \quad (2)$$

Where:
I_e = equivalent moment of inertia for a continuous "liner" element in model,
I_{joint} = moment of inertia of joints between lining segments (= 0 if no structural connection),
$I_{segment}$ = moment of inertia of segments,
n = number of segments (n = 22 in current case)

The tunnel lining were modelled as a liner structure element in the FLAC ^{3D} model that can take the tunnel hoop stress, bending moment and shear stress and also friction between the soil and the tunnel lining. The secant pile wall and base slab of the GSR were also modeled as liner structure elements, having isotropic linear elastic properties of the concrete material. Beam structure elements were adopted for the struts modelling.

4.4 Proposed works and modelling sequence

(a) Establishing initial conditions

To establish the existing conditions of the ground and the existing underground structures, the 3-D model was set up to include the major construction history of the existing tunnels including the construction year and tunnel face volume loss during tunnelling. The West Bound (WB) Tunnel was constructed first and then East Bound (EB) Tunnel. The tunnel face volume loss was simulated by excavating the tunnel area allowing a 2% volume loss in term of tunnel cross-sectional area. Tunnel lining is then installed to support soil stresses around.

The tunnel construction stage is followed by long-term consolidation in which any excess pore pressure generated due to tunnel excavation would be fully dissipated, assuming a permeable tunnel lining. After full consolidation, present (or existing) condition of the domain has been arrived at. All displacement vectors are then set to zero before commencement of the proposed works.

(b) Modelling of construction Sequence

The excavation and GSR construction are designed to be carried out in 3 bays. Subsequent to the installation of secant pile wall which is assumed as "wished-in-place", excavation to 1mbgl and installation of the first layer of 711 x 14 CHS struts and bridge deck are modelled. Construction of the GSR is then carried out bay by bay in three stages as shown in Figure 3. Further excavation, installation of second layer of 711 x 14 CHS struts and casting of base slab in one bay would then be completed, before a similar operation for the next bay.

Upon completion of base slab construction for the Bay 3, all struts would be removed. Construction of the airfield pavement would then be modelled. Finally, a long-term consolidation is then carried out. The construction stages modelled are detailed in Section 3.

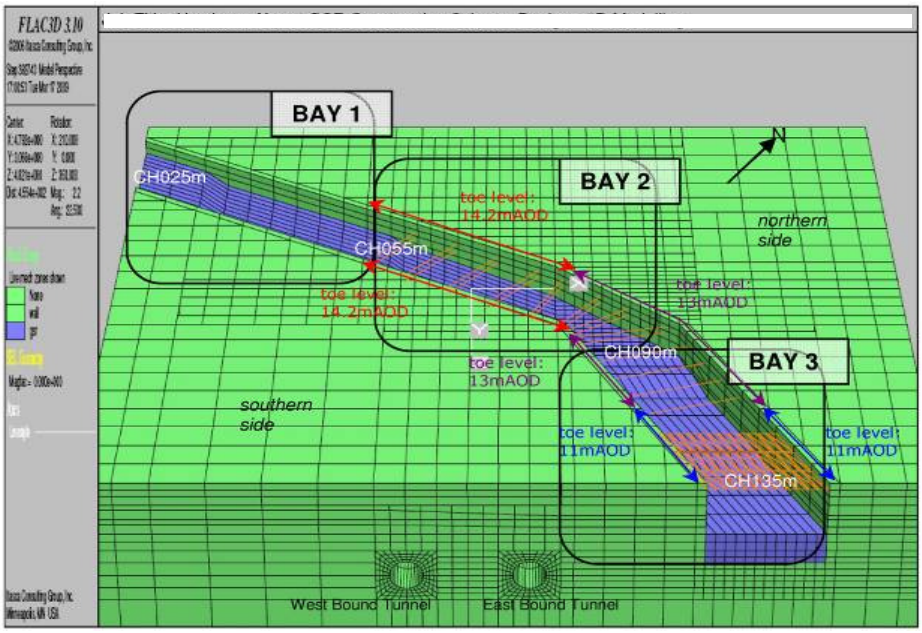

Figure 3: 3-bay Construction in FLAC ^{3D} Model

5 RESULTS AND DISCUSSIONS

5.1 Predicted tunnel movement

Long term ground movement in a horizontal plane is presented in Figure 4 below. It can be observed that the line of zero transverse (in x-direction, see Figure 4) ground movement vector generally matches the centreline of GSR. The ground heave effect including ground movement towards the excavation from both sides is illustrated in Figure 5 below.

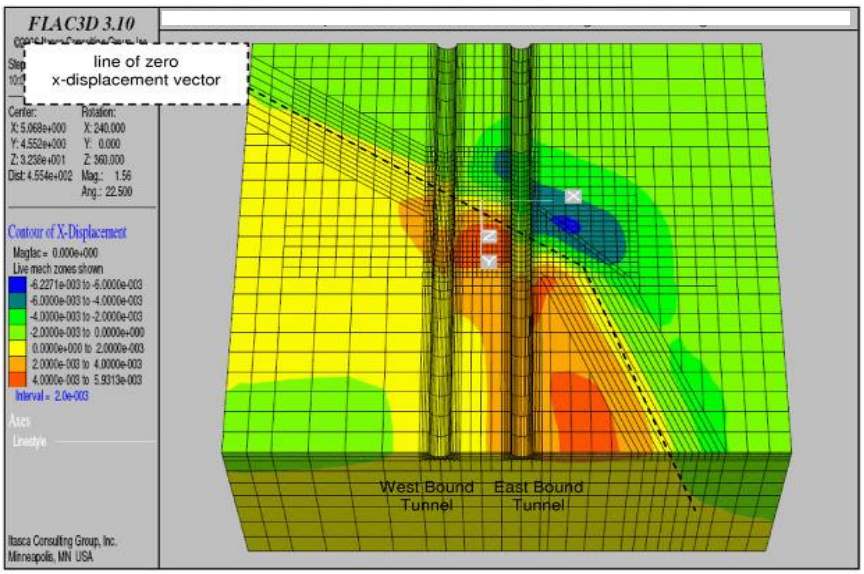

Figure 4: Contours of Transverse Ground Movement in Horizontal Plane

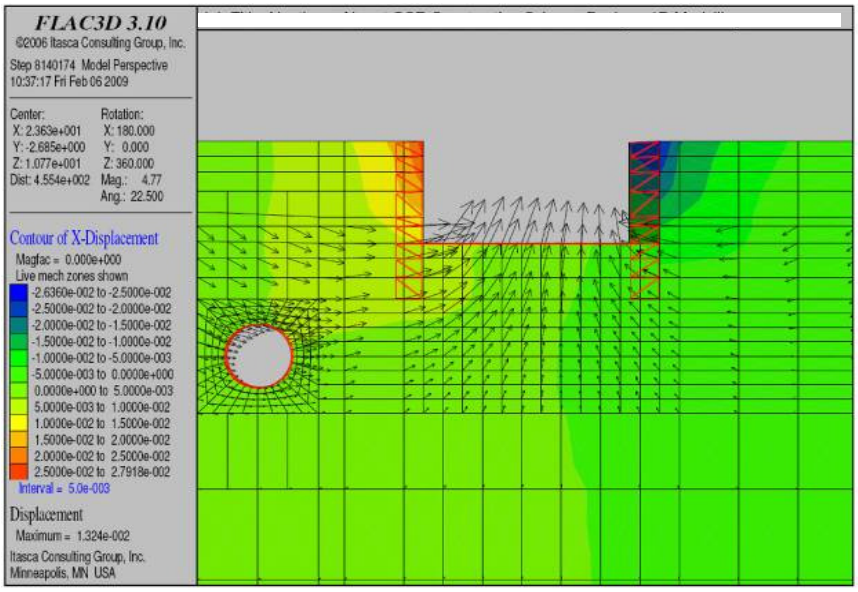

Figure 5: Typical Ground Movement Vector below Proposed GSR

(a) Eastbound tunnel

The predicted maximum tunnel lining deformation of the crown and invert along the longitudinal direction for the EB Tunnel is given in Figure 6. The tunnel lining deforms in a similar way to the surrounding ground. Maximum deformation of the tunnel lining occurs at the area where the proposed GSR runs across the EB Tunnel. It experiences an upward movement of around 8.5 mm and 1.8 mm at the crown and invert respectively at this critical location, inducing a differential vertical movement of approximately 6.6 mm (moving apart). It is also worthwhile to notice that such maximum deformation occurs at the end of excavation to the final excavation level in Bay 2, when the excavation is directly above the tunnel.

The predicted tunnel lining deformation of the critical section for the EB Tunnel is plotted in Figure 7. The tunnel is squeezed by approximately 4.8 mm at the end of excavation to final excavation level in Bay 2.

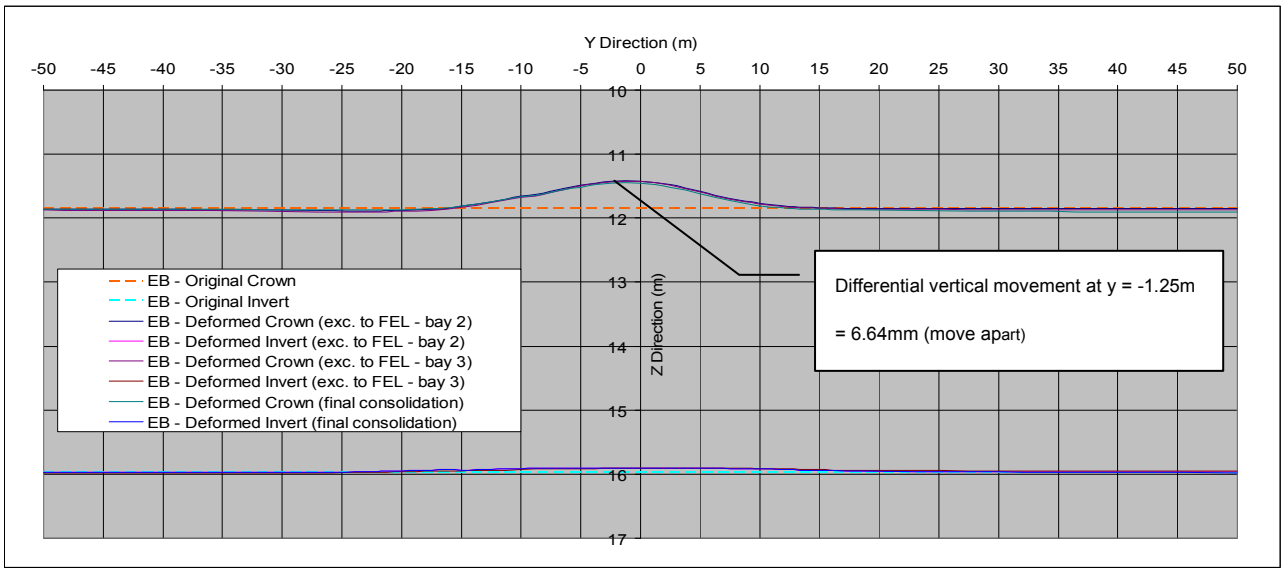

Figure 6: Predicted Lining Deformation along EB Tunnel (exaggerated by 50 times)

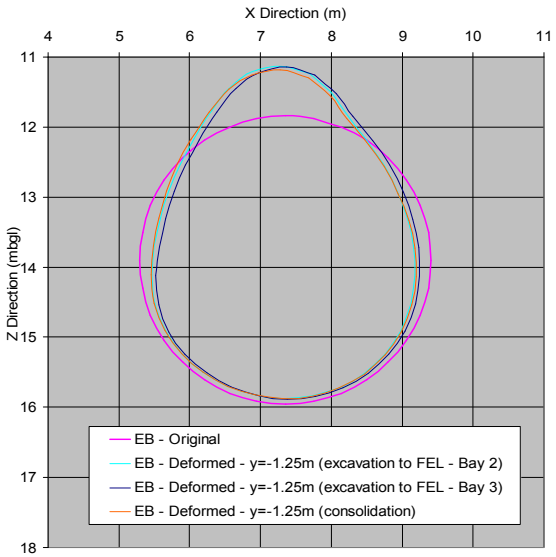

Figure 7: Predicted Transverse Lining Deformation (exaggerated by 100 times)

(b) Westbound tunnel

Maximum lining deformation of 4.1 mm and 1.4 mm are predicted respectively at the crown and invert along the longitudinal direction for the WB Tunnel, inducing a differential vertical movement of about 2.7 mm (moving apart). Again, the maximum deformation occurs at the end of the excavation to the final excavation level in Bay 2, when the excavation is directly above the tunnel. The predicted maximum differential horizontal movements of the tunnel lining side walls is 1.9 mm with a maximum lateral movement of 2 mm occurring at the eastern side wall of the tunnel after excavation to final level in Bay 2.

5.2 Predicted tunnel lining forces

The predicted bending moment of the tunnel lining in the transverse (hoop) direction after excavation completion remains small throughout the GSR construction as expected. The hoop force of the tunnel lining is reduced slightly after GSR excavation, from average 403 kN/m of the tunnel lining compression at the existing condition down to average of 397 kN/m. Therefore the overall structural force change of the existing tunnels associated with the proposed GSR construction is expected to be small.

5.3 Predicted long term behaviour

Figure 8(a) below presents the contours of total pore pressure along critical section (i.e. y = -1.25m) at the end of proposed construction. Negative excess pore pressure is developed in London Clay due to clay swelling upon unloading in the undrained condition.

Subsequent to completion of all proposed construction activities in the model, consolidation is carried out for long term behavior. Excess pore pressure generated in previous construction stages would be dissipated within around 10 years time. Contours of total pore pressure at the end of full consolidation are given in Figure 8(b).

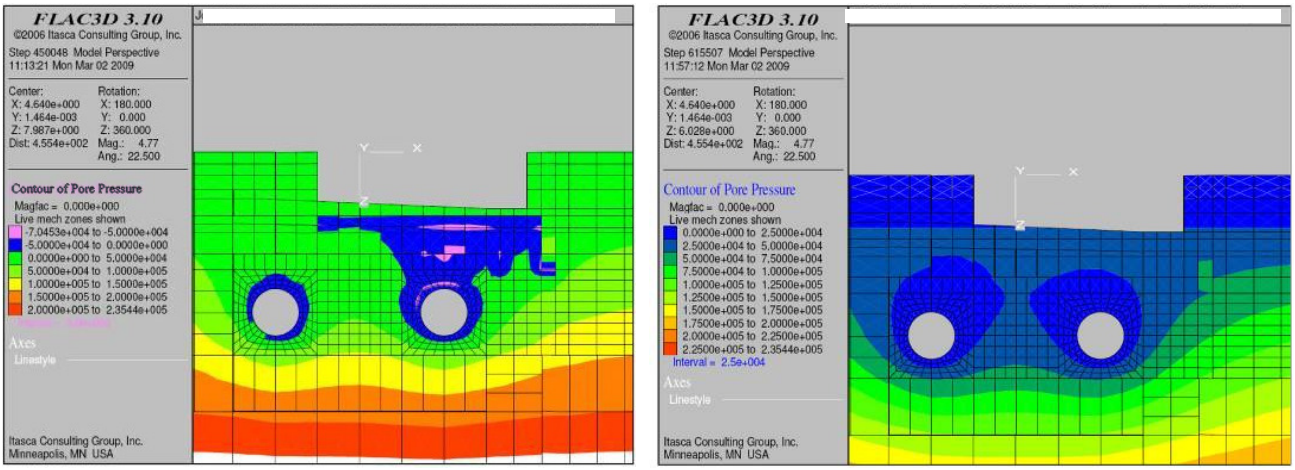

(a) End of GSR Construction (b) Long Term Consolidation

Figure 8: Predicted Total Pore Pressure Distribution at Different Stages

Figure 9 below shows a development of the lateral movements of the secant-pile wall at various locations during and after GSR construction. The restraining effects on the wall deflection from the bridge deck of the taxilane underpass are shown in the Figure 9. The predicted wall top deflection at the end of excavation from 3D modelling is similar at various locations as indicated in Figure 9 (a). However, the long term wall top deflection developed from less than 2mm at the decking area, to around 9.5 mm and 22 mm respectively at 4.5 m and 13 m away from the underpass decking (see Figure 9(b)).

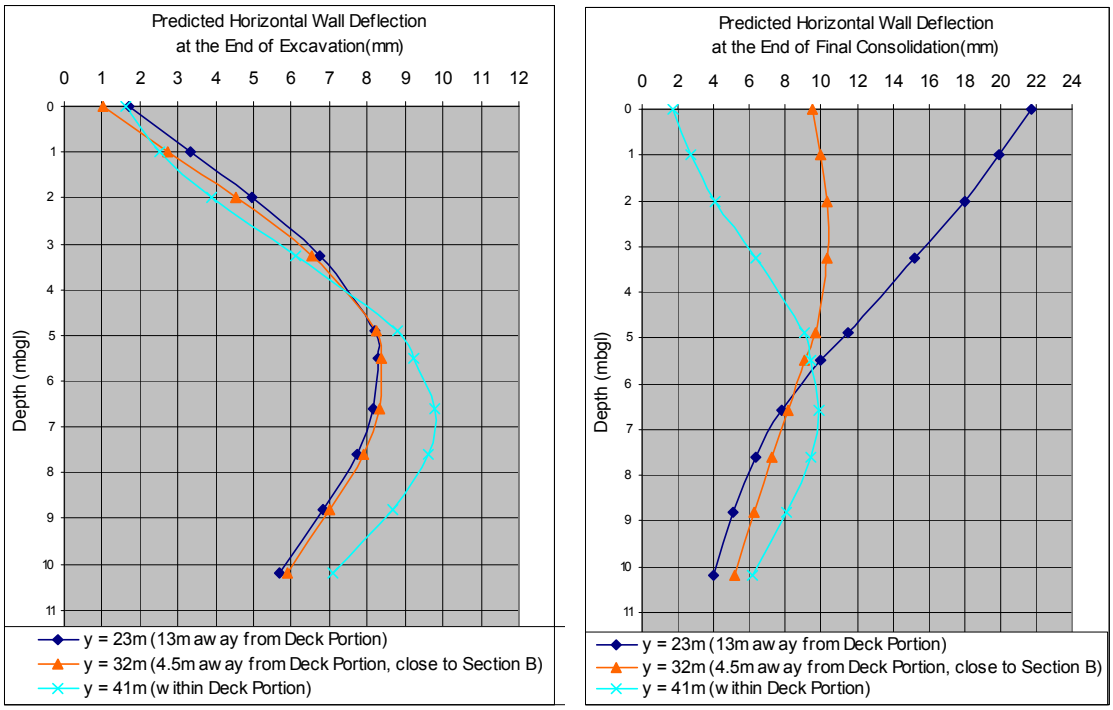

(a) During GSR Construction (b) After GSR Construction

Figure 9: Development of lateral movements of the secant-pile wall

2D analysis at section B which is about 4.5m away from the decking with a y value of 32 m (see Figure 2) was also carried out using geotechnical software Plaxis. The numerical model boundary was placed sufficiently remote from the excavation region and the existing tunnel structures to minimise boundary effects, having a model of 120m wide and over 60m high with lower boundary setting at -40m AOD. The model was restrained laterally on the 2 vertical boundaries but fixed at both horizontal and vertical directions at the lower boundary.

The Plaxis 2D analysis adopted Hardening Soil Model with small strain stiffness (HSsmall) for London Clay while Mohr-Coulomb soil model having properties as given in Table 4.2 was used for other soil stratus. Conventional bottom-up construction sequence with one layer strut was followed at section B. The 2D analysis results give a wall top deflection of 23 mm at long term compared with less than 10mm predicted by 3D analysis. The 2D analysis of the section B is unable to consider the restraining effects from the adjacent underpass deck, hence significantly overestimate the wall movements. It is also interesting to note that, from 3D modelling, the wall top deflection reached 22 mm at the location of about 13m away from the underpass deck, which is similar to the deflection predicted by 2D analysis at section B. Thus the restraining effect on the wall deflection from the underpass deck decreases to negligible at a distance of about 1.5 times of the retaining height away from the restraint. Maximum of 22 mm and 23 mm of the wall deflection were predicted by 3D analysis and 2D modelling respectively, both occurring at wall top and having similar values.

6 CONCLUSION

Impacts on the existing live underground tunnels caused by the proposed GSR construction were assessed with numerical modelling including a 3D modelling. The 3D model analysis results suggest that the deformation of the segmental tunnel lining is small and the structural force change of the tunnel lining is also insignificant. Therefore, with the ELS scheme developed and the construction in sequential bays, the likely impact on the existing tunnels associated with the proposed GSR construction is expected to be small. Though much more computation efforts is required for 3D modelling compared with a simpler 2D analysis, adoption of 3D modelling would be necessary for some 3D problems which is large in scale or has sensitive properties. Comparison of the 3D and 2D analysis results for the long term behaviour of the retaining wall near the underpass deck also illustrated the 3D modelling ability to analysis problems in a 3D environment.

REFERENCES

Itasca 2006. *FLAC^{3D} Ver 3.1*, Reference Manual.

Jardine R J, Potts D M, Fourie A B and Burland J B 1986. Studies of the influence of non-linear stress-strain characteristics on soil-structure interaction. *Geotechnique*, 36(3): 377-396.

Muir Wood, A.M. 1975. The circular tunnel in elastic ground, *Géotechnique,* 25(1): 115–127.

Outward Wall Movements Induced by Jet Grouting

L.W. WONG
SMEC Asia Ltd, Hong Kong
R.N. HWANG
Moh and Associates, Inc., Taiwan

ABSTRACT

The model on distribution of lateral earth pressure due to jet grouting is reviewed and verified by numerical analyses. The result of studies demonstrates that the pressure increments induced by jet grouting depend on the grouting technique adopted and range from 0.6 to 1.2 times the total vertical soil pressure. The pressure increments due to jet grouting are inversely proportional to the radial distance to the jet grout columns.

1 INTRODUCTION

Jet grouting has been extensively used as the supplementary measure for cut-and-cover construction of underground structures. The soil mass could achieve undrained shear strengths ranging from 1 MPa to 4 MPa. Jet grout columns are used as grouted slabs to act as an internal strut below the bottom excavation level to reduce the magnitude of wall and ground movements caused by the excavation. Grout curtains formed by jet grout columns are installed to seal the gaps where diaphragm walling is obstructed by existing utilities.

There are case histories recording that jet grouting would induce ground movements. Berry et al. (1987) reported ground heave as large as 550 mm observed during jet grouting for the Singapore MRT bored tunnel sections. Wong et al. (2000) and Poh et al. (2001) reported ground heave of 24 mm and lateral soil movements as large as 35 mm due to installation of the jet grout slab for Singapore Post Centre. Chen et al. (1997) reported jet grouting causing maximum lateral wall movements of 59 mm and 35 mm at Station BL13 (City Hall Station) and at Station BL14 (Yong Chun Station) of Taipei MRT respectively.

This paper reviews the mechanism of ground movements caused by jet grouting. The lateral earth pressures inducing the wall movements are assessed from the jet grouting trials. Numerical analyses are conducted on the case history for Station BL13 to verify the magnitude of lateral earth pressures.

2 PRESSURES IN THE GROUTHOLE

Jet grouting uses high speed water jet to undermine soils then replaces and mixes the disturbed soils with cement grout. The grouting techniques are described by Kauschinger et al. (1989). With the jetting nozzles of 2 mm to 3 mm in diameter, the jet stream has the sub-sonic speed of about 200 m/s. Although the pressures at the grout pump range from 20 MPa to 40 MPa, the potential energy is transformed into the kinetic energy for imparting the soil and for mixing it with cement grout. Once the fluid leaves the nozzles, the pressure promptly drops to the atmospheric. As long as the return slurry is freely flowing to the surface, the pressure inside the grouthole is balanced by the atmospheric pressure. Collapsing of the grouthole would however block the passage of the return grout. Under these circumstances the pressure in the grouthole will then be equal to the pump pressure. Buttling et al. (1988) pointed out that such blockage will cause the hydraulic fracture mode of failure in the surrounding ground.

The magnitude of the cavity pressure in the grouthole could be assessed from the principle of fluid mechanics. Wong et al. (1994) proposed that the cavity pressure, P_c, could be expressed by Eq. 1 to Eq. 3:

$$P_c = P_{sl} + P_{fr} \tag{1}$$

$$P_{sl} = \gamma_{sl} H \tag{2}$$

$$P_{fr} = f H \tag{3}$$

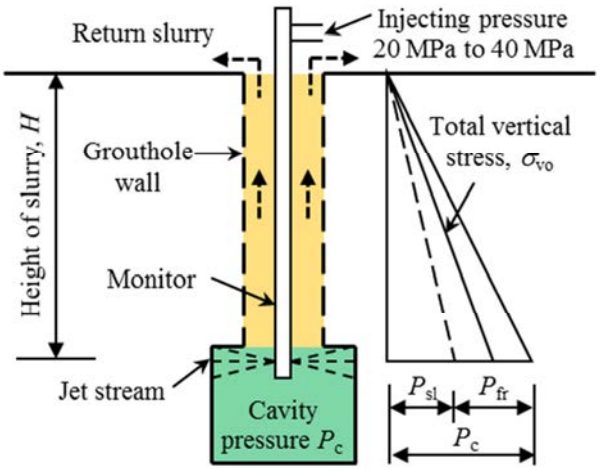

Figure 1: Distribution of Pressures in the Grouthole

where P_{sl} is the hydrostatic pressure of the return slurry, P_{fr} is the head loss due to friction f between the grouthole wall and the return slurry, γ_{sl} is the density of the return slurry and H is the height of the slurry in the grouthole. Figure 1 depicts the distribution of the fluid pressures in the grouthole during jet grouting. The P_c value may exceed the total vertical stress, σ_{vo} , and cause cylindrical expansion along the grouthole wall. The P_{sl} and the P_{fr} values have been estimated from the performance of trial grouting. Sections 3 to 5 present three case histories to verify the cavity pressures estimated by various methods.

3 CASE 1 – CHUNGHO LINE

3.1 Ground conditions

Wong et al. (1994) reported the result of the jet grouting trial panels conducted at a MRT station of Chungho Line, Taipei MRT. The ground is composed of the Sungshan Formation of 45 m in thickness overlying the Gingmei Formation of cobbles and gravel deposits. The Sungshan Formation located at the southern portion of Taipei Basin is mainly composed of silty clay that the N values vary with depth and range from 2 to 20. At the depths of 22 m to 27 m, there is a silty sand layer with the N values ranging from 9 to 20. The groundwater level is located at 1 m below ground surface.

3.2 Trial grouting

Three trial panels using the single-fluid, double-fluid and triple-fluid jet grouting techniques were conducted. The jet grout columns were installed to as deep as 24 m. The panel using the single-fluid method composed of 32 jet grout columns of 0.9 m in diameter arranging in two rows. For trial panels using the double-fluid and the triple-fluid methods, each panel composed of 9 inclined jet grout columns of 1.5 m and 1.6 m in diameter with the angles to the vertical varying from 44^o to 59^o.

The friction loss values along the grouthole wall have been estimated with the velocity of the upward slurry flow, the dimension of the annular void between the grouthole wall and the monitor as well as the viscosity of the return slurry. Table 1 summarizes the jet grouting parameters for the various methods. As the triple-fluid technique uses compressed air to sheath the jet stream of cement grout, its return slurry had lower unit weight.

Table 1: Estimation of Friction Loss in Grouthole during Jet Grouting

Jet grouting method	Unit weight of return slurry kN/m^3	Diameter of grouthole mm	Diameter of monitor mm	Rate of fluid injected l/s	Velocity of slurry flow m/s	Friction along grouthole $kN/m^2/m$
Single-fluid	15.7	180	90	2.9	0.15	9.5
Double-fluid	15.3	146	90	30	1.4	18.3
Triple-fluid	13.4	146	90	33	1.6	10.2

The viscosity for the return grout for the triple-fluid, measured with the Marsh funnel, was 53 centi-poise. The return slurry for the single and the double-fluid were too viscous to flow through the funnel. The estimated initial shear was 0.13 kN/m^2. The estimated frictions per metre length of the groutholes were 9.5 kN/m^2, 18.3 kN/m^2 and 10.2 kN/m^2 for the single, double and the triple-fluid methods respectively. It is noted that the flow rate for the single-fluid was 2.9 l/s and that for the triple-fluid was 33 l/s. The uncased grouthole for the single-fluid was 180 mm in diameter, which is larger than the 146 mm for the triple-fluid system. Therefore the return slurry of the single-fluid system has a bit lower friction loss.

3.3 Horizontal pressure increment

The P_{sl} and the P_{fr} values are normalized with the total vertical stress, σ_{vo}, of the ground. As summarized in Table 2, the P_c / σ_{vo} ratio for the single, double and the triple-fluid methods are about 1.4, 1.9 and 1.3 respectively. Results of this trial grouting show that the cavity pressure, P_c, in the groutholes during jet grouting range from $1.3\sigma_{vo}$ to $1.9\sigma_{vo}$, which are far less than the pumping pressure ranging from 20 MPa to 40 MPa. The in-situ horizontal pressure, σ_{ho}, is defined as $\sigma_{ho} = K\,\sigma_{vo}$ where K is the earth pressure coefficient. The lateral pressure increment, ΔP_h, due to jet grouting immediately next to the wall of the grouthole is expressed in Eq. 4:

$$\Delta P_h = P_c - \sigma_{ho} \quad (4)$$

The K value could be taken as 0.5 for ground prior to jet grouting. However, after the first jet grout column is installed, the stiffness of the surrounding ground is improved. The K value of 0.9 could be adopted. Relating the ΔP_h value with the σ_{vo} value and adopting an average K value of 0.7, the $\Delta P_h / \sigma_{vo}$ ratio due to jet grouting using single, double and triple-fluid methods would be 0.7, 1.2 and 0.6 respectively. The average $\Delta P_h / \sigma_{vo}$ ratios for various types of jet grouting are summarized in Table 2.

Table 2: Estimation of Cavity Pressure in Grouthole during Jet Grouting

Jet grouting method	Unit weight of return slurry γ_{sl}, kN/m^3	Friction along grouthole f, kN/m^2/m	Unit weight of soil γ_s, kN/m^3	$P_c / \sigma_{vo} = (\gamma_{sl} + f) / \gamma_s$	$\Delta P_h / \sigma_{vo}$		
					K = 0.5	K = 0.9	Average
Single-fluid	15.7	9.5	18	1.4	0.9	0.5	0.7
Double-fluid	15.3	18.3	18	1.9	1.4	1.0	1.2
Triple-fluid	13.4	10.2	18	1.3	0.8	0.4	0.6

4 CASE 2 – SINGAPORE POST CENTRE

4.1 Observation of pressure increments

The basement excavation of the Singapore Post Centre involved extensive jet grouting to improve the soft marine clay presence within the excavation of 88 m in width. Poh et al. (2001) reported the results of monitoring on the jet grouting trial. As depicted in Fig. 2, the field trial comprised 18 jet grout columns of 1.8 m in diameter and 20 m in depth. The top and the bottom levels for the jet grout mass were 93 m and 84 m respectively. Arranged in 5 rows, the jet grout columns had a triangular spacing of 1.55 m. The centerline for the Row 1 columns had a distance of 0.45 m to the three diaphragm wall panels of 0.8 m in thickness, 32 m in depth and 18.6 m in total length. The triple-fluid system was used for installing the jet grout columns.

The soil consists of 4 m of fill overlying a 13 m thick soft marine clay stratum. The marine clay is underlain by a 5 m thick stiff silty clay, a 3.5 m thick loose clayey sand and a 3.5 m thick stiff silty clay layer that is underlain by hard clayey sandy silt of the Old Alluvium Formation. The unit weights for fill and for the marine clay are 17 kN/m^3 and 15 kN/m^3 respectively. The groundwater level was at 102.0 m.

The ground movements induced by trial grouting were monitored by eleven inclinometer casings in soil and by one inclinometer in diaphragm wall. The lateral pressures were measured by eleven total pressure cells, six pneumatic piezometers and two standpipe piezometers. As shown in the section in Fig. 2, the total pressure cells and the pneumatic piezometers were installed at the mid-depth of the jet grout columns and at the level of 88.5 m. The instruments were installed on both sides of the diaphragm wall. It is noted that four pressure

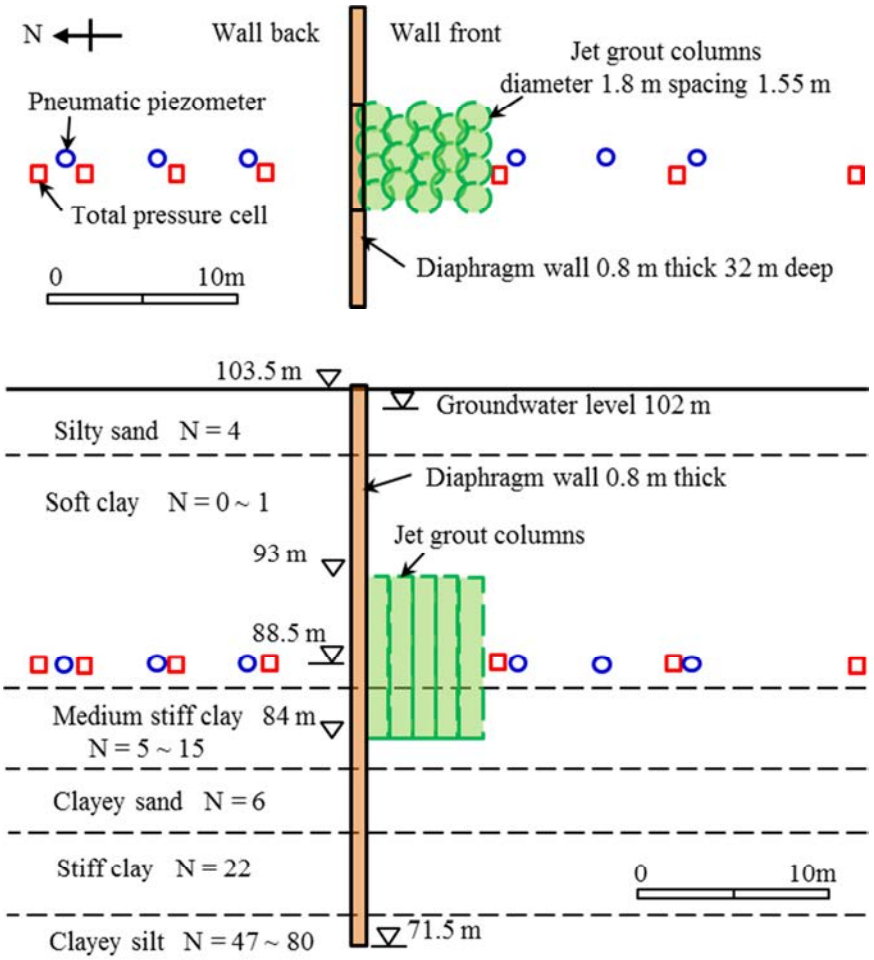

Figure 2: Plan and Section for Jet Grout Columns, Pressure Cells and Piezometers - Case 2

cells, located at 20 m and 30 m east and west from the centre of the mid diaphragm wall panel, are not shown in the plan for sake of clarity.

The numbers of the jet grout columns are the sequence of their installation. Two columns were installed in each day. Columns no. 1 and 2 were installed on Day 1 and columns no. 17 and 18 were on Day 9. Instrument readings were taken after completion of jet grouting for each column.

4.2 Distribution of pressure increments

During the jet grouting trial variation in lateral earth pressures and in piezometric pressures were observed. As the readings were taken after completion of each jet grout column, the peak pressure increments occurred during grouting may not be observed. The monitoring results are presented in Fig. 3, showing the pressure increments are inversely proportional to the radial distances to the jet grout columns. The pressure increments versus the radial distances could be expressed by Eq. 5 and Eq. 6:

$$\Delta P_r = \Delta P_0 \, r_0 / r \tag{5}$$

$$\Delta u_r = \Delta u_0 \, r_0 / r \tag{6}$$

where ΔP_r and Δu_r are the lateral earth pressure increment and the piezometric pressure increment at the radial distance r to the jet grout column respectively, ΔP_0 and Δu_0 are the lateral earth pressure increment and the piezometric pressure increment respectively at the radius, r_o , which is the radius of the jet grout column.

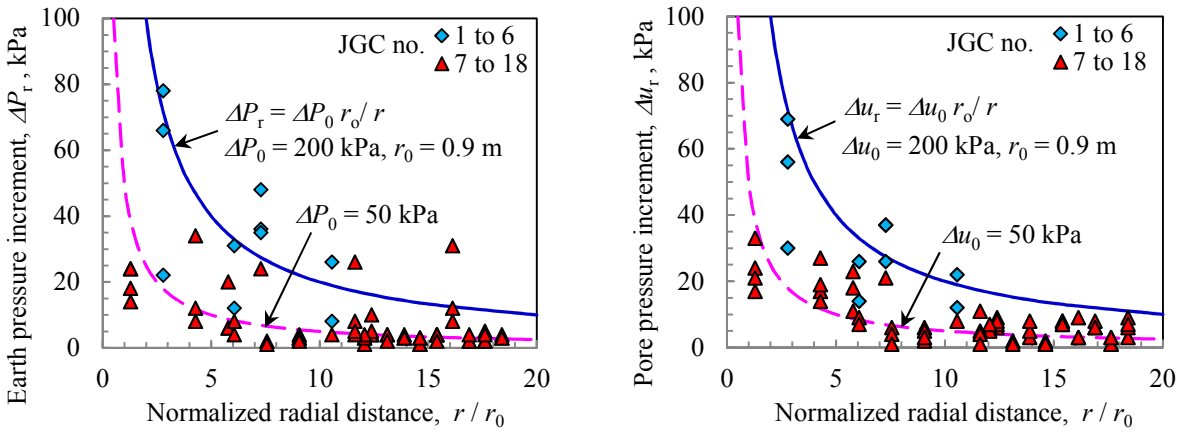

Figure 3: Variation of Earth and Piezometric Pressure Increment with Distance to Jet Grout Column

The jet grout columns installed in the early stage induced larger pressure increments than those in the later stage. Columns no. 1 to 6 were installed on Day 1 to Day 3 while columns no. 7 to 18 were installed on Day 4 to Day 9. As shown in Fig. 3, jet grouting for columns no. 1 to 6 and for 7 to 18 induced the ΔP_0 values of 200 kPa and 50 kPa respectively. Similarly, installing jet grout columns in the early and in the later stages induced Δu_0 values 200 kPa and 50 kPa respectively. It appears that as jet grouting proceeds, the ground becomes stiffer and stiffer. In the later stage the pressure increments are about 25 % of those induced in the early stage.

The same value of ΔP_0 and Δu_0 is an indication that the ground deformation is in undrained condition. This finding agrees with Poh et al. (2001) interpretation that there is a linear relationship between the earth pressure increment and the pore water pressure increment.

The pressure increments are measured at the depth of 15 m. The σ_{vo} value at that depth is 233 kPa. Adopting the unit weight and the friction loss values established from Case 1 and summarized in Table 2, the P_{sl} and the P_{fr} values for the triple-fluid method in Case 2 would be 201 kPa and 153 kPa respectively. Deducting the σ_{ho} value of 116 kPa, the ΔP_c value induced by jet grouting would be about 238 kPa.

The ΔP_0 value of 200 kPa for early stage jet grouting as inferred from Fig. 3 would be an indication of dissipation of cavity pressure. Since the pressure increments were presumably measured at 1 hr to 2 hr after completion of jet grouting, the increments had been dropped by 16 %, from the estimated 238 kPa to the inferred pressure of 200 kPa.

5 CASE 3 – CITY HALL STATION

5.1 Ground conditions

The case history of using the jet grout slab to minimize ground movements outside diaphragm wall was reported by Chen et al. (1997). Station BL13, the City Hall Station, Nankang Line of the Taipei MRT, is located on the eastern side of the Taipei Basin. The ground level is 106.8 m. The soil deposits belong to the K1 Zone of the Sungshan Formation underlain by the Gingmei Formation. In this project site the Sungshan Formation is dominated by soft clay of 50 m in thickness. The underlying Gingmei Formation, encountered at the level below 56 m, is composed of sandy gravel and cobbles.

Station BL13 is 24 m in width and 278 m in length. The excavation of 18.8 m in depth was supported with diaphragm walls of 1.2 m in thickness and 44.5 m in length. Five levels of struts preloading to 50% of the design load were installed. According to Chen et al. (1997), it was anticipated that the cut-and-cover construction would cause lateral wall deflection of about 80 mm. In order to reduce wall deflections and to minimize the settlement effect to the adjacent buildings, a jet grout slab of 4 m in thickness was installed. Figure 4 shows the extent of the jet grout slab for Station BL13.

Thirteen inclinometers casings were installed at the Station BL13 area. Seven of them were installed in diaphragm wall and six were in ground. The toes of the inclinometers installed in wall were 3 m below the toes of the diaphragm wall. Inclinometer no. SID7 was installed in the diaphragm wall at Station BL13.

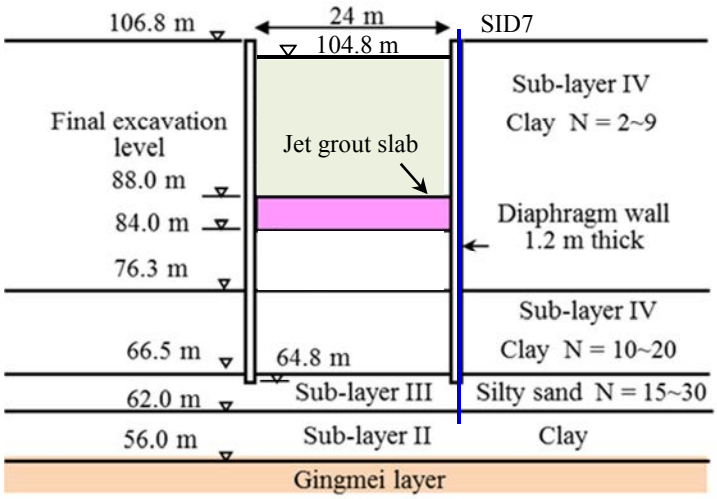

Figure 4: Soil profile for Station BL13 - Case 3

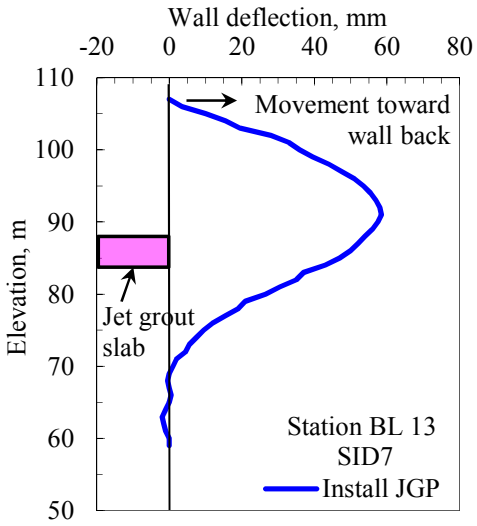

Figure 5: Observed wall deflection profile

5.2 Jet grout slab

Jet grouting for Station BL13 was reported by Wong et al. (1997). The jet grout slab was mainly formed by ten rows of JSG columns spacing at 2.2 m centre-to-centre with a triangular pattern. JG columns of 1.2 m in diameter were installed along the diaphragm wall at 1.04 m spacing to fill the gap between the wall and the JSG columns. The JSG and the JG columns were installed by the double and the single-fluid methods respectively. During installation of the JSG and JG columns, the pumping pressures were as high as 40 MPa with the rate of injection 200 l/min. Chen et al. (1997) reported that due to traffic diversion arrangement, the jet grout slab was installed in bays. Each bay was divided into 3 zones. Grouting commenced at the northern zone, followed by the central and finally at the southern zone. In order to avoid the return slurry from flowing outside the works area, 2 m to 2.5 m depth of excavation was conducted prior to jet grouting.

5.3 Pressures due to jet grouting

As shown in Fig. 5, installation of the jet grout slab induced outward wall deflections as large as 59 mm in SID7. Apparently the pressure increments due to jet grouting caused the wall deflections. Since the wall deflections are proportional to the cavity pressure, the total wall deflection could be computed by superimposing the movement effect due to all jet grout columns taking into account the various distances to the diaphragm wall, the pressures in the groutholes and the soil strengthening effect caused by jet grouting. Calculation for wall deflections caused by jet grouting would comprise the following procedures:

(1) Estimation on the cavity pressure in a jet grout column due to jet grouting. The cavity pressure induced by a single jet grout column has been established in Case 1and summarized in Table 2.
(2) Estimation on the pressure transmitted from a jet grout column to the diaphragm wall during jet grouting. The pressure increment versus radial distance relationship has been developed in Case 2 and expressed by Eq. 5.
(3) Superimposing the cavity pressures acting on the diaphragm wall caused by jet grout columns with various distances to the wall.
(4) Using the cumulative pressures to conduct the numerical analysis to obtain the total wall deflection.

Due to various reasons, the procedure in Item 3 would be difficult. Superimposing the jet grout columns in the entire grouted slab would come to large cumulative pressure or large magnitude of wall deflection. Take Case 3 as an example, the 12 rows of JSG and JG columns would end up with unrealistic large cumulative pressure increment. With the ground level at 104.8 m inside the diaphragm wall and the bottom level of the jet grout slab at 84 m, the σ_{vo} value at the base of the slab was about 381 kPa. Adopting the $\Delta P_h / \sigma_{vo}$ ratios of 0.7

and 1.2 summarized in Table 2 for the single and the double-fluid methods, the minimum ΔP_h values in a single grouthole would be 267 kPa and 457 kPa for the JG and the JSG columns respectively. Superimposing the 12 rows of columns would get the total pressure increment as large as 5,100 kPa. Inputting such a large cumulative pressure for numerical analysis would obtain wall deflection 10 times of the observed value.

In line with the procedure given in Item 2 above, it is proposed that reduction factors could be applied on the cumulative pressure. As observed in Case 2 and shown in Fig. 3, the pressure transmitted from the grouthole to the point of interest is reduced in the later stage. Among the 18 jet grout columns, 1/3 of them (no. 1 to 6) induced ΔP_0 and 2/3 of them (no. 7 to 18) induced $0.25\Delta P_0$. The weighted average for the entire 18 columns would be $0.5\Delta P_0$. Further than that, the jet grout slab in Station BL13 was implemented in 3 sub-zones. During installation of the columns in the later zones, the surrounding soil had already been improved by jet grouting in the earlier stages. The larger in ground stiffness, the smaller in radial strains would be induced. The pressure reduction factor $F_1 = 0.5$ is allowed for the ground stiffening effect.

The jet grout slab in Station BL13 is 4 m in thickness. The groutholes above the top level of the slab for JSG is 146 mm in diameter. At the radial distance of 1.27 m, the influence for pressure increment applying Eq. 5 is 146/1270 = 0.11, which is negligible small. As depicted in Fig. 8, the area for the trapezoidal pressure of ΔP_h and 4 m in height is equivalent to a triangular distributed pressure of $0.4\Delta P_h$ and 21 m in height. The pressure reduction factor $F_2 = 0.4$ is allowed for the effect of jet grout slab with limited thickness.

Thirdly, the pressure imposing on the wall would be reduced as the wall moved backward. The reduction factor however could be assessed by numerical analyses. It is proposed that the pressure reduction factor $F_3 = 0.5$ shall be allowed for the wall movement effect.

Applying the reduction factors F_1 to F_3, the total reduction in cumulative pressure increment would be 0.5 x 0.4 x 0.5 = 0.1. The estimated cumulative pressure increment of 5,100 kPa is then reduced to 510 kPa. In the numerical analysis, the ΔP_h values of 400 kPa and 500 kPa acting on the diaphragm wall have been adopted. The triangular distribution of earth pressure increment adopted for analysis is depicted in Fig. 6.

5.4 Numerical analyses

The wall deflection profile for inclinometers no. SID7 located at Station BL13 has been selected for numerical analyses. Back-analyses have been conducted to estimate the earth pressure increment due to jet grouting. This is achieved by comparing the results obtained in back-analyses with the observed performance of wall. For the case of interest, analyses have been performed by using the finite element program PLAXIS (PLAXIS BV, 2011) developed at Delft University. Figure 6 shows the finite element mesh adopted in the analyses. Since Gingmei Formation is a competent stratum and ground movements therein are expected to be small, the base of the finite element mesh is placed at a depth of 5 m below the surface of this formation.

The ground strata are modeled by 15-node elements. The Mohr-Coulomb model is adopted for simulating the behavior of the soil of the Sungshan Formation and the Gingmei Formation. The clayey sub-layers II, III and IV of the Sungshan Formation are modeled as the Undrained Type C material. The Gingmei Formation is modeled as the Drained Type material.

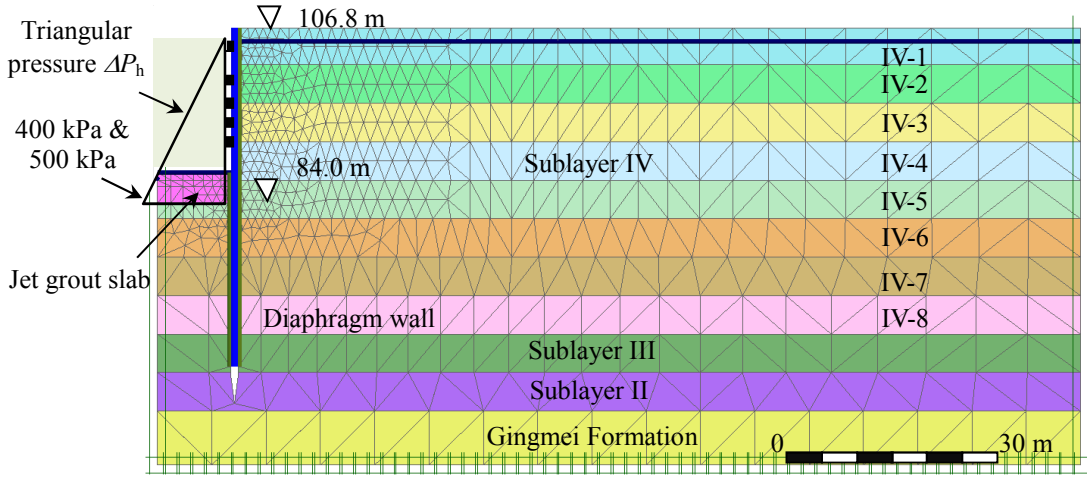

Figure 6: Finite Element Mesh Adopted in Numerical Analysis

Table 3: Soil Parameters Adopted in Numerical Analysis

Soil strata		Unit weight kN/m^3	Effective strength Cohesion kPa	Effective strength Friction angle degree	Aver-age N value	Undrained shear strength s_u, kPa	Undrained Young's modulus E_u, MPa	Poisson's ratio ν_u, ν'
Sub-layer	IV-1	18.6	0	28.0	3	55	11	0.495
IV	IV-2	18.6	0	28.0	2	59	12	0.495
	IV-3	18.8	0	28.5	3	63	13	0.495
	IV-4	18.8	0	28.5	3	78	16	0.495
	IV-5	18.8	0	29.0	4	105	21	0.495
	IV-6	19.4	0	29.0	5	131	26	0.495
	IV-7	19.4	0	29.5	6	158	32	0.495
	IV-8	19.4	0	29.5	14	184	37	0.495
Sub-layer III		19.4	0	30	20	211	42	0.495
Sub-layer II		19.4	0	31	26	237	48	0.495
Gingmei layer		20.0	0	42	100	-	100	0.35

The diaphragm walls are simulated by plate elements and the Young's modulus for concrete, the E_c value, of 25,000 MPa is adopted with the characteristic strength of 42 MPa. As suggested by Gaba et al. (2003), the stiffnesses of the diaphragm wall, the $E_c I$ and the $E_c A_c$ values, where I and A_c are the moment of inertia and the sectional-area of concrete respectively, are reduced by 30 %, giving a value of 2,520 MN-m for the former and 21,000 MN/m for the latter to account for the influence of tremieing and degradation of concrete.

The Young's modulus of the soil, E_u , is assessed by the empirical relationship with the s_u value of the clayey Sungshan deposits:

$$E_u \ / \ s_u = 200 \tag{7}$$

The soil parameters adopted in the analyses are summarized in Table 3.

5.5 Piezometric pressures

Extensive dewatering in the Taipei basin was conducted during the period between 1960 and 1990. The groundwater drawdown conditions have been summarized by Hwang et al. (2013). Due to past pumping in the Taipei Basin, the piezometric level in the Gingmei Formation was as low as 55 m in 1975. Since then the piezometric level started to recover. In 1994 the piezometric level in the gravel layer recovered to about 90 m.

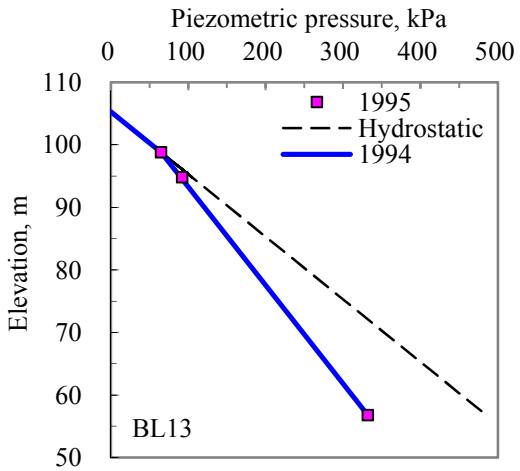

Figure 7: Water Pressure Outside Excavation area

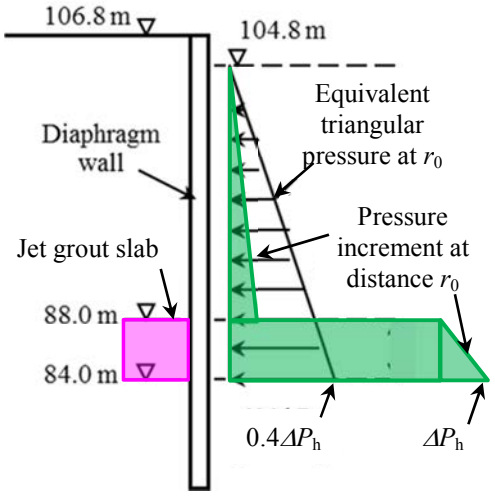

Figure 8: Pressure Increment at Distance r_0 to a Grouthole

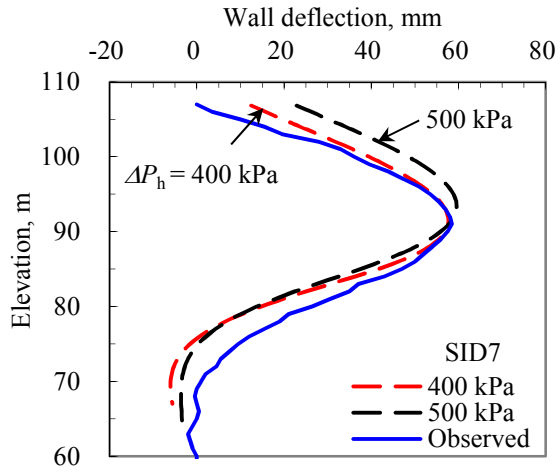

Figure 9: Observed and Computed Wall Deflection Profiles Due to Jet Grouting

Chen et al. (1997) reported the distribution of piezometric levels in the Sungshan Formation. The groundwater at the uppermost strata between the elevations of 106.8 m and 99.0 m had the piezometric level of 105 m in the early stage of excavation in around 1994. Below the elevation of 99.0 m, the groundwater pressure was non-hydrostatic, gradually reducing from the piezometric level of 105.0 m (65 kPa) at the elevation of 90 m to the piezometric level of 90 m at the base of Sungshan Formation at the elevation of 56.8 m (332 kPa). Figure 7 depicts the water pressures adopted in the numerical analyses.

5.6 Result of numerical analyses

The calculated wall deflection profiles under ΔP_h values of 400 kPa and 500 kPa are presented in Fig. 9. The observed wall deflection profile for SID7 could be best matched with the calculated deflection profile using the ΔP_h value of 450 kPa. The reduction factors proposed in Section 5.3, in particular, the factor F_3, are verified by the numerical analysis.

It is however noted that more case histories on jet grouting should be collected and studied so that the various contributing effects to wall movements could be identified.

6 CONCLUSIONS

Case histories on jet grouting causing lateral ground movements have been critically reviewed. A model on the distribution of lateral earth pressure has been established. The factors for transmitting the pressure increment from the grouthole wall to the point of interest have been verified by numerical analyses. Based on results of this study, the following concluding remarks could be drawn:

(1) The lateral ground movements caused by jet grouting is induced by static pressure of the return slurry emerging from the grouthole and by friction loss between the return slurry and the grouthole wall.
(2) Depends on the grouting techniques adopted for installing the jet grout columns, the total pressure in the grouthole during jet grouting would range from 1.3 to 1.9 times the total vertical stress. Therefore the pressure along the wall of the jet grout column is far less than the pumping pressure ranging from 20 MPa to 40 MPa.
(3) The pressure increment that will cause the lateral ground or wall movements depends on the jet grouting technique. Assuming the in-situ horizontal earth pressure is about 0.7 times the total vertical pressure of the surrounding ground, the pressure increments induced by the single, double and the triple-fluid methods would be about 0.7, 1.2 and 0.6 times the total vertical pressure.
(4) The pressure increments due to jet grouting are inversely proportional to the radial distances to the jet grout columns.
(5) Due to ground improvement effect, the pressure increments transmitting from the groutholes installed

in the later stage would be about 25 % of those installed in the early stage.

(6) The less thickness of the jet grout slab, the less cavity pressure would be transmitted from the grouthole to the point of interest.

(7) Result of preliminary analysis suggests that the outward wall movement would cause pressure reduction transmitting from the groutholes.

Understanding the magnitude of the lateral earth pressure increment induced by jet grouting, the ground movement effect to adjacent ground and to nearby underground structures such as diaphragm wall, sheet pile wall, basements, pile foundations and tunnels could then be reliably assessed. With the aid of numerical analyses, application of jet grouting for jacking the diaphragm wall outward and to minimize the ground settlements behind diaphragm wall could be properly controlled.

REFERENCES

Berry, G.L., Shirlaw J.N., Hayata, K & Tan, S.H. 1987. A review of grouting techniques utilised for bored tunneling with emphasis on the jet grouting method. *Proc. Singapore Mass Rapid Transit Conference, April*.

Buttling, S. & Shirlaw, J.N. 1988. Review of ground treatment carried out for tunnels of the Singapore Mass Rapid Transit System. *Proceedings, Tunnelling '88, Institution of Mining and Metallurgy, London, 1988*.

Chen Y.K., Huang C.C. & Wang, F.G. 1997. Use grouted raft for building protection of excavation in soft clay. *Proceedings of 7th Conference on Current Research in Geotechnical Engineering, Chishan, Taiwan, August, Vol. 1*, pp 593-600. (in Chinese)

Gaba, A.R., Simpson, B., Powrie, W. & Beadman, D.R. 2003. *Embedded Retaining Walls – Guidance for Economic Design, CIRIA Report, C580, London*.

Hwang, R.N., Moh, Z.C. & Hu, I.C. 2013. Effects of consolidation and specimen disturbance on strengths of Taipei Clays. *Geotechnical Journal of the SEAGC & AGSSEA*, 44(1): 9-18.

Kauschinger, J.L. & Welsh, J.P. 1989. Jet grouting for urban construction, *Proc. of the 1989 Seminar, Design, Construction and Performance of Deep Excavations in Urban Areas, MIT Cambridge, MA*.60pp.

PLAXIS BV 2011. *Reference Manual PLAXIS BV: Amsterdam, the Netherlands*.

Poh, T.Y. & Wong I. H. 2001. A field trial of jet grouting in marine clay. *Canadian Geotechnical Journal*, 38: 338-348.

Wong I. H. & Poh, T.Y. 2000. Effect of jet grouting on adjacent ground and structures. *Journal of Geotechnical and Geoenvironmental Engineering*, 126(3): 247-256.

Wong, L.W. & Hwang R.N. 1997. Evaluation of jet grouting by in-situ tests. *Proceedings of the International Conference on Ground Improvement Techniques, Macau, May*, pp641-647.

Wong, L.W. & Kao, H.S. 1994. Failure mechanism induced by jet grouting in cohesive soils, *Sino-Geotechnics*, 47, pp107-120 (in Chinese).

Wong, L.W., Shirlaw J.N. & Kao, H.S. 1994. Application of jet grouting in geotechnical engineering. *Proc. of International Structure and Foundation Symposium, Hanzhou, October* (in Chinese).

Effects of Soil-structure Interactions on the Design of ELS Systems

Albert T. Yeung & Iris C.Y. Ng
University of Hong Kong, Hong Kong

ABSTRACT

The conventional design methodology for the excavation and lateral support (ELS) system maintains the equilibrium of lateral earth pressures and support forces in the design. It does not account for the stiffness of the lateral support system and its effects on the magnitudes of the lateral earth pressures. However, it is well known that the magnitude of the lateral earth pressure, either active or passive, depends on the lateral movement of the lateral support system. Therefore, using the conventional design methodology may not yield the most efficient or appropriate design. More importantly, it may not be able to give a reasonable estimate of the lateral movement of the lateral support system and the resulting ground settlement in the vicinity of the excavation. In this paper, the effects of these soil-structure interactions on the design of ELS are evaluated and presented. In particular, the effects of the stiffness of the lateral support system on the required embedment depth, strut loads, and bending moments in the lateral support system are evaluated.

1 INTRODUCTION

The excavation and lateral support (ELS) system is an essential component for the construction of foundations, basements or other underground structures. The system provides temporary support to maintain stability of the excavation. The conventional design methodology adopts the concept of limit equilibrium among the active earth pressures, passive earth pressures and strut loads. The required embedment depth, and bending moments and shear forces in the lateral support system, i.e. sheetpiles, pipe piles etc. are determined and designed accordingly. The stiffness of the lateral support system is not explicitly taken into account. However, the stiffness of the lateral support system may affect the magnitudes of the lateral earth pressures, as the lateral earth pressure is a function of the magnitude of deflection of the lateral support system. Therefore, a conservative approach is normally taken in practice. Current design software can take into account of the lateral earth pressure as a function of the deflection of the lateral support system, and iterate the lateral earth pressures to obtain the equilibrium forces. As a result, the effects of soil-structure interactions are taken into consideration for the design implicitly.

In this paper, the effects of these soil-structure interactions on the design of ELS are evaluated and presented. In particular, the effects of the stiffness of the lateral support system on the required embedment depth, strut load, and bending moment in the lateral support system are evaluated.

2 BACKGROUND

2.1 Traditional approach

Typical temporary ELS systems include cantilever walls, anchored or propped walls and braced excavations, as classified by the earth retaining mechanism (Knappett & Craig 2012).

Cantilever walls are used only when the retained height of soil is relatively low. The stability of the wall is provided entirely by the passive resistance of soil mobilized in front of the wall. The mode of failure is by rotation about a point O near the wall toe as shown in Figure 1(a). Passive resistance acts in front of the wall above O and behind the wall below O as shown in Figure 1(b), thus providing a restoring moment. The design is generally based on the simplification shown in Figure 1(c), assuming the net passive resistance below point O is represented by a concentrated force R acting at a point C which is located slightly below O, at depth d below the excavation level. Using the traditional method of analysis, the embedment depth d is determined by

equating the moments about C. A factor of safety F is applied to the available passive resistance in front of the wall. The value d so determined is then increased by 20% to allow for the simplification taken in the method of analysis. The concentrated force R can be obtained by equating the horizontal forces. It is advisable to check that the net passive resistance available over the additional 20% embedded depth is equal to or greater than R. The shear force and bending moment distributions in the wall are then determined for subsequent selection of the appropriate structural section for the wall.

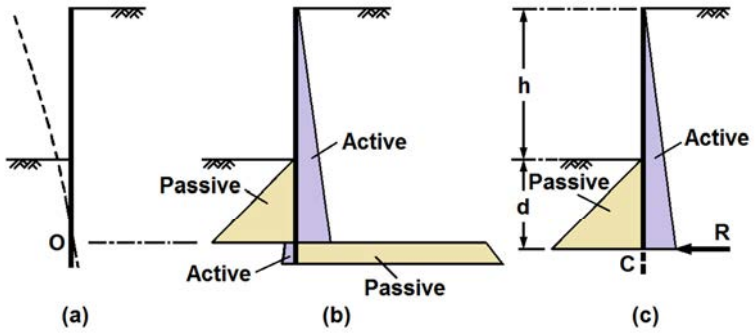

Figure 1: Cantilever Sheetpile Wall

Anchored and propped walls are usually constructed of steel sheetpiles, steel pipe piles or reinforced concrete diaphragm walls. Additional support to embedded walls is provided by a row of tie-backs (anchors) or props near the top of the wall, as shown in Figure 2(a). It is assumed that the depth of embedment below the excavation level is insufficient to produce fixity at the wall toe. The wall is thus assumed to be free to rotate about its toe, the resulting bending moment distribution is shown in Figure 2(b). To satisfy the equilibrium conditions, the sum of the restoring moments about the anchor or prop must be greater than or equal to the sum of the overturning moments. The anchor or prop force is determined from the equilibrium of horizontal forces. The shear force and bending moment distributions in the wall are then determined for subsequent selection of the appropriate structural section for the wall.

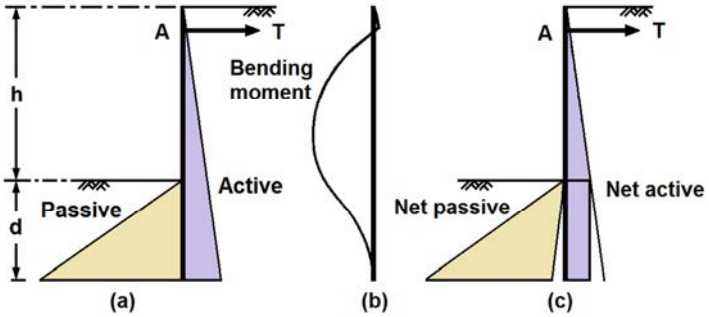

Figure 2: Anchored Sheetpile Wall: Free Earth Support Method

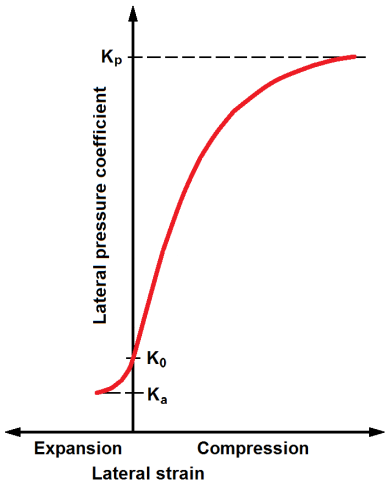

Figure 3: Relationship between Lateral Strain and Lateral Pressure Coefficient

In both cases, the structural section for the wall is selected after the shear force and bending moment distributions in the wall have been determined from limit equilibrium conditions. Therefore, the stiffness of

the wall has no effect on the lateral earth pressure, shear force and bending moment distributions, and soil-structure interactions are not taken into consideration at all.

The coefficients of active and passive lateral pressures used in these limit equilibrium analyses are obtained from the lower bound limit analyses, assuming the soil mass is subjected to lateral expansion (active case) or compression (passive case) and reaches a state of plastic equilibrium. In the active case, a specific (minimum) value of lateral expansion strain would be necessary for the development of the active state within the soil mass. If the deformation of the wall cannot satisfy this minimum deformation requirement, the soil adjacent to the wall would not reach a state of plastic equilibrium and the lateral pressure would be between the active and at-rest values. In the passive case, a specific (minimum) value of lateral compression strain would be necessary for the development of the passive state within the soil mass. In practice, only part of the potential passive resistance would normally be mobilized. The relatively large deformation necessary for the development of full passive resistance would be unacceptable. As a result, the lateral earth pressure under working conditions would be between the at-rest and passive values. Experimental evidence indicates that the mobilization of full passive resistance requires a wall movement of the order of 2-4% of embedded depth in the case of dense sands and of the order of 10-15% in the case of loose sands. The corresponding percentages for the mobilization of active pressure are of the order of 0.25 and 1%, respectively. Generally, for any condition intermediate to the active and passive states, the value of the coefficient of lateral earth pressure is unknown. The form of the relationship between the strain and the coefficient of lateral earth pressure is shown in Figure 3. It is evident that the lateral earth pressures acting on the ELS system depend on the lateral movement of the ELS system which depends on the stiffness of the lateral support system. These important effects of soil-structure interactions are not taken into account in the traditional design of the ELS system using limit equilibrium.

2.2 FREW

FREW (**F**lexible **RE**taining **W**alls) is a computer software developed by Oasys Ltd., which enables engineers to define and solve complex embedded flexible retaining wall design problems efficiently. The program performs two-dimensional pseudo-finite element analyses to allow the user to study the deformations of, and stresses within, the structure through a specified sequence of construction (Oasys Ltd. 2014). The wall is modeled as a series of nodal points connected by elastic material elements. Lateral earth pressures acting the lateral support system, displacements, bending moments, shear forces and strut (or anchor) forces occurring in the system during each stage in construction can be calculated by the program. The wall deflection is governed by the wall stiffness and the lateral earth pressure (Wang *et al*. 2013), while the lateral earth pressure is controlled by the wall deflection as shown in Figure 3. These soil-structure interactions are thus inter-related. However, a realistic analysis should take these soil-structure interactions into consideration. The approach of the pseudo-finite element analysis is completely different from that of the limit equilibrium analysis. A detailed comparison of the two different analyses is tabulated in Table 1.

3 CASE STUDIES

The results of a few case studies on ELS systems using sheetpiles with or without lateral struts are presented in this paper to demonstrate the effects of soil-structure interactions on the design of ELS systems. The geometry of the ELS system used in these case studies is shown in Figure 4. The depth of excavation is 6 m and the width of the excavation is 18 m. The groundwater table is at 1.5 m below the existing ground level. The lateral struts, if installed, are located at 1 m below the existing ground level. The embedment depth of the sheetpiles required to maintain stability of the ELS system is denoted as d in the figure. The king posts for internal support of the lateral struts are omitted for clarity.

In the analyses, the coefficients of active and passive lateral earth pressure are taken to be 0.3 and 4.2, respectively. The bulk unit weight of soil and water are taken to be 20 kN/m^3 and 9.81 kN/m^3, respectively. Sheetpiles of different flexural rigidities as tabulated in Table 2 are used in the analyses.

Table 1. Comparison between Limit Equilibrium and Pseudo-Finite Element Analyses
(Excerpted From Gaba *Et Al*. 2003)

Type of Analysis	Advantages	Limitations
Limit equilibrium	• Needs only the soil strength • Simple and straightforward	• Does not model soil-structure interaction, wall flexibility and construction sequence • Does not calculate deformations. Hand calculations of deformations possible by relating mobilized strength, soil shear strain and wall rotation (rarely done); or through empirical databases • Statically indeterminate systems (e.g. multi-propped walls), non-uniform surfaces and berms require considerable idealization • Can model only drained (effective stress) or undrained (total stress) conditions • Two-dimensional only • Results take no account of pre-excavation stress state
Pseudo-finite element e.g. FREW	• Full soil-structure interaction analysis is possible, modeling construction sequence, etc. • Soil modeled as an elastic solid with soil stiffness matrices calculated using a finite element program • Soil-structure interaction taken into account • Wall movements are calculated • Relatively straightforward • Takes account of pre-excavation stress state	• Two-dimensional only • Limited to linear elastic soil model, with active and passive limits • Berms and certain structural connections are difficult to model • Global effects not modeled explicitly • Ground movements around wall are not calculated

Table 2. Flexural Rigidity of Sheetpiles

Type of Sheetpile	Young's Modulus E (kPa)	Second Moment of Area I (cm^4/m)	Flexural Rigidity EI ($kN\text{-}m^2/m$)
FSP III	205,000,000	16,800	34,440
FSP IV	205,000,000	38,600	79,130
FSP V	205,000,000	63,000	129,150

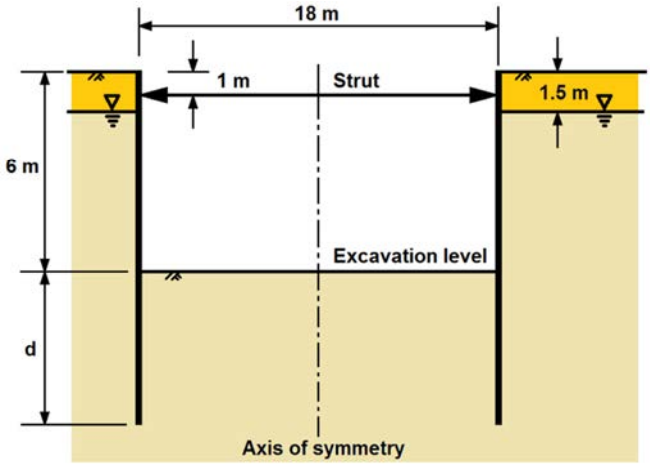

Figure 4. Geometry of ELS System Used in Case Studies (Not to Scale)

The levels of the groundwater tables on the two sides of the sheetpile wall are different after excavation. Assuming steady state seepage conditions have developed and maintained, the pore water pressure distributions on the two sides of the wall will be unbalance as shown in Figure 5(a). The dotted lines indicate the hypothetical and unrealistic hydrostatic pressure distributions. A flow net analysis on the steady state seepage condition can be performed to determine the net pore water pressure distribution. A simplified pore water pressure distribution as shown in Figure 5(a) was proposed by Padfield and Mair (1984), assuming the total hydraulic head dissipates linearly along the back and front wall surfaces between the two groundwater table levels.

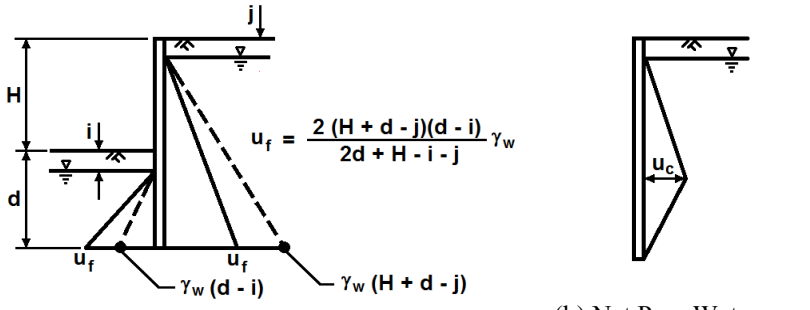

(a) Pore Water Pressure across a Wall

(b) Net Pore Water Pressure under Seepage

Figure 5: Distribution of Pore Water Pressure across a Retaining Wall

The maximum net pore water pressure occurs at the level of the lower groundwater table level as shown in Figure 5(b) and is given by

$$u_c = \frac{2(H + i - j)(d - i)}{2d + H - i - j}\gamma_w \quad (1)$$

where γ_w = unit weight of water.

The seepage force j can thus be estimated by

$$\mathrm{j} = \frac{(H + i - j)}{2d + H - i - j}\gamma_w \quad (2)$$

The effective unit weight of the soil below the groundwater table is increased to ($\gamma' + \mathrm{j}$) behind the wall where seepage is downwards, and reduced to ($\gamma' - \mathrm{j}$) in front of the wall where seepage is upwards. These values should be used in the calculation of active and passive pressures if steady seepage is maintained. It should be noted that the assumption of hydrostatic pressures on both sides of the wall is generally conservative as the net pore water pressure acting on the wall is excessive. However, the approach underestimates the active lateral earth pressure behind the wall and overestimates the passive lateral earth pressure in front of the wall simultaneously. Therefore, the use of hydrostatic pressures for ELS design may not be conservative all the times.

3.1 Case study 1 – cantilever retaining wall

Sheetpiles are installed for a cantilever retaining wall as shown in Figure 1. The required embedment depth d determined by limit equilibrium using the Burland-Potts-Walsh approach (Burland *et al*. 1981) is 8.85 m when the factor of safety is unity. The deflections of the wall constructed of different types of sheetpiles computed by FREW for the embedment depth of 9 m are depicted in Figure 6. The maximum deflections of FSP III, IV and IV sheetpiles are 954.5 mm, 451.8 mm and 295.0 mm, respectively. These deflections are unacceptably large. The relative maximum deflection is thus 3.24 : 1.53 : 1.00. The relative flexural rigidities of these

sheetpiles as tabulated in Table 2 is 1.00 : 2.30 : 3.75. If the active lateral earth pressures on these different types of sheetpiles are identical, the deflection should be inversely proportional to the flexural rigidity of the sheetpile, i.e. the product of the relative maximum deflection and the relative flexural rigidity should be a constant. However, this is not the case as revealed by the results of the analyses. In fact, the products for FSP III, IV and V sheetpiles are 3.24, 3.52 and 3.75, respectively, indicating the relative maximum deflection increases with the flexural rigidity of the sheetpile.

It can be observed in Figure 3 that the coefficient of active lateral earth pressure decreases with deflection of the wall. When the wall is relatively more rigid, the active earth pressure acting behind the wall is increased, resulting in a relatively larger deflection. Similarly, the passive earth pressure acting in front of the wall is smaller, resulting in less passive resistance supporting the cantilever retaining wall. Therefore, the effect of soil-structure interactions makes a more rigid sheetpile less efficient in terms of deflection control. However, it should be noted that the absolute deflection decreases with increase in flexural rigidity of the sheetpile.

The results also demonstrate the deficiencies of the limit equilibrium approach. Firstly, the required embedment depth so determined is independent of the flexural rigidity of the sheetpiles used. It is evidently demonstrated in Figure 6 that the deflection of the sheetpile depends heavily on the flexural rigidity of the sheetpile. Secondly, the approach does not give an estimate of the lateral movement of the ELS system, which may cause excessive settlement and/or distress of nearby structures. As demonstrated by the results of this case study, the minimum embedment depth may yield a maximum deflection of 295 mm even when FSP V sheetpiles are used.

It is recommended that the factor of safety of 1.2 should be applied to the calculated embedment depth (Knappett & Craig 2012). As a result, the design embedment depth would be $1.2 \times 8.85 = 10.62$ m. The deflections of the wall constructed of different types of sheetpiles computed by FREW for the embedment depth of 10.6 m are depicted in Figure 7. It can be observed that the extra embedment depth can only reduce the deflection slightly. The design embedment depth may yield a deflection of 289.1 mm even when FSP V sheetpiles are used. The impact of embedment depth on wall deflection is minimal.

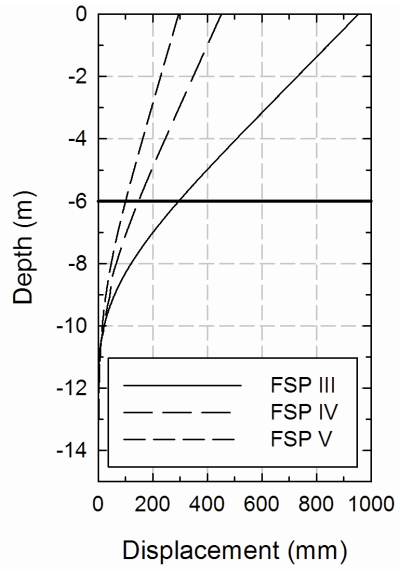

Figure 6: Displacement of Cantilever Walls of Embedment Depth of 9 m

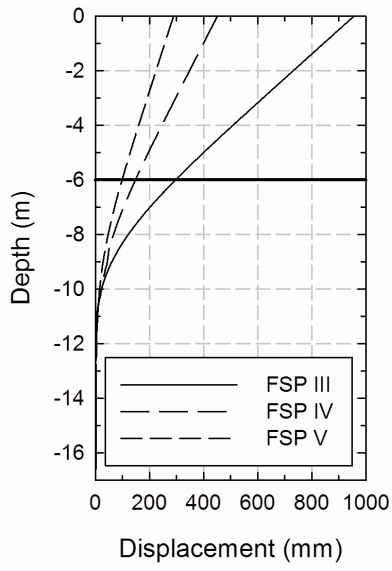

Figure 7: Displacements of Cantilever Walls of Embedment Depth of 10.6 m

The distributions of lateral earth pressures as a function of depth acting on the cantilever sheetpile retaining wall are depicted in Figure 8. The solid lines denote the lateral earth pressure behind the wall which is taken to be negative. The dotted lines denote the lateral earth pressure in front of the wall which is taken to be positive. As the movement of soil behind the wall is quite large above the excavation level, the active condition has been developed. As a result, the lateral earth pressure is practically independent of the flexural rigidity of the sheetpile. Similarly, the soil in front of the wall down to approximately 4 m below the excavation level is in

the passive plastic equilibrium state. The distribution of lateral earth pressure further down the excavation level depends on the flexural rigidity of the sheetpile. The effects of soil-structure interactions are also depicted in the bending moment distributions shown in Figure 9. It should be noted that maximum bending moments occur well below the excavation level. It can also be observed that the bending moment in the sheetpile close to the wall toe increases slightly with increase in flexural rigidity of the sheetpile. The phenomenon can be attributed to the differences in lateral earth pressure distributions as shown in Figure 8.

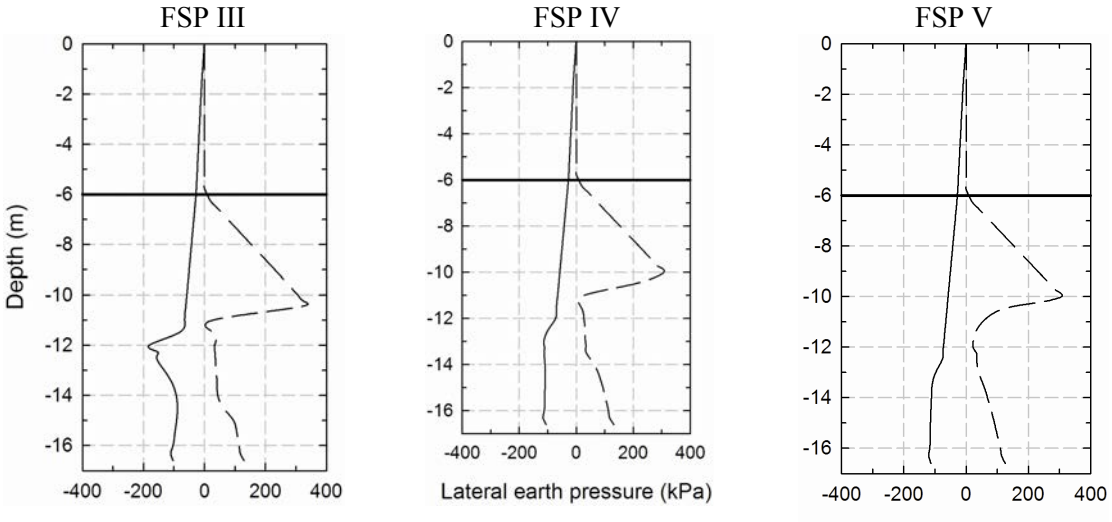

Figure 8: Distributions of Lateral Earth Pressures as a Function of Depth in the Cantilever Retaining Wall

3.2 Case study 2 – propped wall

Sheetpiles are installed for a propped cantilever retaining wall as shown in Figure 1. The required embedment depth d determined by limit equilibrium using the free earth support analysis is 4.2 m when the factor of safety is unity. Applying the factor of safety of 1.2 to the calculated embedment depth, the design embedment depth becomes 5.04 m. Therefore, an embedment depth of 5 m was adopted in this case study. The horizontal struts used in the analyses are 305×305×137 kg/m UC at 4 m center-to-center. The Young's modulus of steel is taken to be 205,000,000 kN/m^2 and the cross-sectional area of the strut is 0.0174 m^2. Therefore, the stiffness of the strut in the analysis is determined to be (205,000,000×0.0174) / (9×4) = 99,083 kN/m/(m run of sheetpiles).

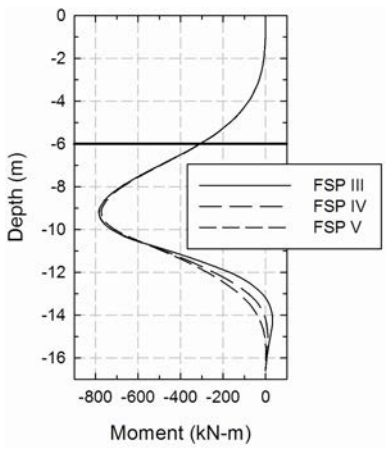

Figure 9: Distributions of Bending Moment in the Cantilever Retaining Wall

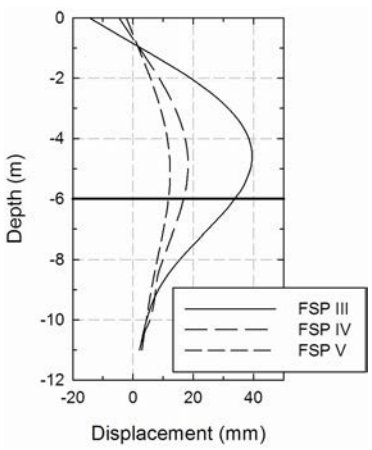

Figure 10: Lateral Displacements of the Propped Cantilever Wall

The lateral displacements of the propped cantilever retaining wall as a function of depth are shown in Figure 10. The maximum deflections of the wall occur at approximately 1 m above the excavation level. The maximum deflections for FSP III, IV and V sheetpiles are calculated to be 39.49 mm, 18.27 mm and 12.31 mm, respectively. The relative maximum deflection is thus 3.21 : 1.48 : 1.00. The relative flexural rigidities of these sheetpiles as tabulated in Table 2 are 1.00 : 2.30 : 3.75. If the active lateral earth pressures on these different types of sheetpiles are identical, the deflection should be inversely proportional to the flexural rigidity of the sheetpile, i.e. the product of the relative maximum deflection and the relative flexural rigidity should be a constant. However, this is not the case as revealed by the results of the analyses. In fact, the products for FSP III, IV and V sheetpiles are 3.21, 3.41 and 3.75, respectively, indicating the relative maximum deflection increases with the relative flexural rigidity of the sheetpile. It can also be observed from the deflection of the sheetpile wall that passive condition has been developed in front of the wall. The phenomenon is consistent with the lateral earth pressure distributions shown in Figure 11. However, the shortening of the strut decreases with the flexural rigidity of the sheetpile. As a result, the strut load decreases with increase in flexural rigidity of the sheetpile. In this case study, the strut loads are determined to be 262.61 kN/m, 211.66 kN/m and 182.33 kN/m for FSP III, IV and V sheetpiles, respectively.

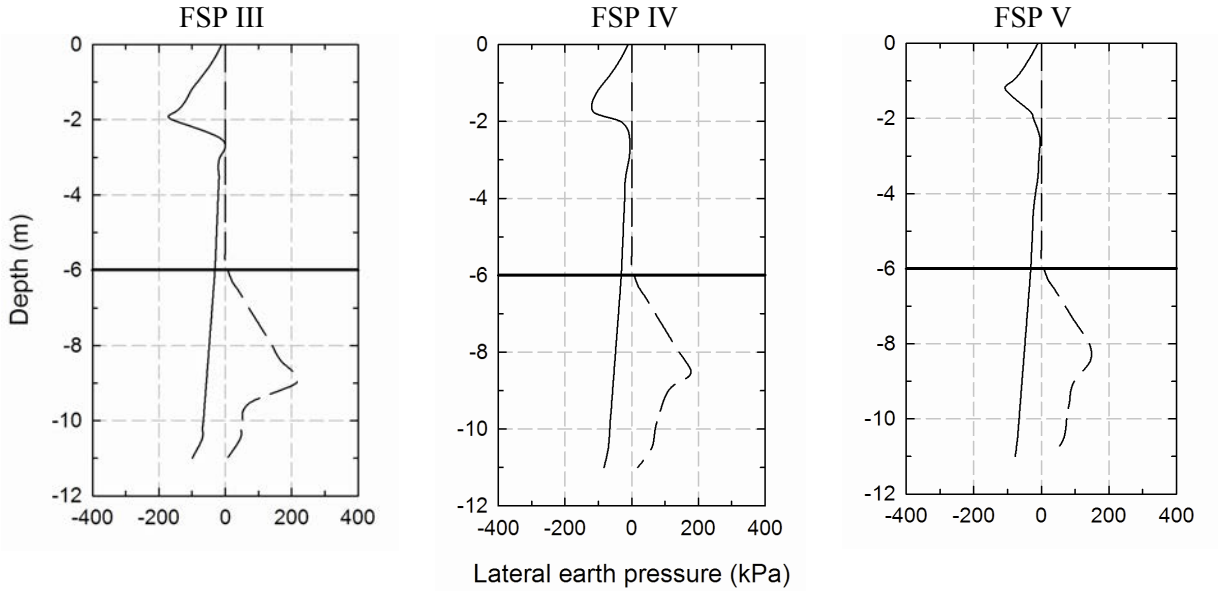

Figure 11: Distributions of Lateral Earth Pressures as a Function of Depth in the Propped Cantilever Retaining Wall

The distributions of lateral earth pressures for the propped cantilever sheetpile retaining wall are depicted in Figure 11. It can be observed that the soil behind the retaining wall is generally in the active plastic equilibrium state regardless of the flexural rigidity of the sheetpile, as the deflection of the wall is adequate to mobilize the coefficient of active lateral earth pressure K_a as shown in Figure 3. The lateral earth pressure in front of the retaining wall remains in the passive state, as the wall deflects towards the excavation. However, the coefficient of lateral earth pressure decreases with depth when the deflection of the wall decreases. When the lateral displacement is adequately large to mobilize the soil in front of the wall to the passive plastic equilibrium, the coefficient of lateral earth pressure equals K_P as depicted in Figure 3. The resulting lateral earth pressure thus increases linearly with overburden pressure as shown in Figure 11. As the deflection of the retaining wall below the excavation level decreases with depth as shown in Figure 10, the coefficient of lateral earth pressure decreases below a threshold depth which decreases with the flexural rigidity of the wall as shown in Figure 11.

The distributions of bending moments in the propped cantilever sheetpile retaining wall as a function of depth are depicted in Figure 12. It can be observed that the bending moment in the sheetpile below the strut decreases with increase in flexural rigidity of the sheetpile. The phenomenon can be attributed to the decrease in strut load with increase in flexural rigidity of the sheetpile.

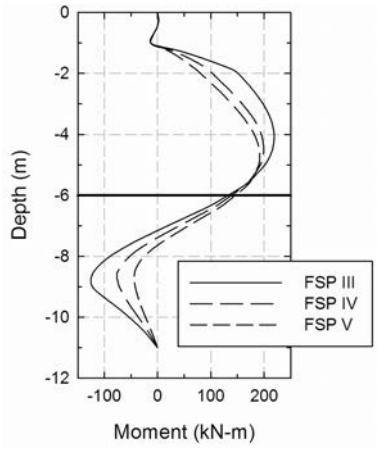

Figure 12: Distributions of Bending Moments in the Propped Cantilever Retaining Wall

4 CONCLUSIONS

The following conclusions can be drawn from this study:

(1) The limit equilibrium approach in the design of ELS systems without considering any soil-structure interactions is conservative in the determination of embedment length, strut load, bending moment in the sheetpile etc. However, the resulting design may not be practical. For example, the deflection of the retaining wall may be excessive.
(2) The engineering behavior of a propped cantilever retaining wall is different from that of a cantilever retaining wall.
(3) When soil-structure interactions are considered, the flexural rigidity of the sheetpile and the stiffness of the strut have significant impacts on the engineering behavior of the ELS system.
(4) The design of ELS system can be significantly improved by taking soil-structure interactions into consideration.

ACKNOWLEDGEMENTS

The first author is grateful to Ir James W.C. Sze of Ove Arup & Partners Hong Kong Ltd. for the detailed discussion on the software FREW.

REFERENCES

Burland, J.B., Potts, D.M. & Walsh, N.M. 1981. The overall stability of free and propped embedded cantilever retaining walls. *Ground Engineering*, 14(5):28-38.

Gaba, A.R., Simpson, B., Powrie, W. & Beadman, D.R. 2003. *Embedded retaining walls – guidance for economic design*. Report No. C580, CIRIA, London.

GEO 1990. *Review of design methods for excavations*. GCO Publication No. 1/90, Geotechnical Engineering Office, Civil Engineering & Development Department, Hong Kong SAR Government, Hong Kong.

Knappett, J.A. & Craig, R.F. 2012. *Craig's soil mechanics*. 8th Edition, Spon Press, New York, New York.

Oasys Ltd. 2014. *FREW - Version 19.2*. Oasys Ltd., London.

Padfield, C.J. & Mair, R.J. 1984. *Design of retaining walls embedded in stiff clay*. Report No. 104, CIRIA, London.

Wang, S.-T., Vasquez, L. & Xu, D. 2013. Application of soil-structure interaction (SSI) in the analysis of flexible retaining walls. In J. Hu, J. Ma, J. Meneses, T. Qui, X. Yu & X. Zeng (ed.), *Challenges and recent advances in geotechnical and seismic research and practices, Proc., IACGE 2013*, Geotechnical Special Publication No. 232, ASCE, Reston, Virginia, 567-577.

Numerical Modelling of Flexible Barriers Subject to Landslide Debris Impact

C. Lam & R.C.H. Koo
Geotechnical Engineering Office, Civil Engineering and Development Department, the Government of Hong Kong SAR
Z.H. Zhou, Y.P. Liu & S.L. Chan
Department of Civil and Environmental Engineering, The Hong Kong Polytechnic University, Hong Kong

ABSTRACT

Steel flexible barriers are commonly used as defence measures to intercept rockfalls in Hong Kong. Due to their ability to absorb high impact energy through elasto-plastic deformation, they have also been found capable of retaining landslide debris in different site settings. However, thus far there is no widely accepted test procedure to verify the performance of these barriers under debris impact. To facilitate the design of flexible debris-resisting barriers, a finite element program named NIDA-MNN has been developed under the collaboration between geotechnical and structural engineering professionals. A special feature of this program is that it can simulate the sliding action of the metallic nets along the support cables, i.e., the so-called curtain effect. This program was recently used to back-analyse the structural behaviour of a flexible barrier intercepting landslide debris in Jordan Valley, Hong Kong. It was found that the back-analyses can reproduce some of the salient field observations and provide insights into the behaviour of the barriers under impact loading. In this paper, the key features of NIDA-MNN and its use for the back-analysis of the Jordan Valley case history are discussed.

1 INTRODUCTION

1.1 Background

Steel flexible barriers are commonly used to intercept rockfalls and snow avalanches around the world. Due to their ability to sustain large deformations and absorb impact energy, these barriers have also been found capable of containing landslide debris in different site settings (Roth et al. 2004). The use of flexible barriers to mitigate landslide hazard is highly desirable since they are less intrusive to the surrounding environment than the conventional rigid barriers which are made of reinforced concrete. Flexible barriers also have the advantage of relatively easy construction since they are made of pre-fabricated components that can be transported individually and assembled on site. No heavy machinery is typically required during installation.

1.2 Design of flexible debris-resisting barriers

When flexible barriers are used as rockfall fences, their energy-absorbing capacities are typically verified by full-scale tests performed in accordance with standardized procedures (Duffy and Badger 2012; European Organisation for Technical Approvals 2013). However, at present there is no widely accepted test procedure to verify the performance of flexible barriers to withstand landslide debris. Testing a full-scale barrier under debris impact loading is intrinsically difficult as it will involve producing an artificial debris flow or pre-installing a barrier at a location that is prone to debris flows. Full-scale testing is thus relatively rare, and so far only has been carried out by barrier manufacturers and research institutions (e.g. Wendeler et al. 2006; Bugnion et al. 2008; Luis-Fonseca et al. 2011).

In light of the above, numerical simulations present an attractive alternative because they can be performed on modern computers and the results can be used to identify critical barrier components in the design. However, the program must be able to simulate the dynamic behaviour of all barrier components, and the

numerical modeller must possess the relevant knowledge in order to correctly interpret the simulation results. Previous authors such as von Boetticher et al. (2011) and Volkwein et al. (2014) have discussed the use of numerical modelling for the design of flexible debris-flow barriers. This paper further demonstrates the value of numerical analyses by presenting a landslide case history in Hong Kong, where the falling debris was arrested by a flexible barrier originally designed to intercept rockfalls. Numerical simulations were carried out using the finite element program NIDA-MNN to understand the structural behaviour of the barrier upon debris impact. Before the simulation results are presented, information about the landslide and the computer program is given as follows.

2 LANDSLIDE IN JORDAN VALLEY, HONG KONG

2.1 Location and barrier information

Figure 1 shows the locations of the landslide and the flexible barrier in Jordan Valley. The landslide scar is 10 m wide and 7 m long and the source volume is about 110 m^3. The flexible barrier, which is a proprietary product and has a designed energy capacity of 1000 kJ, was originally designed to retain boulders with a volume up to 1 m^3. The barrier consisted of 5-m tall steel posts made of 140-mm square hollow sections. The spacing between the posts was about 10 m. The posts were anchored to the ground by uphill and lateral wire ropes. Metallic ring nets and secondary wire mesh were hung down from wire ropes attached between the steel posts. The posts were founded on 400-mm square concrete pad footings with an embedment depth of about 500 mm. Energy-dissipating devices were fitted to some of the uphill cables to absorb impact energy.

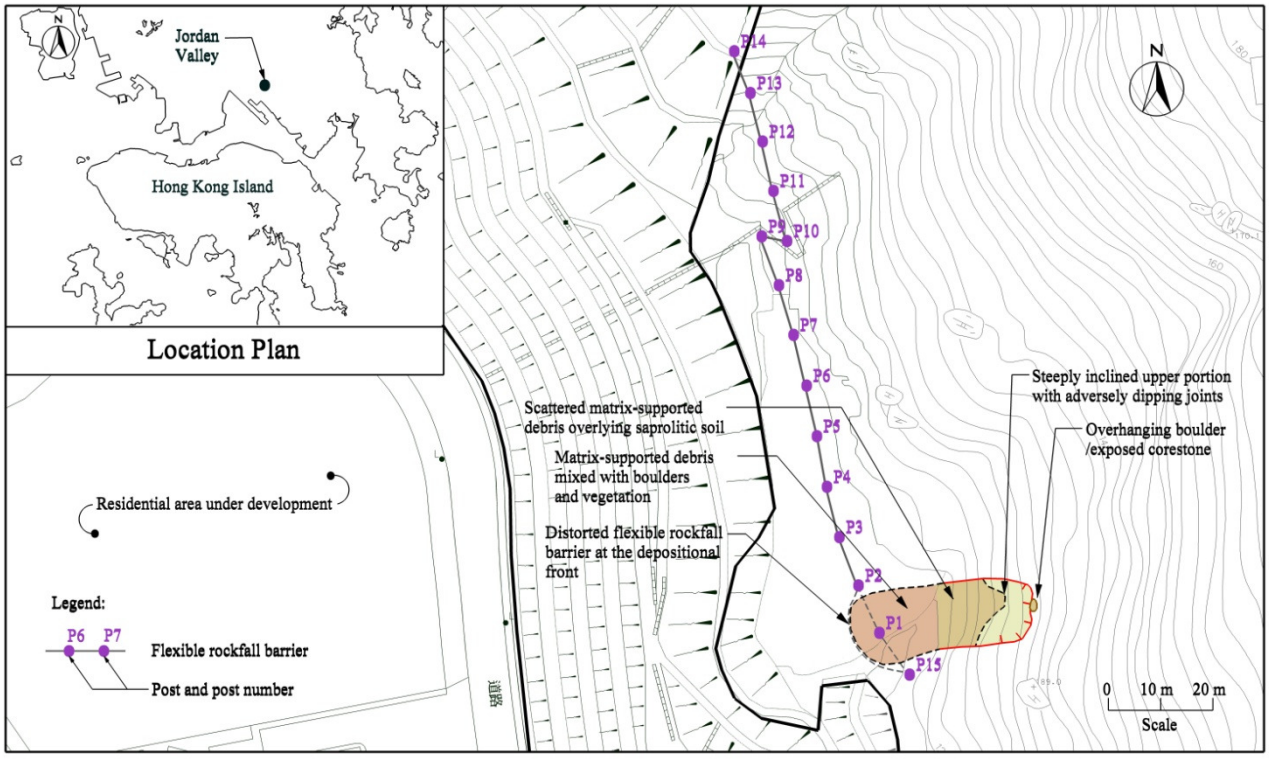

Figure 1: Location of the Landslide and the Posts of the Flexible Barrier (Kwan et al. 2014)

2.2 Post-landslide barrier conditions

When the landslide occurred, the debris struck post P1 and two adjacent netting panels spanning across posts P1-P2 and posts P1-P15. Figure 2 shows the barrier retaining the debris and the severely damaged post P1. Post P15 was also bent though it was not subjected to any direct impact by the debris. Both posts P1 and P15,

together with their concrete footings, were found to have moved forward by 1 to 2 m. It is worth noting that the construction details of post P15 were slightly different from those of posts P1 and P2. The netting was attached to post P15 by nine layers of stainless steel bands, whereas posts P1 and P2 were not tied to the net. This difference might have contributed to the failure of post P15 as shown in Figure 3.

Figure 2: Landslide Debris Intercepted by a Flexible Barrier at Jordan Valley, Hong Kong (Kwan et al. 2014)

Figure 3: The Damaged Steel Post P15 and Its Uplifted Foundation Block

2.3 Debris mobility analysis

A mobility analysis of the landslide debris was carried out using the computer program 2d-DMM (Kwan and Sun 2006). The results showed that the debris could have reached the barrier at about 4 s after the onset of the landslide, and that the maximum frontal debris velocity could be about 4 m/s at the location of the barrier. The calculated debris thickness ranges from 0.8 to 1.2 m.

3 NUMERICAL ANALYSIS

3.1 Finite element program NIDA-MNN

The numerical back-analysis was conducted using the non-linear finite element program NIDA-MNN (Chan et al. 2012). This program can simulate elasto-plastic deformation of the energy-dissipating devices by the use of non-linear structural elements. It can also simulate the sliding action of the metallic nets along the support cables, that is, the so-called curtain effect. This modelling capability has proven to be essential in the realistic modelling of the structural behaviour of flexible barriers. For example, Figure 4 shows the original and the deformed shape of a net subject to the impact of a falling rock. It can be seen that the deformed net elements concentrate around the region of impact as would be expected in a real physical test. The stretching of the net is also realistically simulated in the computer model.

NIDA-MNN is on the pre-accepted computer program list maintained by the Buildings Department in Hong Kong. This program is not computationally demanding so that it is suitable for routine design use.

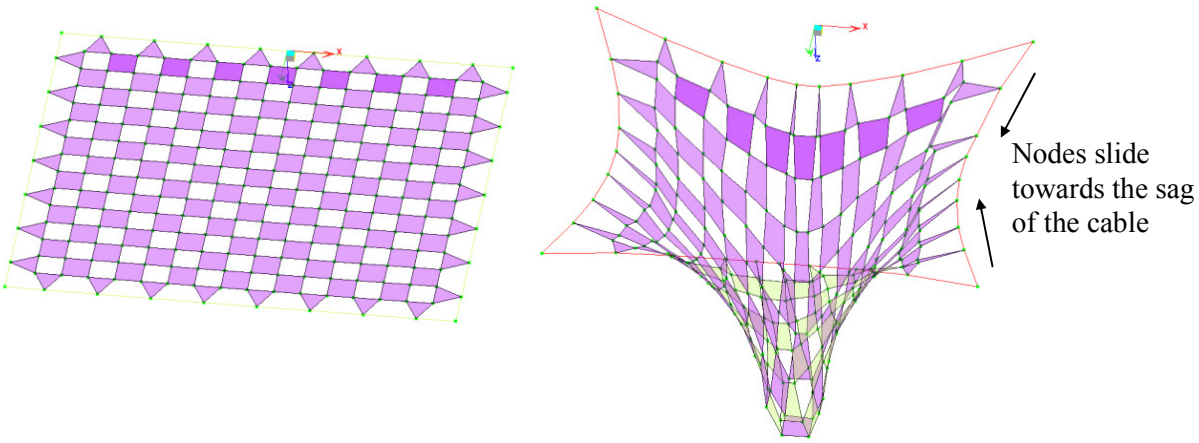

Figure 4: Deformation of Metallic Net due to Rockfall

3.2 Modelling of the flexible barrier

The finite element model was set up according to the physical dimensions of the various structural components (e.g. steel posts, netting, wire ropes) as shown in the as-built drawings of the barrier. The energy-dissipating devices were not included in the model because the post-landslide inspection showed that they were not mobilised. The foundations of the steel posts were modelled as pin supports because shallow footings cannot provide high rotational restraint. This assumption agrees with site observations that the footings of posts P1 and P15 failed by rotation after the landslide impact. The computer model of the barrier is shown in Figure 5.

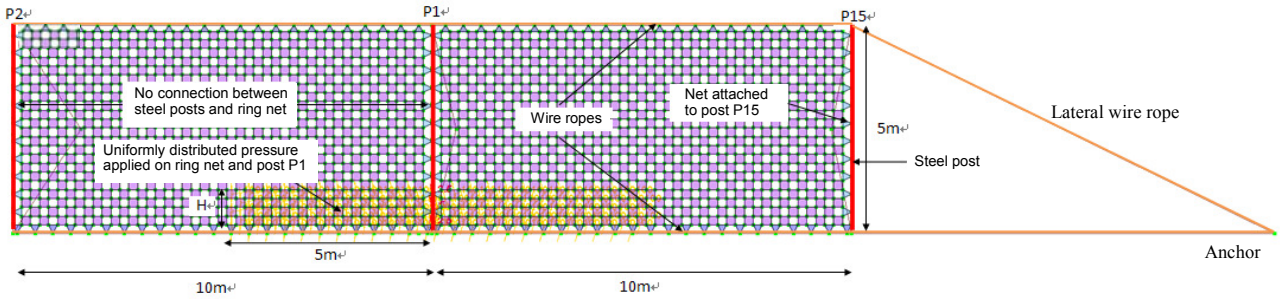

Figure 5: Computer Model of the Flexible Barrier for Structural Analysis

3.3 Modelling of debris impact load

The debris impact load was modelled as a uniformly distributed pressure acting perpendicular to the barrier. Site observation indicates that the landslide debris could have impacted on post P1 and the netting on the both sides of the post. From the results of the post-landslide inspection and the debris mobility analysis, the thickness of the debris hitting the barrier was about 1.0 m thick. Thus, the height of the loaded area is assumed to be 1.0 m. The width of the loaded area is taken as 10 m, which is based on the result of post-landslide inspection. A single impact was considered in the analysis because there was no evidence of multiple impacts.

In view of the fact that posts P1 and P15 failed both structurally and geotechnically, the magnitude of the debris impact pressure was adjusted to replicate this in the numerical model. It was found that some of the steel posts would fail when the debris impact pressure reached 50 kPa and the wire ropes would reach their ultimate tensile strength (270 kN) when the pressure reached 66 kPa.

3.4 Results

Table 1 summarises the calculated maximum axial compressions (P), bending moments (M), shear forces (V) in posts P1, P2 and P15 for the two load cases. It should be noted that these member forces and moments considered nonlinear effects in the deformed location. The calculated maximum horizontal reactions at the post bases and the cable forces are also given in the table. The bending moment and shear force diagrams for the posts for a debris pressure of 50 kPa, together with the computed deformation of the barrier, are shown in Figures 6 and 7 respectively. The analysis shows that maximum calculated deformation of the netting is about 2.5 m.

Table 1: Numerical Analysis Results from NIDA-MNN (Kwan et al. 2014)

Uniformly distributed pressure (kPa)	Post no.	P (kN)	M_x (kNm)	M_y (kNm)	Section capacity R (-)	V_x (kN)	V_y (kN)	Post base horizontal reaction in y-dir. (kN)	Wire rope force (kN)
50	P2	21	0	0	0.1	0	0	47	227
	P1	68	13.9	0.2	1.0[a]	1.2	86.6	333	227
	P15	92	4	20.4	1.6[a]	15.6	3.4	51	227
66	P2	25	0	0	0.1	0	0.1	62	271[b]
	P1	83	19.8	0.1	1.4[a]	1.6	123.3	438	271[b]
	P15	107	5.5	26.6	2.1[a]	20.7	4.8	67	271[b]

[a] Posts fail in buckling [b] Cables fail in tension

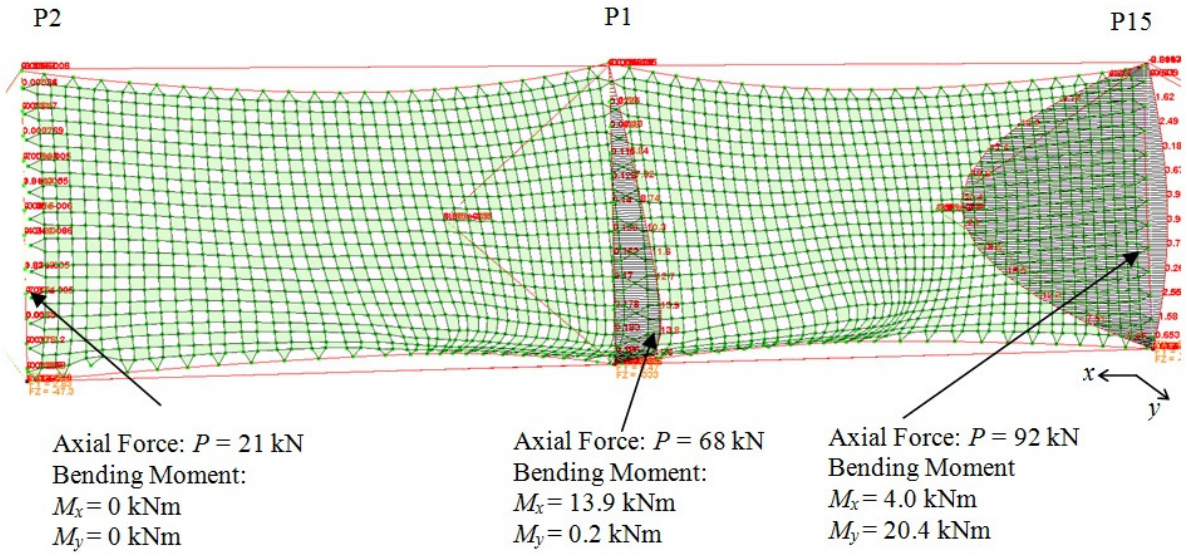

Figure 6: Bending Moment Diagrams for the Steel Posts under a Debris Pressure of 50 kPa

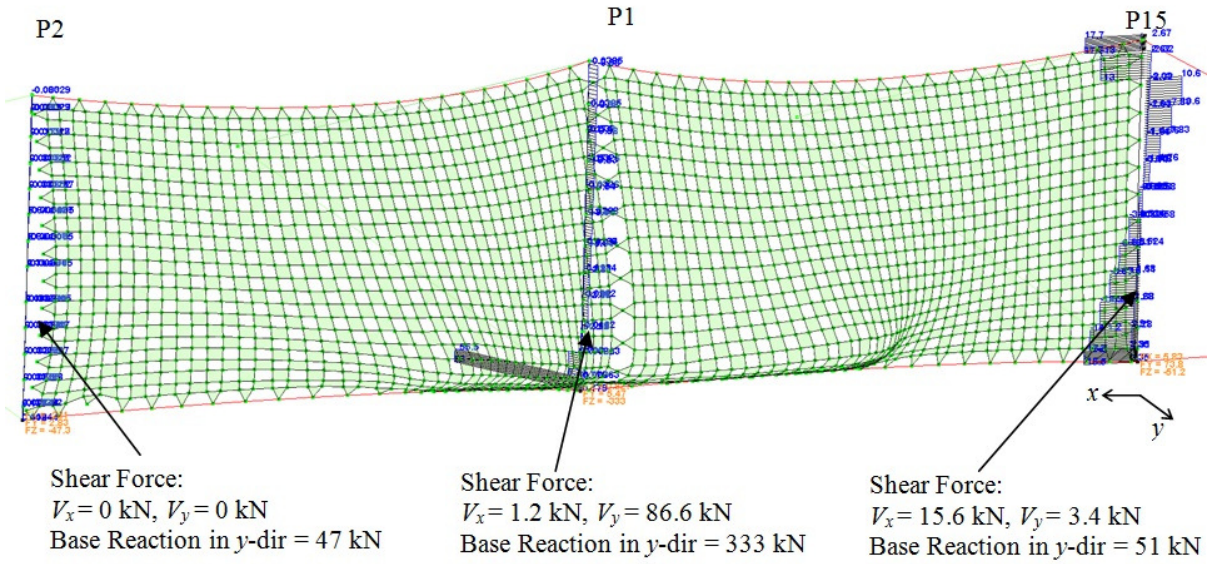

Figure 7: Shear Force Diagrams for the Steel Posts under a Debris Pressure of 50 kPa

3.5 Discussion

The analysis results show that the steel posts could have been subjected to a combination of axial load and bending moments about the two principal axes of the cross section. According to Buildings Department (2011), buckling failure of a steel column would occur if the section capacity factor (R) as defined in Equation (1) is greater than unity:

$$R = \frac{P}{P_{sq}} + \frac{M_x}{M_{CX}} + \frac{M_y}{M_{CY}} \quad (1)$$

where P is the calculated axial force, M_x and M_y are the calculated bending moments about x- and y-axes, M_{CX} and M_{CY} are the bending moment capacities about x- and y-axes (= 17 kN·m), and P_{sq} is the squash load (=

critical yield strength × cross-sectional area = 372 kN). The steel post has a critical yield strength (σ_{yield}) of 174 MPa and a cross-sectional area of 2.14×10^3 mm^2.

By applying Equation (1) to examine the results given in Table 1 and Figures 6 and 7, it can be deduced that both posts P1 and P15 probably failed by buckling when the debris pressure reached 50 kPa. The large bending moment about *x*-axes (M_x) in post P1 could have been caused by the debris pressure acting directly on the post, whereas the large bending moment about *y*-axes (M_y) in post P15 could have been caused by the lateral deformation of the netting attached to it. Failure of both posts P1 and P15 could be due to the combined actions of bending moment and axial compression load, as shown by their high *R* values. In addition, post P15 could have experienced an axial compressive load (*P*) higher than that in post P1. This is thought to be due to the downward forces brought about by both the anchored uphill and the lateral wire ropes attached to the top of the post. The shear forces (V_x and V_y) induced in the posts were all lower than the shear capacity (= 263 kN in this case), so they were not critical in terms of structural capacity.

As regards the effect of the debris impact on post foundations, it can be seen from Table 1 that the calculated horizontal reaction force at the base of post P1 is in the order of 330 to 440 kN for the two load cases. It is very likely that this reaction force exceeded the sliding resistance of the footing. This numerical result is in line with the site observation that the footing of post P1 was displaced from its original location. The footing of post P15 was also displaced (Figure 3) and this is probably due to the bending failure of the post. However, the post-failure mechanism is not modelled in the present analysis.

3.6 Dynamic pressure coefficient

The dynamic pressure coefficient (α) can be deduced from the back-analysis results. In the current design practice (Kwan and Cheung 2012), debris impact pressure (*p*) can be estimated by using the following equation:

$$p = \alpha \rho_d v^2 \tag{2}$$

where ρ_d is density of debris in Mg/m^3 and *v* is debris velocity in m/s. As discussed previously, the numerical analyses indicate that posts P1 and P15 would buckle when the debris pressure reaches 50 kPa, and that the wire rope cables would fail in tension when the pressure reaches 66 kPa (Table 1). It follows that the actual debris pressure should lie within this range, because the posts were indeed severely damaged by the landslide but the cables did not fail. By assuming a debris density of 2.0 Mg/m^3 (typical value) and a debris velocity of 4 m/s (from debris mobility analysis), the back-calculated dynamic pressure coefficient (α) therefore ranges from 1.6 to 2.1.

3.7 Limitations of the analysis

The numerical analysis discussed above is subject to the following limitations:

(1) the analysis does not consider the post-failure behaviour of the barrier and the foundation, so that the possibility of progressive failure is not considered;
(2) the weight of the debris retained in the bulged portion of the netting is neglected in the present analysis. However, if the self-weight of the debris is considered important, this can be modelled by adding a downward loading to the bulged portion of the net;
(3) the strength and stiffness of the landslide debris are not considered; in the computer model the debris impact pressure is modelled as a pseudo-static pressure.
(4) the debris pressure is assumed constant and uniformly distributed throughout the impact. Debris-barrier interaction is therefore not considered.

4 CONCLUSIONS

The structural behaviour of a flexible barrier under debris impact has been analysed by using the finite element program NIDA-MNN. The numerical analysis successfully reproduces the key salient field observations and provides useful insights into the conditions of major barrier components. The dynamic pressure coefficient (α) for debris impact has been back-calculated from the analysis results.

With the continuing increase of computing power and technology, it is expected that the use of numerical tools for the analysis of flexible barriers will become more popular in the future. For the study of coupled soil-structure interaction problems, other numerical tools such as LS-DYNA may also be used (Huang et al. 2014; Kwan et al. 2015).

ACKNOWLEDGEMENTS

This paper is published with the permission of the Head of Geotechnical Engineering Office and the Director of Civil Engineering and Development of the Government of the Hong Kong Special Administrative Region.

REFERENCES

Bugnion, L., Denk, M., Shimojo, K., Roth, A. & Volkwein, A. 2008. Full-scale experiments on shallow landslides in combination with flexible protection barriers. In *Proceedings of the 1st World Landslide Forum, 18-21 November 2008*. International Consortium on Landslides.

Buildings Department. 2011. *Code of practice for the structural use of steel*. Buildings Department, the Government of Hong Kong Special Administrative Region.

Chan, S.L., Zhou, Z.H. & Y.P. Liu. 2012. Numerical analysis and design of flexible barriers allowing for sliding nodes and large deflection effects. In C.K. Lau, E. Chan & J. Kwan (eds.), *Proceedings of the One Day Seminar on Natural Terrain Hazards Mitigation Measures. Hong Kong, 16 October 2012*. The Association of Geotechnical and Geoenvironmental Specialists (Hong Kong) Ltd.

Duffy, J.D. & Badger, T.C. Flexible Rockfall Fences. In A.K. Turner & R.L. Schuster (eds.), *Rockfall: Characterization and Control*: 526-553. Transportation Research Board.

European Organisation for Technical Approvals. 2013. *Guideline for European technical approval of falling rock protection kits, ETAG 027*. European Organisation for Technical Approvals.

Huang, Y., Yiu, J., Pappin, J., Sturt, R., Kwan, J.S.H. & Ho, K.K.S. 2014. Numerical investigation of landslide mobility and debris-resistant flexible barrier with LS-DYNA. In *Proceedings of the 13th International LS-DYNA Users Conference. Dearborn, Michigan, 8-10 June 2014*. Livermore Software Technology Corporation.

Kwan, J.S.H. & Sun, H.W. 2006. An improved landslide mobility model. *Canadian Geotechnical Journal*, 43(5): 531-539.

Kwan, J.S.H. & Cheung, R.W.M. 2012. *Suggestions on design approaches for flexible debris-resisting barriers. Discussion Note DN 1/2012*, Geotechnical Engineering Office, Hong Kong.

Kwan, J.S.H., Chan, S.L., Cheuk, J.C.Y., Koo, R.C.H. 2014. A case study on an open hillside landslide impacting on a flexible rockfall barrier at Jordan Valley, Hong Kong. *Landslides*, 11(6): 1037-1050.

Kwan, J.S.H., Pun, W.K., Shiu, Y.K., Ng, C.W.W., Song, D. & Yiu, J. 2015. Study of interaction between landslide debris and debris-resisting structures. In *Proceedings of the HKIE Geotechnical Division 35th Annual Seminar. Hong Kong, 22 May 2015*. Hong Kong Institution of Engineers.

Luis-Fonseca, R., Raïmat, C., Hürlimann, M., Abancó, C., Moya, J. & Fernández, J. 2011. Debris-flow protection in recurrent areas of the Pyreness. Experience of the VX systems from output results collected in the pioneer monitoring station in Spain. In *Proceedings of the 5th International Conference on Debris-flow Hazards Mitigation: Mechanics, Prediction and Assessment. Padua, Italy, 7-11 June 2011*. Casa Editrice Universita La Sapienza.

Roth, A., Kästli, A. & Frenez, T. 2004. Debris flow mitigation by means of flexible barriers. In *Proceedings of the 10th International Congress INTERPRAEVENT. Riva del Garda, 26 May 2004*. INTERPRAEVENT.

Volkwein, A. 2014. *Flexible debris flow barrier – Design and application*. Swiss Federal Institute for Forest, Snow and Landscape Research WSL.

von Boetticher, A., Hübl, J., Wendeler, C. & Volkwein, A. 2011. Modeling the impact of shallow landslides on flexible protection barriers. In R. Marschallinger & F. Zobl (eds.), *Mathematical Geosciences at the Crossroads of Theory and Practice, Proceedings of the IAMG 2011 Conference. Salzburg, Austria, 5-9 September 2011*. International Association of Mathematical Geosciences.

Wendeler, C., McArdell, B.W., Rickenmann, D., Volkwein, A., Roth, A. & Denk, M. 2006. Field testing and numerical modeling of flexible debris flow barriers. In C.W.W. Ng, L.M. Zhang & Y.H. Wang (eds.), *Proceedings of the 6th International Conference on Physical Modelling in Geotechnics. Hong Kong, 4-6 August 2006*. Taylor & Francis.

Effects of Positioning of Debris-resisting Baffles on Impediment of Debris Flows

R.P.H. Law
Geotechnical Engineering Office, Civil Engineering and Development Department, HKSAR Government, Hong Kong

ABSTRACT

Debris flow is a common form of natural terrain landslides in Hong Kong. Because of its potential of high mobility, even a small-scale debris flow that occurs in a dense urban setting is liable to result in severe consequences. Mitigation of debris flow hazard has been one of the important initiatives in Hong Kong's slope safety system. Option and design of debris flow mitigation measures have evolved in response to experience and through continuous research and development effort and technology advances. With an improved understanding of the dynamic soil-structure interactions between debris flows and mitigation measures, largely through numerical modelling and simulations, more innovative designs of landslide mitigation measures are anticipated.

In particular, recent research using numerical simulation by discrete element method (DEM) shows that debris-resisting baffles, which act as one form of debris straining structures, can be tactically positioned to substantially impede debris velocity. This paper will present the use of DEM in simulating landslide mobility and soil-baffles interactions, using the flow path of a historical landslide as a demonstration, and discuss the performance of debris-resisting baffles in impeding debris velocity at various locations along the flow path. Important considerations and insights from the simulation will also be discussed.

1 INTRODUCTION

Debris flow is a mass wasting process of poorly sorted sediments surging down a slope in response to gravitational attraction (Iverson 1997). The landslide debris travels along the natural recessed drainage channel at high velocity as it mixes with the channel water. Debris flow is a common form of natural terrain landslides in Hong Kong. Because of its potential of high mobility, even a small-scale debris flow that occurs in a dense urban setting is liable to result in severe consequences. Mitigation measures, such as rigid and flexible barriers, are deployed to intercept debris flows. The structural requirements of the mitigation measures depend heavily on the design load exerted by the impacting landslide debris, which increases with the impact velocity of debris (e.g. Kwan, 2012).

The dynamic interaction of debris flow with baffles is still an emerging area of research to both the academics and the practitioners. Both continuum modeling (e.g. Pudasaini & Hutter 2007; Pudasaini & Domnik 2012) and discrete element method (DEM) modeling (e.g. Ng et al. 2013) are adopted to analyze the flow characteristics of granular debris flows. The interactions (e.g. development of dead zone and deposition profile) between debris and protection structure such as breaking mound (H´akonard´ottir & Hogg 2005), rigid walls (Teufelsbauer et al. 2011) and individual obstacle (Gray et al. 2003) are elaborated in the literature. Effect of granular debris flow baffles installed immediately upstream of rigid barriers on dissipation of flow energy has also been studied (Choi et al. 2014a, 2014b; Law 2015; Ng et al. 2014). Further to these, this paper will present the use of DEM in simulating landslide mobility and soil-baffles interactions, using the flow path of a historical landslide as a demonstration, and discuss the performance of debris-resisting baffles in impeding debris velocity at various locations along the flow path. Important considerations and insights from the study will also be discussed.

2 DEM SIMULATION

DEM was introduced in geomechanics by Cundall & Strack (1979) and was later adopted as a research tool by many other researchers (e.g. Labra et al. 2008; Sibille et al. 2008; Thompson et al. 2009). It is an appropriate tool to model debris flow and snow avalanche because of their granular flow nature (Zwinger 2000; Nicot 2004; Hutter et al. 2005; Pudasaini & Hutter 2007). In DEM modelling, the discrete elements displace

independent of one another and interact only at contacts between the particles and the boundary. The particle motion of each discrete element is calculated from the forces acting on it by the Newton's laws of motion. The displacements and rotations of the discrete elements are computed as the calculation progresses. New contacts and complete detachment between discrete elements are recognized automatically. The contact forces and displacements of a stressed assembly of particles are found by tracing the movements of the individual particles. The simulation is implemented by a timestepping algorithm in which the velocities and accelerations are constant within each timestep. The recent advancement of computer hardware and parallel computing technology enables the analysis of granular flows using three-dimensional DEM efficiently.

The capability of DEM to simulate the soil-baffles interactions is verified by benchmarking with flume model test results. The capability of DEM to carry out debris mobility modelling is verified by benchmarking with the field evidence of the debris flow event that occurred above Yu Tung Road, Lantau in June 2008. The open source 3D software called LIGGGHTS (Kloss & Goniva 2010) is adopted to model landslide debris. The software is developed based on Large-scale Atomic/Molecular Massively Parallel Simulator (LAMMPS), which is developed for molecular research by Sandia National Laboratories, US Government. The verifications using flume model test and the historical debris flow event are elaborated below.

Details of the calibration using flume model test results are reported in Choi et al. (2014b). Flume model tests were carried out to validate DEM in carrying out analysis of debris-baffles interactions. The input parameters adopted by the DEM is given in Choi et al. (2014b). The comparison of the flow profile between the flume model test and DEM is given in Figure 1, which indicates consistent outcomes.

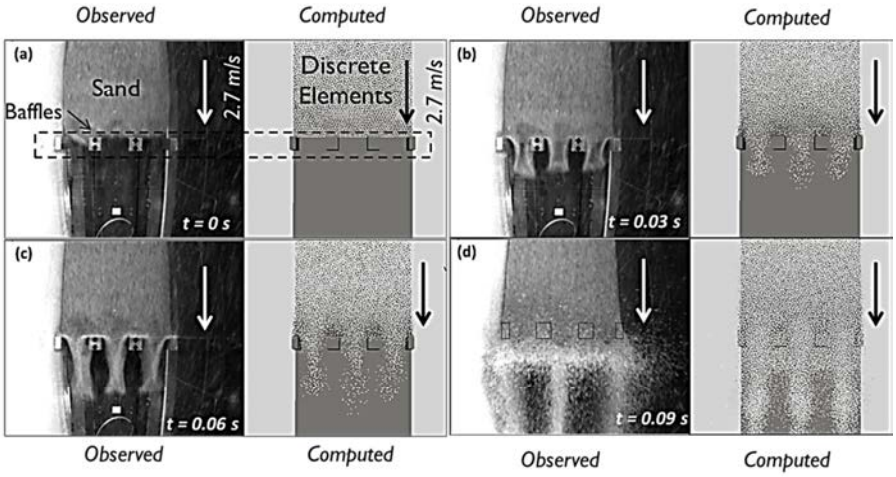

Figure 1: Comparison of Flume Experiments and Computed Flow Kinematics using DEM (Choi et al. 2014b): (a) t = 0 s; (b) t = 0.03 s; (c) t = 0.06 s; (d) t =0.09 s

Field data obtained from the June 2008 Yu Tung Road event is used to validate DEM in terms of debris mobility modelling. Figure 2 shows the aerial view of the debris flow above Yu Tung Road taken on 9 June 2008 (AECOM 2012). The debris flow involved a single landslide source area. The landslide source comprised subangular to subrounded cobbles with many gravels and occasional boulders in a silty/clayey sandy matrix. The landslide debris reached Yu Tung Road, resulting in blockage of both westbound lanes and flooding of the adjacent Cheung Tung Road. About 2,600 m^3 of debris was involved which had a runout distance of about 600 m, and all the debris reached Yu Tung Road. The lower portion of the channelized debris flow was captured on video by a member of the public, although the exact time of the failure is not known.

According to AECOM (2012), the velocity of the debris was estimated to be about 12 m/s at chainage = 100 m based on the super-elevation data measured (Hungr et al., 1984). The measured velocity data beyond chainage = 400 m is based on both the super-elevation data and the video footage. Further details of the field evidence is documented in AECOM (2012). The computed frontal velocity from the DEM is compared with the field data. The frontal velocity is calculated by the average tangential velocity of the most frontal 10% of

the discrete elements that simulate the landslide debris. Discrete elements which have a coordination number of zero are considered to be isolated particles and are not counted in the calculation of the frontal velocity. The input parameters adopted by the DEM are given in Table 1. Derivation of the input parameters is discussed in Section 4 in detail. No baffle is placed on the flow path in this validation exercise. Figure 3 shows the comparison between the computed velocity profile and the measured data point. A close match between the computed velocity profile and measured data point is observed. It is interesting to note that the measured frontal velocity is increasing from Point B to E, but the DEM calculations give an opposite trend. According to AECOM (2012), the flow path from B to E becomes less channelized and the gradient decreases to less than 15 , which explains the computed decrease in velocity in DEM. The relatively high measured frontal velocity from Point B to E might deserve further research.

Figure 2: Aerial View of the Debris Flow Event above Yu Tung Road Taken on 9 June 2008

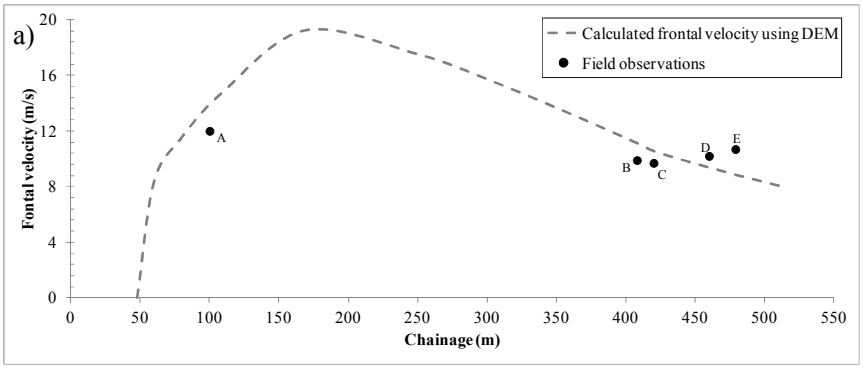

Figure 3: (a) Comparison between the Computed Velocity Profile using DEM and Field Evidence of Debris Flow above Yu Tung Road in June 2008 and (b) the Flow Profile at time = 32 s; the Dashed Lines represent the locations where field evidence of flow velocities are available

3 MODEL CONFIGURATION

The same DEM software, i.e. LIGGGHTS, is also adopted to model the motion of debris impacting on baffles. Figure 4 shows the numerical model setup. The topography is developed based on the data obtained using the Light Detection and Ranging technology. The computation domain is 650 m in length and 180 m in width.

The grid size of the terrain is 2 m x 2 m. The natural terrain above Yu Tung Road is represented by mesh solid which is specified using interconnected triangulated meshes. The stereolithography (STL) file format is used to store the location and dimension of the triangles. The source area of the debris flow is indicated in Figure 4. Two rows of baffles are installed at staggered pattern at four different locations along the flow path (i.e. locations 1, 2, 3 and 4 in Figure 4). The transverse spacing between each adjacent baffle (D) is 3 m. The baffle height is equal to 3 m. The row spacing (L) between two adjacent rows of baffles is 9 m. The ratio between the row spacing and transverse spacing (L/D) is equal to 3. The L/D =3 corresponds to the optimum row spacing for baffle arrays to maximize the impedance effect on impacting debris (Law 2015).

Table 1: DEM Input Parameters

Input parameter	Value
Number of discrete elements	200, 000
Particle diameter (m)	0.3
Particle stiffness (N/m)	1×10^8
Discrete element friction angle (^{o})	11^o
Coefficient of restitution	0.5
Coefficient of rolling friction	0.7

In each simulation, only one location is installed with baffles. The chainage of baffle locations 1,2,3 and 4 are 100 m, 200 m, 340 m and 450 m respectively. A terminal rigid barrier is assumed to be installed at chainage = 500 m to retain landslide debris. Baffle location 1 is characterized by its proximity to the source area. Baffle location 2 is characterized by the high frontal velocity (i.e. ~18 m/s) of debris (see Figure 3a). Baffle location 3 is approximately halfway from the location of peak frontal velocity to the terminal barrier. Baffle location 4 is characterized by its proximity to the terminal barrier. The performance of debris-resisting baffles in impeding debris velocity at the four locations along the flow path is studied.

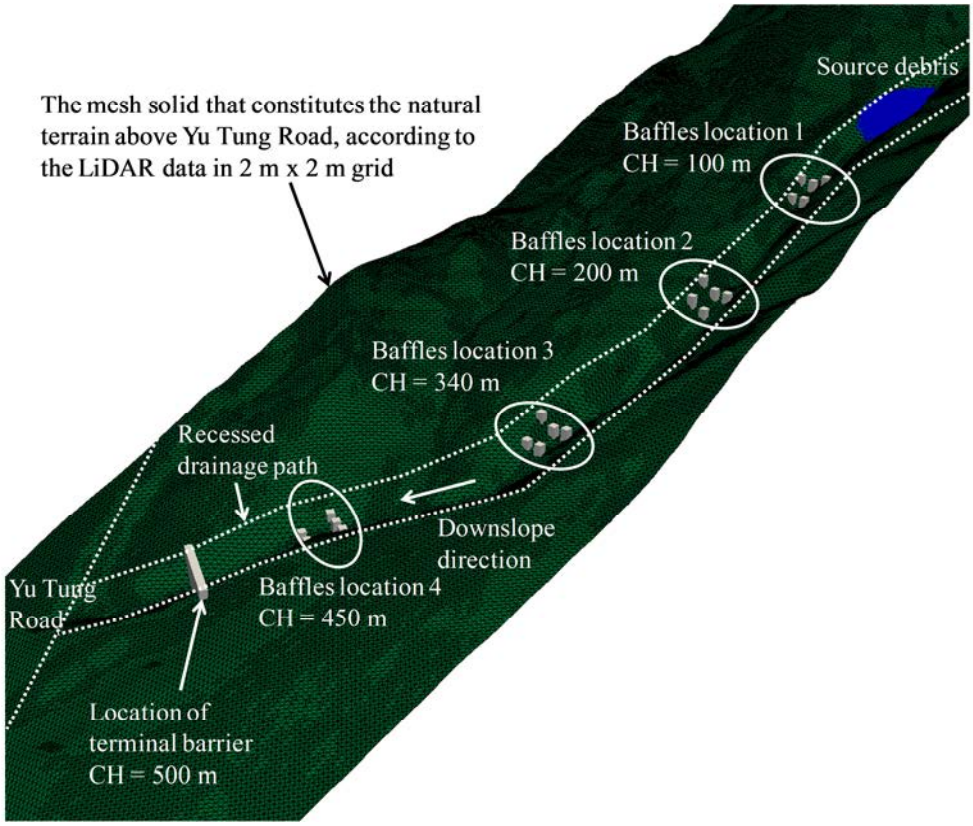

Figure 4: Numerical Model Setup

4 INPUT PARAMETERS

The simulation of the motion of landslide debris using DEM requires the use of a number of key input parameters, including the size of discrete element, the contact friction angle, the coefficient of restitution, the contact stiffness, as well as the coefficient of rolling friction. The input parameters for this study (see Table 1) are determined through a review of the literature, except the coefficient of contact friction for any two contacting bodies, which is obtained through benchmarking using the June 2008 Yu Tung Road event.

Due to the constraint of computation capacity, it is not possible to model the motion of individual grains in debris flow. Based on the study by Law (2015), the size of discrete elements has to be at least 10 times smaller than the baffle spacing in order to avoid unrealistic clogging. Further reduction of particle does not result in any change of the computed results. The spacing between baffles in one row is set to be 3 m. The diameter of each discrete element should therefore be less than 0.3 m. The required number of discrete element of 0.3 m in diameter is around 200,000 to give the volume of the landslide debris of 2,600 m^3.

The local rheology of the flow material is simulated through the assignment of contact behaviour of the discrete elements and the flow path. Frictional granular flow is the focus of this study. The relative translational and rotational motions between the discrete elements are mainly resisted by the contact friction. Assuming that the two objects in contact have the same roughness, the frictional force (F_f) between two contacting bodies is calculated using the following equation:

$$F_f = \mu_f * F_s \tag{1}$$

where μ_f is the coefficient of friction between the two objects. Based on benchmarking using the June 2008 Yu Tung Road event, the coefficient of friction is set as 0.2.

Discrete elements experience repulsive force when they are in contact with each other. The stiffness model calculates repulsive forces between discrete elements. Given the contact stiffness is not unreasonably low, the contact stiffness of the discrete element has negligible influence on the computed mobility of granular material (Crosta et al. 2001). The stiffness of discrete element and barrier are both chosen to be $1x10^8$ (N/m).

Calvetti & Nova (2004) observed that, as a consequence of the non-angular shape of the particles, the macroscopic friction angle of the granular mass is generally very low, typically much less than 30°, irrespective of the value of the inter-particle friction angle adopted. Calvetti et al. (2003) and Tamagnini et al. (2005) emphasized the need to inhibit rolling resistance in the discrete spherical particles. The directional constant torque models (e.g., Zhou et al. 2003) apply a constant torque on a particle to represent the rolling friction. The direction of the torque is always against the relative rotation between the two contact entities. The torque is applied in pairs on each pair of particles in contact. An example of the directional constant torque model could be found below, which is a simplified version of the formula reported by Zhou et al. (1999):

$$M_r = -(\omega_{rel}/|\omega_{rel}|)\mu_r R_r F_s \tag{2}$$

$$\omega_{rel} = \omega_i - \omega_j \tag{3}$$

where ω_i and ω_j are the angular velocities of sphere i and j respectively, ω_{rel} is the relative angular velocity between them, μ_r is the rolling friction coefficient, F_s is the normal contact force, and R_r is the radius of the discrete element. The value of the rolling friction coefficient μ_r is an unknown and can be determined through calibration with experiments. Based on the parametric study presented in Law (2015), the coefficient of rolling friction is set to be 0.7.

Based on the benchmarking results discussed in Section 2, the input parameters are therefore considered to be appropriate to simulate the motion of debris in this study.

5 MODELLING PROCEDURES

Each numerical analysis is divided into two stages, namely preparation and flow stages. In the preparation stage, an assembly of discrete elements with random packing is positioned on the source area under the action of gravity. In the flow stage, the discrete elements are allowed to move beyond the source area and travel

downslope under the action of gravity. The velocity and the displacement of the frontal debris are recorded and analyzed throughout the process. In each simulation, only one location (either location 1, 2, 3 or 4) is installed with baffle arrays. The performance of debris-resisting baffles in impeding debris velocity at various locations along the flow path is observed and evaluated.

6 IMPEDENCE EFFECTS OF BAFFLE ARRAYS AT DIFFERENT LOCATIONS

Figure 5 shows the comparison between the computed velocity profile without baffles (i.e. the control case, indicated by solid line) and those with baffles at different positions (indicated by dotted line, dashed line, dot-dashed line and hollow line at location 1 (chainage = 100 m), location 2 (chainage = 200 m), location 3 (chainage = 340 m) and location 4 (chainage = 450 m) respectively).

The key observations are given below.

(a) No significant drop of frontal velocity is observed right at the baffle location.
Based on the findings reported by Law (2015), the frontal debris that passes through the baffle arrays is not instantaneously decelerated due to the absence of debris deposit behind the baffle arrays during the frontal impact. As a result, the frontal velocity of debris right at the baffle location is found to be similar to the case without baffles.

(b) Debris slows down after passing through the baffle arrays, as compared to the control case.
As compared to the control case, the slow-down process is due to by the reduction of discharge due to the run-up and pile-up processes of debris behind the baffles (Law 2015). The relationship between the discharge and frontal velocity of debris can be explained by the following equation, which calculate the lateral driving force (P) acting on the frontal debris due to the lateral earth pressure of the upstream debris. The equation is derived based on the work done by Hungr (1995).

$$P = \gamma k \frac{\Delta H}{\Delta s} H \cos\alpha \tag{4}$$

where γ is the unit weight, k is the lateral earth pressure coefficient, H is the thickness, ΔH is the difference in thickness of two adjacent blocks of landslide debris, Δs is the tangential distance between the two adjacent blocks of landslide debris and α is the slope inclination. Graphical illustration of each term in Equation 4 is given in Figure 6. As shown in Equation 4, the lateral driving force (P) acting on the frontal debris decrease when the thickness of the upstream debris is reduced. After passing through the baffle arrays, the thickness of the debris reduces as its discharge from the baffles decreases, resulting in a drop in its frontal velocity.

(c) Debris further slows down at bend, as compared to the control case.
The difference in the frontal velocity between the control case and those with baffles at location 1, 2 and 3 increases after chainage = 400 m, where a relative sharp bend of the recessed drainage path is present. In other words, debris travelling through the bend has larger deceleration when the velocity of debris is lowered by the baffle arrays.

(d) Impedance effect of baffle arrays increases with the impact velocity to baffle arrays.
The percentage reductions of frontal velocity at the terminal barrier, as compared with the control case, are 49% (location 1), 56% (location 2), 30% (location 3) and 6% (location 4) respectively. The baffles at location 2 area are able to achieve a higher reduction of frontal velocity in the end probably because they intercept the landslide debris at a higher impact velocity.

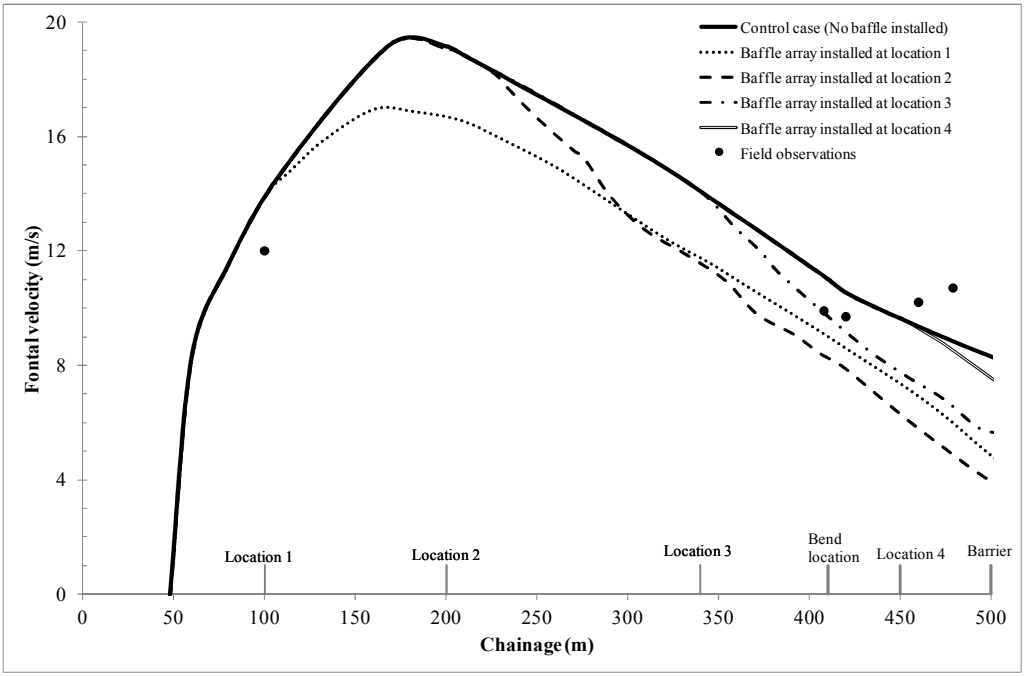

Figure 5: Comparison between the Computed Velocity Profile without Baffles and those with Baffles at Different Positions

(e) Baffle arrays that are located too close to the source area or the terminal barrier are relatively ineffective in reducing the frontal velocity at the terminal barrier.

The frontal velocity close to the source area is far below its peak velocity. There is still certain distance along the flow path for the debris to pick up its velocity before slowing down. Therefore, the baffle arrays close to the source area are not in optimal performance in reducing the frontal velocity of debris reaching the terminal barrier. As there is no significant drop of frontal velocity right at the baffle location, and there is insufficient distance for the debris to further slow down, baffle arrays located too close to the terminal barrier are also not in optimal performance in reducing the frontal velocity of debris reaching the terminal barrier.

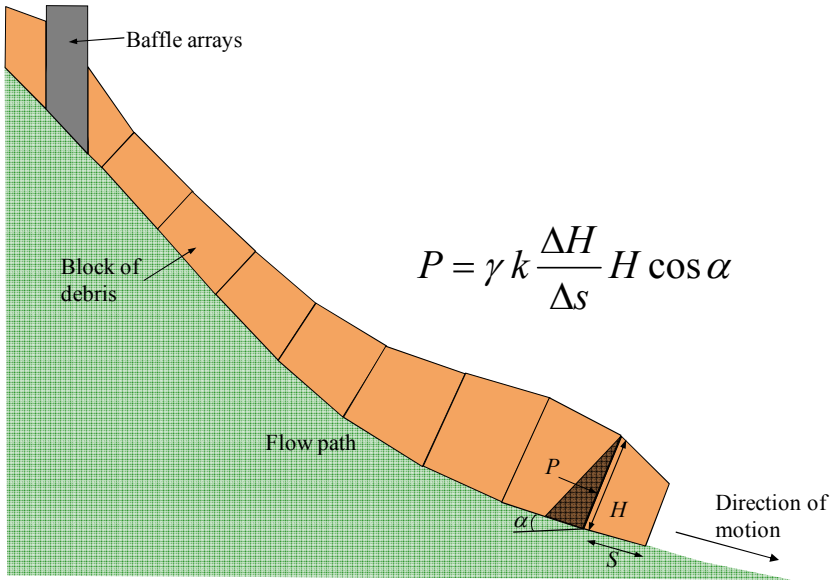

Figure 6: Lateral Driving Force (P) Acting on the Frontal Debris Due to the Lateral Earth Pressure of the Upstream Debris (Hungr, 1995) (please refer to Equation 4 for the definition of each term)

7 CONCLUSIONS

The performance of debris-resisting baffles in impeding debris velocity at various locations along the flow path is studied using DEM. A number of key observations are presented. The baffles are found to reduce the frontal velocity of landslide debris that reaches the terminal rigid barrier. Since the impact pressure of landslide debris on a rigid barrier depends on the impact velocity (Kwan, 2012), and the peak impact force experienced by a rigid barrier is contributed mainly by the frontal impact (Law, 2015), the reduction of frontal debris velocity will reduce the peak impact force on a rigid barrier. The actual performance of baffle arrays are affected by a number of factors, such as the channel topography, debris rheological characteristics, entrainment behaviour, etc. The observations may not be fully applicable to all debris flow events. Also, the frontal velocity of impacting debris is not the only controlling factor that determine the structural requirements of structural protection measures. Other factors, such as discharge rate and deposition mechanisms, are equally important.

ACKNOWLEDGEMENTS

This paper is published with the permission of the Head of the Geotechnical Engineering Office and the Director of Civil Engineering and Development, Government of the Hong Kong Special Administrative Region.

REFERENCES

AECOM 2012. *Detailed Study of the 7 June 2008 Landslides on the Hillside above Yu Tung Road, Tung Chung*. GEO Report No. 271. Geotechnical Engineering Office, Hong Kong.

Calvetti, F. & Nova, R. 2004. Micromechanical Approach to Slope Stability Analysis. In F. Darve & I. Vardoulakis (eds), *Degradation and instabilities in Geomaterials*: 235-254. Springer, Verlag.

Calvetti, F., Viggiani, G. & Tamagnini, C. 2003. A numerical investigation of the incremental behavior of granular soils. *Rivista Italiana di Geotecnica*, 37(3): 11-29.

Chiou, M.C. 2005. *Modelling Dry Granular Avalanches Past Different Obstructs: Numerical Simulations and Laboratory Analyses*. Dissertation, Technical University Darmstadt, Germany.

Choi, C.E., Ng, C.W.W., Song, D., Kwan, J.H.S., Shiu, H.Y.K., Ho, K.K.S. & Koo, R.C.H. 2014a. Flume investigation of landslide debris baffles. *Canadian Geotechnical Journal*, 51(5): 540-533.

Choi, C.E., Ng, C.W.W., Song, D., Law, R.P.H., Kwan, J.H.S., & Ho, K.K.S. 2014b. A computational investigation of baffle configuration on the impedance of channelized debris flow. *Canadian Geotechnical Journal*, published online 14 July 2014 (In press).

Crosta, G.B., Calvetti, F., Imposimato, S., Roddeman, D., Frattin, P. & Agliardi, F. 2001. *Granular Flows and Numerical Modeling of Landslides*. Contract No EVG1–CT-1999-00007, Universita delgi Studi di Milano, Bicocca.

Cundall, P.A. & Strack, O.D.L. 1979. A discrete numerical model for granular assemblies. *Geotechnique,* 29(1): 47-65.

Gray, J.M.N.T., Tai, Y.C. & Noelle, S. 2003. Shock waves, dead zones and particle-free regions in rapid granular free-surface flows. *Journal of Fluid Mechanics*, 491: 161-181.

Hákonardóttir, K.M. & Hogg, A. 2005. Oblique shocks in rapid granular flows. *Physics of Fluids*, 17(7): 1-10.

Hungr, O., Morgan, G.C. & Kellerhals, R. 1984. Quantitative analysis of debris torrent hazards for design of remedial measures. *Canadian Geotechnical Journal*, 21: 663-677.

Hutter, K., Wang, Y. & Pudasaini, S.P. 2005. The Savage-Hutter avalanche model: how far can it be pushed? *Philos Transact A Math Phys Eng Sci*., 363(1832): 1507-1528.

Iverson, R.M. 1997. The physics of debris flow. *Review of Geophysics*, 35(3): 245-296.

Kloss, C., Goniva, C., Hager, A., Amberger, S., Pirker, S. 2012. Models, algorithms and validation for opensource DEM and CFD-DEM. *Progress in Computational Fluid Dynamics*, *An Int. J*., 12(2-3): 140-152.

Kwan, J.S.H. (2012). Supplementary Technical Guidance on Design of Rigid Debris-resisting Barriers. GEO Report No. 270. Geotechnical Engineering Office, Hong Kong, 91 p.

Labra, C., Rojek, J., Onate, E. & Zarate, F. 2008. Advances in discrete element modelling of underground excavations. *ActaGeotech*., 3(4): 317-322.

Law, R.P.H. 2015. *Computational Study of Granular Debris Flow Impact on Rigid Barriers and Baffles*. Doctorial thesis. Hong Kong University of Science and Technology, Hong Kong.

Ng, C.W.W., Choi, C.E. & Law, P.H. 2013. Longitudinal spreading mechanisms of channelized granular flow. *Geomorphology*, 194: 84-93.

Ng, C.W.W., Choi, C.E., Song, D., Kwan, J.H.S., Koo, R.C.H., Shiu, H.Y.K. & Ho, K.K.S. 2014. Physical modelling of baffles influence on landslide debris mobility. *Landslides*, Published online on 28 February 2014.

Nicot, F. 2004. Constitutive modelling of snow as a cohesive granular material. *Granular Matter*, 6(1): 47-60.

Pudasaini, S.P. & Domnik, B. 2012. Full two-dimensional rapid chute flows of simple viscoplastic granular materials with a pressure-dependent dynamic slip-velocity and their numerical simulations. *Journal of Non-Newtonian Fluid Mechanics*, 173-174: 72-86.

Pudasaini, S.P., Hsiau, S., Wang, Y. & Hutter, K. 2005. Velocity measurements in dry granular avalanches using particle image velocimetry technique and comparison with theoretical predictions. *Physics of Fluids*, 17(9): 1-10.

Pudasaini, S.P. & Hutter, K. 2007. *Avalanche Dynamics: Dynamics of Rapid Flows of Dense Granular Avalanches*. Springer, Berlin.

Sibille, L., Donze, F.-V., Nicot, F., Chareyre, B. & Darve, F. 2008. From bifurcation to failure in a granular material: a DEM analysis. *Acta Geotechnica*, 3(1): 15-24.

Tamagnini, C., Calvetti, F. & Viggiani, G. 2005. An assessment of plasticity theories for modeling the incrementally nonlinear behavior of granular soils. *Journal of Engineering Mathematics*, 52(1-3): 265-291.

Teufelsbauer, H., Wang, Y., Pudasaini, S.P., Borja, R.I. & Wu, W. 2011. DEM simulation of impact force exerted by granular flow on rigid structures. *Acta Geotechnica*, 6(3): 119-133.

Thompson, N., Bennett, M.R. & Petford, N. 2009. Analyses on granular mass movement mechanics and deformation with distinct element numerical modelling: implications for large-scale rock and debris avalanches. *Acta Geotechnica*, 4(4): 233-247.

Zhou, Y.C., Wright, B.D., Yang, R.Y., Xu, B.H. & Yu, A.B. 1999. Rolling friction in the dynamic simulation of sandpile formation, *Physica A: Statistical Mechanics and its Applications*, 269(2-4): 536-553.

Zhou, Y.C., Xu, B.H., Zou, R.P., Yu, A.B. & Zulli, P. 2003. Stress distribution in a sandpile formed on a deflected base, *Advanced Powder Technology*, 14(4): 401-410.

Zwinger, T. 2000. *Dynamik einer Trockenschneelawine auf beliebig geformten Bergha ngen*. Ph.D. Thesis. Vienna University of Technology, Austria.

Study of Interaction between Landslide Debris and Debris-resisting Structures

J.S.H. Kwan, W.K. Pun & Y.K. Shiu
Geotechnical Engineering Office, Civil Engineering and Development Department, the Government of the Hong Kong SAR

C.W.W. Ng & D. Song
Department of Civil and Environmental Engineering, Hong Kong University of Science and Technology

J. Yiu
Ove Arup and Partners Hong Kong Limited, Hong Kong

ABSTRACT

Natural terrain hillside catchments are systematically selected and their landslide risk dealt with under Government's Landslip Prevention and Mitigation Programme. Experience shows that landslide debris-resisting structures can provide practical and effective means for mitigating the natural terrain landslide risk. While state-of-the-art engineering approach is being adopted, there is still much uncertainty in the design of such structures. Concerted efforts of the geotechnical profession and experts in other engineering disciplines have been made to enhance understanding of the dynamic interaction between landslide debris and debris-resisting structures as well as the performance of landslide debris-resisting structures for optimisation of the design approach. A series of studies including physical tests and numerical investigations have been carried out. This paper introduces the studies and presents some initial key findings.

1 INTRODUCTION

1.1 Landslide Risk in Hong Kong

In the past 30 years, resources had been devoted to upgrading substandard man-made slopes close to developments. While landslide risks posed by man-made slopes have been substantially reduced, the landslide risk associated with natural hillside failures increases progressively due to encroachment of more urban development or redevelopment on steep natural hillsides.

Disruptions caused by the landslides during and after the rainstorm on 7 June 2008 are the vivid examples which indicate the risk that Hong Kong is now exposed to. The rainstorm on that day hit the western part of Lantau Island resulting in more than 2,400 natural terrain landslides in the area. Many of the landslides affected important facilities. For example, one of the major landslides developed into debris flow which affected the North Lantau Expressway and as a result the road had to be closed for 16 hours.

To deal with the natural terrain landslide risk, the Landslip Prevention and Mitigation Programme (LPMitP) was commenced in 2010 to dovetail the Landslip Preventive Measures Programme that focused on upgrading of man-made slopes. The LPMitP commits a substantial part of its annual funding to the study and risk mitigation works of 30 vulnerable catchment areas each year.

1.2 Natural terrain hazard mitigation measures

Natural terrain catchments are sizable; slope stabilisation works as a means to mitigate landslide hazard are often impractical and environmentally undesirable. The preferred approach is to provide defense measures to mitigate the hazard caused by landslide debris. In most cases, the defense measures adopted in Hong Kong consist of the provision of a rigid (concrete) barrier or a flexible barrier at the toe of a natural hillside catchment (see Figure 1).

(a) Rigid debris-resisting barrier

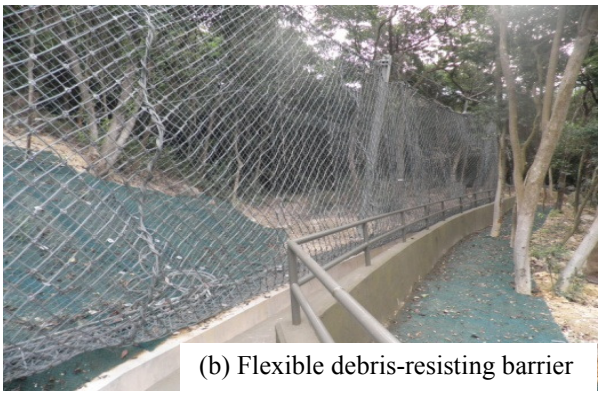

(b) Flexible debris-resisting barrier

Figure 1: Debris-resisting Barriers

2 DESIGN OF DEBRIS-RESISTING BARRIERS

2.1 Current design practice

Rigid barriers are typically constructed using reinforced concrete to intercept channelised debris flows. They are designed to resist the impact force of the debris and occasional boulders in the debris front. Lo (2000) recommends the use of the hydrodynamic pressure equation (i.e. $p = \alpha \rho v^2$ where p = debris impact pressure, α = dynamic pressure coefficient, ρ = debris density and v = debris impact velocity) to estimate the debris impact load. For estimation of the boulder impact load, Lo (op cit) suggests using the Hertz Equation (with an appropriate load reduction factor of 10). Kwan (2012) updated the above recommendation in respect of the value of dynamic pressure coefficient, with the coefficient α revised down from 3 to 2.5. The current guidelines recommend the consideration of multiple phases of landslide debris impacting on a barrier, and the use of the maximum calculated debris impact velocity for design.

Proprietary rockfall barriers are available from many suppliers. They are mostly based on empirical design with capacity verified by full scale testing. Rockfall barriers are rated by the energy that a set of panels can absorb without being breached. They are tested and certified against various national or European standards (EOTA 2008). Over the past years, flexible rockfall barriers have occasionally been hit by debris flows and landslide debris in different countries. A number of field cases and physical tests have demonstrated that flexible barriers would be capable of arresting a certain amount of landslide debris (Duffy 1998).

The use of flexible rockfall barrier as landslide risk mitigation measure is a highly attractive option, as it is visually less intrusive compared to rigid barriers e.g. built using reinforced concrete. Flexible barriers also have the advantage of relatively easy construction, as they are usually made of relatively light-weight materials. However, there lacks well-established design guidelines for flexible debris-resisting barriers.

Lo (2000) reviewed the use of flexible debris-resisting barriers. Implicit in its recommendation is the design of the barrier to resist the full energy of landslide debris. This is likely to be conservative because as the debris deposits behind the barrier, the deposited debris will dissipate some of the impact energy through base friction or internal deformation. Sun & Law (2012) proposed analytical solutions for calculating the energy loading with consideration given to energy loss caused by basal resistance experienced by landslide debris. Wartmann & Salzmann (2002) described a design approach under which the energy from the first 4 seconds of the estimated peak flow of debris is to be resisted. Subsequently, WSL (2009) proposed to design flexible barriers based on the dynamic impact pressure and hydrostatic pressure from debris disposition.

GEO put forward an empirical design approach for the prescriptive use of flexible rockfall barriers to mitigate risk of open hillside failures (GEO 2014). It is based on the consideration of landslide risk and a statistical assessment of the scale and the mobility of previous landslides. A number of qualifying criteria have to be satisfied before such prescribed flexible barriers can be adopted.

Interim design guidelines based on the force approach were proposed by Kwan & Cheung (2012). Hydrodynamic pressure equation is employed for estimation of the debris impact pressure. The recommended value of α for flexible debris-resisting barriers design is 2.0. This value includes the effects of impact boulders

of an equivalent dimension less than 2 m in diameter.

2.2 The need to understand debris-barrier interaction

When landslide debris is intercepted by a barrier, landslide debris gradually fills up the space behind the barrier. This filling-up process involves rebound of a certain amount of debris materials and this leads to turbulent mixing. Debris deposited against the barrier could provide cushioning effects conducive to alleviate the impact of debris from behind. The debris-barrier interaction is highly dynamic. For flexible debris-resisting barriers, the interaction is even more complicated since the barriers deform non-linearly under the impact load.

The present design methodology does not consider the debris-barrier interaction. The design debris impact velocity is determined with consideration of a 'free field' condition. A number of R&D initiatives are being carried out with a view to driving technical advances in design of natural terrain mitigation measures.

3 RECENT TECHNICAL DEVELOPMENT WORKS

3.1 R&D initiatives

The ongoing R&D initiatives include physical tests and numerical investigation viz. (a) physical flume tests of dry sand impacting on rigid barriers, (b) centrifuge tests of dry sand and viscous fluid impacting on flexible barriers, and (c) numerical modelling using LS-DYNA.

3.2 Physical flume tests of dry sand impacting on rigid barriers

A 5 m long flume with a channel base width of 0.2 m was used for the tests. Side walls are about 0.5 m in height, perpendicular to the channel bed. Dry sand was used in the test to simulate a debris flow. The angle of repose of the sand was 33^{o} and the interface friction angle between the sand and flume bed was 23^{o}. The initial bulk density of the sand mass was about 1,680 kg/m^3. At the top end of the flume was a sand storage tank. Sand can be released into the flume by opening a flip gate that was attached to the tank. A 0.1 m high vertical barrier model was installed in the flume. A plastic film was placed on the flume bed to reduce the basal resistance so that the sand flow can attain a velocity at the position of barrier model. The interface friction

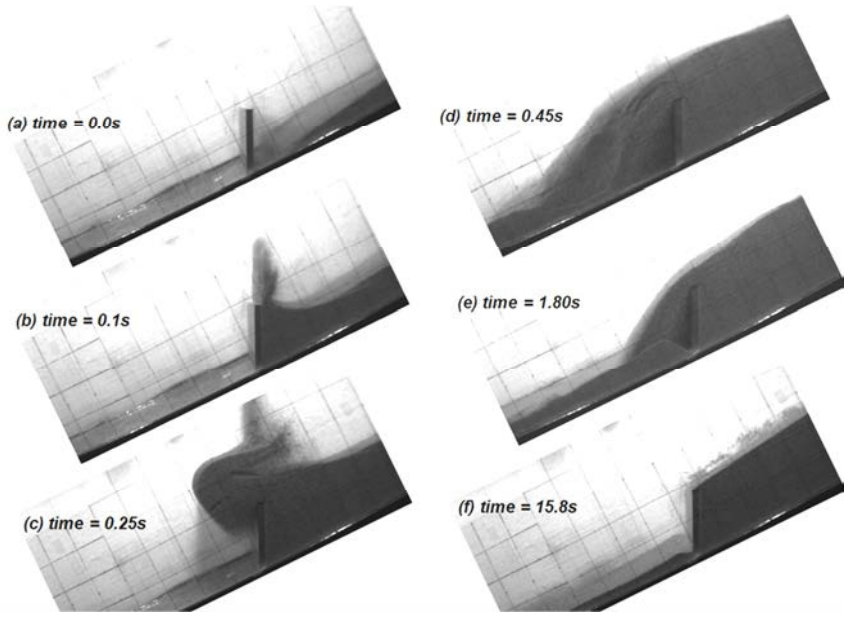

Figure 2: High-speed Camera Images

angle was measured following the procedures described by Savage and Hutter (1989), of which the sand was filled into a cylinder placed inside the flume, the interface friction angle was measured by increasing the inclination of the flume until the cylinder starts to slide.

The flume inclination was set to be 26° to facilitate the development of sand flow corresponding to a Froude number of 2.6 ($F_r = v / (g\,h)^{0.5}$, where v is debris velocity, g is gravitational acceleration and h is debris depth), similar to the local design scenarios where $F_r \approx 3$.

The flume test was recorded with the use of a high-speed camera which could capture 100 images per second. Figure 2 shows the image records in sequence.

Figure 2(a) shows the instant when the dry sand flow arrived at the barrier location. For discussion purposes, the time of this instant is denoted as t = 0.0 s. After 0.1 second, the sand flow filled up the retention zone behind the barrier and splashing of the sand is also evident. At t = 0.25 s, debris that was not trapped behind the barrier started the overtopping process and launched into a ballistic flight. Subsequently, debris overflowing from the crest of the barrier travelled along a projectile path and landed on the flume bed at a distance of about 0.2 m downstream of the barrier (see Figure 2(d)). This process continued for about 16 seconds. At the end of the test, sands piled up behind the barrier and the deposition angle was about 33°. The study did not only reveal the dynamic debris deposition mechanism behind rigid barriers but also provided parameters for design of multiple barriers (Kwan et al. 2015).

3.3 Centrifuge tests

A series of centrifuge tests of landslide debris impacting on flexible barriers has been conducted by the Hong Kong University of Science and Technology. A specially designed spring system, which exhibited a bilinear stiffness profile, was developed to replicate the load-deformation characteristics of energy dissipation devices in flexible barriers. Tests using dry sand and viscous fluid as landslide debris had been carried out. The density of the dry sand was 1530 kg/m^3 and the internal friction angle was 31°. The viscous fluid was a mixture of zinc chloride solution and glycerol and carboxyl methyl cellulose with a density of 1580 kg/m^3.

The tests were carried out under 25-g. During the test, the testing materials were released on to a ramp inclined at 25°. A flexible barrier model comprising 4 cables attached to the specially designed spring system was installed at the end of the ramp. Control experiments undertaken without the flexible barrier model indicated that the Froude number of the debris flow at the position of the flexible barrier model was about 4. The scaling laws stated in Bowman et al (2010) are followed, of which a factor of unity is applied to the flow velocity.

Instrumentation included high-speed cameras, load cells and laser sensors. High resolution images, loading of cables and extension of cables were obtained. Figure 3 shows the image of the viscous fluid at the instant when it was impacting on the flexible barrier model as well as the vector plot of the velocity of the viscous fluid.

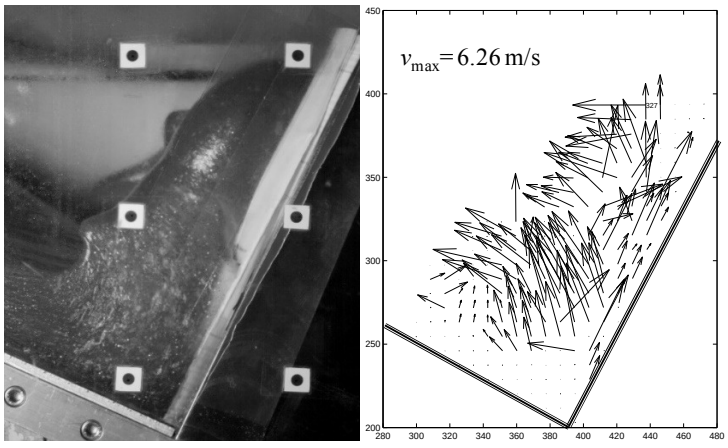

Figure 3: Viscous Fluid Impacting on the Flexible Barrier Model

Interpretation on the measured cable forces is in progress. The cable forces would be used to back calculate the dynamic impact pressure and the corresponding value of α. The test results could be used for further calibration of the numerical analyses introduced in Section 3.4.

3.4 Numerical modelling using LS-DYNA

Depth-averaged continuum numerical models, viz. 2d-DMM (Kwan & Sun 2006) and DAN/W (Hungr 1995), prove practical for debris mobility analysis to produce design debris velocity and thickness. They are commonly adopted in local design practice where free field conditions are considered. In the depth-averaged formulations, debris is discretised into a series of inter-connected slices or columns. The use of these models to investigate the debris-barrier interaction is constrained by the connectivity requirement. Moreover, vertical debris movements within the debris slices or columns are not considered by the depth-averaged formulations, and thus simulations of turbulent mixing at the debris-barrier impact location are not possible.

A more advanced numerical model LS-DYNA has been used for numerical investigation purpose. It is a multi-purpose finite element program used to analyse the nonlinear response of structures. A special module has been developed to incorporate into LS-DYNA for debris mobility analysis. It handles scalar advection in an Eulerian grid and solves equations of motion based on an Arbitrary Lagrangian-Eulerian description of finite-element method. Landslide debris is assumed to be elasto-plastic which follows Drucker-Prager yield criteria. The computational domain is discretised into an array of hexahedral elements which allows for a genuine 3-dimenional debris mobility analysis. The ground surface on which landslide debris travels on is modelled using rigid shell elements. Coulomb frictional rule is assumed at the interface between the landslide debris and the shell surface.

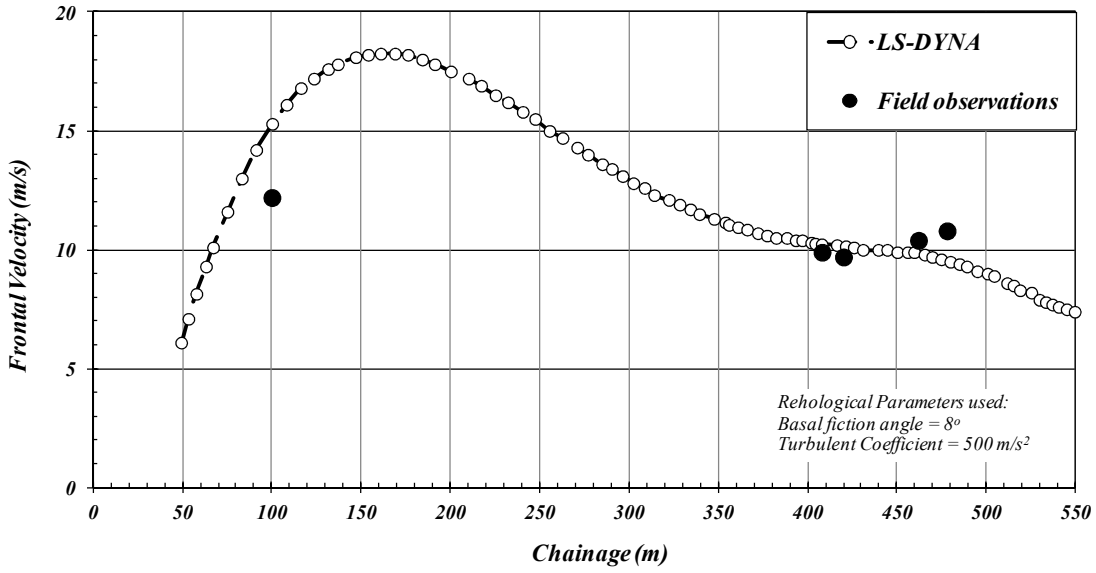

Figure 4: Frontal Velocity of Yu Tung Road Debris Flow

The LS-DYNA model had been benchmarked against several well-documented laboratory and field studies. Kwan et al. (2015) reported the back analysed results of Yu Tung Road Debris Flow. In the analysis, an additional damping force proportional to the square of the debris velocity was applied to retard the debris motion. This damping force accounted for the energy loss due to the turbulence of debris flows similar to Voellmy rheology. Figure 4 shows the calculated debris frontal velocity compared with the velocity estimated using the super-elevations observed in the field.

Simulations of flexible barriers subject to debris flow impact had also been carried out. The debris flow impact test of flexible barriers in Illgarben reported by Wendeler et al. (2006) was numerically replicated. Figure 5 shows the simulation results. LS-DYNA was capable of capturing the debris-barrier interaction reasonably well. The calculated maximum cable forces of the barrier are also comparable with the

measurement results. ARUP (2013) reported details of the study. Further calibration using the centrifuge data (see Section 3.3) and more well-documented case histories of flexible barriers hit by landslide debris, e.g. the Jordan Valley cases reported by Kwan et al. (2014), will be carried out. The technical development work aims to promote use of advanced numerical tools for design of natural terrain hazard mitigation measures.

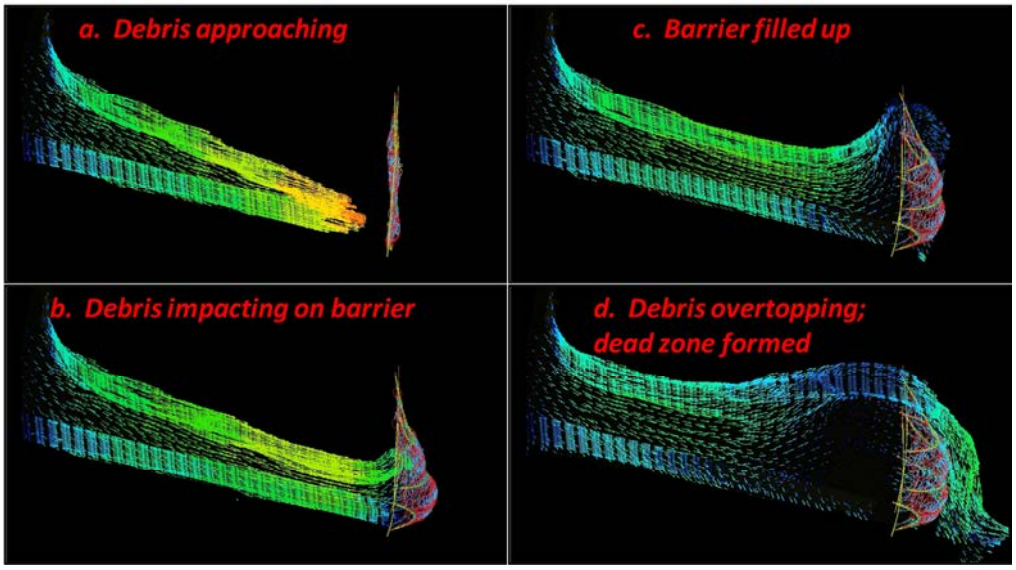

Figure 5: Simulated Debris-barrier Interaction by LS-DYNA

4 CONCLUSIONS

Technical development work to enhance the understanding of the dynamic interaction between landslide debris and debris-resisting structures has been initiated with the ultimate goal of optimizing the current design approach and possibly developing new design methods. Notable areas of recent technical development have been presented in this Paper. The subject involves study of debris dynamics and structural response of barriers through physical tests and numerical analyses. It calls for the collaboration between geotechnical profession and experts in other engineering disciplines. Much remains to be learnt and developed, and further knowledge-based and technology-driven advances are anticipated.

ACKNOWLEDGEMENTS

This paper is published with the permission of the Head of the Geotechnical Engineering Office and the Director of Civil Engineering and Development, the Government of the Hong Kong SAR.

REFERENCES

ARUP 2013. *Pilot Numerical Investigation of the Interactions between Landslide Debris and Flexible Debris-resisting Barriers.* Report prepared for Geotechnical Engineering Office, Hong Kong. ARUP, 143p.

Bowman, E.T., Laue, J., Imre, B. & Springman, S.M. 2010. Experimental modelling of debris flow behaviour using a geotechnical centrifuge. *Canadian Geotechnical Journal*, vol 47, pp 742-762.

Duffy, J.D. 1998. Case studies on debris and mudslide barriers systems in California. *Proceedings of the One Day Seminar on Planning, Design and Implementation of Debris Flow and Rockfall Hazards Mitigation Measures, Hong Kong*, 27 October 1998. Edited by C.K. Lau, R.P. Martin and K.T. Chau, The Association of Geotechnical Specialists (Hong Kong) Ltd. and The Hong Kong Institute of Engineers (Geotechnical Division), pp 77-90.

EOTA 2008. *Guideline for European Technical Approval of Falling Rock Protection Kits.* European Organisation for Technical Approvals (EOTA), 53 p.

GEO 2014. *Guidelines on Enhanced Approach for Natural Terrain Hazard Studies*. GEO Technical Guidance Note No. 36 (TGN 36), Geotechnical Engineering Office, Hong Kong, 18 p.

Hungr, O. 1995. A model for the runout analysis of rapid flow slides, debris flows and avalanches. *Canadian Geotechnical Journal*, vol. 32, pp 610-623.

Kwan, J.S.H. 2012. *Supplementary Technical Guidance on Design of Debris-resisting Barriers* (GEO Report No. 270), Geotechnical Engineering Office, Hong Kong, 88 p.

Kwan, J.S.H., Chan, S.L., Cheuk, J.C.Y. & Koo, R.C.H. 2014. A case study on an open hillside landslide impacting on a flexible rockfall barrier at Jordan Valley, Hong Kong. *Landslides*, vol. 11, pp 1037-1050.

Kwan, J.S.H. & Cheung, R.W.M. 2012. *Suggestions on Design Approaches for Flexible Debris-resisting Barriers* (GEO Discussion Note 1/2012). Geotechnical Engineering Office, Hong Kong, 91p.

Kwan, J.S.H., Koo, R.C.H & Ng, C.W.W. 2015. Landslide Mobility Analysis for Design of Multiple Debris-resisting Barriers. *Canadian Geotechnical Journal*, accepted (in press).

Kwan, J.S.H. & Sun, H.W. 2006. An improved landslide mobility model. *Canadian Geotechnical Journal*, vol. 43, pp 531-539.

Lo, D.O.K. 2000. *Review of Natural Terrain Landslide Debris-resisting Barrier Design*. GEO Report No. 104, Geotechnical Engineering Office, Hong Kong, 91 p.

Savage, S.B. & Hutter, K. 1989. The motion of a finite mass of granular material down a rough incline. *Journal of Fluid Mechanics*, vol 199(1), pp 177–215.

Sun, W.H. & Law, R.P.H. 2012. *A Preliminary Study on Impact of Landslide Debris on Flexible Barriers* (GEO Technical Note No. TN 1/2012). Geotechnical Engineering Office, Hong Kong, 43 p.

Wartmann, S. & Salzmann, H. 2002. Debris flow and floating tree impacts on flexible barriers. *In Proceedings of the Conference on Natural Terrain - A Constraint to Development, Hong Kong*, 14 November 2002. Institution of Mining and Metallurgy, Hong Kong Branch, pp 125-131.

Wendeler, C., McArdell, B.W., Rickenmann, D., Volkwein, A., Roth, A. & Denk, M. 2006. Field testing and numerical modelling of flexible debris flow barriers. *Proceedings of the Sixth International Conference of Physical Modelling in Geotechnics, Hong Kong*, 4-6 August 2006. Edited by C.W.W. Ng, L.M. Zhang, and Y.H. Wang, pp 1573-1604.

WSL 2009. *Full-Scale Testing and Dimensioning of Flexible Debris Flow Barriers.* Swiss Federal Institute for Forest, Snow and Landscape Research (WSL), 22 p.

Performance Monitoring of a 50 m High 75° Cut Slope Reinforced with Soil Nail Bars Made from Glass Fibre Reinforced Polymer (GFRP) at Ho Man Tin Station

A.K.L.Kwong* & J.S.S.Chim
MTR Corporation, Hong Kong

ABSTRACT

The MTR Corporation (MTR) Kwun Tong Line Extension (KTE) project is a 2.5 km long underground extension of the existing Kwun Tong Line (KTL) running from the current terminus at Yau Ma Tei (YMT) station to a new station terminus in the Whampoa District. An intermediate station at Ho Man Tin (HOM) will serve as an interchange station with the future Shatin to Central Link (SCL).

Site formation for the HOM station was carried out by open cut excavation with a maximum depth of 50 m in soil/weathered rock, and 60 m in weathered rock/competent rock at sections where the KTE caverns span across the station. As there is a future development proposed to the north of the station box, and given that piling works will be required for this development, glass fibre reinforced polymer (GFRP) bars were used as a substitute for high yield steel deformed bars in the soil nailing system.

The station box's excavation outline was formed by phased cutting of slopes in fill, completely decomposed granite (CDG) and highly decomposed granite (HDG). The cutting and strengthening works were carried out in stages as excavation proceeded downward. Steep slopes ranging from 45° to 75° were formed and soil nails were used to reinforce these slopes.

A total of 35 nos. of soil nails (both high yield steel and GFRP) have been strain gauged and have surface prisms installed at the proximal ends. Twenty inclinometers were installed and numerous ground settlement markers and piezometers covered the whole site, targeting the crest of the formed slopes. Utility monitoring points were used to monitor any nearby sensitive receivers. The instrumentation was used to assess the state of deformation of the soil cut slopes and the buildup of loads in the soil nails.

This paper describes the detailed monitoring system to validate the soil nail system during construction. 5% of the installed soil nails were selected for monitoring of their movement and tensile forces of the soil nail system by setting AAA response levels based on Plaxis modeling. Surveying tools such as prism targets on soil nail heads and on the slope's shotcreted surface were also used. The motivation for this comprehensive instrumentation scheme was to adhere to an observational method to monitor and validate the performance of the soil nail system as the excavation progresses. After significant horizontal movement of about 40 mm was observed during the intermediate stage of the excavation, additional nails with load cells were installed and nail installation method refined. This paper discusses the benefit of such observational approach that made use of the measured movement and interactive forces between the nail and the soil to calibrate the finite element models for subsequent validations and predictions.

**Note: Formerly MTR Corporation, Hong Kong*

1 INTRODUCTION

1.1 Project background and description

The KTE project is an extension of the existing MTR Kwun Tong Line from Yau Ma Tei Station to Whampoa, with two new stations at HOM and Whampoa. Passengers can interchange at the proposed HOM

Station with the future Shatin to Central Link. It will provide convenient, fast and reliable means of public transport between Yau Ma Tei and Whampoa, and will enable residents in Ho Man Tin, Hung Hom and Whampoa area to have direct access to MTR service, saving time for interchange from road transport to the railway network. The alignment of the KTE will extend from the existing overrun tunnel of Yau Ma Tei Station, run along Gascoigne Road cross Wylie Road and reach HOM Station at the site of the ex-Valley Road Estate. It will then run through Chatham Road North via Wuhu Street and Tak Man Street, and extend to Whampoa Station at Tak On Street.

HOM Station is located at the site of the former Valley Road Estate (Figure 1). The station comprises a large box that will contain the KTE station cavern (KTE platforms) and the SCL station box, which is located above the KTE station. The station is to be constructed beneath the filled platform (+37 mPD) occupied by the former Hong Kong Housing Authority's Valley Road Estate and is bounded by Fat Kwong Street (to the North), Chung Hau Street (to the West) and Yan Fung Street (to the East). The site is also allocated to a MTR property development including two level of semi-basement parking and 10 numbers of 25-storey residential towers. There are no buildings or structures adjacent to the western slopes of this study but there is a live 900 mm WSD freshwater main running parallel and offset 3 m from the slope crest.

Figure 1: Site Location Plan

1.2 Geological setting

The station lies almost entirely within the Kowloon Granite which comprises a mantle of decomposed granite overlying bedrock to varying depths. The granite is fine to medium grained in the HOM and Whampoa areas. The dominating feature for the northern HOM station box is a NW-SE trending fault zone, which has resulted in the formation of a deep valley with extensive weathering and shearing of the underlying rock mass. It is noted that in the deepest part of the valley, weathered rock extends to an approximate depth of -35mPD or more. This zone is about 10 m wide at -12 mPD (formation level of HOM) and extends through Chatham Road to the Wuhu Street playground area to the SE. There is evidence of small amounts of alluvium and colluvium along the valley floor.

The natural catchment (Lo Lung Hang) of the HOM area, prior to backfilling in the 1960s, has been interpreted as having a SE descending valley passing through the present Chatham Road North and ending in Wuhu Street and discharging to the sea to the south.

Fill materials up to 30 m thick are present to the north of HOM Station, and they are comprised of predominantly sand with varying degrees of silt, clay and gravel with SPT varying from 5 to 40. Underlying the fill is localized alluvium of up to 5 m thick which comprises of clay materials with silt of reddish/yellowish brown in color with SPT varying from 5 to 30. Saprolite has a thickness varying from 5 m to 20 m in general, which is described as CDG comprised mainly of sand, with silt and gravel with SPT varying from 10 to 100. Grave IV (HDG) is comprised mainly as gravel size rock fragments and quartz, with generally sand and silt materials.

2 DESIGN BASIS

The station box's excavation outline was formed by phased cutting of slopes in fill, and in weathered rock (CDG/HDG). The slopes ranging from 45° to 75° were strengthened with soil nails as the excavation proceeds down from the existing road elevation (+37 mPD) to the final excavation level at about -12 mPD, which results in an overall total excavation height of about 50 m in this study within the fault zone.

In the implementation of slope strengthening works, conventional high yield deformed steel bars and glass fibre reinforced polymers (GFRP) bars were used as soil nails. Given that piling works may be required for the future development to the north, the use of GFRP bars was warranted as a substitute for conventional high yield deformed steel bars in the soil nail system so that they could be broken out later. Material properties and testing of GFRP bars were described in detail by Swann et al. (2013).

The slope under this study has cut through the Fill material which has a thickness of about 28 m, whereas those in CDG, HDG and MDG are 7 m, 10 m and 5 m respectively. The slope angle formed in Fill was 45°, in CDG and HDG was 75° and that in MDG was 90°. In order to maintain the slope in stable condition with a global factor of safety in limiting equilibrium greater than 1.2, 40 mm GFRP soil nails were installed typically 2 m vertical spacing in Fill and 1.3 m vertical spacing in CDG and HDG. The horizontal spacing of all the nails was 2 m. The soil nail was typically 20 m long. Figure 2 shows the simplified geological Section 20 for this study.

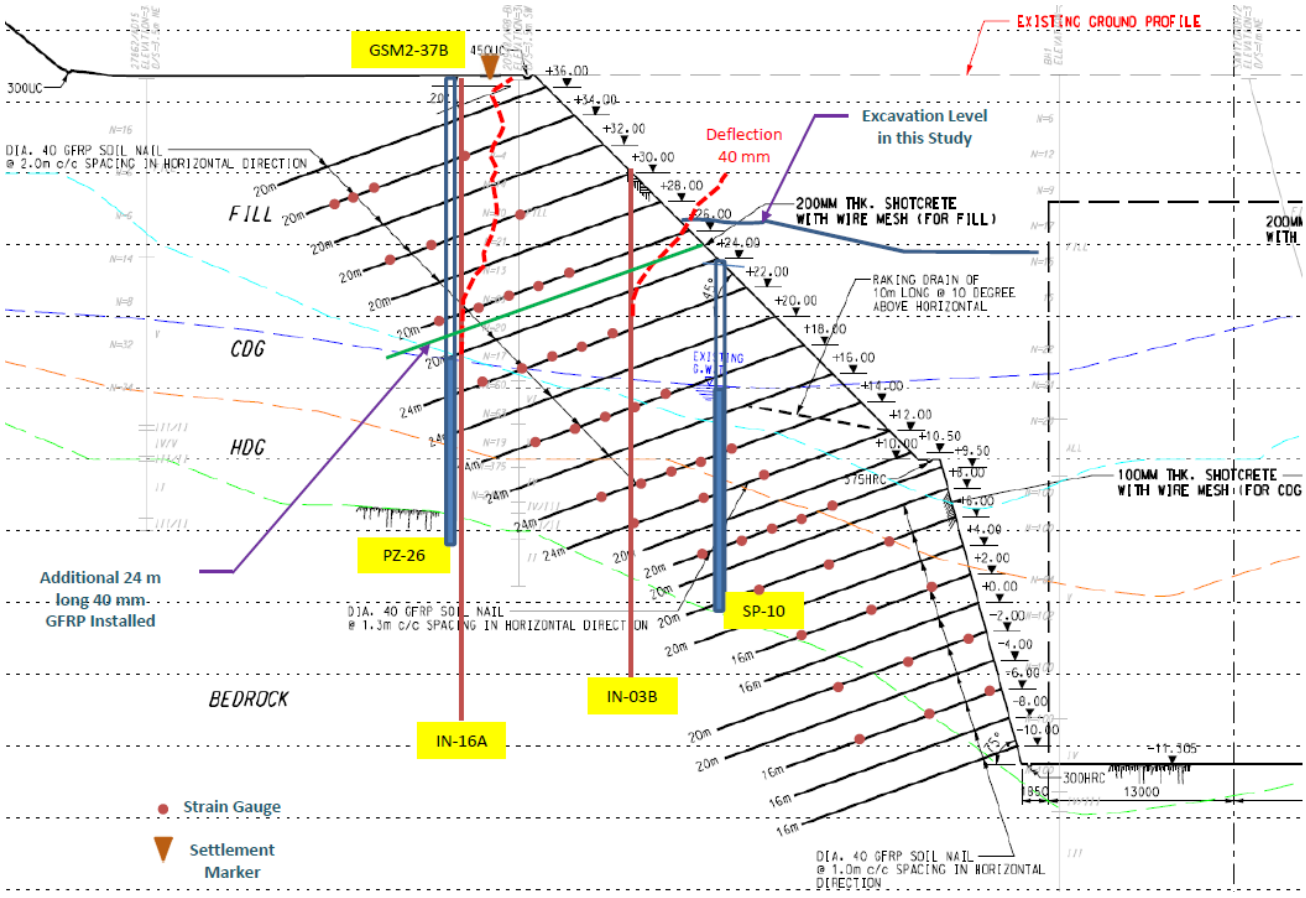

Figure 2: Typical Geology in Section 20 (Section A-A in Figure 1)

The ground movements were estimated for Section 20 in this study by using the computer program Plaxis. Soil nails and shotcrete were modelled to be in place prior to excavation for the next level of soil nails. The settlement along the crest of the west portions of the cut slope was calculated as 20 mm. Details of the material properties and design can be found in Jacobs China Limited (2011).

The following response levels (ALERT, ACTION and ALARM) based on general empirical rule were applied:

ALERT LEVEL - set at 50% of maximum allowed movement.
ACTION LEVEL - set at 80% of maximum allowed movement.
ALARM LEVEL - set at 100% of maximum allowed movement.

Table 1: Summary of Action Response Levels

Monitoring Type	ALERT	ACTION	ALARM
Ground Settlement	25 mm	40 mm	50 mm
Building Settlement and Tilting	12.5 mm 1:600	20 mm 1:375	25 mm 1:300
Utilities Settlement and Tilting	10 mm 1:600	16 mm 1:375	20 mm 1:300
Groundwater Drawdown	500 mm below reference GWL	800 mm below reference GWL	1000 mm below reference GWL
Inclinometer	25 mm	40 mm	50 mm

3 CONSTRUCTION METHOD AND SEQUENCE

Construction was based on excavation in alternating panels of limited width (12 m to 15 m) in fill such that any induced slope movements will be minimised. The construction sequence (Figure 3) was as follows:

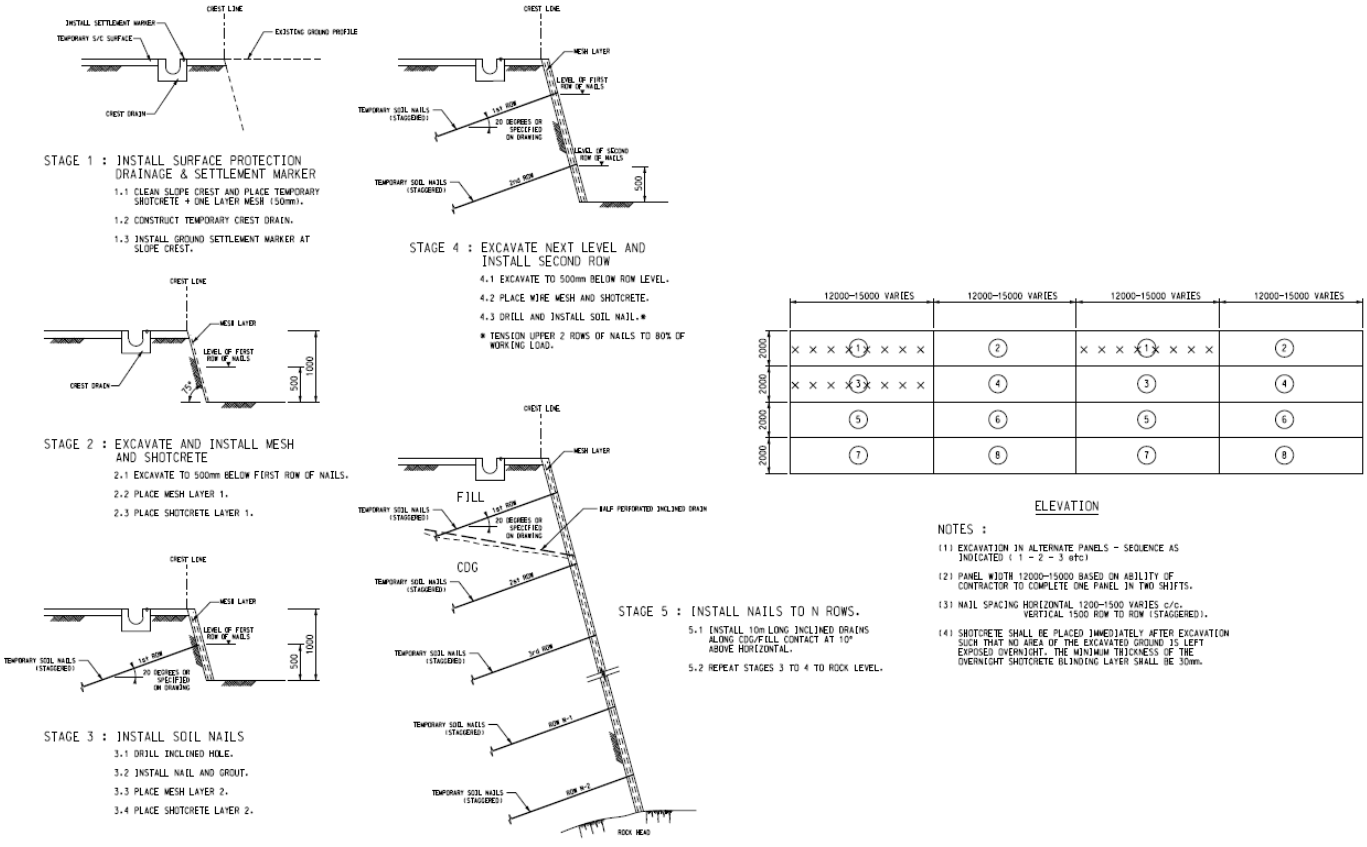

Figure 3: Nail Installation Sequence

i) Excavation to the level 500 mm below the 1st row of soil nails to form a temporary slope profile, followed by installation of A393 wire mesh and shotcreting (100 mm thick).

ii) Installation of 1st row of soil nails.
iii) Applied second layer of A393 wire mesh and shotcreting (100 mm thick) to the 1st row of soil nails.
iv) Excavation to the level 500 mm below the 2nd row of soil nails to form a temporary slope profile, followed by installation of A393 wire mesh and shotcreting (100 mm thick).
v) Installation of 2nd row of soil nails.
vi) Applied second layer of A393 mesh and shotcreting (100 mm thick) to the 2nd row of soil nails.
vii) Repeat until all rows of nails were formed.

4 EXCEEDANCE OF AAA LEVELS

Excavation and installation of the soil nails began in the middle of March 2012 at elevation of +37 mPD. After the 4th layer of soil nails was completed at elevation of +30 mPD in early May 2012, horizontal movement and vertical settlement started to increase between Sections 19 to 21 (horizontal length of about 50 m) to a magnitude that became a safety concern if further movement continued at the same rate.

The monitoring instruments between Sections 19 and 21 comprise inclinometers, settlement markers, prisms mounted on the soil nail head, strain gauges along the nail and piezometers.

Section 20 (half way between Sections 19 and 21) was considered the most critical section because of the largest thickness of fill here.

The monitoring instrument at this section showed the following readings when excavation reached +26 mPD:

i) Inclinometers – 40 mm horizontal movement at the middle and 16 mm at the crest of the slope, had exceeded the Action Level (set at 40 mm) as indicated by IN-03B and IN-16A.
ii) Settlement Markers – 30 mm to 35 mm vertical settlement at the crest, had exceeded the Alert Level (set at 25 mm) as indicated by GSM2-37B.
iii) Prisms – 10 mm to 20 mm horizontal movement towards the open face and 5 mm to 15 mm vertical downward movement, had reached the Alert Level (set at 10 to 20 mm for vertical).
iv) Strain Gauges – recorded 60 to 100 kN in tension in mid May 2012 at the row at +30 mPD.
v) Piezometers - showed groundwater table was below the intermediate excavation level.

The predicted horizontal movement at the excavation level (+24 mPD, 7th layer) was about 20 mm. Based on the monitoring results, at one third of the current excavation level, the recorded horizontal movement was already 40 mm which had exceeded 2 times the prediction. The concern was that if excavation continued downward to the final formation level of -12 mPD, and with the current rate of horizontal movement and settlement, excessive movement of the slope could cause failure and no remedial works would be considered effective in stabilizing it.

5 ACTION PLAN

The use of GFRP soil nails in loose to medium dense fill slope at angle of 45° and a thickness of about 28 m was unprecedented. Together with the site observations that washout was observed in one of the nail heads during heavy rain in April 2012 and higher than normal grout intake was recorded in 2 to 3 nos. of nails, a number of upgrading works were implemented as follows:

i) Entire area above the slope crest to have concrete paved.
ii) Acceptance tests carried out on those nails which had high grout intake.
iii) Additional settlement monitoring points installed at the 900 mm water mains.
iv) Additional raking drains installed to relieve the build-up of water pressure within the slope.
v) Change unsupported air-lifting drilling to wash boring with temporary casing supported during drilling.
vi) Soil nails along 8th layer increased to 24 m long from 20 m so that bondage could be set in the CDG layer.
vii) Installed one additional layer of 24 m long, 40 mm GFRP nails between 6th and 7th layer, pre-stressed to 120 kN and monitored with a load cell.

viii) Based on the observed movement and nail force recorded in the nail, Plaxis modelling was refined and arrived with a new prediction of horizontal movement to about 120 mm, vertical settlement to about 100 mm under the following scenario when the final formation level was reached.

a. Frictional angle of fill reduced from 37° to 33°.
b. Shotcrete thickness increased from 200 mm to 300 mm.
c. Case A. Fill constitutive model using Mohr-Coulomb (ϕ=37°)
d. Case B. Fill constitutive model using Hardening soil (ϕ=37°, unload modulus $E_{ur}^{ref}=2.5xE_{50}^{ref}$), where E_{ur}^{ref} refers to unloading modulus and E_{50}^{ref} refers to loading modulus at 50% peak load.
e. Case C. Fill constitutive model using Hardening soil (ϕ=37°, unload modulus $E_{ur}^{ref}=2.0xE_{50}^{ref}$)
f. Case D. Fill constitutive model using Hardening soil (ϕ=33°, unload modulus $E_{ur}^{ref}=2.0xE_{50}^{ref}$)
g. Case E. Same as Case D but slope surface without immediately meshed and shotcreted.

Since the Mohr-Coulomb model predicted heave in the early stages of unloading which was unrealistic, the hardening model in Case E was considered appropriate in the refined modelling for prediction of AAA's levels down to the final formation level because it closely matched the measured movement at IN-03B and nail force up to the study level of +20 mPD. Details of the hardening model parameters and modelling sequence can be found in Jacobs China Limited (2011).

Table 2 shows the horizontal movement of IN-03B at each stage of unloading for each of the scenarios studied.

Table 2: Sensitivity of horizontal movement (mm) under Different Cases Studied

Stage	Case A	Case B	Case C	Case D	Case E
Apply Surcharge	2.07	1.60	1.62	2.76	
Create Initial Benched Profile	10.87	13.46	16.01	18.01	
Install 1st Row	10.87	13.70	16.28	18.69	
Install 2nd Row	10.84	13.42	15.93	18.36	
Install 3rd Row	10.83	13.18	15.56	18.02	
Install 4th Row	10.98	15.64	18.17	20.66	
Install 5th Row	11.45	18.67	20.90	24.32	31.68
Install 6th Row	13.99	22.28	24.68	29.12	32.54
Install 7th Row	16.09	27.48	29.81	35.57	38.38
Grout additional Row	18.26	27.47	29.84	35.67	38.51
Install 8th Row	18.74	30.72	33.25	41.23	43.27
Install 9th Row	20.52	35.38	37.74	46.09	48.77
Install 10th Row	21.62	39.58	42.34	52.19	54.98
Install 11th Row	23.12	39.58	42.34	52.19	59.82
Install 12th Row	25.35	44.03	46.29	57.04	59.82
Install 13th Row	27.64	48.94	50.40	62.56	65.46
Install 14th Row	29.44	52.23	53.95	68.08	70.57
Install 15th Row	30.53	54.05	56.03	69.33	72.21
Install 16th Row	34.46	56.85	58.08	73.88	74.23
Install 17th Row	37.00	61.47	63.11	76.70	79.34
Install 18th Row	42.45	67.77	68.77	81.83	84.74
Install 19th Row	44.80	72.04	73.37	86.87	89.72
Install 20th Row	47.56	75.81	77.03	88.62	93.27
Install 21st Row	51.02	81.89	81.17	95.83	96.04
Install 22nd Row	53.54	85.30	85.63	99.20	101.02
Install 23rd Row	58.19	94.35	94.57	107.66	109.52
Install 24th Row	62.58	101.11	103.65	116.69	118.43
Install 25th Row	66.30	103.28	108.20	122.26	119.50
Install 26th Row	70.06	109.36	114.73	124.06	130.17
Install 27th Row	71.50	110.74	114.83	125.66	130.28
Rock Excavation	71.80	111.47	115.46	126.28	130.89

Comparing the lateral movement between Cases D and E at the stage "Install 5th Row", it was noted that excavation to a lower bench without immediate application of shotcrete would result in 30% additional movement caused by relaxation.

Results of the sensitivity on thickening the shotcrete layer indicated no obvious reduction of movement can be detected and therefore shotcrete thickness was not increased for the subsequent layers.

For Case E (Figure 4), there was no apparent shear strains developed within the fill material and it can be concluded that preferential shear plane cannot be developed when reaching the final formation level.

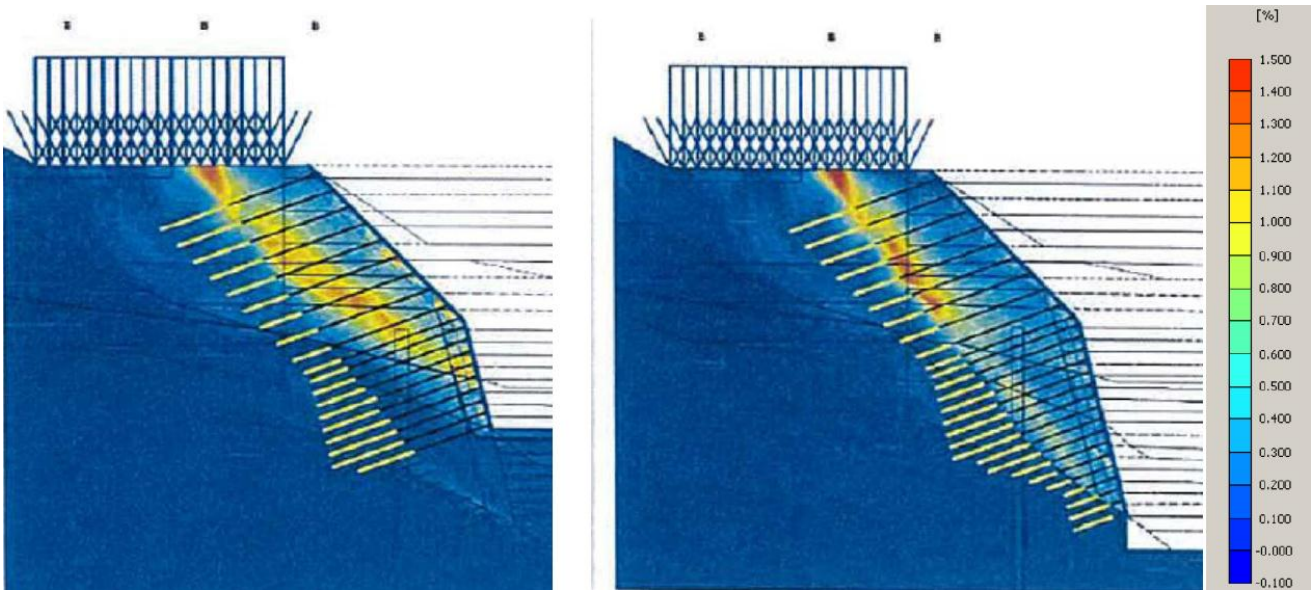

Figure 4: Shear Strain Concentration Down to Final Excavation Level

Revised AAA values as shown in Table 3 were re-established based on the worst case scenario of back-analysis carried out from Case E, which assumed a delayed in shotcrete applied for the subsequent layer.

Table 3: Summary of Revised AAA Levels

	For IN-03B, to base of fill	For IN-03B, to base of CDG	For GSM2-37B, to base of fill	For GSM2-37B, to base of CDG
ALERT (80% of FEM Prediction)	71 mm	88 mm	75 mm	89 mm
ACTION (100% of FEM Prediction)	75 mm	93 mm	79 mm	93 mm
ALARM (120% of FEM Prediction)	83 mm	102 mm	87 mm	103 mm

For Case E, the predicted horizontal movement to the base of CDG is presented in Figure 5.

Figure 6 shows a comparison of the FEM prediction versus the actual readings of vertical settlement up to the study level of +20 mPD and down to the base of the fill (~+8 mPD).

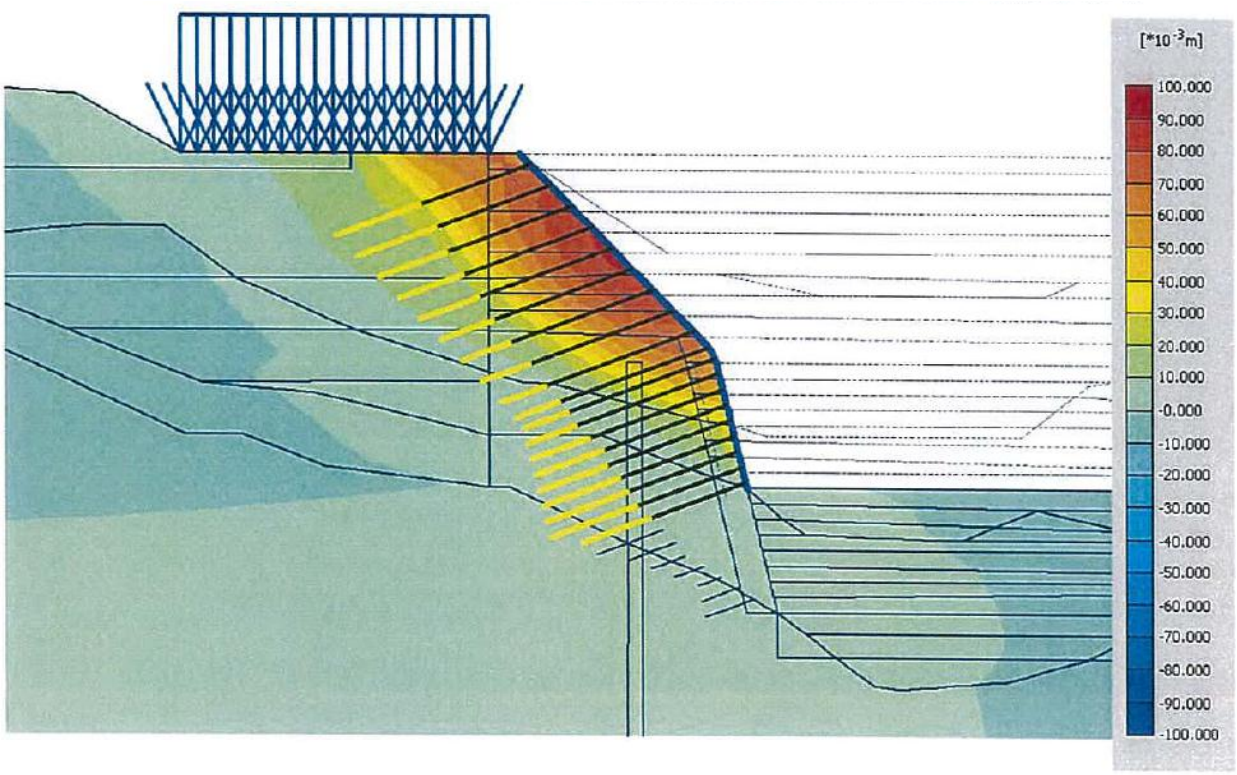

Figure 5: Predicted Horizontal Movement from Case E to base of CDG.

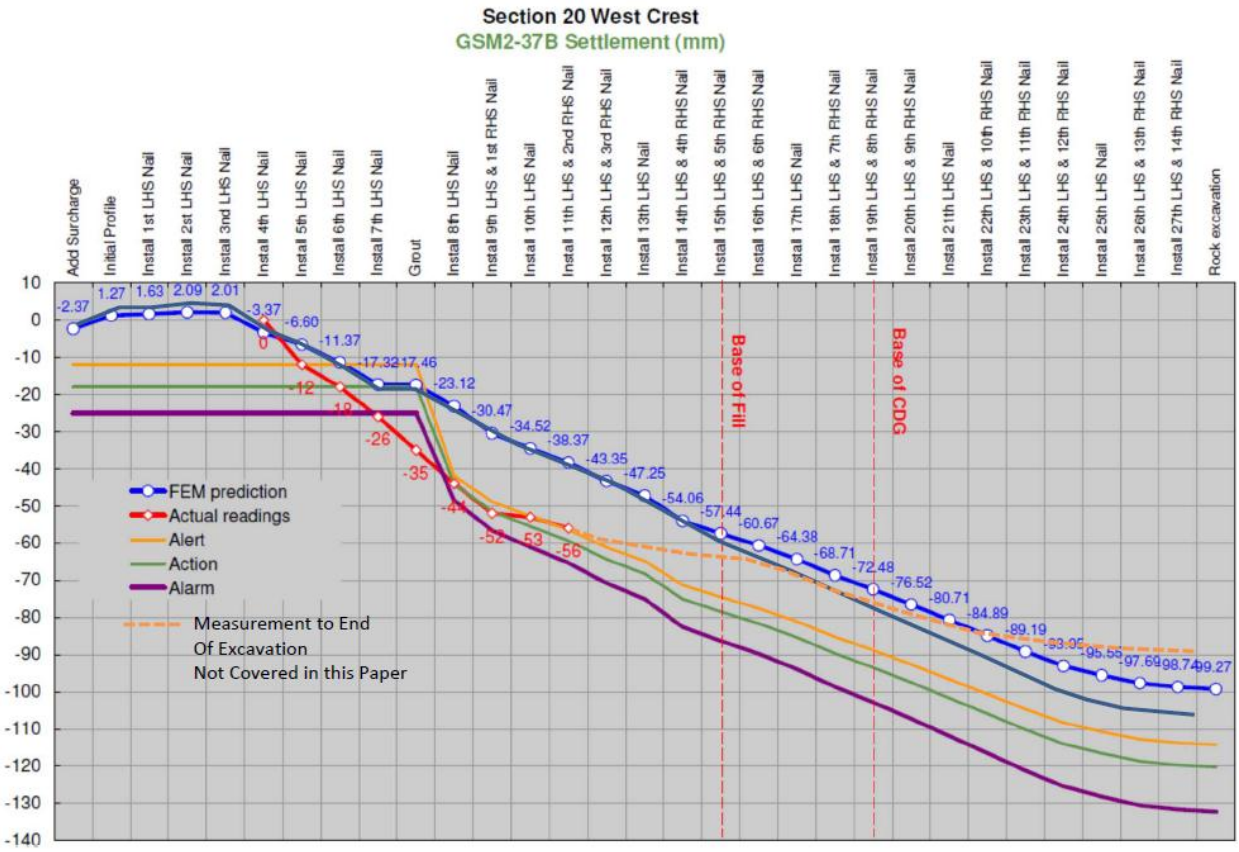

Figure 6: Case E, Predicted Vertical Settlement Compared to Actual Reading.

6 CONCLUSIONS

Close monitoring continued as excavation continued down to the final formation level of -12 mPD. Due to the additional nails installed together with improved drilling process, there were very little additional movement and settlement recorded after the AAA values were reset. IN-03B recorded a final horizontal movement of about 70 mm (predicted 120 mm) and GSM2-37B recorded a final vertical settlement of about 90 mm (predicted 100 mm) was achieved when the final formation level was reached in August 2013. The horizontal movement was over predicted about 50 mm, but the vertical settlement was very close when the final level was reached. There were no distresses observed on the slope and all the nail forces were well within the working load. Station structures and slope backfilling was completed in early 2015.

The motivation for this comprehensive instrumentation scheme was to allow validation of the computer model in assessing the performance of the soil nail system as the excavation progresses. In this study, additional nails with load cells were installed and installation method refined based on re-assessment of different constitutive models adopted and material shear strength. The study provided a good case history which reinforced the benefit of such observational approach, allowing economical and safe design and construction of high and steep slopes reinforced with GFRP nails.

ACKNOWLEDGEMENTS

The writers are grateful for the support of MTR and Jacobs China Limited. Their support contributed in expediting the approval process. However, the contents of this paper do not necessarily reflect the views and policies of these supporting organizations, nor does the mention of trade names and commercial products constitute endorsement or recommendation for use.

REFERENCES

Jacobs China Limited November 2011. *Temporary Works Design Report, Package B1, Temporary Works for Soil Cut Slopes in HOM North Station Box*, 206 p.

Swann, L.H., Ng, A. and Mackay, A.D. 2013. The Use of Glass Fibre Reinforced Polymer Bars as Soil Nails to Permit Future Housing Development, Hong Kong Special Administrative Region. *HKIE Geotechnical Division Annual Seminar*, pp. 165 to 171.

Considerations for Consolidated Undrained Triaxial Testing of Saprolites for Soil Structure Interaction Design

Ada Chan
Leighton Asia, India and Offshore (LAIO)
A. D. Mackay
ALYSJ joint venture, Doha, Qatar
N. R. Wightman
Aquaterra Consultants Limited

ABSTRACT

Hong Kong's sub-tropical climate results in weathering of in-situ rock to a saprolite. These have unique physical characteristics with similarities to both rock and soil, influencing the shear strength values determined from the Consolidated Undrained (CU) triaxial test. The parent rock forming the saprolite retains a relict structure increasing the shear strength at relatively small strains, of say 3% or less, represented by the peak shear strength during the CU test. After this structure, termed bonding, is ruptured the shear strength decreases and is mobilised by the inter-particulate interaction. This paper summarises the main test stages for the CU test in Hong Kong and how these are influenced by relict structure from random test specimens of granitic saprolite. The difference in the peak and residual shear strength at different strain ranges is presented. It is concluded that the "upper bound" shear strength parameters of saprolite representing the relict structure prior to rupture should be adopted for engineering works where small strain displacement may be anticipated.

1 INTRODUCTION

Numerous Consolidated Undrained (CU) triaxial tests are routinely carried out in Hong Kong to determine effective shear strength parameters. Saprolites have variable and unique physical characteristics that need to be identified to better understand the influence on the engineering works. The presence of the relict structure may lead to inconsistent saturation, swelling and / or volume reduction during the consolidation stage of the CU testing process, rupturing the relict structure (bonds) and, in extreme situations, restructuring the particles. This paper provides examples from random specimens where the shear strength has been reduced due to rupture of the specimen during testing. Recommendations for more sensitive testing, such as the use of side drains to provide a more even permeation is made. The effects of variable shear strength values, representing strain ranges within the in-situ and failed (residual) saprolite conditions is given.

2 TEST PROCEDURE

2.1 Hong Kong laboratory testing

In Hong Kong "great importance is given to representative accurate soil test data to support proposed site investigation, design and construction" (BA, 2005). This requirement is emphasised in the Building Ordinance, CAP 123, Section 17 (1) subsection 6(b), which requires "material testing" to be carried out in order to "gain approval for the building plan submission". If these requirements are not fulfilled; as set out in GEO, 2001 & HKAS, 2009; the Building Authority (BA) "may refuse approval of plans or consent for commencement of building works" (BA, 2009). Hong Kong therefore sets very high levels of quality and stringent testing standards for construction works to proceed. The testing procedure and standards for Hong Kong laboratory testing is set out in GEO, 2001.

2.2 The Consolidated undrained triaxial test

The CU test determines effective shear strength parameters from soil specimens using triaxial testing apparatus, presented in Figure 1, and follows stringent accreditation procedures (HKAS, 2009).

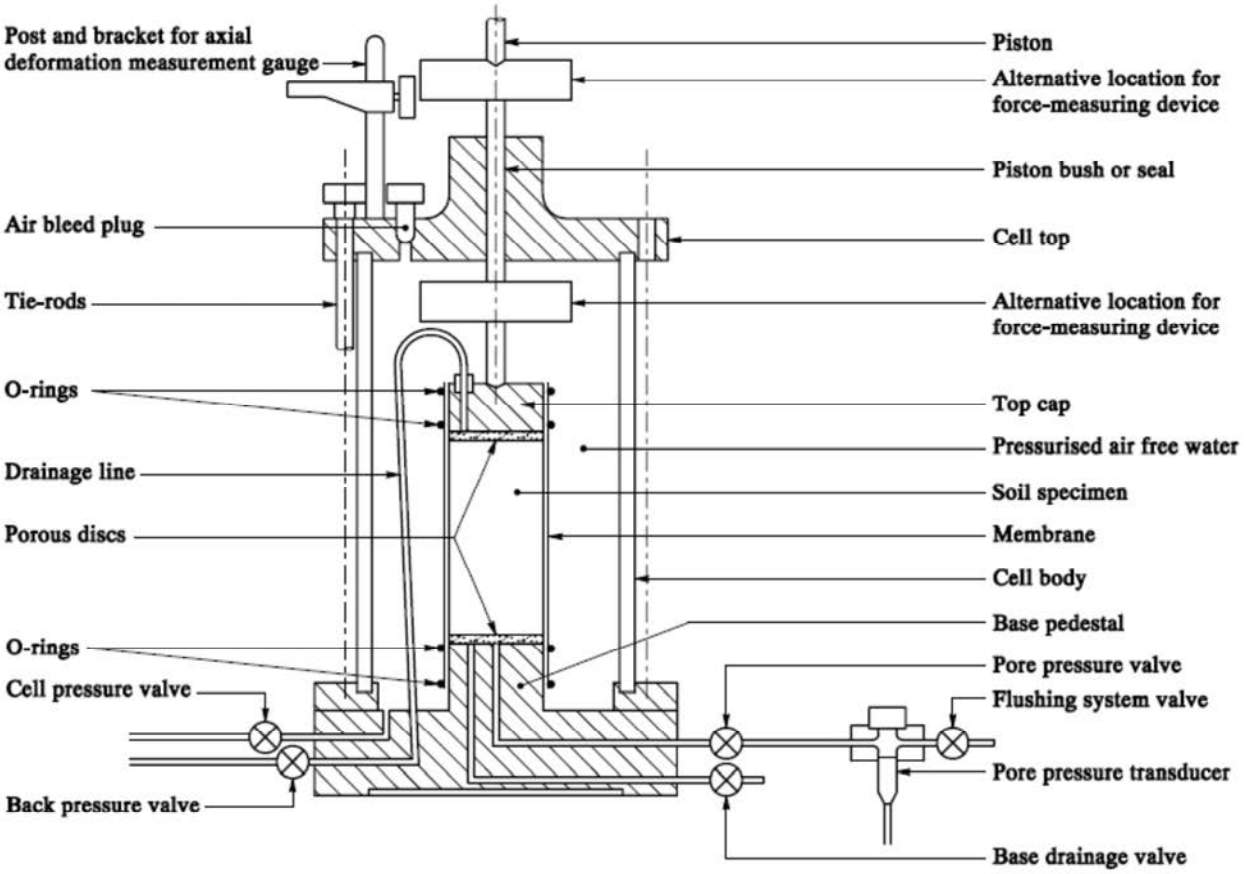

Figure 1 - Triaxial test apparatus (GEO, 2001)

The main stages of the CU test procedure are saturation, consolidation and compression, each of which need consideration for the type of ground being tested to ensure representative results are obtained. A summary of the aim, procedure and relevant considerations for each test stage is summarised in Table 1 with considerations how each stage may influence the shear strength.

Table 1 – Considerations for Each Stage of the CU Test

Aim	Test Procedure (GEO, 2001)	Important Considerations
SATURATION - ensure voids between particles in the test specimen are saturated	Increase in back pressure (pore water pressure) to cell pressure application (B) not exceeding increments between 5 to 25kPa or until B exceeds say 0.95.	• The effective pressure increase in the specimen may exceed the in-situ effective pressure, • The rate of back pressure application ensuring consistent permeation throughout the specimen; • Ensuring the volume increase is not excessive and or localised.
CONSOLIDATION - Ensure desired state of effective stress is achieved prior to compression	Increase to the desired effective stress by raising the cell pressure, if required, and / or dissipating back pressure during the test. The back pressure does not fall below the final saturation pressure	• The rate of cell and back pressure application, • Suitable incremental increases in the cell and back pressure as the confining pressure is applied, • The rate of "steady" pore water pressure change to determine the completion of the consolidation, • Dissipation of excess pore pressure. Typically taken as 95% dissipation, • Ensuring volume increase is not excessive and / or localised.
COMPRESSION - Shear failure.	Increase the axial pressure by a consistent increase in axial strain	• Rate of axial strain (typically based on the time taken to achieve pressure) • Defining failure, either by volume increase or rapid decrease in compression

For soils, which have shear strengths sensitive to their in-situ environments, such as saprolites, particular attention for the test scheduling and supervision may include:

- The use of side drains to enhance permeation during saturation;
- The location(s) of pore-water (back) pressure application and measurement, typically taken from the top and base of the test specimen respectively, refer to Figure 1;
- Effects of variations within the test specimen;

A three day testing period is considered "normal" (MTRCL, 2009). Whilst a suitable test period is needed this must not influence the time needed to obtain representative results, particularly for a fine grained soils with a low permeability, typical of saprolites.

2.3 Key roles, responsibilities and interaction for the testing

Given the importance of identifying variations in the test specimen, particularly effects on the permeability, key individuals, roles and particular tasks for individuals responsible for the laboratory test schedule and supervision are outlined in GEO, 2001; HKAS, 2009; BA, 2006 and BA, 2010. This is summarised in Table 2.

Table 2 – Summary of Key Individuals, Roles and Particular Tasks in Laboratory Testing

Lead Role	Role	Ref.	Tasks (GEO, 1992 & 2001)
Specifier	Laboratory scheduling	BA, 2006 & 2010	• Prepare a soil description, including the possible origin and whether the soil particles are susceptible to crushing; • Request details of the Supervising Engineer;
Supervising Engineer	Supervision & reporting	HKAS, 2009	• Verify the field description is appropriate, in particular presence of fabric, discontinuities, and other geological effects affecting the test • Upon completion specimen description, including fabric and unusual features affecting the result

The qualifications for both the Specifier and Supervising Engineer are "Qualified Geotechnical Engineer and / or Engineering Geologist" (GEO, 2001) and a "Corporate Member of a professional body" and a "Registered Professional Engineer, Geotechnical" with designations RPE/G (BA, 2001; BA, 2010 and HKAS, 2009).

The GI and laboratory contractors often have different contractual requirements and reporting streams. It is therefore vital that the laboratory test scheduling, typically prepared by the ground investigation (GI) supervisor, and the laboratory technicians, headed by the Supervising Engineer, have a common understanding

of the specimens being tested and flexibility in testing procedure as more information becomes available. This needs to be incorporated in the contractual set up.

As the initial soil description is typically based on a jar sample from the GI contractor, this should be updated during laboratory test specimen preparation, with feedback provided to the Specifier (GEO, 2001). An update of the drillhole log and final GI report following specimen preparation and ideally test completion, should be carried out to ensure consistency between the GI log description and the laboratory test findings. Notwithstanding as GI reports typically require prompt submission the additional time taken to incorporate laboratory test findings can be problematic.

3 CHARACTERISTICS OF SAPROLITES

3.1 Engineering geological properties influencing shear strength

"Weathering has a significant effect on the engineering properties of rock", therefore "careful description of the state of weathering" is required (GEO, 1992). Weathering can either be disintegration (mechanical) and / or decomposition (chemical) with saprolites being the product of more intense chemical weathering. For rocks with a plutonic and volcanic origin, common in Hong Kong, decomposition effects are dominant. However, if disintegration processes have affected the specimen, ultimately influencing the shear strength, this needs inclusion in the sample and laboratory specimen description (GEO, 2007). Important influences on the physical properties of the rock from both mechanical and chemical weathering processes are summarised in Table 3:

Table 3 – Weathering Effects Affecting Engineering Properties (Shear Strength) of Saprolites

Processes	Relevant descriptions and / or effects (GEO, 2007)
MECHNICAL - water absorption and release; stress and temperature changes	Micro-fracture growth. Typically resulting from de-stressing from the decomposition of quartz and feldspar components in the rock, becoming more obvious in coarse grained granite
DECOMPOSITION - breakdown of minerals to a more stable chemical state	• Increase in more stable low strength clay minerals; • Increase in pore space and associated void ratio and porosity; • Variable weathering front with associated permeability variation; • Reduction in grain bonding, decreasing material strength, • Clay mineral concentration along discontinuities; particularly in saprolites close to rock and soil interfaces.

The stress history imposed by influences such as groundwater fluctuation, recent erosion and recent deposition needs consideration when judgments for the test schedule.

3.2 Physical parameters for saprolites

Typical ranges of physical parameters including void ratio, unit weight, effective shear strength and permeability for different types of granitic saprolites from published data are summarised in Table 4.

Table 4 – Typical Ranges of Values for Geotechnical Parameters for Completely Decomposed Granite (CDG) (GEO, 1992, 1997, 2000 & 2007 & Martin, 2003)

Reference	Description (GEO, 1992)	Void Ratio	Unit Weight (kN/m^3)			Shear Strength Parameters		Permeability
			Sat. Bulk	Bulk	Dry	Angle friction	Cohesion	
GEO, 2000				16-21	14-19	35 – 44	5 - 15	10E-5 – 10E-7
Martin, 2003	Upper CDG limit	0.4 – 0.6			16-18	38-44	0-10	
	Lower CDG limit	0.7 – 1.1			12-15	33-36	2-6	
GEO, 1997	HDG, Mod weak		22 – 25	20 – 24				
	HDG, Very weak –weak		20.5 – 22.5	17 – 20				
	CDG, Very dense		20 – 21	16 – 19				
	CDG, Dense		18.5 – 20	14 – 16				
	CDG, Loose		17.5 –18.5	12 – 14				

As shown a reduced unit weight or density corresponds with decreased shear strength, increased permeability and greater weathering grade.

An example of the variability of particle size distribution (PSD) from a saprolite with decreased weathering grade with depth is shown in Figure 2 (Wightman, 2009). The borehole retrieved samples with an increase in gravel in less weathered saprolite (highly decomposed rock layer) and an increase in silt and clay in more intensely weathered saprolite, located immediately below the residual soil layer. The increased density and decreased fines content corresponded was increased strength accordingly.

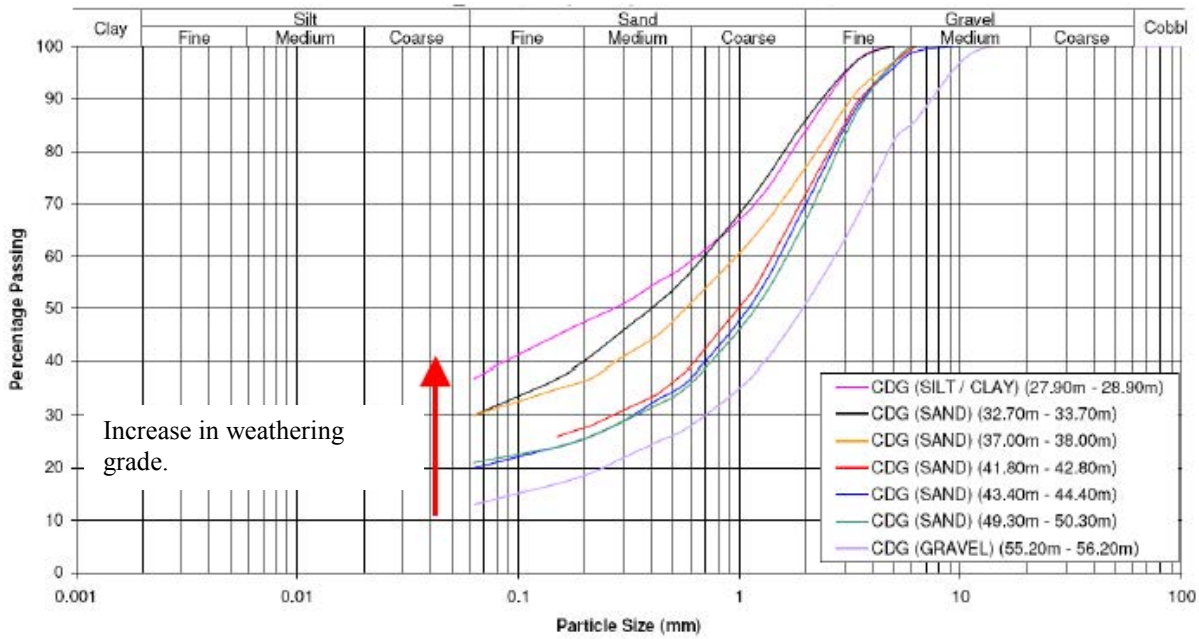

Figure 2 - Change in PSD of Saprolite with Depth Showing Increasing Silt and Clay Content (Wightman, 2009)

As referenced in GEO, 2000, the Completely Decomposed Volcanics, comprising Tuffs and Rhyolites, have the same bulk and dry unit weight and permeability ranges as CDG with shear strength parameters ranging from 5 to 15kN/m^2 (cohesion) and 32 to 38 degrees (angle of internal friction). The clay content, fabric and grading associated with the upper and lower limits of CDG decomposition grade are summarised in Table 5.

Table 5 – Grading of Remolded Samples of CDG (Martin, 2003).

Limit	Clay, % by weight	Grading (2)			
		Description	Gravel (%)	Sand (%)	Silt / Clay (%)
Upper	10 – 25	Silty clayey, very sandy gravel or very gravelly sand	30 - 50	30-50	10-20
Lower	30 - 50	Slightly gravelly, sand silt / clay	10-30	30-50	30-45

Many of the saprolite's physical properties referenced above, particularly fabric, mineralogy, grading clay content, density can be approximately estimated from an accurate geological description. This can then be used for advance considerations in preparing the test schedules and appropriate procedures.

4 EFFECTS OF THE TRIAXIAL TEST ON SAPROLITES

A number of Hong Kong laboratory tests were checked as part of the routine input to site investigation, design and construction works. In almost all reports the saprolite laboratory tests included a brief geological description sent from the "Specifier" obtained from "jar" samples with no subsequent update. It is noted that GEO, 2001 requires the following important information:

- Representation of the geological units and update of inaccurate description to the specifier;
- A detailed test specimen description, including the features that may render the test results invalid;

- Incorporation of classification tests results (particle size distribution and Atterberg limits), carried out on the sample into the geological description;
- Presentation of both laboratory and jar sample descriptions, including detailed soil description, soil fabric and any unusual features, in accordance with GEO, 1992.

Random test specimens of CDG from a laboratory test report, which included CU triaxial test on CDG for an MTRCL project, dated mid-2009, was checked in further detail by the authors, as summarised in Table 6.

Table 6 – Depth (metres below ground level, mbgl), Sample Type and Soil Descriptions for Randomly Selected CDG Specimens

Specimen No.	Specimen mbgl	Soil Description	
1	17.2 – 17.45	Dark brown, very silty, very gravelly SAND	(17.0 – 17.45 mbgl)
2	23.8 – 24	Orangish brown, slightly gravelly, clayey SILT	(23.0 – 24.10 mbgl)
3	34.3 – 34.5	Brown, very silty, very gravelly SAND	(33.5 – 34.60 mbgl)

For the specimen and sample disturbance, affecting the results, it was revealed that Specimen 1 had been taken from a U76 sample; contrary to the requirements in Table 9, GEO, 1997 and the test specimens were generally taken at or near the base of the sample which have greater sampling disturbance. A summary of the test results and divergence from the each test stage (GEO, 2001) is summarised in Table 7.

Table 7 – Soil Properties, during Saturation and Consolidation

Spec No.	Saturation*(1)				Consolidation*(2)							Compression*(3)			
	Pressure (kN/m^3)			Ratio (B)	Time (min)	Pressure (kPa)		Volume (mm^3)			Strain Rate, (mm/ min)	Dry Density (kN/m^3)		Wet Density (kN/m^3)	
	Cell	Back	Pore			Cell	Effective	Before	After	%		Before	After	Before	After
1	205	200	200	0.97	150	370	170	680	643	5.4	0.05	14.6	15.5	19.0	19.6
2	205	205	205	1	2880	430	230	606	547	9.6	0.046	12.5	13.8	17.6	18.6
3	205	200	200	1	90	540	340	606	557	8.0	0.047	15.0	16.4	19.4	20.1

Notes:

*(1)
- "Small effective pressure", typically taken as 5kPa, not implemented.
- The cell and back pressures often being equal and the pressure ratio reaching unity.
- The pore pressure (u) kept to the maximum allowable (200kPa), in specimen 1 this is greater than the in-situ effective stress.
- Effective pressure exerted on specimens retrieved from the greater depths was significantly less than in-situ effective pressure.

*(2)
- Rate of volume change increased in Specimen 1 towards completion, suggesting rupture of the specimen.
- Volume change during consolidation, which approaches 10% in some specimens, is significantly greater than the change that cemented bonds can withstand thereby causing rupture

*(3)
Time taken to reach consolidation for all specimens was significantly different, yet the strain rate used in compression for all specimens was similar, say 3mm/ hr

A summary of the parameters recorded for each test specimen at different presumed failures, including report reference, greatest stress ratio (σ1/ σ3) and maximum pore water pressure, are presented in Table8.

Table 8 – Soil Parameters at Different Test Failure Stages

No	Failure stage	u	ε	ó$_1$	ó$_3$	s'	t'	p'	q	ó1/ ó3
1	Reported	250	19.5	454	120	287	167	231	334	3.8
	Greatest "u"	307	2.69	254	62	158	96	126	192	4.1
	Greatest σ1 / σ3	294	6.06	339	75	207	132	163	264	4.5
2	Reported	337	7.9	369	92.9	231	138	158	277	4
	Greatest "u"	346	3.97	342	83.4	212	129	169	258	4.1
	Greatest σ1 / σ3	345	5.07	356	84.7	220	136	175	271	4.2
3	Reported	360	20	673	179	426	247	344	493	3.8
	Greatest "u"	429	3.3	449	111	280	169	224	338	4
	Greatest σ1 / σ3	420	5.6	521	120	321	201	254	401	4.3

The reported specimen failures for 1, 2 and 3, had reached a reported strain (ε) of approximately 20%, 8% and 20.5% respectively which had drastically exceeded the rupture of the cemented bonds between particles, in the order of 20% to 100% greatest pore water pressure value ("u") at about 4% to 5% strain. The results were therefore unrepresentative of the reported "peak" shear strength values. The failures referenced in Table 7 recorded at the maximum pore pressure and stress ratios occurred at relatively similar strains and could be more representative of the peak failure at or prior to the bond failure and show a significant increase in effective cohesion and internal angle of friction when compared with the values reported.

Plate 1: Specimen 1 - Failure

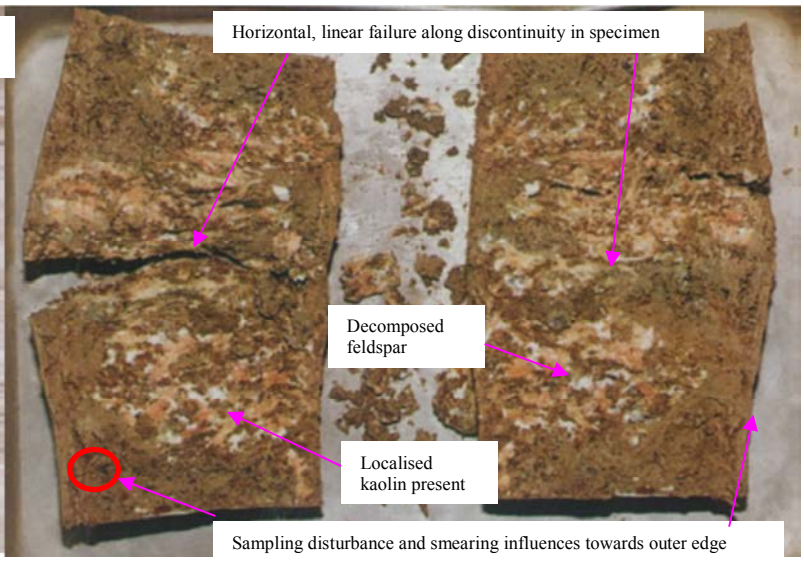

Plate 2: Specimen 1 - Failure Cut Section

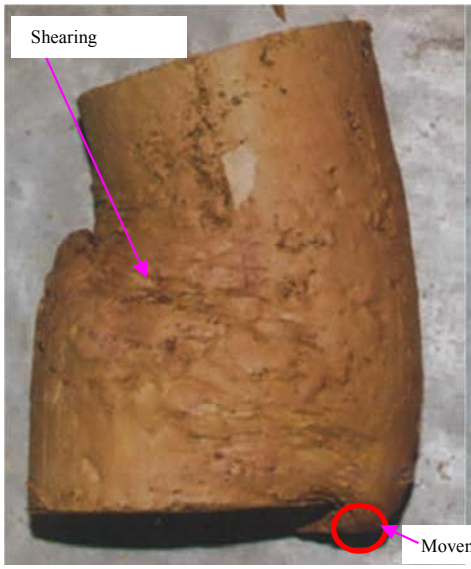

Plate 3: Specimen 2 - Failure

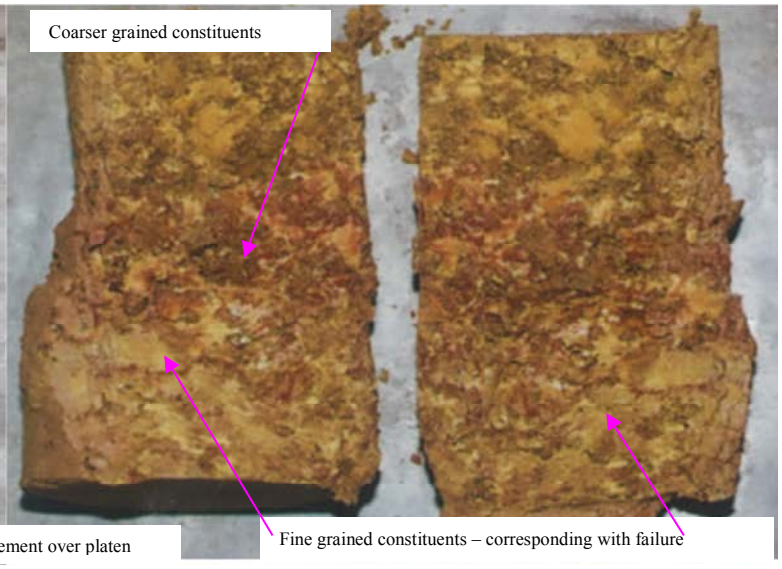

Plate 4: Specimen 2 - Failure Cut Section

Plate 5: Specimen 3 - Failure

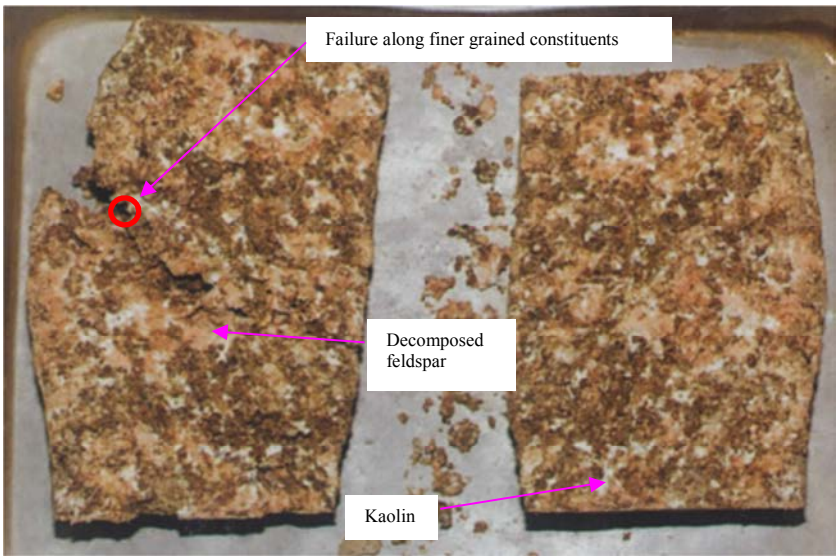

Plate 6: Specimen 3 - Failure Cut Section

The specimen photographs are presented in Plates 1 to 6 and generally show failures corresponding with finer grained constituents, possibly resulting from inconsistent permeation through the specimen. The clays are generally derived from decomposed feldspar and kaolin, which could not have been described from a jar sample. Specimen 1 shows a horizontal failure, which may be due to the sample disturbance during retrieval using the U76 tube.

5 CONSIDERATIONS FOR FUTURE TRIAXIAL TESTING ON SAPROLITES

Considerations on improvements, most of which require a closer review of the Hong Kong standards, are set out below:

- Detailed soil descriptions including effects on the laboratory testing. Whilst Hong Kong sets high standards for the supervising and vetting of staff (BA, 2009 and HKAS, 2009), the qualifications are ultimately derived from a Corporate Membership of a recognised body (mainly civil engineering background). As this lacks the knowledge needed for soil descriptions, relevant to the parameters derived, a more appropriate requirement would be Chartered Geologist with relevant engineering experience. This would still satisfy the GEO (2001) requirements;
- Greater collaboration and interfacing between the GI works and laboratory test team representatives, ensuring consistency in documentation. Due to the demand for rapid submission of the GI documentation, early incorporation of the laboratory data, possibly during specimen preparation, should be carried out;
- For saprolite testing, a realistic strain and effective pressure should be adopted during saturation and consolidation. This prevents rupture of the "bonds" prior to compression;
- Representative effective pressures during schedule preparation, accounting for the soil stress history;
- Different permeability ranges within specimens often prevent a consistent saturation. As a result localised swelling and volume reduction may occur during consolidation. These changes may also rupture the cemented bonds and, in extreme situations, allowed particles to restructure resulting in a significant shear strength reduction;
- The test procedure should consider routine use of side drains to provide more rapid pore water permeation and back pressure application and pore water measurement through the top and base of the specimen; and
- Accurate volume measurement, recording localised specimen failure, should be considered.

6 CONCLUSIONS

A random review of CU triaxial test results reveal the tests have minimal, recorded geological detail and that the results obtained may not represent the peak shear strength results and the strength generated between the cemented bonds from the parent rock. A focus is needed to understand the significance of geological features on the test result, which may require a greater interaction between the GI and laboratory test sub-contractors teams and a greater understanding of the significance of the findings from the designer. Although the results may provide a robust approach to the design they have a danger of being misrepresentative and / or misunderstood.

ACKNOWLEDGEMENTS

The contents of this paper do not necessarily reflect the views and policies of these supporting organizations, nor does the mention of trade names and commercial products constitute endorsement or recommendation for use.

REFERENCES

British Standards Institute (BSI). 1990. Methods of Test for Soils for Civil Engineering Purposes (BS 1377, 1990, Parts 1 to 9). British Standards Institute, London, 1990, 406p.

Building Authority (BA). 2005. Practice Notes for Authorised Persons, Registered Structural Engineers and Registered Geotechnical Engineers, PNAP 167 (APP 64), Methods for Testing Hong Kong Soils (GEOSPEC 3 - Model Specification for Soil Testing), Buildings Department (BD), Hong Kong Special Administration Region (HKSAR) Government.

BA. 2006. PNAP 132 (APP 49), Site Investigation and Ground Investigation. BD, HKSAR Government.

BA. 2010. Code of Practice for Site Supervision, BD, HKSAR Government.

Chen, Y.J. & Kulhawy, F.H. 1993. Undrained strength interrelationships among CIUC, UU and UC tests. J. of Geotechnical Engineering, American Society of Civil Engineers, vol. 119, no. 11, pp 1732-1750.

Cheung, C.K., Greenway, D.R. & Massey, J.B. (1988). Direct shear testing of a completely decomposed granite. Proceedings of the Second International Conference on Geomechanics in Tropical Soils, Singapore, vol. 1, pp109-118.

Eurocode. 1994. ENV 1997-1, 1994, Eurocode 7 Geotechnical Design - Part 1, General Rules. 318

Eurocode. 1999. ENV 1997-2, 1999, Eurocode 7 Geotechnical Design - Part 2, Design Assisted by Laboratory Testing.

Geotechnical Control Office (GCO). 1987. Guide to Site Investigation (Geoguide 2). Geotechnical Control Office, Hong Kong, 362p.

GCO. 1988. Guide to Rock and Soil Descriptions (Geoguide 3), Hong Kong, 189p.

Geotechnical Engineering Office, (GEO). 2007. Engineering Geology Practice in Hong Kong, Government of HKSAR.

GEO. 1992. Guide to Rock and Soil Description, Geoguide 3. Geotechnical Engineering Office, Civil Engineering Development Department, Government of HKSAR.

GEO. 1993. Guide to Retaining Wall Design (Geoguide 1). GEO, Hong Kong, 276p.

GEO. 1994. Geotechnical Manual for Slopes. GEO, CEDD, Government of the HKSAR.

GEO. 1997. Mineralogical and Fabric Characterisation and Classification of Weathered Volcanic Rocks in Hong Kong. GEO Special Report No. SPR 1/97. GEO, Civil Engineering Development Department (CEDD), Government of HKSAR.

GEO. 2000. Guide to Retaining Wall Design, Geoguide 1. GEO, CEDD, Government of the HKSAR.

GEO. 2001. Model Specification for Soil Testing. GEO, CEDD, Government of the HKSAR.

Head K.H. (1992). Manual of soil laboratory testing, Volume 3: Effective stress tests, second edition, John Wiley & Sons, New York.

HKAS. 1998. Regulations for Laboratory Accreditation (2002, Fifth Edition). Hong Kong Accreditation Service, 25p.

Hong Kong Accreditation service (HKAS). 2009. Hong Kong Laboratory Accreditation Scheme (HOKLAS), 003 (9th Edition).

Martin, R.P. (2003). Review of geological aspects of slope engineering. Transactions of the Hong Kong

Institution of Engineers, Vol. 10, No. 3, pp26-33.
Mass Transit Railway Corporation Limited (MTRCL). 2009. Materials and Workmanship Specification for Civil Engineering Works, Volume 3 of 3, Sections 22–25.
Parry, S. & Hart, J.R. 2007. Challenges Facing the Profession. Engineering Geology in Risk Management; Geological Society of London Bicentennial Celebration 1807-2007, 10 November 2007, pp41–44.
Wightman, N.R. 2009. Destabilisation of natural slopes relating to soil density loss – strength reduction. HKIE Geotechnical Division, Proceedings of 29th HKIE Annual Seminar entitled "Natural Hillside – Study and Risk Mitigation Measures, 17 April 2009, pp85-90

Interface Modelling - A Comparison Study Using Finite Element and Boundary Element Methods

H. C. Mark Chan
Geotechnical Engineering Office, Civil Engineering and Development Department, Hong Kong SAR, China
Chao Li
Lambeth Associates Limited, Hong Kong SAR, China

ABSTRACT

Interfaces are often formed during soil-structure interactions. Examples include localised failure within the soil/rock and slippage between the ground and structure during loading. The interface usually has a large length-to-width ratio and non-linear slip-stress relation, which cause substantial difficulties in its modeling. Case studies have been carried out to investigate how the interface can be properly modeled by examining the behaviour of a Direct Shear Test on a rock sample with a joint. The Test is first modeled by a Boundary Element Method using a computer program named FROCK, which incorporates specialised elements to represent interfaces/fractures. Then the Test is modelled using PLAXIS 2D (based on a Finite Element Method), which incorporates interface elements to handle slippage. The results from the two studies are compared. Interesting observations on the sliding behaviour of the interface have been made and the pros and cons of using the two methods are discussed. Practical applications in the conducting of laboratory tests and numerical modeling involving interfaces are also suggested.

1 INTRODUCTION

Interfaces are often formed during soil-structure interactions. Examples include localised failure within the soil/rock and slippage between the ground and structure during loading. The interface usually has a large length-to-width ratio and non-linear slip-stress relation, which cause substantial difficulties in its modeling. Common numerical methods to deal with this problem include the Finite Element Method (Bathe 1982; PLAXIS 2012), the Displacement Discontinuity Method (Crouch and Starfield 1983; Curran and Vadamme 1983) and the Direct and Indirect Boundary Element Methods (Brebbia et al. 1984; Crouch and Starfield 1983).

Case studies have been carried out to investigate how the interface can be properly modeled by examining the behaviour of a Direct Shear Test on a rock sample with a joint. The Test is first modeled by a Boundary Element Method which employs a hybridized scheme using the Displacement Discontinuity and the Indirect Boundary Element Methods (Chan et al. 1990; Vásárhelyi and Bobet 2000). The scheme has been implemented in a computer program named FROCK, which incorporates specialised elements to represent interfaces/fractures. Then the Test is modelled using PLAXIS 2D (based on a Finite Element Method), which incorporates interface elements to handle slippage. The results from the two studies are compared. Interesting observations on the sliding behaviour of the interface have been made and the pros and cons of using the two methods are discussed in this paper.

2 ROCK JOINTS AS INTERFACES

Rock joints (or bedding planes) in otherwise sound rock represent weak zones in which shear failure or slippage could occur when the rock mass is loaded. A common observation of the shearing behavior of a rock joint is shown in Figure 1 (Hoek 2015). The rock joint can be viewed as an interface which has a large length-to-width ratio and non-linear slip-stress relation.

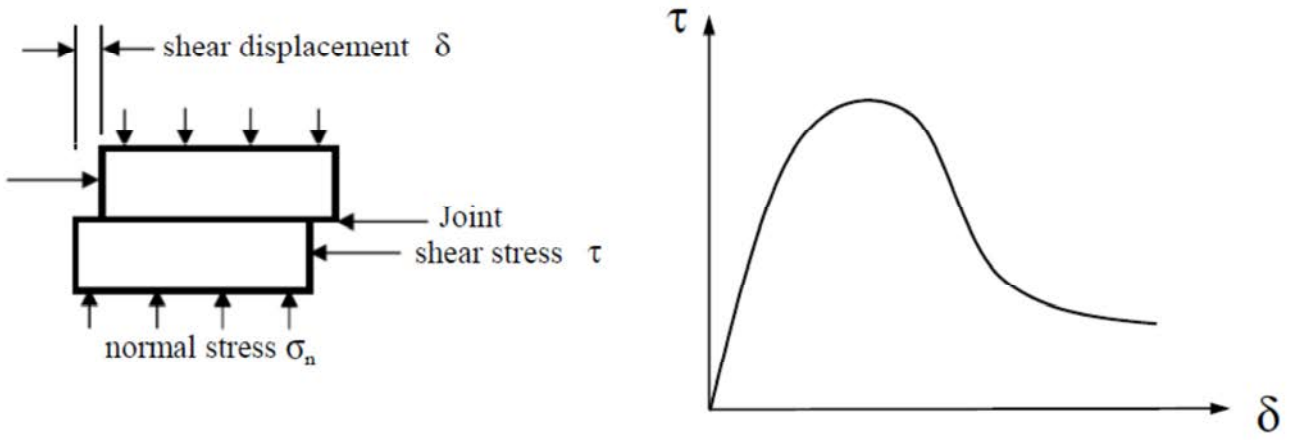

(a) Rock Joint under Shearing (b) A Common Slip-stress relation

Figure 1: Shearing behavior of a rock joint

The relation governing the shear behavior of the joint can be represented by:

$$\tau = \sigma_n f(\delta) + c \tag{1}$$

where τ, σ_n = shear and normal stresses on the joint surfaces respectively, δ = slip (or shear displacement) across the joint surfaces, $f(\delta)$ = friction coefficient as a function of δ and c = cohesive resistance.

3 MODELLING OF THE INTERFACE USING THE DIRECT SHEAR TEST

3.1 Schematic set-up

A basic case of the modeling of an interface is the Direct Shear Test on a rock sample with a joint, which can be shown schematically in Figure 2. The intact rock is assumed to be linear elastic with elastic constants given by Table 1 below.

Table 1: Material Properties of Intact Rock Sample

Young's Modulus (E)	2×10^7 kPa
Poisson's Ratio (ν)	0.25

The joint is assumed to have a small aperture and $f(\delta)$ is approximated by a multi-linear function shown in Figure 2(b).

The bottom of the rock sample is kept fixed. It is noted that the stress/displacement conditions at the left and right ends of the joint (i.e. no shear stress on the vertical and horizontal planes if the end point is regarded to be on the vertical edge and having a shear stress on the vertical and horizontal planes according to the slip-stress relation if it is on the joint) could be ambiguous. However, use of the approximate slip-stress relation at the end of the joint will not introduce additional external forces or moments at the end point, when compared with the case where the true slip-stress relation is used. It is considered that only the stress distribution in a small zone around the end point is affected by the approximation. Therefore, by Saint-Venant's Principle (Sternberg 1954) or the more general Principle of Asymptotic Proportionality (Chan 1990), the effect of the approximation on the overall behavior of the sample is negligible. A seating load of p = 1000 kPa is applied and the top of the sample is slowly sheared. The stresses and displacements in the shearing test are modeled using a Boundary Element Method in Section 3.2 and then modeled using a Finite Element Method in Section 3.3.

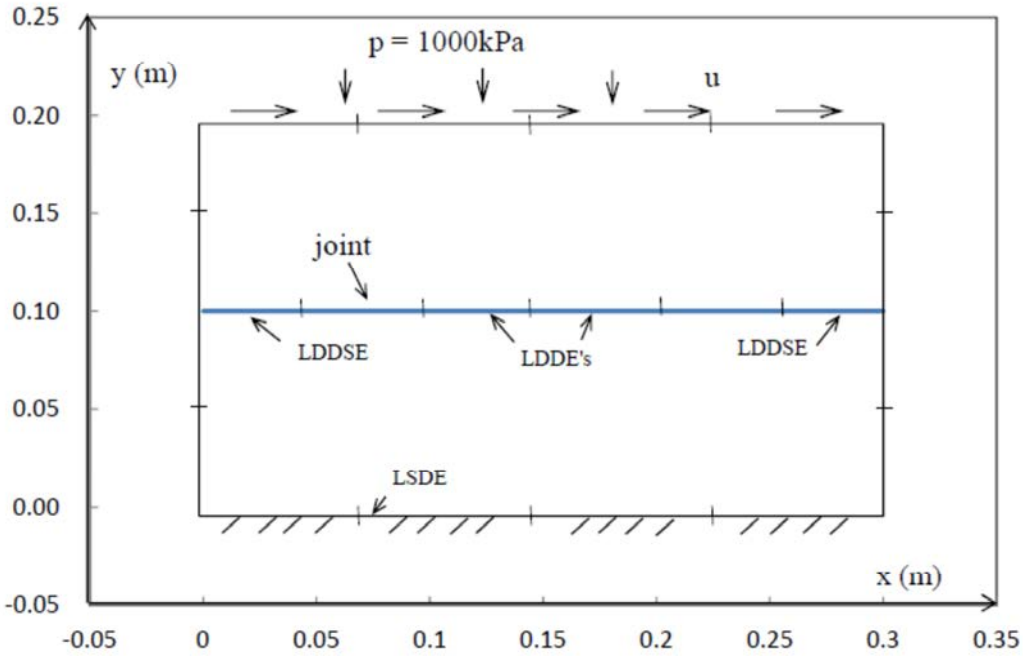

(a) Problem Set-up

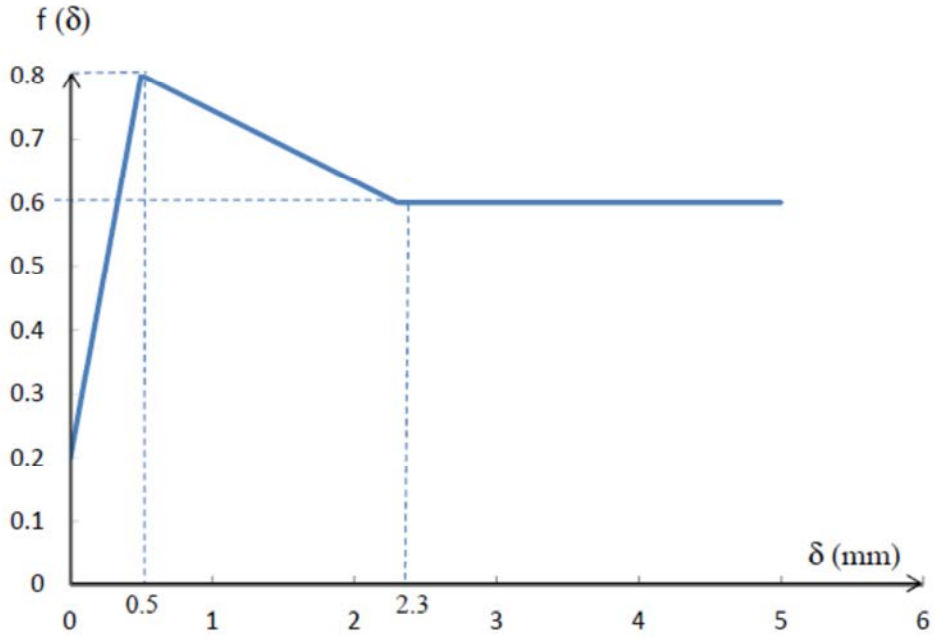

(b) Friction Coefficient

Figure 2: Schematic Set-up of the Direct Shear Test (Chan 1986)

3.2 Modelling using the computer program FROCK

The computer program FROCK (Chan et al. 1990; Vásárhelyi and Bobet 2000; Chan 1993; Chan 1986) basically uses a Boundary Element Method to model a rock mass with discontinuities such as joints and fractures. The intact rock is assumed to be homogeneous and linear elastic while the discontinuities can possess non-linear slip-stress relations. Four Linear Stress Discontinuity Elements are used to model each

edge of the rock sample and the rock joint is modeled by four Linear Displacement Discontinuity Elements with a Linear Displacement Discontinuity Surface Element each at the right end and the left end of the joint.

After application of the seating load, a uniform displacement u is applied slowly to the top edge of the sample. At smaller values of u the joint does not slide and the shear stress along the joint takes an approximately parabolic shape. For example, at u = 8 x 10^{-6} m the shear stress is shown in Figure 3. The normal stress along the joint is shown in Figure 4. It is noted that the normal stress is higher on the right side due to induced stresses which maintain moment equilibrium of the sample.

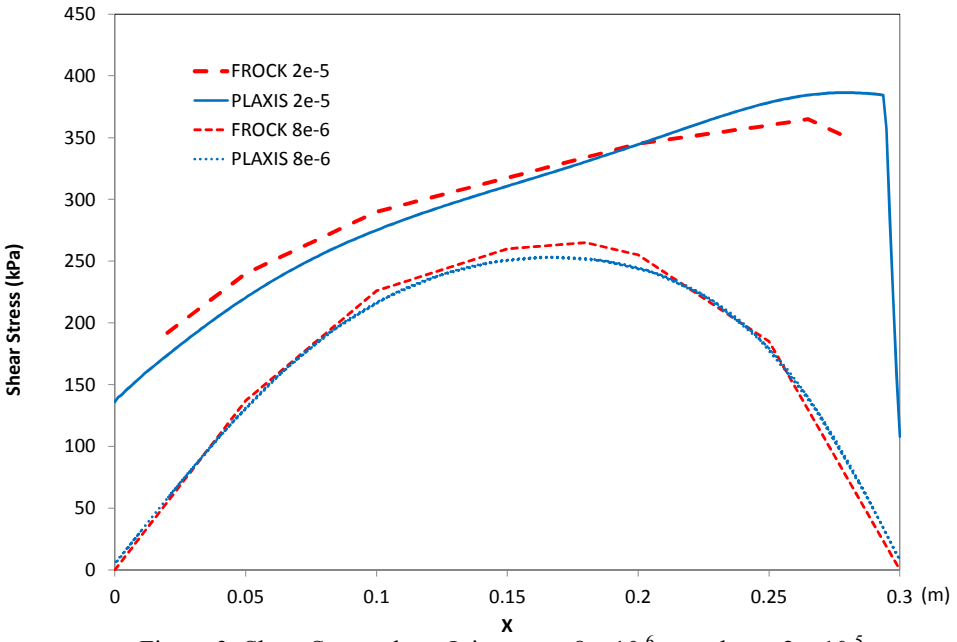

Figure 3: Shear Stress along Joint at u = 8 x 10^{-6} m and u = 2 x 10^{-5} m

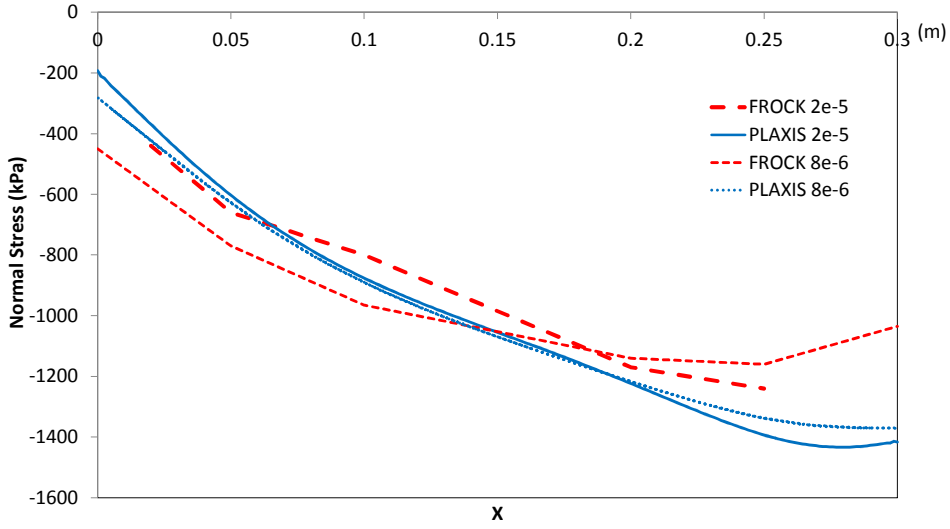

Figure 4: Normal Stress along Joint at u = 8 x 10^{-6} m and u = 2 x 10^{-5} m

As the shear load increases sliding occurs first in the central part of the joint and then spreads towards the two vertical edges of the sample. At u = 2 x 10^{-5} m the entire joint has slid. The normal stress along the joint is plotted in Figure 4. Again it is higher on the right side as required by moment equilibrium. The shear stress is also higher (in magnitude) on the right side partly due to the higher normal stress there (Figure 3). The slip (δ or DS) across the joint is plotted in Figure 5. The slip magnitude is smaller on the right mainly because the

higher normal stress there hinders sliding. The slip magnitude is higher in the middle than on the left because sliding starts in the central part, despite the lower normal stress on the left. As the shear load increases further the slip on the left catches up. The x-displacement u_x along the mid-vertical section at u = 2 x 10^{-5} m is plotted in Figure 6. It can be seen that a jump occurs at the middle due to the slip at the joint. The continuous increase of u_x with y (apart from the joint) is due to the shear deformation of the intact rock. Larger shear loads are not considered in this paper.

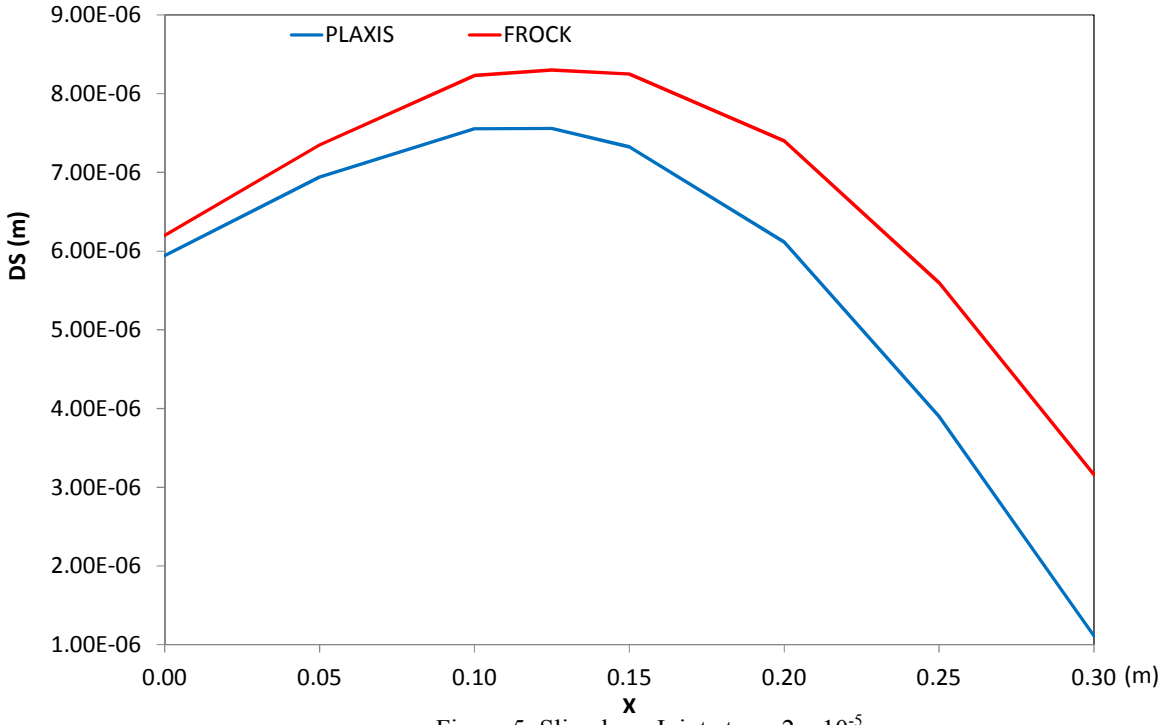

Figure 5: Slip along Joint at u = 2 x 10^{-5} m

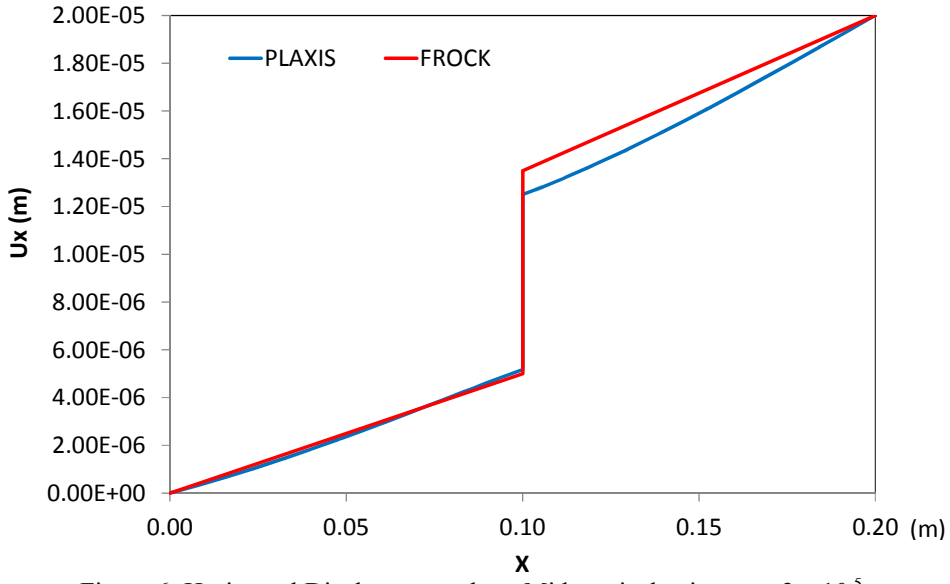

Figure 6: Horizontal Displacement along Mid-vertical axis at u = 2 x 10^{-5} m

3.3 Modelling using the computer program PLAXIS 2D

The computer program PLAXIS 2D (PLAXIS 2012) employs a Finite Element formulation to model general solid mechanics problems. Using interface elements, slip surfaces such as the rock joint in Section 3.2 can be modeled. 15-noded triangular elements are used to represent the intact rock while interface elements are used for the joint. The same seating and shearing loads are applied to the sample (Figure 7).

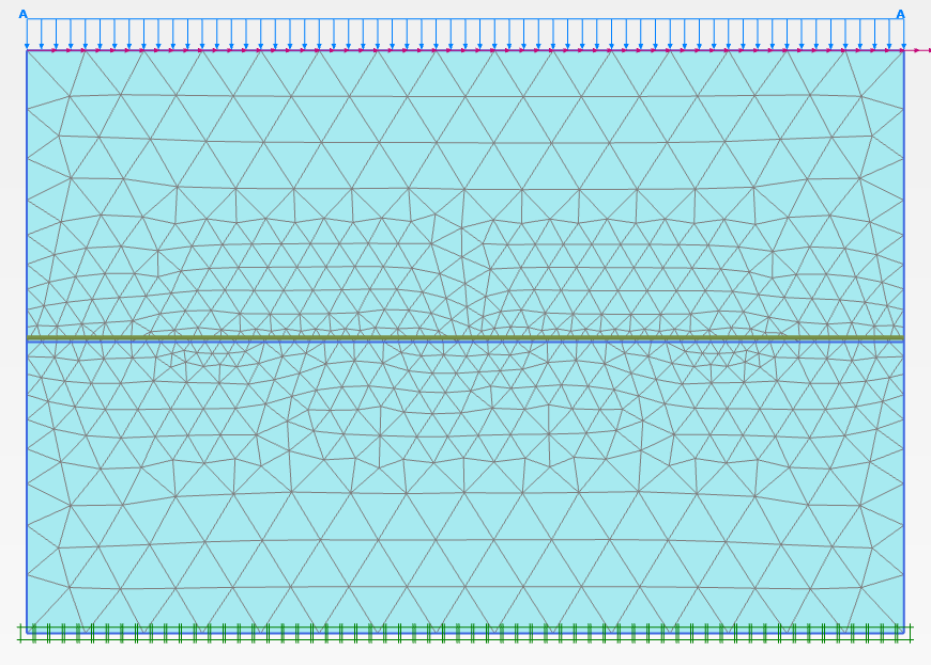

Figure 7: Finite Element Mesh in PLAXIS 2D

Horizontal and vertical fixity is specified at the bottom of the sample. Pressure and horizontal displacements are applied at the top of the sample. The two vertical sides are stress-free except for the top and bottom points.

It is noted that the interface element in PLAXIS is based on a formulation similar to a continuum element. which is convenient for Finite Element Formulation but also implies a number of limitations. Similar to a continuum element, a constitutive model can be directly assigned to an interface. However, post-yielding behavior, and the evolution of yield surface is not straightforward to implement. As a result, the curve in Figure 2 cannot be directly included in PLAXIS 2D.

Interface elements with Mohr Coulomb constitutive law are used in PLAXIS to represent the rock joint. As a result, the strength parameters of the interface element are constant under shear loading. Slippage is developed a result of plastic deformation. After the entire surface has yielded, the load-displacement relationship can only be specified by a hardening-law, which is not included in the Mohr Coulomb formulation. The elastic parameters of the interface elements are the same as the rock while the strength parameters taken from Figure 2(b) are used as in Table 2 below.

Table 2: Material strength properties of the interface element at small slip

cohesion (interface)	100 kPa
$f(\delta)$	0.2

Note that $f(\delta) = 0.2$ was implemented by specifying a Mohr Coulomb material with a friction angle of 14.3 degree.

3.4 Comparison between PLAXIS and FROCK and observations

The comparisons between PLAXIS and FROCK are made in this section.

At u = 8E-6 m, the output normal and shear stresses at the joint are compared with those of FROCK in Figures 3 and 4. As u increases, it is interesting to note that yielding first occurs near the middle of the joint, which is consistent with the observation in the simulation using FROCK. At about u = 1.2E-5 m yielding occurs at the middle portion of the joint and at u = 2.0 E-5 m the entire joint has yielded. At u = 2.0E-5 m, the output normal and shear stresses at the joint are compared with those of FROCK in Figures 3 and 4.

It is noted that the normal stress distributions from the two programs are comparable while the shear stresses show fairly good comparison. It is noted that near the left and right ends of the joint the computed shear stresses are not reliable for the reason given in Section 3.1 above, and thus the stresses there may not be shown in Figures 3 and 4. To show the effect of the joint slip on the behavior of the rock sample, the x-displacement along the mid-vertical section of the sample is plotted in Figure 6. The displacement distributions from the two programs compare fairly well. The slip distributions along the joint from the two programs are compared in Figure 5. The slips on the left side compare satisfactorily while near the right side there are lower slip values from both programs but higher relative differences. This phenomenon is considered to be caused by the two different modeling techniques.

3.5 Observations on the use of the interface element in PLAXIS

It is noted that the "normal way" of using a PLAXIS interface element is to assume that its strength parameters are proportionally reduced from those of its adjacent materials. For example, Page 29 of the PLAXIS 2D 2012 Tutorial Manual suggets that the interaction between the wall and the soil be modelled at bothsides by means of interfaces. The interface allows for the specification of a reduced wall friction compared to the friction in the soil. The proportion of reduction is called $R_{int,}$ the Interface Factor (PLAXIS 2012). The parameter R_{int} relates the strength of the soil to the strength of interface, according to the equations:

$$\tan\phi_{\text{int}\,erface} = R_{\text{int}} \tan\phi_{soil} \tag{2}$$

$$c_{\text{int}\,erface} = R_{\text{int}} c_{soil} \tag{3}$$

In this paper, the interface element is specified directly with independent cohesion and friction coefficient. This would reflect the physical reality in a better fashion.

The users of PLAXIS should also be aware of the limitation that post-yield strength is assumed to be constant, which is an intrinsic characteristic of the Mohr Coulomb model.

To model the slippage development after yielding, a plasticity model with appropriate hardening law could be used. But it appears that this type of interface element has not been recommended in PLAXIS 2D. Also the robustness of the problem and calculation speed may be significantly affected if large plastic zones are involved. It is more desirable to be able to use special elements to simulate an interface, rather than using continuum elements. These special elements do not involve plastic zones or numerical difficulties and are more suitable for large-scale simulation.

We do recognize that the development of a realistic interface element is never an easy task, but we would encourage continuous development which imparts more diversity and flexibility to the program. Alternatively, the authors of PLAXIS may consider representing the interface with Boundary Elements.

4 CONCLUSIONS, FURTHER COMMENTS AND PRACTICAL APPLICATIONS

Modelling of a rock joint with a non-linear slip-stress relation has been carried out using Boundary Element and Finite Element formulations. The computed stresses, displacements and slips from the two programs used are largely in agreement, indicating that the two approaches are sound.

Interesting observations on the sliding behaviour of the interface have been made: As shearing is applied, slippage occurs first in the middle portion of the joint and spreads towards the right and left ends of the joint.

The horizontal displacement at the top of the sample can be considered to comprise the displacement due to the slippage on the joint and the shear deformation of the intact rock. One has to consider this fact when investigating the shear behavior of a rock joint by experiment. To measure the slip of the joint more accurately, pairs of monitoring points should be located close to the joint surfaces, instead of just measuring the relative displacement (u) between the top and bottom of the sample. Normally only one shear stress, one normal stress and one slip value is measured at one time during the shearing test. However, the analyses in this paper show that different portions of the joint could have different stress and slip values at one time. Thus the measured stresses and slip actually represent aggregated values and not point-specific values, and the resultant slip-stress curve actually depends on the experimental set-up and the way loading is applied. To minimize this source of inaccuracy, one may consider measuring the stresses and slips at different locations along the joint. The mesh used by FROCK is much simpler because only the boundaries of the sample are modeled, while PLAXIS 2D models the entire domain. However, PLAXIS 2D is more versatile as different material types are allowed while FROCK deals with a single linear elastic material only, even though the discontinuities can possess non-linear slip-stress relations. Based on this study, it is recommended that the PLAXIS interface element should be modelled by directly specifying the material properties, rather than by specifying an Interface Factor. This recommendation can be implemented in many practical applications. We have also proposed potential improvements of PLAXIS.

ACKNOWLEDGEMENTS

This paper is published with the permissions of the Head of the Geotechnical Engineering Office and the Director of Civil Engineering and Development, The Hong Kong SAR Government.

REFERENCES

Brebbia, C.A., Telles, J.C.F. & Wrobel, L.C. 1983. *Boundary Element Techniques*. Springer-Verlag, NY.

Chan, H.C.M. 1986. Automatic two-dimensional multi-fracture propagation modelling of brittle solids with particular application to rock. MIT Sc.D. thesis. (unpublished).

Chan, H.C.M. 1990. The Principle of Asymptotic Proportionality. *Journal of Applied Mechanics (ASME Transactions)*, Vol 57, March.

Chan, H.C.M. 1993. Fracture Mechanics Analysis of the North West Fault Block of the Prudhoe Bay Field. *International Journal of Rock Mechanics and Mining Sciences,* 30(2).

Chan, H.C.M., Li, V. & Einstein, H.H. 1990. A Hybridized Displacement Discontinuity and Indirect Boundary Element Method to Model Fracture Propagation. *International Journal of Fracture*, Vol. 44.

Crouch, S.L. & Starfield, A.M 1983. *Boundary Element Method in Solid Mechanics*. Allen & Unwin.

Hoek, E. 2015. *Practical Rock Engineering.* Available at http://www.rocscience.com.

PLAXIS 2012. *PLAXIS Finite Element Code for Soil and Rock Analyses: Reference Manual 2D-Version 12.* Delft, The Netherlands.

Sternberg, E. 1954. On Saint-Venant's principle. *Quarterly Appl. Math.,* Vol 11, pp. 393-402.

Vásárhelyi B. & Bobet, A. 2000. Modeling of Crack Coalescence in Uniaxial Compression. *Rock Mechanics and Rock Engineering* 33(2): 119-139.

Evaluation of the Consolidation Behavior of a Settling Ground at Reclaimed Ground of a Container Port in South China

S.L. Chiu, T.T. Fong & S.H. Yung
AECOM Asia Co. Ltd., Hong Kong

ABSTRACT

In reclamation projects, it is often that consolidation of marine deposits would be occurring throughout a long time such that the primary settlement is still ongoing during operation stage of the facility on the reclaimed land. For port work facilities, uneven settlement of the reclaimed ground would cause different settlement of port work structures placed on it, which affects the performance of the port work facilities.

In this paper, site investigation and settlement analysis as well as projection of amount of ongoing settlement in a portion of a container port in South China is presented. At this portion of the Port, uneven settlement of the ground was observed and the performance of gantry crane was affected. The settlement analysis was conducted based on existing settlement monitoring, additional site investigation (including laboratory tests and field tests) and pore water pressure monitoring. The current degree of consolidation was back calculated based on the available information and further residual settlement was estimated. Based on the estimation results, different options of remedial measures to cater for the residual settlement are suggested.

1 INTRODUCTION

1.1 Background

At a portion of a container port in South China which the construction was completed in 2010 and has operated for a few years, uneven settlement was reported within two areas of approximately 55m x 25m and 54m x 21m. In order to maintain good serviceability and performance of the port work facilities, the Authors were commissioned by the port owner (client) to evaluate and provide preliminary advice on the settlement issue.

Based on the information provided by the client and site inspection, the differential settlement within the settlement area was approximately 600mm.

1.2 Site history

Ground improvement was carried out in the site during the construction of the port. As indicated in the as-built drawings provided by the client, the area that uneven settlement occurred included a mud pit, where ground improvement works - dynamic compaction was carried out after the installation of prefabricated band drains (PVD) and surcharging. The relative location of the mud pit and the uneven settlement area are shown in Figure 1.

It was reported that the clay/silt in the mud pit was very weak, and mud wave of approximately 1m in height and 100m in width had occurred during the sand filling in the course of site formation. This information also suggested that the disturbance of clay/silt and low stiffness and strength in the mud pit could be a source of the problem causing uneven settlements between this area and the adjacent areas.

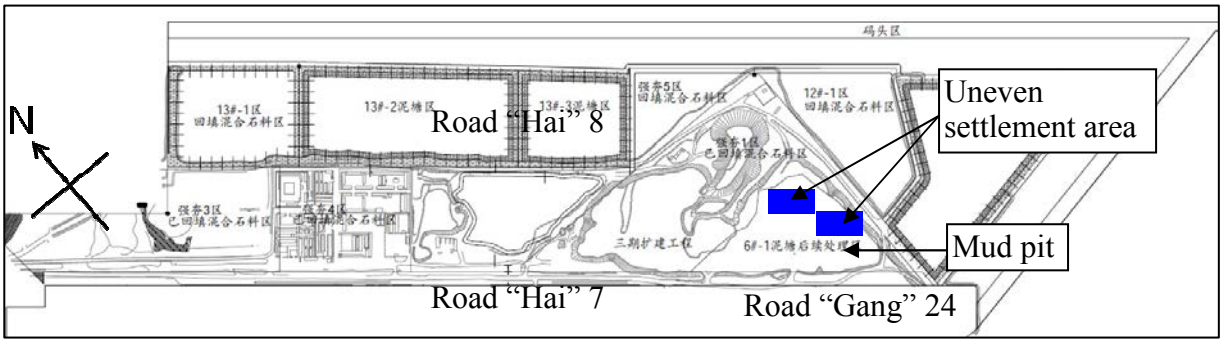

Figure 1: Location of mud pit and uneven settlement area in the port

2 SETTLEMENT MONTORING RESULTS

2.1 Monitored settlement

Ground level survey carried out in this study was compared with the levels shown on the as-built site plan. The results indicated that level difference within the concerned area ranges from 420mm to 1000mm, indicating an average differential settlement of 600mm observed. Figure 2 shows the settlement contours generated based on the surveyed ground level differences aforementioned.

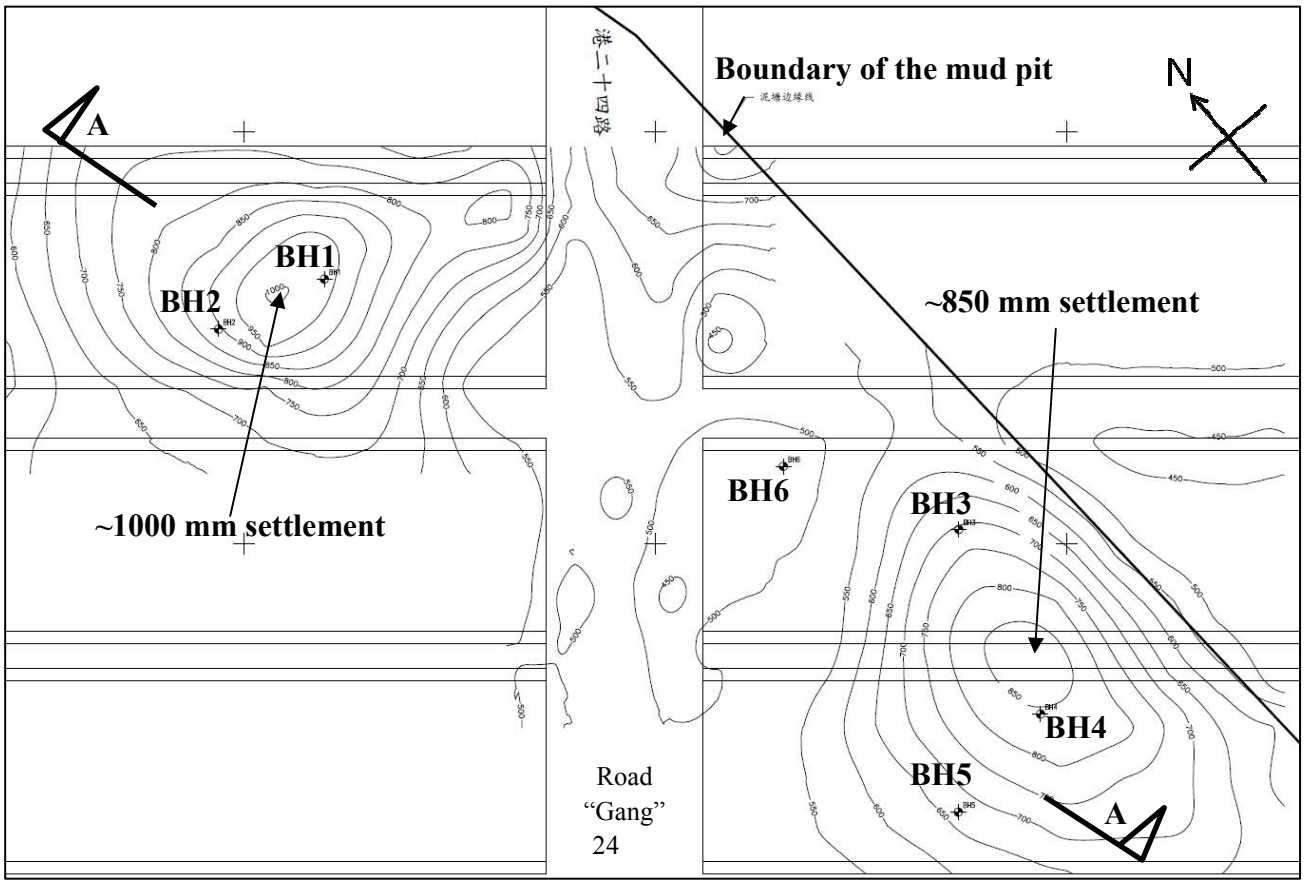

Figure 2: Location of mud pit and uneven settlement area in the port

3 ADDITIONAL GROUND INVESTIGATION AND THE RESULTS INTERPRETATION

3.1 Additional ground investigation

In order to investigate the geological profile of the problematic areas, additional ground investigation including 6 exploration boreholes (locations as shown in Figure 2) was carried out. Field tests and laboratory tests on undisturbed samples collected were also conducted to determine soil parameters and estimate sub-soil conditions of the study areas. Based on the additional ground investigation results, the geological profile of the site is given in Table 1 below. The clay/silt layers were considered to be the layers attributable to the settlement of the ground. A typical geological profile (Section A-A), based on the GI results, is shown in Figure 3. The location of Section A-A is shown in Figure 2.

Table 1: Summary of geological layers of the area with uneven settlement

Soil layer	Depth（m）	Avg. thk. (m)
Rock Fill	0.0 - 8.5	7.1
Clay/silt（upper）	5.8 - 19.6	10.7
Sand	17.1 – 21.8	3.0
Clay/silt（lower）	20.0 – 26.0	4.4
Coarse sand / gravel	23.9 - 28.4	1.9
Highly decomposed granite (HDG)	Below 25.8	--

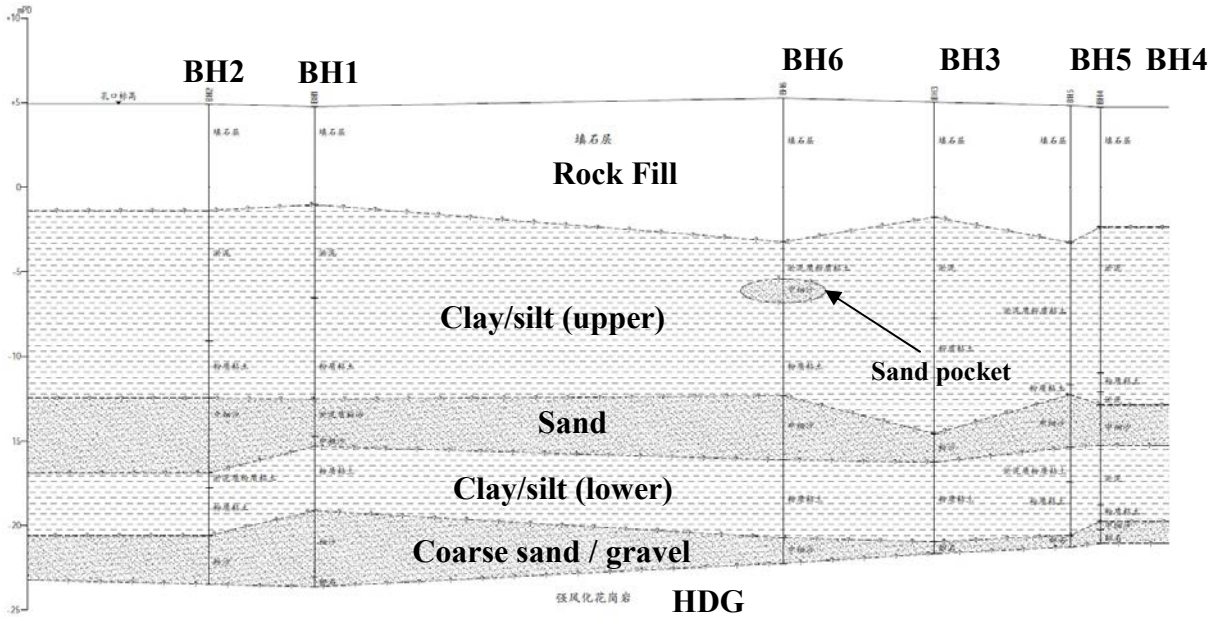

Figure 3: Geological section A-A

3.2 Observations and interpretations from field tests and laboratory tests

Field tests including vane shear tests, Cone Penetration Tests (CPT), piezometers and laboratory tests including unit weight measurements, triaxial tests (Consolidated Undrained, CU and Unconsolidated Undrained, UU), Oedometer tests, Atterberg limits tests were carried out. The data points of plasticity index and liquid limit of the clay/silt are shown in the plasticity chart in Figure 4. The results indicate that the soft layer is generally silt (or clayey silt) of intermediate plasticity. The unit weight and consolidation parameters of the soft layer as determined from the results of laboratory testing are also summarized in Table 2.

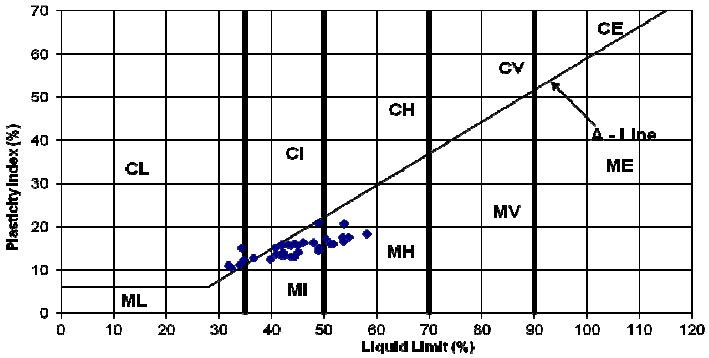

Figure 4: Plasticity index and liquid limit of the clay/silt layer

Table 2: Consolidation parameters of the soft layer

Soil layer	Saturated unit weight, γ (kN/m^3)	Initial void ratio, e_0	Compression index, C_c	Coefficient of vertical consolidation, c_v (m^2/yr)
Mud (淤泥)	16	1.69	0.508	1.081
Clay (黏土)	17.4	1.23	0.313	2.701
Silty clay (粉质黏土)	18.7	0.886	0.188	8.799

The undrained shear strength (S_u) results of the clay/silt layer are also plotted against depth in Figure 5. The data points of vane shear test results are also plotted against its estimated preconsolidation stress (σ_p) when consolidation is completed. It is taken as the effective vertical stress (σ_{vf}') based on the estimated final soil profile and loading when no excess pore pressure remains. The relationship of S_u and σ_{vf}' in Figure 5 is compared with the published data in the literatures for vane shear test data from different sites and its relationship with effective vertical stress (σ_v'). e.g., Figure 58 of FHWA-IF-02-034 (2002).

The data of undrained shear strength (S_u) (uncorrected by Bjerrum's factor) of this study generally ranges from 0.1 to 0.4 p_a, and the estimated preconsolidation stress (σ_p) when consolidation completed are generally at 2 p_a, which lies slightly above the average range of the data points in Figure 58 of FHWA-IF-02-034; and the ratio of S_u/σ_{vf}' of the site is lower than the fitted line in the Figure 58 of FHWA-IF-02-034. It suggests that the effective vertical stress (σ_v') of the test locations are lower than its expected final effective vertical stress (σ_{vf}') when all excess pore pressure is dissipated at the end of primary consolidation.

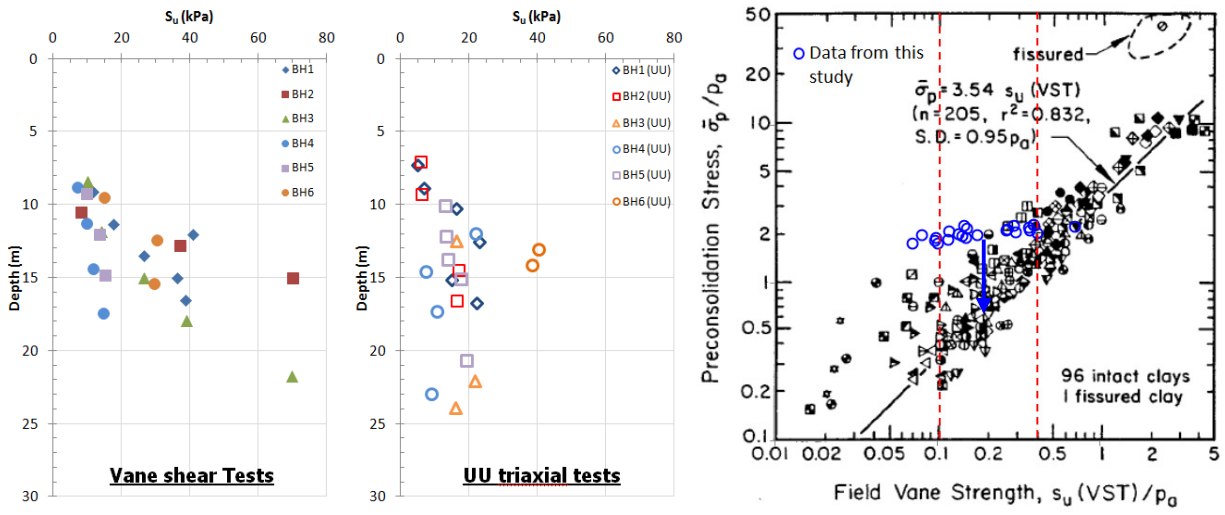

Figure 5: Undrained shear strength of the clay/silt layer and its relationship with final preconsolidation stress when consolidation is completed, the base plot of the rightmost is extracted from Sabatini et.al. (2002), FHWA-IF-02-034 "Evaluation of Soil and Rock Properties", where p_a is atmospheric pressure (~100kPa)

The relationship between undrained shear strength (S_u) and effective vertical stress (σ_v') have been studied by different researchers:

In Figure 58 of FHWA-IF-02-034 by Sabatini et.al. (2002), most data points are located at around $S_u/\sigma_v' = 0.25$.

Mesri (1975) proposed the relationship of the ratio of $S_u/\sigma_v' = 0.22$.

Skempton (1957) proposed the relationship of the S_u/σ_v' ratio with plasticity index (I_p) which is $S_u/\sigma_v' = 0.11 + 0.37I_p$. For the case of this study, the plasticity index of the clay/silt layer generally ranges from 12% to 18%, the S_u/σ_v' ratio would be approximately 0.166 for the mid value 15% taken.

Bjerrum (1972) also proposed a relationship of S_u/σ_v' ratio with plasticity index. The proposed curve and the data that the curve is based on are extracted and copied in Figure 6. For this site with I_p generally ranges from 12% to 18%, the S_u/σ_v' ratio would be approximately 0.18.

Leroueli el. al. (1983) also proposed a relationship of S_u/σ_v' ratio with plasticity index. The proposed curve and the data that the curve based on are extracted and copied in Figure 7. For this site with I_p generally ranges from 12% to 18%, the corresponding S_u/σ_v' ratio would be around 0.20 to 0.24.

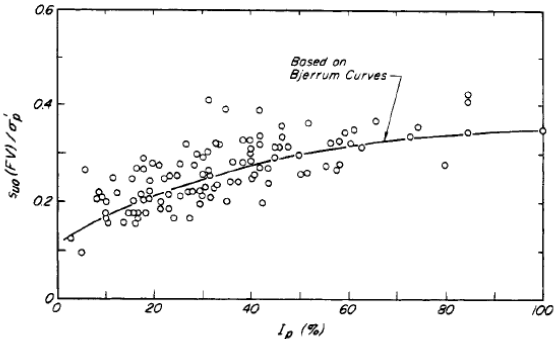

Figure 6: Relationship of S_u/σ_v' and plasticity index I_p by Bjerrum (1972) (figure extracted from "Soil mechanics in engineering practice" by Terzaghi et. al., 1996)

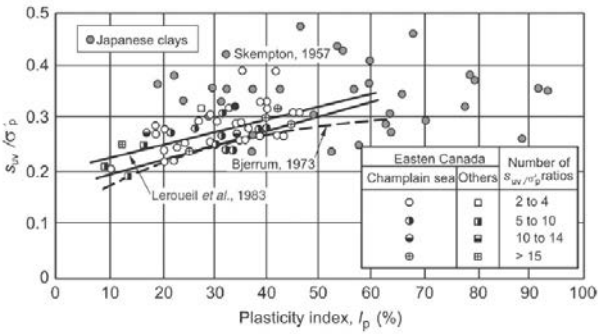

Figure 7: Relationship of S_u/σ_v' and plasticity index I_p by Leroueli et. al. (1983) (figure extracted from "In situ testing in geomechanics" by Schnaid, 2009)

From the above literatures, it is noted that the values of S_u/σ_v' ratio are 0.25, 0.2, 0.18, 0.166 and 0.22, which are around 0.2. In this study, a ratio of S_u/σ_v' for 0.2 has been assumed in back calculation of σ_v' from the measured undrained shear strength (S_u). Figure 8 compares the S_u of vane shear tests and UU tests with the adopted empirical relationship of 0.2 σ_{vf}' that is based on final soil profile and loadings.

The following observations can be made from the plot of S_u from vane shear test and UU triaxial test:

1. At borehole BH3, BH6 and bottom of BH1, BH2, the difference between S_u and $0.2\sigma_v'$ is closer, suggesting that its clay/silt layer might have achieved a higher degree of consolidation.
2. At top of BH1 and BH2, the difference between S_u and $0.2\sigma_v'$ is still large, indicating that at the time of present study its clay/silt layer was still at low degree of consolidation such that excess pore water pressure was still to be dissipated.

Based on the assumed relationship of $S_u = 0.2\sigma_v'$, the effective vertical stress σ_v' is back calculated. Together with the fill thickness and final soil profile, the degree of consolidation (U) is estimated and summarized in Table 3.

The results show that the degree of consolidation at BH4 is the lowest, and the degrees of consolidation at top of BH1 and BH2 are also relatively low. It matches with the observation that the observed settlement near these boreholes is larger (lower settlement rate at later part of consolidation). The degree of consolidation at BH6 is relatively high, and the observed settlement during operation near BH6 is less (higher settlement rate at early part of consolidation).

It is also observed that UU triaxial test tend to give lower S_u values than vane shear tests. As triaxial UU test samples are subjected to sample disturbance and the samples are unconsolidated before triaxial shearing, while the vane shear tests are in-situ tests conducted on site, it is considered that the results from vane shear tests would have higher reliability than triaxial UU tests.

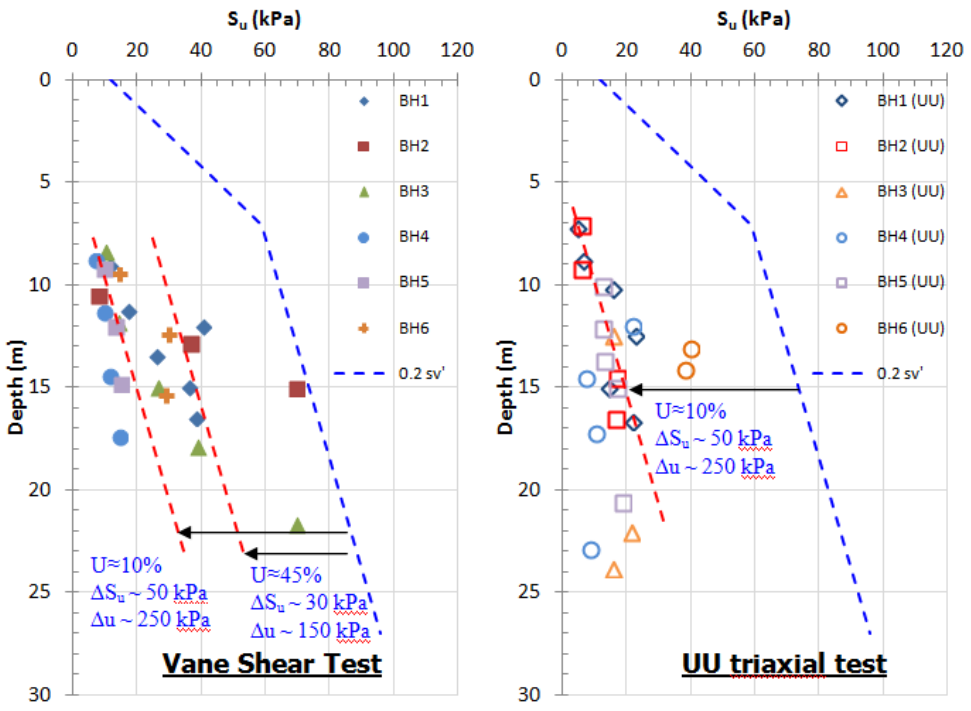

Figure 8: Comparison of undrained shear strength (S_u) with 0.2 σ_{vf}'

Table 3: Estimated degree of consolidation at different boreholes at different depths

Bore-hole	Depth (m)	S_u (kPa)	Fill thk. (m)	σ_{vf}' (kPa)	σ_v' by S_u(kPa)	σ_{v0}' (kPa)	$\Delta\sigma_v$' (kPa)	Degree of consolidation, U
BH1	9.1	11.5	5.8	190.54	57.50	20.43	37.07	**21.8%**
	11.3	17.5	5.8	204.16	87.50	34.05	53.46	**31.4%**
	12	40.6	5.8	208.49	203.00	38.38	164.62	**96.8%**
	13.5	26.3	5.8	217.78	131.50	47.66	83.84	**49.3%**
	15	36.2	5.8	227.06	181.00	56.95	124.05	**72.9%**
	16.5	38.5	5.8	236.35	192.50	66.23	126.27	**74.2%**
BH2	10.5	7.9	6.3	202.68	39.50	26.00	13.50	**7.6%**
	12.8	36.8	6.3	216.92	184.00	40.24	143.77	**81.4%**
	15	69.8	6.3	230.53	349.00	53.85	295.15	**100.0%**
BH3	8.4	10	6.8	179.22	50.00	9.90	40.10	**23.7%**
	11.8	14.1	6.8	200.27	70.50	30.95	39.55	**23.4%**
	15	26.6	6.8	220.07	133.00	50.76	82.24	**48.6%**
	17.9	38.8	6.8	238.03	194.00	68.71	125.29	**74.0%**
BH4	8.8	6.9	7.1	178.78	34.50	10.52	23.98	**14.3%**
	11.3	9.7	7.1	194.25	48.50	26.00	22.50	**13.4%**
	14.4	11.6	7.1	213.44	58.00	45.19	12.81	**7.6%**
	17.4	14.5	7.1	232.01	72.50	63.76	8.74	**5.2%**
BH5	9.2	9.6	8.1	188.69	48.00	6.81	41.19	**22.6%**
	12	13.3	8.1	206.02	66.50	24.14	42.36	**23.3%**
	14.8	15.1	8.1	223.35	75.50	41.47	34.03	**18.7%**
BH6	9.5	14.8	8.5	195.18	74.00	6.19	67.81	**35.9%**
	12.4	30.1	8.5	213.14	150.50	24.14	126.36	**66.9%**
	15.4	29.3	8.5	231.71	146.50	42.71	103.79	**54.9%**

4 REVIEW OF DESIGN

4.1 As-built records of works carried out in the mud pit area

The as-built records of the area that the mud-pit area with uneven settlement occurred were reviewed. Prefabricated vertical drains (PVD) were installed in the area and followed by application of a surcharge preloading. After that, dynamic compaction was carried out with an impact-energy per blow (WH) of 3000 kJ.

Based on FHWA-SA-95-037 "Dynamic compaction", the depth of improvement can be estimated by the equation $D = n (WH)^{0.5}$ (WH in ton-m). The value of n can be referred to Table 7 of the document. For previous soil deposits, the recommended n value is 0.5. By n = 0.5 and WH = 300 ton-m, the improvement depth can be calculated to be 8.7m.

From the borehole logs, the fill thickness is 6m to 8m. Hence the improvement depth of dynamic compaction should be sufficient to improve the fill layer. Also, as the improvement depth of dynamic compaction only reached the top surface of the clay/silt layer, it is unlikely that the dynamic compaction has caused significant disturbance to the clay/silt layer. Excess pore pressure during transient loading would not persist to permanent condition.

4.2 Review on the lower clay/silt layer

As observed from the geological section shown in Figure 3, thickness of the lower clay/silt layer is generally 1/2 to 1/3 of the upper clay/silt layer. Also, the lower clay/silt layer is mainly composed of silty clay, while the compression index (C_c) of silty clay (0.188) is lower than C_c of mud (0.313) which is the main component of upper clay/silt layer. Therefore, for the same increase of effective vertical stress, the total primary consolidation settlement of lower clay/silt layer would be approximately 1/5 to 1/8 of the upper clay/silt layer. It may suggest that the settlement of area is mainly caused by the upper clay/silt layer.

5 SETTLEMENT EVALUATION

5.1 Evaluation of the current site situation

Referring to as-built records of the project, the time from project completion to time of the present study is 7.3 years. The measured settlement after the project completion ranged from 500 to 1000mm. The back-calculated degree of consolidation of clay/silt layer indicated that the consolidation of clay/silt layer is higher at the bottom of clay/silt layer than at the top, it might be probably due to:

1. Mud wave occurred within the area which caused disturbance to the top part of soft clay/silt layer, resulting in damaging of band drains near the top of layer. The function of the drains was affected.
2. Mud wave may have caused a smear zone of low permeability of clay/silt in contact with band drains.
3. Damage to PVD and reduction of permeability lead to lower process of consolidation at the time of surcharge removal. The soil had not been properly over-consolidated under the design load.
4. Excess pore pressure had not yet been fully dissipated and settlement occurred during operation.

5.2 Estimation of current degree of consolidation and residual settlement

As the average fill thickness is 7.1m, and water depth is 4.4m, with 60kPa design loading, the increase of final effective vertical stress is 175.9 kPa. With average increase of effective vertical stress ($\Delta\sigma_v'$) of 78.8kPa occurred as back calculated from $S_u/\sigma_v' = 0.2$, the overall degree of consolidation, U = 78.8 / 175.9 = 44.8%.

As the overall settlement of the area is 500 to 1000mm, taking mid value 750mm, the final settlement is 1674mm. Hence the residual settlement is 924mm.

As the time of consolidation is 7.3 years, with an average clay/silt layer thickness of 11.1m, by equations from Terzaghi's 1-D consolidation theory (as it is observed that the consolidation rate is very slow and performance of PVD within this area is questionable, the back analysis is conducted by vertical drainage), the overall coefficient of consolidation is back calculated to be 0.67 m^2/yr. The overall c_v value based on actual site performance is smaller than the laboratory test value, suggesting that disturbance to the clay/silt layer caused reduction of permeability or increased the clay/silt layer thickness.

Also, based on compression index from laboratory tests and the above loadings, the calculated total primary settlement is 1421mm, which is of similar magnitude to the estimation from overall site performance.

5.3 Pore water pressure measurements

Pore pressure measurements records from piezometers were also reviewed. The monitoring period was approximately one month. By comparing the pore pressure measurements with the hydrostatic water pressure based on the observed water level, the measured pore pressure is slightly above the hydrostatic line and quickly dropped to below the hydrostatic line within the 1 month monitoring period (see Figure 9). The rate of dissipation of pore pressure in the piezometer is much quicker than observed from surface settlement. It is considered that the measured pore pressure could be generated during installation of instruments and quickly dissipated over the monitoring period. Hence the measured pore pressure may have not reflected the actual pore pressure in the soil stratum.

5.4 Limitations of the evaluation method

The method of evaluation in this study is mainly based on the empirical correlation of S_u/σ_v' ratio. As the soil properties of different sites are different, the S_u/σ_v' ratio can be varied among different sites. If the site specific S_u/σ_v' ratio is different from that adopted based on other studies, the estimated degree of consolidation would also vary. However, it is essential that the settlement evaluation based on the empirical correlation had to be verified by the observed site settlement. The settlement evaluation in the present study is generally in good agreement with the site observations and measurements of ground settlement.

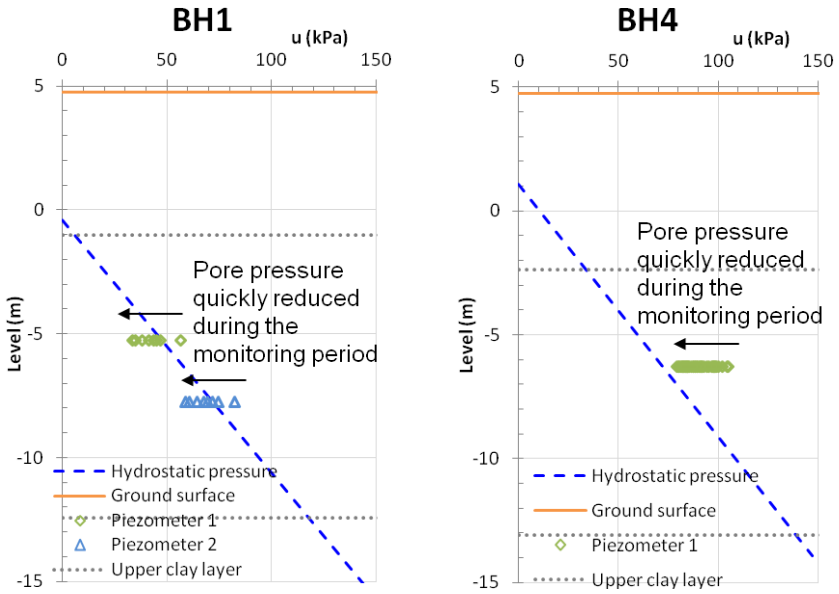

Figure 9: Measured pore water pressure from piezometers installed during additional ground investigation

6 REPAIRING WORKS

6.1 Site constrains to repairing works

Different repairing works were considered for the project. Additional PVD plus surcharge can increase the settlement rate, but require heavy works and long construction time, and penetrating the fill layer would be difficult. Installing soil grout columns can increase the stiffness of the soil to reduce settlement, but would also face construction difficulties for penetrating fill layer and require relatively high construction cost.

Resurfacing is considered to be a more preferred solution as there is no load bearing capacity problem, and the works would require less time and cost.

6.2 Considerations of resurfacing of formation level

Given the site constraints aforementioned, two options were proposed for the resurfacing solution:

1. Resurface the settled ground to be flush with the adjacent areas.
2. Resurface the settled ground to a certain level higher than adjacent areas for future settlement.

As the differential settlement requirement for the gantry crane is 1 : 200, with the settlement area of width 60m, option 1 requires resurfacing for every 150mm settlement, and option 2 requires resurfacing for every 300mm settlement.

Also, additional load would lead to an additional loading of approximately 10 kPa, causing approximately 100mm additional settlement. Hence the total future settlement would be approximately 1000mm.

For option 1, it is estimated that the time of future resurfacing would be at 2.5, 6, 10, 16, 25, 40 years. For option 2, the estimated time of future resurfacing would be at 6, 16, 40 years. The residual settlement-time curve together with the resurfacing time intervals are shown in Figure 10.

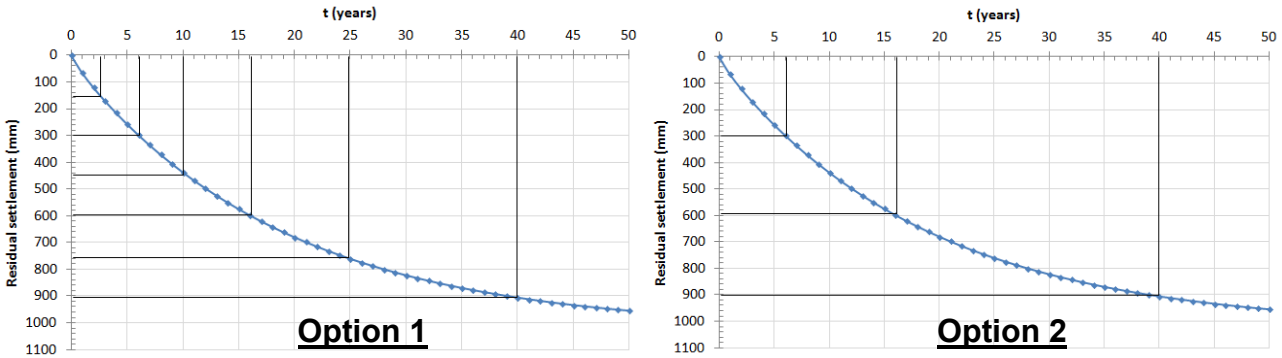

(time t starts from first resurfacing repairing conducted shortly after the study)

Figure 10: Settlement time curve and resurfacing time intervals

7 CONCLUSIONS

This study has made use of the existing monitoring records, additional ground investigation to assess the settlement issue of a site of containing port. The settlement evaluation in the present study is generally in good agreement with the site observations and measurements of ground settlement. Based on the results of present study, repairing works were proposed in order to maintain the site in use as it has been designed for as well as the serviceability of the gantry crane structure for the port operations.

REFERENCES

Bjerrum, L. 1972. Embankments on soft ground. *Proc. ASCE Speciality Conf. on Performance of Earth and Earth-Supported Structures, Purdue University, USA*, 2:1–54.

Bjerrum, L. 1973. Problems of soil mechanics and construction on soft clays. *Proc of 8th Int. Conf. Soil Mech. Found. Engng. Moscow*, 3: 111-159.

Leroueil, S., Tavenas, F., Samson, L. & Morin, P. 1983. Preconsolidation pressure of Champlain clays – Part II: laboratory determination. *Canadian Geotechnical Journal*, 20(4): 803–816.

Lukas, R.G. 1995. *FHWA-SA-95-037 Dynamic compaction*. U.S. Department of transportation.

Mesri, G. 1975. Discussion on new design procedure for stability of soft clays. *ASCE Journal of the Geotechnical Engineering Division*, 101(4): 409-412.

Sabatini, P.J., Bachus, R.C., Mayne P.W., Schneider, J.A. & Zettler, T.E. 2002. *FHWA-IF-02-034 Evaluation of soil and rock properties*. U.S. Department of transportation.

Schnaid, F. 2009. *In situ testing in Geomechanics, the main tests: 275-276*. Taylor & Francis Group.

Skempton, A.W. 1957. Discussion of 'Planning and design of New Hong Kong Airport'. *Proc. Instn Civ. Engrs,* 7: 305–307.

Terzaghi, K., Peck, R.B. & Mesri, G. 1996. *Soil mechanics in engineering practice*. Wiley-Interscience Publication.

AECOM

DESIGNING MORE INNOVATIVELY

With unparalleled underground expertise and worldwide experience, AECOM is always a trustworthy partner to deliver innovative solutions to overcome complex geology challenges faced by our clients.

AECOM, recently joined by URS, is a premier, fully integrated support services firm. With nearly 100,000 employees serving clients in more than 150 countries, we are a leader in all the key markets we serve, including transportation, facilities, environmental, energy, water and government.

www.aecom.com

World's largest underground terminal – aerial view of the West Kowloon Terminus under the Hong Kong Section of the Express Rail Link project